

Magnetically induced dynamics of mesoscopic colloidal systems



Von der Universität Bayreuth
zur Erlangung des Grades eines
Doktors der Naturwissenschaften (Dr. rer. nat.)
genehmigte Abhandlung

von

Johannes Löhr

aus Bayreuth

1. Gutachter: Prof. Dr. Thomas M. Fischer
2. Gutachter: Prof. Dr. Werner Köhler
3. Gutachter: Prof. Dr. Udo Seifert

Tag der Einreichung: 28.11.2017
Tag des Kolloquiums: 12.04.2018

Abstract

This cumulative thesis is dedicated to the experimental and theoretical study of the dynamics of mesoscopic colloidal systems. I am presenting new strategies for the manipulation of micrometer sized living and non-living colloidal particles based on magnetic fields. I am thereby following three different approaches that either aim to design novel mechanisms for the transport of colloidal particles or to use colloids as model systems for dynamic phenomena in other condensed matter systems. The three parts are (i) the topologically protected transport of colloidal particles, (ii) the magnetic guidance of magnetotactic bacteria and (iii) the dynamics of monopole defects in artificial colloidal ice.

In the first part I am presenting a novel approach for the transport of magnetic colloidal particles based on topological protection. The colloids are placed above a periodic magnetic lattice of alternating domains with a lattice constant of the order of the particle size. The system is driven by closed periodic modulation loops of a time-dependent external magnetic field. With a clever choice of modulation loops it is possible to transport the particles via adiabatic or deterministic ratchet motion. The theoretical investigation of the connection between the driving loops and the colloidal motion shows that the transport in our system is topologically protected. In consequence the colloidal motion turns out to be robust, for example against thermal fluctuations or details of the modulation loops. Therefore multiple particles can be transported in a dispersion free manner. Beyond that it is even possible to simultaneously control two different types of particles (paramagnetic and diamagnetic colloids) and to move them into independent directions. The topology is thereby inherently connected to the symmetry of the magnetic lattices. Different symmetries favor distinct transport modes. This is used to implement a colloidal topological insulator. Colloids can be stably guided along arbitrary edges between patterns of different symmetry without explicit information over their location or orientation.

In contrast to the topologically protected transport of passive particles, the mechanism in the second part is based on actively swimming particles. I am using magnetotactic bacteria, which have a internal permanent magnetic moment. This facilitates the manipulation of the bacteria with external magnetic fields. Magnetotactic bacteria are therefore suitable to study the influence of external constraints on the bacterial motion. The bacteria are placed to swim above the magnetic domain structures of garnet films, which allows the stable guidance of magnetotactic bacteria along straight or curved stripe domains. Two features are important for this, the active swimming of the bacteria and the magnetic forces and torques exerted on the magnetic moment of the bacteria. A careful balance of these two ingredients results in a stable guidance of the magnetotactic bacteria.

The last part is not concerned with the transport of the mesoscopic particles themselves

but with their use as a model system for spin ice. The elementary magnetic moments (spins) of this remarkable material are strongly frustrated, which results in a highly degenerate ground state. The basic excitations of the spins turned out to be emergent magnetic monopoles. Here I am using a colloidal system to model the dynamics of spins and monopole defects in a two dimensional projection of the spin ice crystal. The colloidal particles are confined in a gravitational double well structure. The collective behavior of the interacting magnetic colloids resembles the frustrated behavior of the spins in spin ice. With the help of colloidal spin ice I observed the dynamics of monopole excitations in real-time, which allowed to draw conclusions on the interactions between pairs of defects. This way I could experimentally confirm that defects in fact show a characteristic monopole behavior. Beyond that I am using colloidal spin ice to realize a universal logic gate based on monopole excitations and suggest a novel approach to recover the degenerate ground state of the original 3D spin ice in the 2D colloidal model system.

Kurzdarstellung

Diese kumulative Dissertation widmet sich der experimentellen und theoretischen Untersuchung der Dynamik mesoskopischer kolloidaler Systeme. Ich präsentiere neue Strategien zur Manipulation von mikrometergroßen, lebenden und nicht lebenden, kolloidalen Teilchen, die auf Magnetfeldern basieren. Dabei verfolge ich drei verschiedene Ansätze, die entweder darauf abzielen neue Mechanismen für den Transport von Kolloiden zu entwerfen, oder Kolloide als Modellsysteme für dynamische Phänomene in anderen Systemen der kondensierten Materie zu verwenden. Die drei Teile dieser Arbeit sind (i) der topologisch geschützte Transport kolloidaler Teilchen, (ii) die magnetische Führung magnetotaktischer Bakterien und (iii) die Dynamik von Monopoldefekten in künstlichem kolloidalem Eis.

Im ersten Teil präsentiere ich eine neue Herangehensweise für den Transport von magnetischen Kolloiden, die auf topologischem Schutz basiert. Die Kolloide werden auf der Domänenstruktur eines periodischen magnetischen Musters platziert, welches eine Gitterkonstante in der Größenordnung der Teilchengröße hat. Das System wird durch die geschlossene und periodische Modulation eines zeitabhängigen externen Magnetfeldes angetrieben. Durch eine geschickte Wahl dieser Modulation ist es möglich, die Kolloide adiabatisch oder per deterministischer Ratsche zu transportieren. Durch die theoretische Untersuchung des Zusammenhangs zwischen der externen Modulation und der kolloidalen Bewegung konnte gezeigt werden, dass der Transport in unserem System topologisch geschützt ist. Infolgedessen ist die kolloidale Bewegung robust, zum Beispiel gegen thermische Fluktuationen und Details der externen Modulation. Daher können viele Kolloide gleichzeitig und dispersionsfrei transportiert werden. Darüber hinaus ist es sogar möglich, zwei verschiedene Teilchensorten (paramagnetische und diamagnetische Kolloide) unabhängig voneinander zu kontrollieren und in verschiedene Richtungen zu bewegen. Topologie und Symmetrie der magnetischen Gitter sind dabei untrennbar verbunden. Verschiedene Symmetrien begünstigen unterschiedliche Transportmoden. Diese Tatsache wird verwendet, um einen kolloidalen topologischen Isolator zu implementieren. Kolloide können stabil entlang der Grenzen zwischen zwei Mustern, mit unterschiedlicher Symmetrie, transportiert werden. Dabei ist keine explizite Information über die Position oder Orientierung dieser Grenze notwendig.

Im Gegensatz zum topologisch geschützten Transport passiver Kolloide basiert der im zweiten Teil vorgestellte Ansatz auf aktiv schwimmenden Teilchen. Ich benutze magnetotaktische Bakterien, die ein internes permanentes magnetisches Moment besitzen. Dies ermöglicht die Manipulation der Bakterien mit externen Magnetfeldern. Magnetotaktische Bakterien sind daher hervorragend geeignet, um den Einfluss von außen auferlegter Zwänge auf die bakterielle Bewegung zu untersuchen. Die Bakterien werden dazu auf Granatfilmen platziert, sodass sie oberhalb der Domänenstruktur schwimmen können. Diese Konstellation erlaubt die stabile Führung magnetotaktischer Bakterien entlang gerader oder gekrümmter Streifendomänen. Zwei Merkmale sind dafür wichtig. Zum

einen das aktive Schwimmen der Bakterien und zum anderen die magnetischen Kräfte und Drehmomente, die auf das magnetische Moment der Bakterien wirken. Ein sorgfältig ausbalanciertes Gleichgewicht dieser beiden Bestandteile führt zu einer stabilen Bewegung der magnetotaktischen Bakterien.

Der letzte Teil dieser Arbeit befasst sich nicht mit dem Transport der mesoskopischen Teilchen selbst, sondern mit ihrer Verwendung als Modellsystem für Spin-Eis. Die elementaren magnetischen Momente (Spins) dieses bemerkenswerten Materials sind geometrisch frustriert, was zu einem vielfach entarteten Grundzustand führt. Die elementaren Anregungen in Spin-Eis sind magnetische Quasi-Monopole. In meiner Arbeit verwende ich ein kolloidales System, um die Dynamik von Spins und Monopolanregungen in einer zweidimensionalen Projektion des Spin-Eis Kristalls nachzubilden. Die kolloidalen Teilchen werden durch die Gravitation in Doppelmuldenstrukturen eingeschlossen. Das kollektive Verhalten der wechselwirkenden magnetischen Kolloide bildet die Verhalten der frustrierten Spins im Spin-Eis nach. Ich benutze dieses kolloidale Modellsystem, um die Dynamik von Monopolanregungen in Echtzeit zu studieren, wodurch sich Rückschlüsse auf die Wechselwirkungen zwischen Defektpaaren ziehen lassen. Auf diese Weise konnte ich experimentell bestätigen, dass Anregungen in Spin-Eis tatsächlich ein charakteristisches Monopolverhalten zeigen. Darüber hinaus verwende ich das kolloidale Modellsystem, um ein universelles Logikgatter auf der Basis von Monopolanregungen zu realisieren, und stelle einen neuen Ansatz vor, um den entarteten Grundzustand des ursprünglich dreidimensionalen Systems im zweidimensionalen, kolloidalen Modellsystem wiederherzustellen.

Table of Contents

Abstract	iii
Kurzdarstellung	v
I Magnetically induced dynamics of mesoscopic colloidal systems	1
1 Physics of colloidal motion	3
2 Topological protection	11
2.1 The concept of topological protection	12
2.2 Topologically protected colloidal transport	19
2.3 Summary and discussion	25
3 Magnetic guidance of magnetotactic bacteria	29
3.1 Magnetotactic bacteria	30
3.2 Guidance of the fitter	32
3.3 Discussion	33
4 Defect dynamics in spin ice	35
4.1 Geometrical frustration	36
4.2 Water ice and residual entropy	36
4.3 Spin ice and emergent magnetic monopoles	38
4.4 Artificial spin ice	40
4.5 Artificial colloidal ice	44
4.6 Defect dynamics in artificial colloidal ice	47
4.7 Restoring the residual entropy in artificial colloidal ice	48
4.8 Summary and outlook	51
A Materials and Methods	53
A.1 Topologically protected transport and magnetic guidance of bacteria . . .	53
A.2 Artificial colloidal ice	58
Acknowledgments	61
Bibliography	63

II Publications	75
Publication 1	
Lattice symmetries and the topologically protected transport of colloidal particles	77
Publication 2	
Topological protection of multiparticle dissipative transport	111
Publication 3	
Topologically protected colloidal transport above a square magnetic lattice	130
Publication 4	
Colloidal topological insulators	141
Publication 5	
Magnetic guidance of the magnetotactic bacterium <i>Magnetospirillum gryphiswaldense</i>	147
Publication 6	
Defect Dynamics in Artificial Colloidal Ice: Real-Time Observation, Manipulation, and Logic Gate	155

Part I

Magnetically induced
dynamics of mesoscopic
colloidal systems

Chapter 1

Physics of colloidal motion

Motion on the mesoscopic scale is essential for living organisms. Nutrients and other molecular cargo need to be transported through the body in various purposes, either between different cells or within single cells [1]. The investigation of such dynamic processes requires a fundamental understanding of motion at this scale. This thesis aims to contribute to this. I am studying the magnetically induced dynamics of living and non-living mesoscopic colloidal particles.

A colloid is a mixture of mesoscopic nanometer to micrometer sized particles (colloidal particles, often they are also-called colloids), which are dispersed in a continuous phase, e.g. water. I am using particles with a size of a few microns. Colloids appear in a lot of products we use on a daily basis including cosmetics, pharmaceuticals and food [2]. The macroscopic properties like the viscosity of colloidal suspensions are strongly dependent on the microscopic details, e.g. the interaction potential between the colloidal particles [3]. The dynamics of such soft matter systems is of current interest in experimental and theoretical physics [4, 5] and is subject of this thesis. There are several fundamental questions related to motion on the mesoscopic scale. The most important question is of course how to mediate transport. In general there are two opposing strategies to achieve motion, that is passive transport or active locomotion. Passive motion is induced by external forces applied to an object. In contrast, active motion requires an advanced mechanism of the object itself. It is almost always based on periodic changes of the conformation of the object, which are translated into a linear translation in various different ways. The most obvious example is a walking person. The periodic rearrangement of our legs translates us above a solid surface. These two distinct strategies for motion have a very universal character. Nonetheless the details of the realization are of course different on the mesoscopic scale. The central question is therefore how to implement suitable transport mechanisms for mesoscopic particles. This question as well as the two potential solutions, active and passive transport, will guide us through the whole thesis. I am using magnetic fields to manipulate the motion of colloidal particles. Due to the long range of magnetic interactions, magnetism is a perfect candidate to apply forces at the mesoscopic scale. Other microscopic interactions, like for example the van der Waals interaction or electrostatic interaction, which is screened in physiological environments [6], have a low effective range of only a few nanometers and are therefore less suitable candidates for the study of mesoscopic objects. There is a broad availability of paramagnetic and ferromagnetic colloidal particles, both living and non-living. To manipulate the magnetic colloids I am using a combination of a time-dependent external field and the heterogeneous field of ferrite garnet films. Garnets are ferrimagnetic materials which have magnetic domain structures that vary on the size of the colloidal

particles. Therefore they are predestined to control passive as well as active colloidal transport.

Beyond the choice of suitable interactions the surrounding fluid is another important aspect for colloidal motion. Mesoscopic Reynolds numbers $Re \ll 1$ are small¹. Hence inertia becomes negligible and motion is governed by viscous forces. In addition thermal fluctuations become important at the mesoscopic length scale. For stable transport it is thus important to either overcome fluctuations or to harness and to convert them into directed motion [7]. In summary there are a lot of fundamental challenges that have to be faced to achieve reliable mesoscopic transport.

Nature has its own rich toolbox of fascinating transport mechanisms including both, passive and active strategies [1]. The first mechanism is exemplified by the advective carrying of oxygen and nutrients in the blood flow. The second one relies on active micro-transporters, so-called molecular motors. A well known example is Kinesin. It is used for the intracellular transport of molecular cargo or in the mitosis, the division of the cell nucleus [9]. Kinesin moves along predefined tracks on the cytoskeleton of the cells, the microtubule filaments. The motor protein consists of a tail and two heads of which one is always bound to the microtubule. The motion of Kinesin is powered by the hydrolysis of ATP, the energy currency of biological systems. One cycle consists of the binding of ATP, its hydrolysis and the final release of ADP. This chemical cycle is directly related to a cyclic change in the conformation. First the Kinesin protein rotates, then the free head binds to the track and in the last step the other head, that was bound before, is released. This results in a step of 8 nm, which is exactly one repetition unit of the microtubule. Hence one chemical cycle corresponds to one translation step. The periodic repetition of this process allows the motor protein to actively move along its track over huge distance up to the order of micrometers. The commensurability of the chemical cycle and of the step width with the periodicity of the track on which it moves is an essential ingredient for the proper functionality of this molecular motor. Similar commensurability questions will play an important role for the motion in my mesoscopic systems.

Advances in microscopic fabrication technologies favored the emergence of artificial miniaturized micro machines. Natural molecular motors are thereby a constant source of inspiration. Designing, engineering and building micro machines has become one of the major tasks in current soft matter physics. Artificial mesoscopic systems with precisely engineered properties are perfect tools to study existing and to develop new fundamental strategies for mesoscopic motion [10]. Alongside there are also a lot of potential applications for such systems. A prominent example is health care, both inside and outside of living organisms. This includes among many other examples the targeted delivery of drugs [11, 12].

The ultimate goal in this regard is the so-called *lab on a chip* [13]. Some 50 years ago computers used to occupy big halls [14]. Nowadays everyone of us can carry a computing

¹The Reynolds number is defined as $Re = \rho dv/\eta$ [8]. In water the dynamical viscosity is $\eta \approx 1\text{mPas}$ and the density is $\rho \approx 10^3\text{kg/m}^3$. The typical speed of particles in the used colloidal system is $v = 10\ \mu\text{m/s}$ and a typical size is $d = 1\ \mu\text{m}$. This results in a Reynolds number $Re = 10^{-5} \ll 1$.

device, which is even way more powerful, in the pocket. The idea behind lab on a chip devices is the same. Today chemical processing is done by chemists in big laboratories. The dream is to automatize and to miniaturize chemical tasks down to size of a chip card. The accurate mediation of miniaturized chemical reactions requires a reliable transport of smallest amounts of reactants within a very limited space. Therefore one of the first steps towards the realization of lab on a chip devices has to be the fundamental understanding of the required mesoscopic transport processes. Like in the natural archetype there exist two distinct ways of achieving transport on this small scale. The first is passive transport of cargo in advective flows. The investigation and manipulation of flows at the scale of micrometers is known as microfluidics [15]. Smallest volumes (a few microliters) of fluids can be transported in narrow channels of only several micrometers in width. In this thesis however, I will focus on the second approach, which is based on micro-transporters. These carriers are employed to transport cargo to desired locations or along predefined paths. Suitable candidates are biological molecular motors transferred to artificial environments [16] or artificially constructed molecular motors [17]. A third, alternative approach is the use of passive colloidal particles. Here I am referring to colloids in a very classical sense, that is mesoscopic polystyrene or silica spheres dispersed in water.

The advantage of these particles is that their surfaces can be chemically functionalized. Therefore colloids can fulfill a lot of diverse chemical tasks, which makes them important tools for example in medical application. Examples are given by the separation of biological cells from blood on micro-devices [18, 19] or the hyperthermia treatment of cancer [20]. In the latter magnetic colloids are injected into a tumor. Upon application of an oscillating magnetic field the particles start to rapidly move, which generates heat and destroys tumor cells. However, the probably most important role of colloidal particles is their use as micro carriers for molecular cargo [21]. With short DNA strands bound to their functionalized surface [22], the exploitation of hydrodynamic flows [23] or the use of colloidal rings [24] basically any cargo can be attached to colloidal particles. Moving the particles via external fields results in the desired transport of the attached cargo [25].

This thesis is concerned with the fundamental study of the dynamics of mesoscopic colloidal particles. I am presenting two novel approaches, one is based on passive colloids and the other one on actively swimming particles.

The question in the first part is how to achieve reliable transport of passive colloidal particles. There exist a lot of standard techniques to control colloidal particles, including gradient fields [26], liquid crystal based solvent [27] or thermal ratchets [28]. One of the problems is the intrinsic polydispersity of colloids. There is always a certain distribution in the particle properties like size, mass or susceptibility. For this reason transport with the above mentioned strategies will always result in a diffuse broadening of the particle trajectories, which makes these mechanisms unsuitable for the transport of big collections of particles.

I am going to show an alternative to the prior mechanisms which overcomes these limitations. Magnetic colloidal particles are transported above a periodic magnetic pattern

of e.g. a garnet film. The motion is driven by periodic modulation loops of an external magnetic field. The idea to use garnet films for colloidal transport has already been successfully tested [25]. However the transport in these previous systems is based on thermal ratchet motion of colloidal particles. Non-equilibrium thermal fluctuations in the system cause irreversible jumps of the particles between the wells of an underlying potential. The motion can be directed by an asymmetry of the potential [29]. Due to complicated correlations between noise [30], disorder [31] and particle interactions [32], the thermal ratchet motion is complex. It is already difficult to direct the motion of a single particle and hence virtually impossible to maintain simultaneous control over the transport of two different types of particles.

The novel approach that I present in this thesis is based on topological protection. Colloidal particles are transported via adiabatic or deterministic ratchet motion. Therefore the transport no longer relies on the complicated thermal ratchet mechanism. Furthermore the system is extended to two distinct types of particles, paramagnetic and diamagnetic colloids². There exist periodic modulation loops of the external magnetic field, that allow for the simultaneous control over both types of particles. Despite the use of passive particles the basic mechanism of motion is similar to the one applied by active particles. In Kinesin each chemical cycle translates the protein by one step. In the colloidal transport it is an appropriate cycle of the external modulation that transports the passive particles by one unit vector of the magnetic lattice. The externally imposed driving thereby allows to easily manipulate the motion from outside.

To explore the connection between the modulation loops of the external field and the transport of colloidal particles, a new theoretical framework is developed. With the help of this theory I could prove that the transport of colloidal particles in our system is topologically protected. Topological protection ensures a great robustness of the particle transport. It is for example stable against thermal fluctuations, details of the modulation loops or disorder in the magnetic structures. This enables the dispersion free transport of huge collections of particles. Depending on the symmetry of the magnetic pattern it is even possible to transport paramagnetic and diamagnetic particles into independent directions. Lattices of different symmetries are also used to implement a colloidal topological insulator. The colloidal topological insulator as well as the possibility of two independent transport directions offer a whole new variety of possible transport modes, which might be interesting for potential applications. I used the possibility of two independent transport directions to implement an automatic quality control of a chemical reaction.

In the second part of this thesis I present a fundamentally different approach. It is no longer based on passive particles but on active mesoscopic particles. Thus the question is no longer how to use external forces to transport a passive particle, but how to control and direct the motion of the actively swimming particle. Similar to molecular motors, active particles convert chemical energy from their environment into a directed swimming motion. Due to the small Reynolds numbers, swimming on the mesoscopic

²Diamagnetic colloids are actually nonmagnetic particles that are dispersed in ferrofluid. They are thus magnetic holes in the surrounding ferrofluid and therefore effectively diamagnetic.

scale is fundamentally different from the macroscopic scale and requires a non-reciprocal sequence of motion [33]. One possible swimming strategy in the viscous regime is the periodic rotation of a chiral object, similar to a ship's propelling screw [33]. This mechanism is applied by biological microswimmers, such as bacteria like *Escherichia Coli*, which propel themselves by the rotation of a helical bundle of flagella [34]. The rotary motion is again connected to a molecular motor [1]. Obviously the basic idea behind the strategy for motion is similar to the molecular motor Kinesin which was discussed above. The periodic repetition of a process, the rotation of flagella, is converted into a linear motion of the bacterium.

I am using magnetotactic bacteria, a special type of bacteria that has a built-in permanent magnetic moment. In their natural habitat, magnetotactic bacteria use their magnetic moment to navigate in the geomagnetic field. The unique magnetic moment offers the possibility to manipulate the motion of the bacteria with magnetic fields. Considering this and the bacteria size of a few micrometers, it is an obvious choice to use the domains of garnet films to direct the bacterial motion. I will show that magnetotactic bacteria can be stably guided along arbitrary stripe domains of magnetic patterns.

So far I presented two novel strategies to control and to transport mesoscopic particles. On studying these colloidal systems, or in general any physical system, it is often very helpful not to restrict all the considerations to one specific problem but to see a bigger picture. The problems encountered in one discipline are often very similar to those in other areas. To solve problems in one's own system it might therefore be helpful to apply concepts and strategies from other fields. An example is given by the topologically protected colloidal transport. The concept of topological transport originally stems from solid state physics [35]. It is for example important in topological insulators, which are insulating in the bulk but possess topologically protected conducting edge states [36].

I borrowed this concept and applied it to colloids. Topological protection helped to theoretically understand the colloidal transport and to show its robustness. In a second step the inspiration was even more obvious. The motion of electrons in the semiclassical picture of the quantum Hall effect was directly transferred to the motion of the particles in the colloidal topological insulator. Hence a concept from another area of physics helped to understand and to improve transport in our colloidal system.

This exchange, however, is not a one-way road. Beyond the above discussed use for the transport of cargo, there is another intriguing aspect about colloidal particles. The advantage of colloids is their easily accessible size and timescale. The colloidal dynamics are observable in real time with optical microscopy. Furthermore, the interaction between colloids can be easily tuned with external fields. In contrast to this, particles in condensed matter often cannot be visualized. These particles are hidden in the bulk of the material and their length scales are too small or their timescales too fast to observe the dynamics. This has triggered the use of alternative model systems. Due to their unique accessibility, colloids are perfect candidates for the modeling of such systems.

Colloids became an important tool which helps to understand basic mechanisms in systems from other fields of physics. There are various examples for colloidal model systems. Colloids are often used to mimic the behavior of atoms [37] and molecules [38] or to study

phase transitions and coexistence in crystalline systems [39]. It is even possible to model advanced phenomena like the quantization of currents in condensed matter systems [40]. Also the colloidal topological insulator is not only inspired by the quantum Hall effect. At the same time, it is also one of the first experimental visualizations of the motion of electrons within the semi-classical interpretation of the quantum Hall effect.

In the third and last part of this thesis I am going to use a colloidal model system for the behavior of the spin degrees of freedom in spin ice. Spin ice is a fascinating magnetic material, whose elementary magnetic moments are highly frustrated [41]. This results in a multifold degenerate ground state and the unusual property of residual entropy.

Recently another intriguing aspect of this material was discovered. The elementary excitations in spin ice are emergent magnetic monopoles [42]. These can move through the spin ice lattice. The translation from one vertex to the next is thereby related to the flipping of one spin. Thus it is again a stepwise motion on a discrete lattice. This time, however, it is not initiated by periodic repetitions of a driving process. Another difference is of course that it is no longer a massive object that moves, but an excitation in a crystal. However there is little knowledge about the dynamics of the elementary monopole excitations [43]. The spin degrees of freedom and their dynamics, in the bulk of the spin ice material, are not directly accessible in experiments. Considering this it seems an obvious choice to use colloidal particles to study the spin dynamics in spin ice.

In the employed colloidal model system magnetic colloids mimic the elementary magnetic moments in spin ice. The particles are constrained such that their collective behavior mimics the phenomenology of the frustrated spins. I am using this system to observe the dynamics of monopole excitations in real time. This makes it possible to study the interaction potential between defects and to confirm their monopole character.

Beyond that, I am suggesting a design for a universal logic gate based on monopole currents. Although it is probably not very efficient to use a colloidal system for logic operations, it would be a breakthrough to transfer the concept to the original spin ice system. This could foster the realization of computing units based on magnetricity which can be miniaturized to the scale of a few spins in a spin ice crystal. Since the race for smaller and more efficient electronic computing devices is going to cease in foreseeable time [44], magnetricity could be a welcome alternative.

Altogether I am presenting novel routes for the motion of mesoscopic particles based on magnetic fields. Transport is either induced by external fields, by the collective interaction between the colloids or by active swimming of the particles themselves. Besides studying new methods to achieve robust transport of mesoscopic particles, I am using colloids as model systems.

The whole thesis is based on experimental observations which are complemented with theoretical explanations. This involves mathematical methods (topology) and, if required, numerical simulations. In addition, biological particles (magnetotactic bacteria) are used. The insights gained this way address fundamental questions about the dynamics of mesoscopic particles. The results are not limited to colloidal systems but include implications on other areas of physics, e.g. the dynamics of emergent magnetic

monopoles and the presence of topological protection in truly dissipative systems. Some of the results might also be interesting for potential future applications.

This cumulative thesis is organized in the following way. Part I aims to give a short overview over the topics in which my work is embedded. Furthermore it contains brief summaries of the publications and establishes the connection between them. Part II are the publications themselves. They are sorted thematically and are referenced in the text as [P1] to [P6]. The appendix summarizes details of the experimental setups and methods used throughout this thesis.

Chapter 2

Topological protection

The theoretical study of the quantum Hall effect introduced a new way of classifying physical systems based on topology [35]. Thouless and co-workers discovered that topologically protected edge states give rise to the quantized Hall conductance. Due to topological protection the edge channels, and therefore the quantized Hall conductance, are robust against perturbations and disorder in the system.

Within the work on the quantum Hall effect and its variations a fascinating novel type of materials was discovered, the so-called topological insulators [36]. Topological insulators are insulating in the bulk and have topologically protected conducting edge or surface states. Just like in the quantum Hall effect, topological protection ensures the robust and dissipation free transport of quantum mechanical excitations in these edge channels. Their robustness makes them appealing for various applications ranging, from spintronics [45] to quantum computing [46].

The concept of topological protection is not limited to quantum mechanical systems. It can also be used in classical materials for the robust transport of classical waves, e.g. of sound waves in mechanical meta materials [47].

In this chapter I present a new example of topological protection, the driven dissipative transport of colloidal particles. Magnetic colloids are driven above a periodic magnetic film by periodic modulation loops of a time dependent external magnetic field. In publications [P1] to [P4] I show that the colloidal transport in these systems is also topologically protected. In contrast to quantum mechanical excitations or classical waves, here the concept of topological protection ensures the robust transport of classical colloidal particles.

Topological protection is a promising approach to overcome the problems of previous colloidal transport systems that are discussed in the introduction and enables the dispersion-free transport of big collections of colloidal particles. I also succeeded to enhance our system with a second type of particles. It is possible to have independent control over the transport of paramagnetic and diamagnetic colloids.

I start this chapter by explaining the concept of topological protection. The original example of the quantum Hall effect is used to illustrate how topology enters into physics and how topological protection results in robust physical properties. This is completed with a short survey over topological insulators and their presence in a huge variety of different physical systems. The second half is dedicated to the colloidal transport system. I show how the topological classification of modulation loops of the driving field results in the topological protection of colloidal transport. The chapter is completed by a brief summary of the work presented in the appendant publications. In publications [P1] to [P3] I am experimentally studying the colloidal transport. This is

complemented by a new theoretical framework that explains the colloidal motion and proves that it is topologically protected. In addition a direct application an automatic quality control for a chemical hybridization reaction is implemented in publication [P2]. Finally in publication [P4] I realized a colloidal topological insulator which establishes the connection to other topologically protected systems.

2.1 The concept of topological protection

Topology is one of the central areas of mathematics. It is concerned with the characterization of solid figures and spaces. Of special interest are thereby properties of such objects that are invariant under continuous deformations. In the sense of topology two solid figures are similar or homotopic when they originate from one another through continuous transformations. Homotopic figures can be grouped into equivalence classes, which are labeled by topological invariants. Objects with the same topological invariant are similar and belong to the same equivalence class [48].

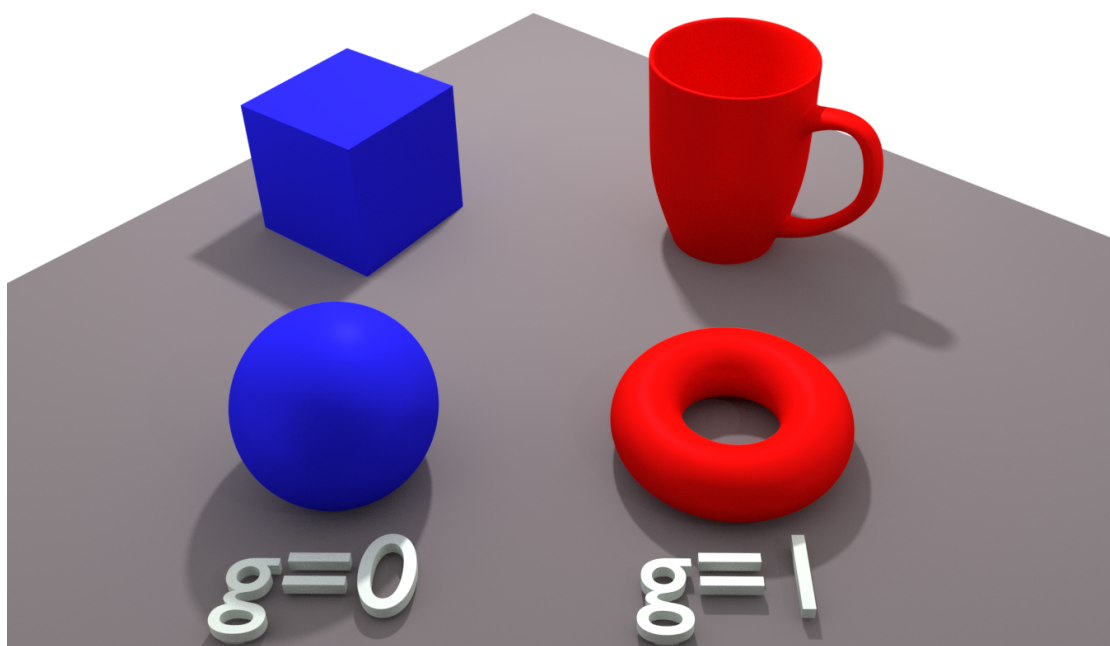


Figure 2.1: Two dimensional surfaces of different genus. A sphere and a cube both have genus $g = 0$. In contrast a torus and a coffee cup both have a hole and therefore genus $g = 1$.

Probably the most concrete example of a topological invariant is the genus g . It is the number of holes in a geometric object. For example a sphere and a cube both have $g = 0$ since they don't have a hole (figure 2.1). Hence they belong to the same equivalence class and can be continuously deformed into each other. In contrast to them a donut or a cup belong to a different class with genus $g = 1$. A sphere cannot be continuously deformed into donut without puncturing the surface at some point. Topological invariants like the genus are robust properties that are invariant under small perturbations. Changing them requires a fundamental change in the system. They are global properties of the system and thus robust against local perturbations such as defects in a physical system. Since they are (mostly) integer valued they do not change continuously, but in discrete steps.

In physics the concept of topological protection relies on topological invariants. A physical quantity that only depends on a topological invariant inherits its robustness and is thus topologically protected.

Quantum Hall effect

The Hall effect was already discovered in 1879 by Edwin H. Hall [49]. Imagine a two dimensional sample with a magnetic field \mathbf{B} perpendicular to it. Upon simultaneous application of a current I a perpendicular Hall voltage U_H can be measured (figure 2.2). Hall determined the Hall conductivity $\sigma_{xy} = I/U_H \propto 1/B$ to be proportional to the inverse magnetic field, which can be explained by the balance of electromagnetic forces. In 1980 Klitzing measured the Hall conductivity again in a two dimensional electron gas (realized with a silicon metal-oxide-semiconductor field-effect transistor) at high magnetic fields $B \sim 15$ T and low temperatures $T < 2$ K [50]. The surprising result was that the Hall conductance is quantized and varies in discrete steps

$$\sigma_{xy} = N \cdot \frac{e^2}{h} \quad (2.1)$$

that only depend on the electron charge e and Planck's constant h , which are both fundamental physical constants. The filling factor $N = 1, 2, \dots$ is an integer which establishes the name integer quantum Hall effect.

The effect is nowadays well understood and can be described on a single electron level without having to consider electron-electron interactions¹. In a magnetic field the energy levels of charged particles are quantized to the highly degenerate Landau levels $E_n = (n + \frac{1}{2}) \cdot \hbar\omega_c$ with the cyclotron frequency ω_c . Each fully filled Landau level contributes to the Hall conductance with e^2/h . The reason for this are one dimensional, perfectly conducting edge states. A semiclassical approach gives an intuitive picture for the presence of these edge channels. As shown in figure 2.2 electrons in the bulk of the material circle around the perpendicular magnetic field. Electrons close to the edge however cannot complete the circles due to the hard boundaries and have to perform

¹In contrast to this, the fractional quantum Hall effect (the filling factor is a rational number) requires an intrinsic many body approach with electron-electron interactions.

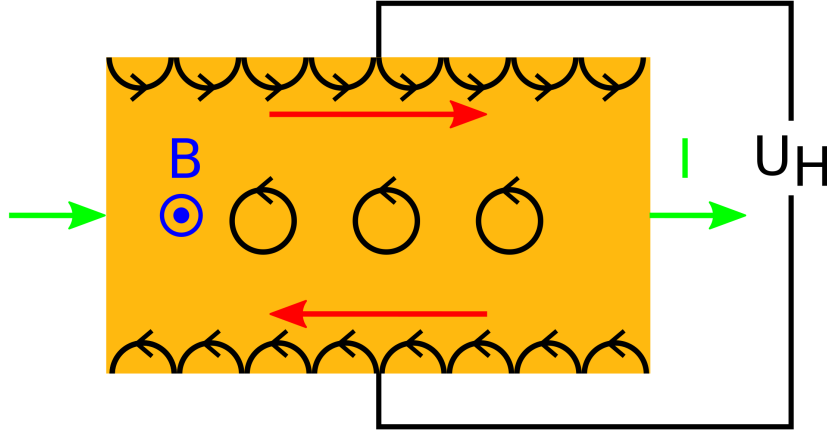


Figure 2.2: Setup to measure the Hall voltage. A magnetic field B is applied perpendicular to the sample. A current along the sample will then result in a transverse Hall voltage U_H . The black circles illustrate the semi-classical picture to explain the edge currents. An electron in the bulk is forced on closed cyclotron orbits around the magnetic flux by the Lorentz force. Electrons close to the edge however cannot complete the circles and perform so-called skipping orbits. Successive skipping orbits result in counter propagating 1D edge channels which are depicted by red arrows.

skipping orbits. A series of these skipping orbits results in helical edge currents along the boundaries of the sample. Each of the one dimensional edge channels contributes e^2/h to the quantum hall conductance σ_{xy} ². Each Landau level generates one edge state. In consequence the filling factor N of the Landau levels determines the quantized Hall conductance [51].

In 1982 Thouless and co-workers succeeded to show that the origin of the edge states and therefore of the quantum Hall conductance is of topological nature [35]. A topologically non-trivial quantum Hall state can't be distinguished from a trivial insulator by only looking at the band structure $E_m(\mathbf{k})$ (m is the band index and \mathbf{k} the crystal momentum). The difference is encoded in the topology of the system. The situation is similar to the descriptive example of the mapping from 2D surfaces to 3D space which is topologically classified by the genus (see section 2.1). Now we have to consider the mapping between the crystal momentum \mathbf{k} and the Bloch Hamiltonian $\mathcal{H}(\mathbf{k})$ as well as the Bloch wave functions $|u_m(\mathbf{k})\rangle$. We can subdivide $\mathcal{H}(\mathbf{k})$ into equivalence classes that can be continuously deformed into each other without closing the energy gap. This allows to topologically classify band structures. The topological invariant that distinguishes different classes is the so-called Chern number n , an integer valued quantity [36]. From a physical point of view the Chern number can be understood in terms of the Berry

²The relation between conducting edge states and Hall conductance can be understood with the Landauer-Büttiker formalism [51, p. 92 et seq.].

phase γ . It is a phase that the Bloch wave function acquires when \mathbf{k} is adiabatically evolved along a closed line in the Brillouin zone [51, p. 48 et seq.].

Thouless and co-workers proved that the filling factor $N = n$ is the overall Chern number n , which is the sum of the Chern numbers of all occupied bands [35]. Therefore the quantized Hall conductance $\sigma_{xy} = n \cdot \frac{e^2}{h}$ as well as the conducting edge channels only depend on the topologically invariant n and are thus topologically protected. That is both are invariant under smooth deformation of $\mathcal{H}(\mathbf{k})$ as long as they do not cause a gap closure.

The topology of the bulk determines the existence of edge states, something known as *bulk-boundary correspondence*: When the Chern number n changes, for example at the boundary between a nontrivial quantum Hall state ($n \neq 0$) and a trivial insulator ($n = 0$, e.g. the vacuum), there has to be an edge mode (figure 2.3a). The edge mode lives in the gap of the bulk band structure (figure 2.3b). This prevents scattering into the bulk since there are no corresponding bulk states of the same energy. Backscattering is also not possible because the backward channel only exists on the opposite boundary, which is well separated by the insulating bulk. Due to the absence of backscattering, the transport in the edge channels is dissipation free. The robustness of the edge states is the manifestation of the topological protection.

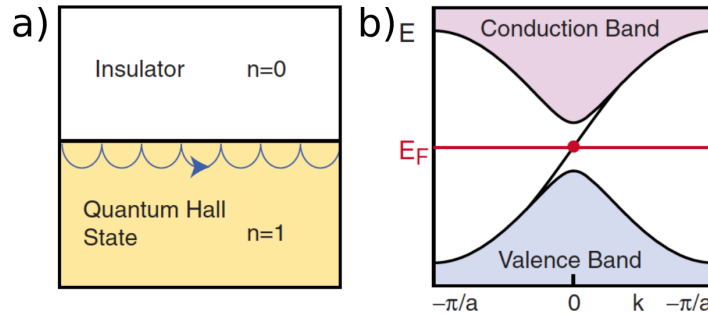


Figure 2.3: a) At the edge between a trivial insulator and a quantum Hall state have to be topological protected edge states. b) These helical edge states sit in the energy gap of the bulk band structure. Picture adapted from [36]

Quantum anomalous Hall effect In 1988 Haldane proposed that there might even be quantum Hall conductance without a net magnetic field [52]. He used a lattice system of spinless electrons with a periodically varying magnetic field, which has the same symmetry as the underlying lattice but is zero in average. Later on it was found that the role of the periodic magnetic field can be replaced by spin-orbit coupling. It was suggested that this so-called *quantum anomalous Hall effect* can be found in ferromagnetic insulators with strong spin-orbit coupling [51]. However only recently, 25 years after the theoretical prediction, this phenomenon was experimentally verified [53]. Even in the absence of a

magnetic field there is still a Hall conductance and conducting edge states. Both are still protected by a Chern number, this time of the electron bands instead of Landau levels.

Topological insulators

A topological insulator is a novel material that has a bulk band gap. In contrast to a trivial insulator it exhibits topologically required conducting edge states similar to those in the integer quantum Hall effect. A 2D topological insulator is also known as a quantum spin Hall insulator [36]. The quantum spin Hall effect consists of an insulating bulk with two counter propagating gapless edge states, one for spin up and one for spin down electrons (figure 2.4)³. The two edge channels result in a vanishing electric current, but in a non zero spin current and a corresponding spin Hall conductance. In contrast to integer and anomalous quantum Hall effect the time reversal symmetry remains intact. Since this requires the Chern number n to vanish, Kane and Mele introduced a new Z_2 topological invariant ν . It distinguishes between a conventional insulator with $\nu = 0$ and a quantum spin Hall state with $\nu = 1$ [54]. Backscattering in the opposite traveling channel is not possible because time reversal symmetry requires that this state is already occupied. Thus the transport in the edge states is again ballistic [36].

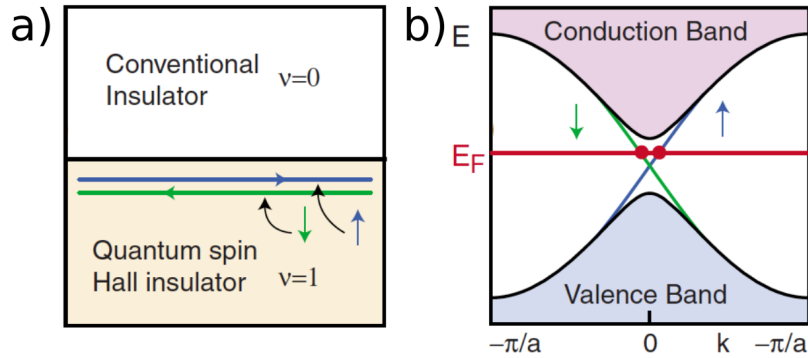


Figure 2.4: a) Counter propagating edge states for the opposite spin directions at the edge between a quantum spin Hall insulator and a trivial insulator. The two edge currents result in a vanishing electric current but exhibit a non zero spin current. b) Both edge states live in the bulk energy gap. Picture adapted from [36]

The quantum spin Hall effect was originally proposed in graphene with spin-orbit coupling by Kane and Mele in 2005 [55]. The spin-orbit coupling effectively emulates the

³In the strict sense, speaking of spin up and down requires the z-component S_z of the spin to be conserved. If this is valid the quantum spin Hall Effect can be understood as two independent copies (for the two spins) of the above discussed Haldane model. In real systems however there are always S_z non-conserving terms. Kane and Mele showed that this nevertheless doesn't destroy the topological order with the two counter propagating edge states [55]. The two different channels are still referred to as spin up and down.

role of the magnetic field in the integer quantum Hall effect and enables a topologically non-trivial band structure with an energy gap. The experimental verification followed in 2007 by König and co-workers. They measured the spin conductance in HgCdTe quantum well structures [56]. Breaking the time reversal symmetry, for example by doping a topological insulator with ferromagnetic materials, can result in topological insulators with unidirectional edge states similar to the quantum anomalous Hall effect [53].

3D topological insulators There is no quantum Hall effect in three dimension. However the topological characterization of the quantum spin Hall insulator can be generalized from 2D to 3D [57]. A 3D topological insulator is still insulating in the bulk and has two dimensional conducting surface states, similar to the one dimensional edge states in 2D topological insulators. In contrast to 2D the topological characterization in 3D requires four Z_2 bulk invariants $(\nu_0; \nu_1, \nu_2, \nu_3)$. The set (ν_1, ν_2, ν_3) can be understood as miller indices indicating the orientation of the surface states. The first invariant ν_0 distinguishes between a strong and a weak topological insulator. In a weak topological insulator ($\nu_0 = 0$) the surface states are not protected by time reversal symmetry. Although they are predicted for clean surfaces they are not robust against disorder and can be trapped there. The surface states of a strong topological insulator ($\nu_0 = 1$), however, are more robust. They form a two dimensional topological metal [57] and cannot be trapped by disorder, which is similar to the situation in 2D topological insulators [36].

The first experimental observation of a 3D topological insulator was in the semiconducting alloy $\text{Bi}_{1-x}\text{Sb}_x$ [58] in 2008, one year after the theoretical prediction. However, directly observing the edge currents with charge transport experiments is more problematic in 3D due to the difficulty of separating bulk and surface contributions [36].

In both, two and three dimension, the robust and spin selective edge currents could be useful for application in spintronic devices or low power consumption electronic devices based on the dissipation free nature of the edge channels [45]. Topological insulators might also foster the development of novel magnetic devices [59].

Floquet topological insulators The topologically classification of band structures can also be applied to periodically driven systems. Periodically driving a system can result in topologically protected edge states in spite of topologically trivial bulk bands [60].

In a driven system the Floquet spectrum is the analogue of the band structures of the static system. It consists of the eigenvalues of the Floquet operator, which is the time evolution operator evaluated over one period of the external drive. Since the operator is unitary, the eigenvalues can be expressed in terms of the quasi energy ϵ as a complex phase $e^{-i\epsilon T}$, where T is the driving period. The quasi energy spectrum is $2\pi/T$ periodic in ϵ . Applying periodic boundary conditions allows to fold the quasi energy zone into a circle.

The quasi energy bands can again be characterized by a topological invariant. However the invariants used in the static case are no longer sufficient to fully characterize the topology of driven systems. This requires a new invariant, the *winding number* ν [61]. The winding number counts the number of times a quasi energy band winds around

the quasi energy zone. This new invariant again allows to establish a bulk-boundary correspondence and predict the existence of topologically protected edge states.

Topological insulators in classical wave systems The concept of topological protection is not limited to the various quantum Hall systems or to quantum mechanics in general. The robustness of transport in topologically protected edge channels might also be a promising tool to stabilize transport of classical waves such as sound and light waves [62]. Artificial meta materials are specially designed to realize topologically non-trivial systems. This results in devices with new functionalities. One example are waveguides with unidirectional transport in only one direction, which is the equivalent to the helical edge states in the integer quantum Hall effect [62]. Other possibilities are vibration isolation, cloaking or adaptive behavior [47].

There are various approaches to design classical topological insulators with topologically protected edge states. The key is to engineer the meta materials in a way that the classical equations, that describe their dynamics, can be mapped onto the quantum mechanical Dirac equation, which describes the quantum mechanical topological insulators [47, 51]. Once this is done the description is similar to the electronic case, nontrivial bulk bands result in topologically required edge states.

A mechanical implementation was for example achieved by Süsstrunk and Huber with a lattice of coupled pendula [63]. Similar to the quantum spin Hall effect, this system exhibits counter propagating edge channels of phonons of opposite polarization. Other realization use active components, such as lattices of driven gyroscopes [64] or resonators with circular flowing air [65]. In both cases the active components break the time reversal symmetry. This situation is comparable to the quantum (anomalous) Hall effect with only one helical edge state in which sound waves are transported around the edge of the lattice.

There are also optical topological insulators. Rechtsman and colleagues realized an optical analog by using a honeycomb lattice of coupled helical waveguides [66]. Marquardt and his group even unified both, sound and light. They realized a Chern insulator that relies on the interaction between photons and phonons [67]. Similar to Floquet insulators, the topological transport of phonons can be manipulated in situ by adjusting a driving laser.

Topological superconductors Another member of the family of topological materials might be superconductors. The Bogoliubov-de Gennes equation for superconductors has a structure which is very similar to the Dirac equation for topological insulators [51]. This might allow to topologically classify superconductors. Tunneling spectroscopy gave first indications for the possible existence of chiral edge states in a Sr_2RuO_4 superconductor [68].

1D topological superconductors are thereby of special interest. Due to particle hole symmetry, the two edge states at the end points are their own antiparticles. They hence fulfill the defining criterion of *majorana fermions* [36]. Kitaev proposed that this topological approach might be an important tool to stabilize quantum computing [46].

The well separated pair of Majoranas form a degenerate two level system with potential application as *qubit* [36].

In summary there are various different types of topological insulators. The variety spans from electronic transport in the original topological insulators to classical wave systems and even topological superconductors. Despite their obvious differences all these systems are based on a very similar mathematical foundation. Another unifying feature is that symmetry plays an important role. Among the most important symmetries is the time reversal symmetry in topological insulators and the particle-hole symmetry in topological superconductors [51]. Also the symmetry of the underlying lattice can be important. Different lattice symmetries can result in physically and topologically distinct effects [69]. The lattice symmetry is for example of importance in topological crystalline insulators [70]. It also plays a central role in our colloidal transport system that I present in the following section.

2.2 Topologically protected colloidal transport

In publications [P1] to [P4] I show that the transport of magnetic colloids in our system can be topologically protected. Here the protection of the transport is different to the previously discussed systems. In contrast to these Hamiltonian systems the colloidal transport is a driven dissipative system. Furthermore the topological transport in our system is not based on edge channels but happens above the bulk of the two dimensional magnetic patterns.

In the following I will introduce our colloidal transport system and I am explaining how the topological classification of the modulation loops results in topological protected transport of colloidal particles. Geometry and topology are thereby deeply connected. We thus study the interplay of the lattice symmetry and the way transport is topological protected. The knowledge on bulk transport is then used to design a colloidal topological insulator with robust transport along the edges between patterns of different symmetries.

Colloidal transport system

The core of the experimental setup are thin magnetic films⁴. The films have magnetic domains with a magnetization along the z -direction normal to the surface. We use films with as much area magnetized in the positive as in the negative z -direction. The alternating domains form a periodic pattern (figure 2.5a). Magnetic lithography allows us to create patterns of any desired rotational point symmetry.

Paramagnetic and diamagnetic colloids are placed above the magnetic structures. Diamagnetic colloids are nonmagnetic particles that form holes in a surrounding ferrofluid and therefore effectively behave diamagnetic. The colloidal particles are confined to a fixed elevation z above the pattern. The two dimensional space in which the colloids

⁴The experimental setup is described in detail in the appendix A.1.

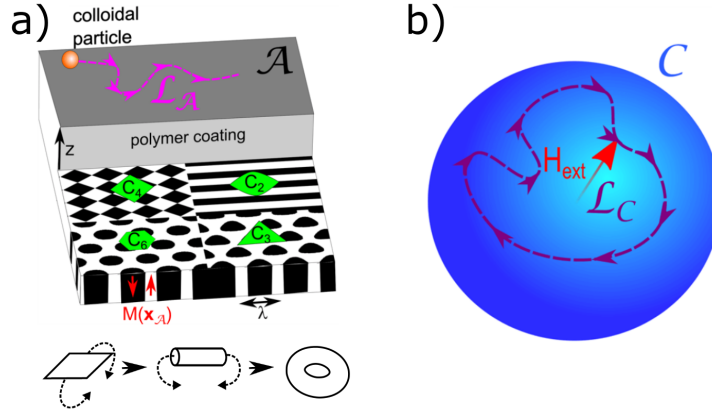


Figure 2.5: a) Magnetic structures of different rotational point symmetries C_N . Black and white areas denote domains of up and down magnetization. Colloidal particles move at a fixed distance z above the magnetic structure in the action space \mathcal{A} . Identifying the periodic boundary conditions the unit cell is topologically a torus as sketched at the bottom. b) The system is driven by an external field \mathbf{H}_{ext} , with a constant magnitude. Therefore all possible field directions live on a sphere, the control space \mathcal{C} . The external field performs closed periodic modulation loops \mathcal{L}_C that induce action loops \mathcal{L}_A of the particles in \mathcal{A} . Picture adapted from [P1].

move is called the **action space** \mathcal{A} . The particle positions are described by the two component vector \mathbf{x}_A . To transport magnetic colloids the magnetic field $\mathbf{H}^p(\mathbf{x}_A)$ of the pattern is modulated by a homogeneous, but time-dependent external field $\mathbf{H}_{ext}(t)$. The external field is varied along closed periodic loops.

In a magnetic field a colloid of effective susceptibility χ_{eff} acquires a magnetic moment

$$\mathbf{m} = \chi_{eff} V \mathbf{H} \quad (2.2)$$

where V is the particle volume and $\mathbf{H} = \mathbf{H}_{ext} + \mathbf{H}^p$ the total magnetic field. The particles thus have a potential energy

$$E = -\chi_{eff} V H^2. \quad (2.3)$$

Defining the colloidal potential $U = H^2$ enables the description of both types of particles. The paramagnetic colloids ($\chi_{eff} > 0$) will go to the maxima of U while diamagnetic particles ($\chi_{eff} < 0$) will go to the minima of U .

Particular interest lies in the motion of colloids at large elevations z , because there the potential U becomes universal. The magnetic field \mathbf{H}^p of the pattern can be expressed as a Fourier series. At high elevations $z \gtrsim \lambda$ of the order of the lattice constant λ only the contributions of the reciprocal lattice vectors with the lowest absolute value are relevant (for details see publication [P1]). The colloidal potential becomes the universal potential

$$U^* \propto \mathbf{H}_{ext} \cdot \mathbf{H}^p. \quad (2.4)$$

It is universal in the sense that it no longer depends on details of the magnetic pattern. Its symmetry becomes the only important property. In the universal potential U^* the position of the extrema is independent of the magnitude of the external field. **Control space** \mathcal{C} , which is the space of all possible external field directions, is therefore a sphere (figure 2.5b).

There exist two distinct ways of transporting the particles from one unit cell to the next along one of the crystallographic directions of the magnetic pattern. The first possibility is adiabatic transport. There are modulation loops of the external field that move an extremum of the colloidal potential from one unit cell to the next. If the modulation is sufficiently slow, a particle that sits in the extremum (a maximum for paramagnetic colloids or a minimum for diamagnetic particles) will stay there and adiabatically follow the motion. Like this the particle can be transported to another unit cell.

The second possible transport mode is a deterministic ratchet. Initially the particle is also transported adiabatically in a stationary point. But the modulation is now such that the transporting extremum disappears at some point. Suddenly the particle is no longer in its energetically favorable position. It therefore performs a ratchet jump along the path of steepest descent of the potential into another extremum. In contrast to the adiabatic motion, the ratchet jumps are irreversible. Reversing the modulation loop will in general not result in a reversed trajectory of the particle.

The fundamental question that has to be answered is: what are the requirements for modulation loops in control space to induce adiabatic or ratchet transport of colloids in action space? In the next section I will explain that the answer to this question is of topological nature.

Topological classification of modulation loops

The periodicity of the magnetic pattern allows to introduce a topological description of our system. Using periodic boundary conditions at the edges of the unit cell we can wrap action space \mathcal{A} to a torus (see figure 2.5a). In this picture transport from one unit cell to the next is translated to winding around the torus. There are two distinct ways of winding around a torus which correspond to transport along one of the two lattice vectors of the magnetic pattern. We can therefore characterize loops $\mathcal{L}_{\mathcal{A}}$ in action space by their two winding numbers $\omega(\mathcal{L}_{\mathcal{A}})$ around the torus. Intercellular transport corresponds to a non-zero winding number.

In contrast to action space, control space \mathcal{C} is a sphere without holes. Therefore every loop $\mathcal{L}_{\mathcal{C}}$ in \mathcal{C} can be continuously deformed into a point and is thus zero-homotopic. In publications [P1] to [P3] I show that non-trivial transport of colloidal particles in action space is possible. In other words there have to be trivial modulation loops $\mathcal{L}_{\mathcal{C}}$ that induce non-trivial transport loops $\mathcal{L}_{\mathcal{A}}$. But what are the topological requirements for a modulation loop to induce non-trivial intercellular transport of colloids in action space? This question has two different answers. In the universal limit of a twofold rotation symmetric pattern (C_2), a stripe pattern (compare figure 2.5a), the answer is rather simple. The pattern is invariant along the stripe direction and therefore quasi one dimensional. Thus we can also restrict control space to this one dimension and the

sphere \mathcal{C} reduces to a circle \mathcal{C}^r . A circle is no longer topologically trivial and in [P1] we show that a non-trivial winding number $\omega(\mathcal{L}_{\mathcal{C}^r}) \neq 0$ around the circle directly induces a nontrivial transport loop $\mathcal{L}_{\mathcal{A}}$ in action space with

$$\omega(\mathcal{L}_{\mathcal{A}}) = \omega(\mathcal{L}_{\mathcal{C}^r}). \quad (2.5)$$

In all other cases the answer is not that simple anymore. Solving it requires to consider the full dynamics of the system, which takes place in the product phase space $\mathcal{C} \otimes \mathcal{A}$. The transport is mostly governed by the stationary points $\nabla_{\mathcal{A}}U = 0$ in action space. Therefore we can restrict our considerations to the two dimensional **stationary manifold** \mathcal{M} , which is the subset of all stationary points in phase space $\mathcal{C} \otimes \mathcal{A}$. In publications [P1] to [P3] we show that the topology of this stationary manifold fully governs the whole variety of possible transport in our system.

Since the whole derivation is described in the publications, I will limit my explanation here to the basic underlying idea. The key lies in the projection of special objects from the stationary manifold \mathcal{M} to control space \mathcal{C} . These projected objects puncture \mathcal{C} at specific points or introduce more complicated, extended objects on its surface. The result is a constrained control space $\tilde{\mathcal{C}}$ which is no longer trivial. The challenging task that remains is to find these objects and to find out how modulation loops have to wind around them in order to induce colloidal transport. Once this is done the initial question again has the simple answer

$$\omega(\mathcal{L}_{\mathcal{A}}) = \omega(\mathcal{L}_{\tilde{\mathcal{C}}}) \quad (2.6)$$

where $\omega(\mathcal{L}_{\tilde{\mathcal{C}}})$ is the winding number of a modulation loop around the projected objects in $\tilde{\mathcal{C}}$.

The winding number $\omega(\mathcal{L}_{\tilde{\mathcal{C}}})$ is the topological invariant of the modulation loops. It allows to divide them into topologically distinct classes that cause different transport in \mathcal{A} . The colloidal transport in action space is directly related to the topological invariant $\omega(\mathcal{L}_{\tilde{\mathcal{C}}})$ in Control space via equation (2.6). Therefore the transport of colloids in our system is topologically protected by the winding number $\omega(\mathcal{L}_{\tilde{\mathcal{C}}})$ of loops in control space.

This relation is illustrated in figure 2.6. In the case of a four fold symmetric pattern control space is punctured at four equally spaced points on the equator e.g. along the \mathbf{Q}_1 direction. All modulation loops in figure 2.6a have a winding number $\omega(\mathcal{L}_{\tilde{\mathcal{C}}}) = 1$ around this point. Therefore all loops induce the same transport of colloids in action space as shown in figure 2.6b. The exact shape of the trajectories in \mathcal{A} is noticeable different. However, the result after one period of the modulation is the same: the particle is transport by one unit vector to the top. Winding around other puncture points will induce transport into another direction.

This nicely demonstrates the robustness that goes along with the topological protection. The transport is independent of the exact shape or speed of the modulation loop. As long as it does not change its winding number the transport in \mathcal{A} is preserved. Topological protection also ensures a high robustness of the transport against thermal noise. Furthermore the transport is independent of small changes in the properties of the colloidal

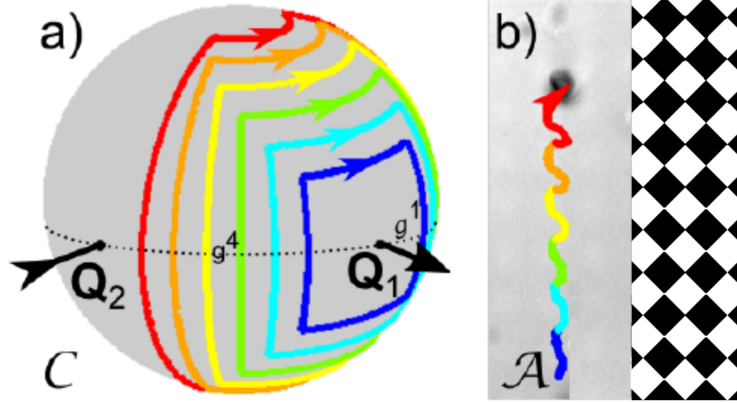


Figure 2.6: a) Control space of the four fold symmetric pattern. It is punctured at four equally spaced points on the equator e.g. along the Q_1 direction. Despite their different shape all shown modulation loops have the same winding number around this point. b) Reflection microscopy image of the 4 fold symmetric pattern with experimental trajectories. All modulation loops induce the same transport by one unit vector to the top. For clarity I added the theoretical pattern at the right hand side. The lattice constant is $7 \mu\text{m}$. Picture adapted from [P1].

particles such as size, mass and effective susceptibility. This enables the dispersion free and precise transport of a big collection of particles despite their intrinsic polydispersity.

From topologically protected transport to the colloidal topological insulator

This section summarizes publications [P1] to [P4] and establishes the connections between them. Similar to crystalline topological insulators, geometry and topology are inherently connected in our colloidal system. The lattice symmetry has a profound impact on the way the colloidal transport is topologically protected. This is directly visible in the topology of the stationary manifold. It is characterized by the genus, which is different for lattices of differing rotational symmetry. This results in a different puncturing of constrained control space $\tilde{\mathcal{C}}$ and different transport modes of colloids in action space \mathcal{A} .

The connection between geometry and topology is the subject in publication [P1]. There I study the topologically protected transport above magnetic films of all possible two dimensional magnetic point group symmetries with lattice vectors of equal length. The first structure is the two fold symmetric stripe pattern (see figure 2.5). As I already discussed in the previous section (2.2) the two fold symmetric pattern has a special role. The pattern and control space \mathcal{C} can be reduced to one dimension. This has the advantage that the phase space $\mathcal{C} \otimes \mathcal{A}$ has only two dimensions and the full dynamics can be visualized. Therefore this special case is used to introduce all the concepts and the terminology that will be important in the higher symmetric patterns. Furthermore we

also use this simplicity to study non universal effect that arise when the elevation of the particles above the magnetic structures is reduced. The transport thereby crosses over from adiabatic via a deterministic ratchet towards a non transporting regime. The other patterns with higher symmetry are more complex. Therefore the study of transport on higher symmetric patterns is limited to the universal case.

The next step, after the stripe pattern, is the four fold symmetric pattern which is a generalization of the two fold symmetry. This truly two dimensional structure enables transport in any direction from one unit cell into one of the eight neighboring unit cells. In the universal case the transport is fully adiabatic. Paramagnetic and diamagnetic colloids are always transported into the same direction.

The three fold symmetry is the most difficult case. It consists of a whole family of patterns. The pattern continuously varies with a phase variable from a six fold symmetric pattern C_6 to a six fold inversion symmetric pattern S_6 ⁵ (see figure 2.5a). We show that this whole variety of patterns can be sorted into two topologically distinct classes. The interesting topological transition in between is theoretically analyzed and experimentally demonstrated.

In addition all three fold symmetric patterns offer more possible transport modes compared to the four fold symmetry. The transport is not restricted to adiabatic motion, it is also possible to have deterministic ratchet motion. The most striking feature, however, is that paramagnetic and diamagnetic colloids are no longer limited to move into the same direction. They can now be transported independently into two different directions of the lattice.

In publication [P2] the C_6 symmetric pattern is examined in a more detailed way⁶. The connection between loops in \mathcal{C} , \mathcal{A} and the stationary manifold \mathcal{M} is analyzed. We answer the interesting question how it is possible to change the transport direction although it is topologically protected. Deterministic ratchets play an essential role for this transition. The ratchets and their irreversible nature are also discussed in detail. In addition I realize a direct application based on the possibility to transport both types of colloids into different directions. An automatic quality control for the chemical reaction between two functionalized colloids is implemented. Paramagnetic and diamagnetic particles are functionalized with complementary strands of DNA. If both particles meet on the pattern and the DNA fragments match, they can bind together and form a quadrupole. This new type of particle can then be transported into a third, independent direction. If the binding reaction is not successful, both initial particles will simply follow their previous directions. This quality control is internal since the system does not require any external input to distinguish between a successful and an unsuccessful reaction.

In the third publication [P3] we initially studied the four fold symmetry pattern⁷. It

⁵The inversion symmetry S_6 consists of a rotation by $2\pi/6$ and a reflection at the film plane, which inverts up and down magnetization.

⁶Note that we used slightly different conventions in [P1] and [P2]. In [P2] the pattern is rotated by 150° . Apart from this shift all results coincide in both publications.

⁷The conventions in [P3] also differ from [P1]. In [P3] we inverted the indices of the submanifolds and the gates. In Consequence the results for diamagnetic particles in [P3] are the same as those for paramagnetic particles in [P1].

contains a detailed derivation of the underlying theory which is confirmed by numerical simulations. Simulations are also used to demonstrate the robustness of the transport against thermal fluctuations. Experiments on the four fold symmetric pattern were made up later and are presented in [P1].

Colloidal topological insulator Finally the connection between our colloidal system and the various topological insulators that I discussed in section 2.1 can be established. In [P4] I apply the theory which was developed in the previous publications to design a *colloidal topological insulator*. It is based on a hexagonal magnetic pattern that has edges towards a stripe pattern. The modulation can be chosen such that only the motion above the hexagonal pattern becomes nontrivial while the stripe pattern remains trivial. The colloids on the bulk of the hexagonal pattern are transported in closed circles. That is after completing one circular orbit they return to their initial position. Thus there is no net transport and the bulk is insulating. Close to the edges towards the trivial stripe pattern, however, the particles cannot complete their full orbits and have to perform skipping orbits. Just like in the semiclassical picture of the quantum Hall effect (see figure 2.2), this results in robust helical edge states that transport colloidal particles along the edge between the two patterns. Above that we also implemented an analogue of the quantum spin Hall effect where particles of opposite susceptibility (paramagnets and diamagnets) are transported into opposing direction along the same edge.

On one hand this is an interesting new approach for stable transport of colloidal particles. The particles can be transported along arbitrary edges into any desired direction and even around corners of these edges. In addition it is possible to transport multiple particles along multiple edges into different directions, all with one and the same external modulation. On the other hand our system is also an interesting model system. It is among the first experimental visualizations of the semiclassical picture of the quantum Hall effect. Often colloids are used as model systems for atoms [37] or molecules [38]. Here I go one step further and use my colloidal system as a model for the motion of electrons.

2.3 Summary and discussion

In this chapter I presented a novel approach for the driven dissipative transport of magnetic colloidal particles. I could show that the transport of colloids in our system is topologically protected. Modulation loops \mathcal{L}_C of the external driving field can be divided into topological classes that cause different transport of colloids in action space. The transport is therefore topologically protected by winding numbers $\omega(\mathcal{L}_C)$ of the modulation loops in control space.

Similarly to the protected robust edge channels in topological insulators, topological protection guarantees robust colloidal transport in our system. The topologically protected transport is a promising tool to overcome the drawbacks of former colloid transport systems, based e.g. on thermal ratchets. Our system allows to transport big collections of particles in a precise and dispersion free manner. Furthermore in a three fold symmetric

pattern we have independent control over two different types of particles, paramagnetic and diamagnetic colloids.

To describe the transport in our system and to show that it is topologically protected we developed a new theoretical framework. This theoretical approach is quite different to the ones used in other topologically protected systems. Instead of Chern number associated to the bulk band structures our explanation is based on the topology of the stationary surface, which is described by its genus.

Despite these different approaches we can establish a connection to the other topologically protected systems. The colloidal topological insulator shows the same phenomenology as all the others: Particles are only transported along the edge between a trivial and a nontrivial pattern.

Discussion and outlook This last analogy might give rise to two interesting open questions. First, is it possible to describe the colloidal system within the theoretical framework of the quantum Hall effect. One possibility might be the fact that we can assign a stationary field⁸ $\mathbf{H}_{ext}^s(\mathbf{x}_A)$ to every point \mathbf{x}_A on the torus of action space \mathcal{A} . This defines a vector bundle [48] which is similar to the mapping between the complex Bloch wave function $|u_m(\mathbf{k})\rangle$ and \mathbf{k} on the torus of the Brillouin-zone and could provide an analysis of the colloidal transport similar to other topological insulators.

The second question is of rather speculative nature. In our system we mainly deal with topologically protected bulk transport. Nonetheless we can find a design that facilitates transport in edge states. In reverse conclusion, one could ask if it's possible to construct a topological insulator such that it exhibits topological bulk modes.

Another intriguing aspect of our system is its dissipative character. So far topological phases are mainly discussed in Hamiltonian systems [71]. It is possible to engineer open quantum systems with dissipation. Diehl and co-workers showed that they can extract topologically protected edge states from such a system [71]. But the final edge modes are nonetheless dissipation free. In contrast to this our colloidal system and especially the deterministic ratchet motion is intrinsically dissipative. It cannot be described by an effective Hamiltonian.

The developed theory is not limited to this specific colloidal transport system. In principle it can be extended to any, not necessarily magnetic, system with the same symmetry. An example that we realized in our working group in Bayreuth is a macroscopic steel pump [72]. There the magnetic pattern is generated by millimeter sized permanent magnets. The external field is emulated by two opposing strong magnets with a tunable orientation. In this macroscopic system we can transport millimeter sized steel spheres (behave like paramagnets) and diamagnetic superconducting particles in the same way we transport colloids in the mesoscopic system. This setup has the advantage that we can simultaneously visualize the particle motion and the external field direction. Furthermore it is possible to observe a special type of ratchets in the S_6 symmetric pattern, which was not possible in the colloidal system due to experimental limitations which are discussed in [P1].

⁸The stationary field $\mathbf{H}_{ext}^s(\mathbf{x}_A)$ is the external magnetic field that renders the point \mathbf{x}_A stationary.

In addition to the above discussed aspects there is probably a lot of room left for further investigations based on the colloidal transport system and the new theoretical approach. So far we could experimentally only confirm our theory by using paramagnetic and diamagnetic colloids. These are suitable to examine the behavior of maxima and minima of the colloidal potential U . However, an experimental verification for the predicted behavior of saddle points U remains elusive. A composite particle built of four dipolar particles (two paramagnets and two diamagnets) in a octupolar configuration might be a promising approach for a saddle point seeker. Within certain approximation, these particles should go to the saddle points of the potential U and can be used to study their behavior.

Another interesting question for future investigations might be the impact of particle-particle interactions and manybody effects. So far the colloidal suspension was highly diluted. Hence different particles moved at sufficient distance and did not influence each other. In reference [40] Pietro Tierno and Thomas Fischer showed that manybody effects can be an important factor in transporting colloidal particles above periodic potentials. The open question is how these multi particle effects can be combined with the topological framework of this thesis. In combination with the possibility of two independent transport directions this might offer interesting routes to construct novel modes of colloidal motion.

Chapter 3

Magnetic guidance of magnetotactic bacteria

The previous chapter dealt with the topologically protected transport of passive micro particles. In this chapter I am following a different route based on the motion of active particles. Hence the challenge is no longer to induce motion but rather to rectify the otherwise non-directional motion of the active particles.

The motion of passive or Brownian particles is governed by Brownian dynamics. The equilibrium thermal fluctuations of the particles are driven by random collisions with molecules of the surrounding solvent [73]. In contrast to passive particles active or self-propelled particles are consuming energy from their environment, which is converted into directed motion of the particles [10]. Their motion is therefore governed by both, Brownian dynamics and the capability of active swimming. The constant consumption of energy drives them into a far from equilibrium state [74].

Active mesoscopic particles were originally studied as a model for the swarming behavior of macroscopic animals, such as birds and fishes [75]. In fact the non-equilibrium nature of these particles gives rise to novel collective phenomena which cannot be observed with passive particles [76]. Examples are swarming, clustering to living crystals [77] or active turbulence [78]. Beyond that active particles are ideal model systems to study aspects of far from equilibrium physics [10, 79].

The ability of active self propulsion is widespread in biological microorganisms such as bacteria. In their natural habitat they use swimming for the efficient search for nutrition and to avoid toxic substances [80]. One of the best studied examples is the bacterium *Escherichia Coli* [34]. It is propelled by a bundle of helical flagella which are rotated by a molecular motor. The motion follows a *run and tumble* pattern. Periods of straight active swimming (run) are interrupted by actively induced but random reorientations (tumble). Using chemotactic sensing E.Coli can navigate in chemical gradients. Run phases are longer when the bacterium swims towards favorable conditions and shorter when it swims in the wrong direction [81].

Like in countless other examples, nature is the inspiration for man-made objects that mimic the behavior of biological microorganisms. The engineering of such artificial microswimmers with precisely designed properties is particularly interesting for studying their motion and understanding the fundamental mechanisms behind it. Meanwhile there are various different approaches for artificial self-propelled particles [10]. The most prominent among them are active Brownian particles. They are driven by a force of constant magnitude whose orientation undergoes rotational diffusion dynamics. Most of such systems are so-called *Janus particles*, which are colloidal particles with a broken symmetry due to local coating with catalytic materials. This asymmetry induces

local gradients in the solvent around the particle, which results in a selfdiffusiophoretic propulsion of the particle [82]. An example is the partial platinum coating which causes a gradient of H_2O and O_2 in a hydrogen peroxide solvent. Other realizations of artificial active particles are based on external fields, for example chiral particles that are rotated by external magnetic fields in a way that they act like propellers [83]. Other externally driven microparticles are rotating colloids [84] or self assembled colloidal wheels [85] in the proximity of a confining wall. Despite the huge effort that is recently invested in the investigation of active particles, their applicability in realistic environments, a fundamental prerequisite for real applications, is still in its infancy [10].

Here and in publication [P5], I present a novel approach that might solve some aspects of this problem. I achieved the precise guidance of single bacteria along arbitrary lines of mechanical instability. I am using *magnetotactic bacteria*, a special type of actively swimming bacteria that additionally has a built-in permanent magnetic moment. This remarkable property is used to manipulate the bacteria with the magnetic fields of a garnet film. Like this it is possible to study the interplay of active motion and the presence of external constraints. These can be chosen such that a stable guidance of the bacteria is achieved.

This chapter starts with the introduction of magnetotactic bacteria. Following this I explain how the interplay of active swimming and the built-in magnetic moment enables the stable guidance of bacteria in the heterogeneous magnetic field of garnet films. Apart from the need for swimming, the guiding process itself is passive. It does not require any active feedback of the magnetic fields on the swimming behavior of the bacteria. The guidance only relies on a careful balance between propulsion and magnetism.

3.1 Magnetotactic bacteria

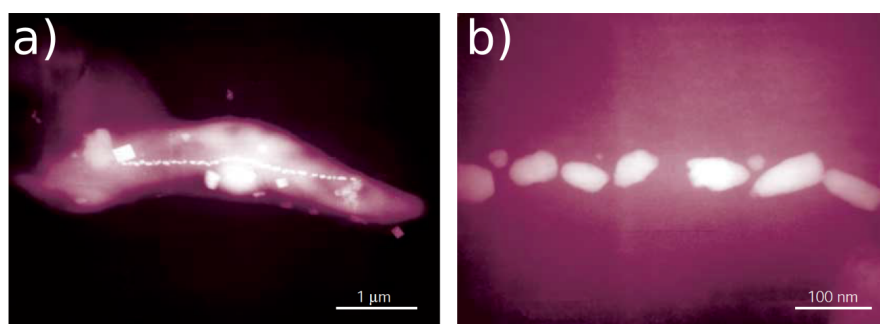


Figure 3.1: a) Dark-field scanning-transmission electron microscope (STEM) image of an uncultured magnetotactic bacterium. The white magnetosome chain along the elongated cell body is clearly visible. b) High magnification image of the ferrite crystals inside the magnetosomes. Picture adapted from [86].

Magnetotactic bacteria are aquatic unicellular prokaryotes [87]. They were first discov-

ered in 1970 by Richard Blakemore [88]. In this thesis I used the bacterium *Magnetotacticum gryphiswaldense* [89]. These bacteria have an elongated shape with few microns in length ($\sim 3 \mu\text{m}$) and approximately one micron in diameter. An example is shown in figure 3.1. They possess two helical flagella located at the opposite poles of the cells [90]. These enable the bacteria to actively swim back and forth. The change of direction is achieved by reversing the sense of rotation of the flagella.

The unique characteristic, that distinguishes magnetotactic bacteria from other conventional bacteria, is the so-called magnetosome chain (see figure 3.1). Magnetosomes are vesicles of magnetite crystals (Fe_3O_4) that are surrounded by lipid bilayers. They have a typical size of 35-120 nm (figure 3.1b). The magnetosomes are arranged in a chain that is oriented along the long axis of the bacterium [86]. This arrangement maximizes the resulting permanent magnetic moment which is of the order of $m \approx 1.5 \cdot 10^{-15} \text{ Am}^2$ [91, 92]. The natural habitat of magnetotactic bacteria is the sediment at the bottom of lakes. In the oxic-anoxic transition zone they find the required oxygen concentration for perfect growth conditions. Magnetotactic bacteria use their unique constructional property to tweak the navigation towards the optimal oxygen concentration. The predominant point of view is that the magnetosome chain and therefore the bacterium is passively aligned with the geomagnetic field and swims actively along the field lines [93].

This so-called magnetotaxis is inherently linked to aerotaxis. The bacteria swim in a *run and reverse* pattern back and forth along the field lines to find the optimal oxygen concentration. This combined process is also known as *magnet-aerotaxis* [94] and provides an efficient way of navigating in oxygen gradients. The process of scanning the oxygen concentration is reduced from the full three dimensional space to the one dimensional field lines.

There exist two different types of magneto-aerotaxis, axial and polar magneto-aerotaxis [93]. In the first case the magnetic field is only used to align the bacteria. These bacteria navigate along the field lines by sensing the oxygen gradient¹. In the second case, the polar magneto-aerotaxis, the bacteria are not only aligned by the field, but the field direction also determines the direction of motion. Therefore these bacteria only need to sense the local oxygen concentration. If it is too high (low) they e.g. swim parallel (anti parallel) to the field direction. The polar magneto-aerotaxis is the predominant mechanism under natural conditions, while the axial type is only present in cultivated bacteria.

The geomagnetic field lines are pointing upwards in the Southern hemisphere and downwards on the Northern hemisphere. For this reason there exist two opposite polarizations of polar magnetotactic bacteria [86]. On the Northern hemisphere they preferentially swim parallel to the field lines and are called *North-seeking*. On the southern hemisphere the situation is inverted, the *South-Seeking* bacteria living there are preferentially swimming anti parallel to the field direction².

¹In reality bacteria cannot measure the oxygen gradient but only its concentration. The gradient is determined by comparing the concentrations at two different locations.

²Strong pulses of a magnetic field ($H \approx 50 \text{ kA/m}$) can invert this property. North seeking bacteria can be converted into South seeking bacteria and vice versa [95].

Magnetotactic bacteria attract a lot of multidisciplinary scientific interest in various areas, even beyond biology. For example the precisely controlled synthesis of biomineral crystals in the magnetosomes makes them interesting for material scientist. Understanding how the mineralization works in the bacteria might help to improve synthesis processes in the lab [96].

They are also of interest for physicists. The possibility to manipulate them with external magnetic fields facilitates the study of the interplay of biological control mechanisms and external constraints. In the next section I show that it is possible to impose external constraints such that the bacteria are forced to swim along predefined arbitrary paths.

3.2 Guidance of the fitter

Within the magnetotactic bacteria's natural run and reverse swimming pattern the trajectories consist of straight lines that are interrupted by sharp edges of approximately 180° . These non differentiable curves make it hard to imagine that it is possible to guide bacteria along smooth curves.

In publication [P5] I showed that this is nonetheless possible. Magnetotactic bacteria can be guided by the heterogeneous magnetic fields of a garnet film. The field conditions are substantially different from the rather weak and homogeneous geomagnetic field. This arrangement allows to guide magnetotactic bacteria along lines of mechanical instability above the garnet.

For the experiments in [P5], I use ferrite garnet films. These are similar to the magnetic structures used in chapter 2. Here the up and down magnetized domains form a pattern of (not necessarily straight) stripes (compare figure A.2 and 2.5). The bacteria are placed above of the magnetic film³. For the experiments and the theoretical description I am assuming that the bacteria remain in the run mode during the whole observation time and that the magnetic field does not generate any active feedback to the swimming behavior of the bacteria. The only effect of the garnet film are magnetic forces and torques acting on the permanent moment of the bacteria.

I performed experiments with three different field strengths of the garnet film and thereby observed three distinct types of motion. If the field is very strong, most of the bacteria are trapped on top of the domain walls. This is the equilibrium position with the lowest magnetostatic energy. The trapping field is too strong and the bacteria cannot escape. If the field strength is reduced some of the bacteria can escape and start to swim. Their active motion no longer restricts them to these equilibrium positions, but enables a new type of motion. The bacteria can now swim along the stripe domains. This is working for straight and curved stripes.

For the swimming bacteria the stripe domains are lines of mechanical instability. If they are right above the center of the stripe and aligned to its direction, they are free of magnetic forces and torques. But as soon as they deviate from this position, the magnetic field repels them further away from the line. To achieve guidance along these lines the

³The experimental setup is described in detail in the appendix A.1.

repelling magnetic forces must be balanced. This is done by the interplay of passive reorientation towards the line and active swimming against the magnetic forces. The swimming directions are thereby sorted on the opposite stripe domain of the magnetic pattern. Bacteria that swim parallel (anti parallel) to their magnetic moment can only be guided above downwards (upwards) magnetized stripes.

In the third and last case of the lowest magnetic field, the percentage of guided bacteria is again reduced. Instead a third type of motion, the ignorant bacteria, emerge. The magnetic field is no longer strong enough to guide these. Therefore they ignore the stripe pattern and follow their current swimming direction.

We complement our experimental observations with a theoretical model. By balancing magnetic and viscous forces and torques, the motion of the bacteria can be explained in terms of their relative fitness

$$f = \frac{F_{propulsion}}{F_{magnetic}} \quad (3.1)$$

which is defined as the ratio of the propulsion force and the maximum magnetic force. The best guidance is achieved for the ideal fitness $f = 2$. For low fitnesses $f < 1$, which corresponds to strong magnetic fields or non motile bacteria ($f = 0$), all bacteria will get trapped above the domain walls. For higher fitnesses $f > 2$, the percentage of ignorant bacteria increases on the expense of the percentage of guided bacteria.

Therefore here it is not the strongest that triumphs over all the others. It is the fitter, but not the fittest bacteria that are guided best.

3.3 Discussion

I showed that the active motion of magnetotactic bacteria in combination with the magnetosome chain and the heterogeneous field of the garnet film can result in a novel pattern of motion. Bacteria are passively guided along (curved) lines of mechanical instability. The precise control over the motion of bacteria makes this system ready for potential applications.

This unusual combination of garnet films and the unique magnetotactic bacteria could serve to answer further interesting questions, both from biology and physics. One implication is already clear from the given experimental results. Bacteria that are swimming parallel and anti parallel to their magnetic moment can only be guided above one of the stripe domains. Both types of bacteria are thereby moving under the same external conditions. They experience the same oxygen concentration and therefore also the same deviation from the optimal concentration. Under natural conditions the moments are aligned along the geomagnetic field and all moments point into the same direction. This implies that, despite the very same external conditions, these two types of bacteria would swim into different directions. In magnetotactic bacteria with polar magneto-aerotaxis this can only be the case for North-seeking and South-seeking bacteria. In consequence, our system can be used as a tool to sort North-seeking and South-seeking magnetotactic bacteria. Both types move on oppositely magnetized stripes.

Another subject of discussion is the validity of the assumption that the magnetic field does not induce an active feedback to the bacterial motion. The dominating point of view is that magnetotactic bacteria are only passively aligned along the geomagnetic field lines without any active reaction to the magnetic field [93]. However, it is still highly debated if the geomagnetic field is actually strong enough to completely align the bacteria. In Ref. [97] the authors show that magnetotactic bacteria can perform active magnetotaxis if the magnetic field is too weak to align them. They sense the direction of the external field and use this information for navigation similar to the chemotaxis of *E. coli* bacteria. In addition magnetotactic bacteria could even be able to sense magnetic forces due to external magnetic gradients [98]. In the natural environment this feature might be useful to avoid trapping at naturally occurring magnetic materials such as iron ore. In the presented experimental setup we cannot observe any active feedback or at least a potentially present feedback was not of importance for the guiding process. The domain structures of the garnet films with their strong magnetic fields and gradients nonetheless seem to be perfect candidates to study potentially existing feedback mechanisms. Maybe different, more sophisticated patterns of magnetic domains could induce active feedback. Once this turns out to be possible, one could dream of engineering magnetic patterns that allow to selectively manipulate bacteria. Possible manipulations could thereby include active inducing of swimming reversals or even the control over the swimming speed. Another interesting direction for future research could be the enhancement of the (passive or active) magnetic manipulation with additional control parameters. An additional oxygen gradient could for example allow to study the competition between these two influence factors, their interplay in the internal signal processing cascade of the bacteria and their impact on the swimming behavior.

Both approaches could be helpful to learn new aspects about magnetotactic bacteria. Moreover they are also interesting for physical applications. Additional control mechanisms could significantly enhance the ability to guide and control the motion of magnetotactic bacteria.

Chapter 4

Defect dynamics in spin ice

So far I discussed the transport of active and passive colloidal particles. Beyond that the colloidal topological insulator was simultaneously a model system for the motion of electrons within the semiclassical picture of the quantum Hall effect. The work presented in this section is also based on colloidal particles but the interest no longer lies in the motion of the particles itself. Here, colloids are purely used as a model system for so-called spin ice. The collective behavior of the mesoscopic particles emulates the dynamics of the spin degrees of freedom in the spin ice crystal. This approach offers the possibility to access the otherwise hidden dynamics of the spins in real space and real time.

Spin ices are rare-earth pyrochlore oxides and form a class of exotic magnetic materials with remarkable properties. Its spins are geometrically frustrated, which prevents ordering of the spins and leads to a macroscopically degenerate ground state. This is observable as a residual entropy that persists even upon cooling of the material to absolute zero. Another striking feature is the existence of emergent magnetic monopoles in spin ice. Despite a huge effort that is invested in the search for magnetic monopoles, there is only one other experimental observation of magnetic monopoles in the synthetic magnetic field produced by a Bose-Einstein condensate [99, 100].

However the spins and their dynamics in bulk spin ice can only be studied by indirect measurements, such as for example neutron scattering [101]. A direct experimental observation remains elusive. The design of two dimensional model systems, so-called artificial spin ices (ASI), avoids these limitations [43]. In publication [P6] I am using a special version of ASI, the artificial colloid ice. Colloids that are confined in bistable gravitational traps take the role of the spin degrees of freedom. The advantage is, that the colloids can be individually observed in real space and time.

In publication [P6] colloidal ice is used to study the dynamics of monopole defects. I experimentally observe the motion of monopole excitations in real time and examine the interaction between pairs of them. Furthermore I am using the system to design a universal logic gate based on the motion of monopole excitations. Transferring this to ordinary ASI or even real spin ice might foster novel circuitry based on magnetism instead of electricity.

I will start this chapter by explaining frustration and how it results in the macroscopically degenerate ground states of water and spin ice. After that I give a brief introduction to the model systems of spin ice, artificial spin ice and colloidal ice. I will then summarize how colloidal ice is used to experimentally measure the interaction of charged excitations in publication [P6]. In the last part of the chapter I present a novel approach to restoring the residual entropy in colloidal ice.

4.1 Geometrical frustration

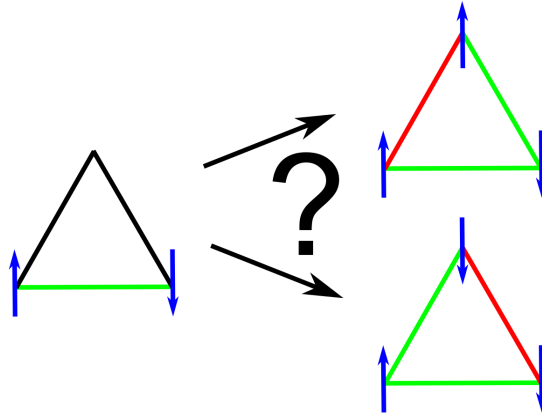


Figure 4.1: Antiferromagnetic spins on the corner of a triangle. The first two spins can be placed in opposite direction such that they minimize their energy. However it is not possible to place the third spin in a way that it simultaneously satisfies all pairwise interactions. This geometric frustration result in two possible lowest energy states.

Geometrical frustration is a widespread phenomenon in physical and biological systems. It is a unifying concept with an important role not only in various fields of condensed matter, but also far beyond [102]. In physics the presence of frustration reaches from magnetic moments in disordered solids [103] to high temperature superconductors [104]. Moreover it is also important in biological systems, exemplified by the folding of proteins [105] or neural networks [106].

Frustration arises when geometric or topological constraints impede the simultaneous satisfaction of all local interactions [107]. A consequence of geometric frustration can be a multifold degenerate ground state. In water ice or spin ices this goes along with the observation of residual entropy [108, 109].

A traditional example of frustration is the antiferromagnetic Ising triangle [107, 110]. It consist of three Ising spins with antiferromagnetic coupling residing on the three corners of a triangle as shown in figure 4.1. The first two spins can be aligned in opposite directions. There is however no possibility to place the third spin anti parallel to the first two spins. The minimization of one of the nearest neighbor interactions is always violated. Like this the triangular geometry causes the system to be frustrated with two possible lowest energy states.

4.2 Water ice and residual entropy

Historically the first frustrated system found was water ice, a material that might seem rather trivial at first glance. Crystalline cubic ice (I_c) has disorder that remains down

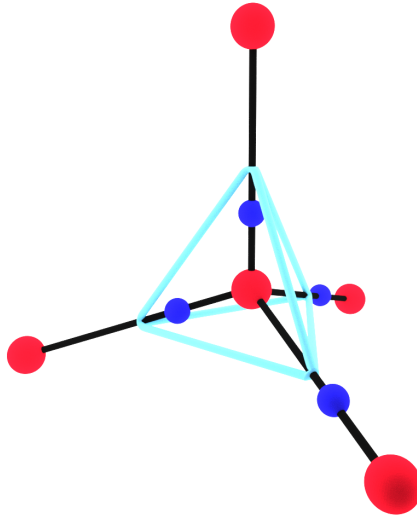


Figure 4.2: In crystalline water ice each oxygen atom (red) is surrounded by a tetrahedral arrangement of four other oxygen atoms. In-between two neighboring oxygens there is one hydrogen atom (blue) which sits close to one of the two oxygen atoms. The ground state configuration is given by the ice rules: Two of the four hydrogen atoms are close to the central oxygen atom.

to extreme low temperatures. The corresponding residual entropy was measured for the first time in 1933 by Giauque and Ashley [108]. Two years later Pauling came up with his famous explanation [111]. He found that there is a discrepancy between the crystal symmetry and the preferred number of bonds of each oxygen atom.

The arrangement of oxygen atoms in crystalline ice is well known. Each oxygen atom is surrounded by four others in a tetrahedral configuration as shown in figure 4.2. Between each pair of oxygen atoms there is one hydrogen atom. These however do not sit right in the middle of the oxygen pairs but have two possible locations closer to one of the two surrounding atoms.

It is known that the concentration of $(\text{OH})^-$ and $(\text{H}_3\text{O})^+$ ions is small in water. This situation is expected to be unchanged in ice. Therefore the hydrogen atoms will be located such that each oxygen has two hydrogen atoms close to it. These local ordering scheme with two hydrogen atoms close to the oxygen atom and two further away obeys the so-called *ice rules* [112].

This gives rise to a huge number of possible crystal configuration with different locations of the hydrogen atoms. Cooling the crystal to low temperatures freezes it into one of the disordered configurations. But it would not turn into a perfectly ordered crystal, at least not in reasonable time scales. The number W of possible configuration is related to the residual entropy $S = k_B \ln(W)$ which persists all the way down to absolute

zero temperature. Here k_B is the Boltzmann constant. In the following the number of configurations W will be calculated. A mole of ice consists of $N = 6 \cdot 10^{23}$ molecules. Each of the two hydrogen atoms of a molecule has two possible locations resulting in 2^{2N} configurations. But from the 16 possible arrangements of the four hydrogen atoms surrounding a central oxygen atom only 6 will fulfill the two “in“ and two “out“ice rules. Hence we have a total number

$$W = 2^{2N} \cdot \left(\frac{6}{16}\right)^N = \left(\frac{3}{2}\right)^N \quad (4.1)$$

of ground state configurations. The residual entropy per mole of ice is thus $S = R \ln\left(\frac{3}{2}\right)$, where R is the universal gas constant. The value for the residual entropy calculated by Pauling shows a remarkable agreement with the experimental values [108].

4.3 Spin ice and emergent magnetic monopoles

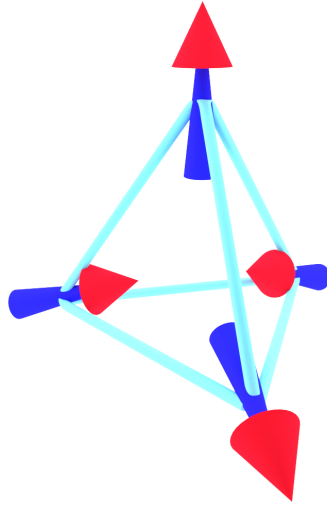


Figure 4.3: Scheme of spin arrangement in spin ice. The spins sit on the corner of a tetrahedron and are restricted to either point towards the center or away from it. The picture shows the ground state with two spins pointing in and two out.

Already in 1956 Anderson thought of a spin system that obeys the ice rule and shows the same highly degenerate ground state of water ice [113]. It took considerably longer to experimentally find such a system. In 1997 Harris and co-workers used neutron scattering to study the rare earth pyrochlore material $\text{Ho}_2\text{Ti}_2\text{O}_7$ [114]. They found that even at extremely low temperatures (down to 0.05 K) this material does not have an ordered ground state, which indicates the presence of strong frustration. They could show that

below $T \sim 1$ K the spins in this system in fact obey the ice rule, which explains the absence of any long range order. This was later confirmed experimentally by measuring the residual entropy. Since it was the first physical realization of a magnetic analogue for water ice, it was called *spin ice* [41].

In this system the spins of the holmium (Ho^{3+}) ions occupy a pyrochlore lattice of corner sharing tetrahedra. The local crystal structure thereby restricts the possible orientations of the spins. They can either point towards the center of a tetrahedron or away from it as shown in figure 4.3 [41]. The magnetic moments are rather large (approximately $10\mu_B$) and are therefore often described classically [43]. The interaction between the spins can be well approximated with nearest neighbor exchange and long range dipolar interaction. Together they result in an effective ferromagnetic coupling between the spins.

The pyrochlore lattice can be directly mapped on the water ice lattice. An inward pointing spin corresponds to a hydrogen atom that is close to the central oxygen atom and vice versa. The ground state of such a tetrahedron of ferromagnetic spins obeys the ice rules with two spins pointing in (towards the center) and two spin pointing out such that the overall spin in the tetrahedron vanishes [109]. This gives rise to the same macroscopic degeneracy as previously described in water ice. Considering the ferromagnetic coupling of the spins, it is surprising to find frustration in this system. Normally one would not expect frustration in a ferromagnetic system [41]. To date $\text{Ho}_2\text{Ti}_2\text{O}_7$, $\text{Dy}_2\text{Ti}_2\text{O}_7$ and $\text{Ho}_2\text{Sn}_2\text{O}_7$ are the only materials in which a spin ice phase could be found [41].

Monopole excitations and the dumbbell model Maybe the most exciting aspect of spin ice is the existence of defects that behave like magnetic monopoles. In 2008 Castelnovo and co-workers found, that the dipole moments of the underlying spin degrees of freedom fractionalize into magnetic monopoles [42]. To overcome the system's complexity they formally replaced the magnetic moments with dumbbells of opposite magnetic charges $\pm q_m$ (Figure 4.4a). The head of the spin is replaced by a positive charge and the tail by a negative charge.

For a vertex that fulfills the ice rule, this means that the overall magnetic charge vanishes. Two positive charges $+q_m$, from the two inward pointing spins, and two negative charges $-q_m$ (from the outward pointing spins) sum up to a total charge $Q = 0$ (Figure 4.4b). The situation however becomes more interesting if we leave the ground state. The simplest case is if exactly one of the spins is flipped. This will create two excited vertices, one with three inward pointing spins and another one with only one inward pointing spin. In terms of the dumbbell model this corresponds to a pair of magnetic monopoles with magnetic charges $Q = \pm 2q_m$ (Figure 4.4c). It is now possible to separate this two monopoles by flipping more spins, without creating additional charged vertices (Figure 4.4d).

Castelnovo *et al.* derived, that two monopoles with charges Q_α and Q_β that are separated by a distance $r_{\alpha\beta}$ really interact via a magnetic Coulomb law with the potential

$$V(r_{\alpha\beta}) = \frac{\mu_0}{4\pi} \frac{Q_\alpha Q_\beta}{r_{\alpha\beta}} \quad \alpha \neq \beta. \quad (4.2)$$

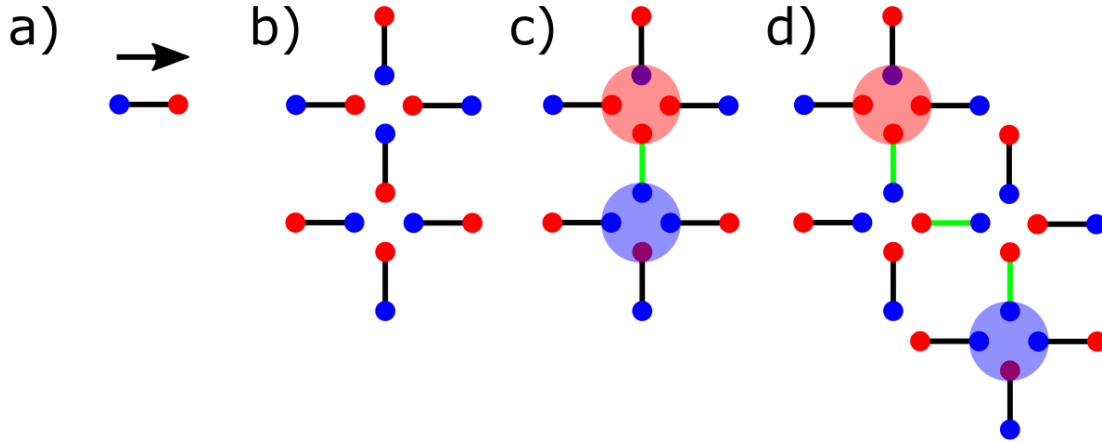


Figure 4.4: **a)** In the dumbbell model each spin (denoted by an arrow) is replaced by a positive charge $q = +q_m$ at the head (red) and a negative charge $q = -q_m$ at its tail (blue). **b)** Excerpt of the charge distribution of two vertices. For simplicity a two dimensional projection of the tetrahedral configuration is used. Both vertices fulfill the ice rule, which corresponds to overall uncharged $Q = 0$ sites. **c)** Flipping one spin (green dumbbell) creates two monopoles. The upper one is positively charged while the lower one carries a net negative charge. **d)** Flipping more spins separates the two monopoles without creating further charged vertices. Both defects are linked by a Dirac string.

This expressions is exact up to small corrections decaying with $1/r^5$ or faster [42]. Two monopoles separated by a distance r will thus experience a potential energy $-\mu_0 q_m^2 / (\pi r)$. They are connected by a Dirac string [115] which is observable but energetically irrelevant. Since it only takes a finite energy to infinitely separate both monopoles, they are deconfined and therefore elementary excitations of the system [42]. Elementary excitations in spin ice are emergent magnetic monopoles.

Only a short time after their theoretical prediction, the existence of emergent magnetic monopoles in spin ice was confirmed in experiments, e.g. by neutron scattering [118] or specific heat measurements [101]. Furthermore the existence of monopoles accounts for phase transitions in spin ice that were observed before [116, 117]. These phase transitions turned out to be liquid-gas transitions of the magnetic monopoles [42].

4.4 Artificial spin ice

As shown in the previous sections spin ice has a lot of interesting properties. However it is not possible to directly observe single spins and their frustrated arrangement in the bulk of the material. Therefore all measurements are restricted to indirect observation, e.g. by neutron scattering [118] or the measurement of averaged quantities such as the heat capacity [119].

One way to overcome this problem is to design two dimensional artificial model systems that do not show these limitations. The idea that came up in 2006 was to model the classical behavior of the spins with nanoscale magnets. To enable the observation of single spins the three dimensional tetrahedral arrangement is projected into two dimensions. There are two different possibilities of doing so, the spins can be arranged either into a square lattice [120] or a honeycomb lattice [121].

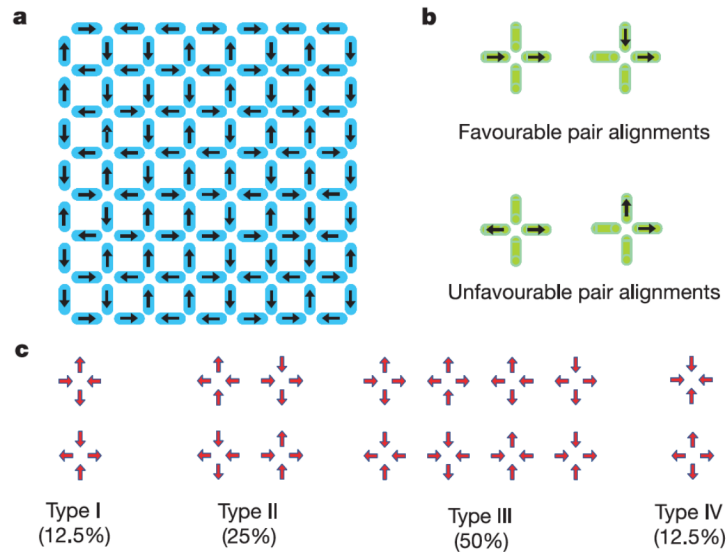


Figure 4.5: a) Arrangement of the nanoislands into a two dimensional square lattice. Each vertex has four adjacent spins. b) Energetically favorable and unfavorable arrangement of a pair of either nearest neighbor spins or opposite spins at the same vertex. c) The 16 possible spin configurations are divided into 4 topologically distinct types sorted according to their energy. The percentage given corresponds to the fraction of vertices in a system of non interacting spins. Picture adapted from [120]

To realize the artificial square ice, Wang and co workers used elongated permalloy nanoislands (80 nm by 220 nm laterally and 25 nm thick) that were built using lithographic methods [120]. The size is chosen such that each island has a single-domain ferromagnetic moment which is stable at room temperature. This stability of the magnetic moments renders artificial spin ice athermal. The shape anisotropy restricts the magnetic moment to point along the long axis of the island. Such islands therefore behave like nanoscale analogues of the Ising spins in spin ice. The direction of the spin could be visualized by magnetic force microscopy (MFM).

The islands are then arranged in a two dimensional square lattice as shown in Figure 4.5a. Each vertex of the lattice has, like in 3D spin ice, four incoming spins which results in 16 possible configurations. However, in the two dimensional projection the interaction between the spins is no longer equal for all pairs. The interaction between two perpendicular nearest neighbors is stronger than the between two opposite parallel spins,

because the latter have a longer distance. Favorable and unfavorable pair alignments for both situations are shown in figure 4.5b. All 6 pairwise interactions add up to the total vertex energy. The 16 possible spin configurations are divided into 4 topologically distinct classes, which are sorted according to their energy in figure 4.5c. Type I and type II fulfill the two in two out ice rule.

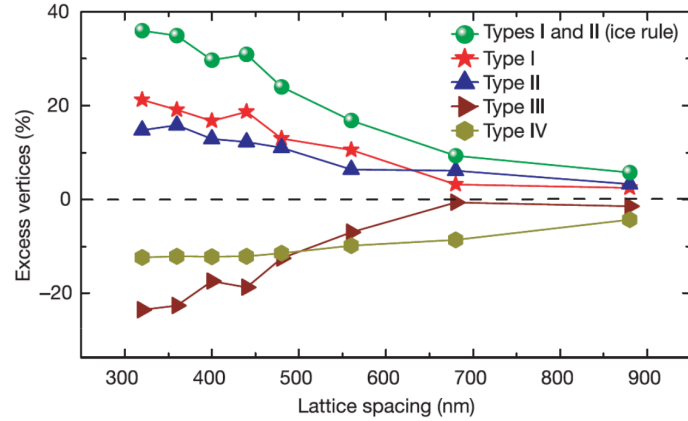


Figure 4.6: Excess percentage of the different vertex types, which is defined as the difference between the observed vertex fraction and the one expected for a random distribution. With an increasing interaction between the spins (decreasing lattice spacing) the percentage of vertices that obey the ice rule (type I and II) increases while the other vertex types are suppressed. Picture adapted from [120]

Wang et. al. could prove that their system in fact mimics the behavior of real 3D spin ice. When the interaction strength between the magnetic moments is increased (which is realized by reducing the lattice spacing) the number of type I and II vertices increases, while the energetically less favorable type III and IV vertices are suppressed. Thus the system follows the ice rule. Its ground state is made of vertices with a two in and two out spin configuration.

A second possibility for artificial spin ice is the honeycomb structure shown in figure 4.7e. Tanaka and co-workers implemented it with a continuous network of ferromagnetic wires [121]. The idea remains the same as in the square artificial spin ice, nanoscale magnetic moments emulate the role of the spins. In contrast to the previous case only three spins meet at each vertex (Figure 4.7). Thus the ground state can no longer follow the ice rule and obeys a pseudo ice rule instead. Three in (Figure 4.7a) and three out vertices (Figure 4.7d) are suppressed. The ground state is made of one in (Figure 4.7c) and two in (Figure 4.7b) sites. However they did not find long range ordering of the two different types of ground state vertices. Note that within the dumbbell model with magnetic charges only the square ice ground state vertices are uncharged. In the honeycomb lattice vertices always carry a charge.

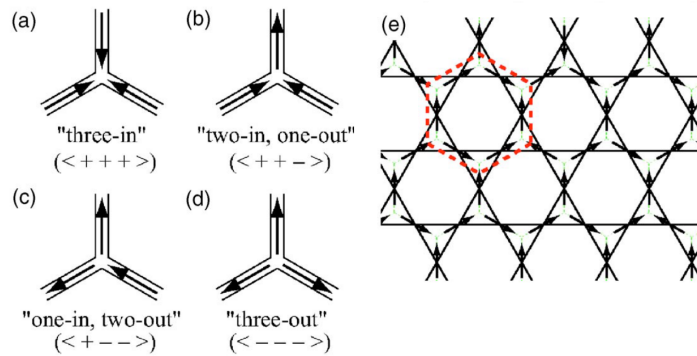


Figure 4.7: a)-d) Possible configurations of the three spins meeting at each vertex. The pseudo ice rule favors the 'one in, two out' and the 'two in, one out' configurations. e) Arrangement of the spins on the honeycomb geometry. While the vertices sit on the corners of a honeycomb lattice, the center of the spins are located on the sites of a kagome lattice. Picture adapted from [121]

Lack of residual entropy in artificial spin ice The biggest drawback in all artificial spin ices is the loss of the ground state degeneracy. In square ice the reason for this is quite obvious. In the three dimensional configuration a spin has the same distance to the other three spins on the same tetrahedron. This is no longer true in the square lattice. The opposite spins have a larger distance than the two neighboring, perpendicular spins. In consequence type I vertices have lower energy than type II vertices (Figure 4.5c). The system's unique ground state is therefore made of a alternating pattern of the two different type I vertices.

In the honeycomb lattice the situation is less obvious. On the vertex level all three spins are equal. The degeneracy is nonetheless lifted because every ground state vertex carries a net charge and also a net dipole moment. Upon cooling honeycomb ice it will first reach ice I phase where the system follows the pseudo ice rule. Further cooling will result in ordering due to the Coulombic interaction of the charged vertices. The system reaches the ice II phase where positive charges reside on one sublattice of the honeycomb and negative on the other one. At even lower temperatures the dipole moments of the vertices start to order and form a long range ordered spin 'solid' without any remaining entropy [43]. First indications for the ice II were found in experiments [122] while the spin 'solid' state was so far only observed in simulations [43].

There have been different approaches to regain the residual entropy in artificial spin ices. One approach is to change the geometry of the two dimensional lattice towards a shakti lattice which in fact shows residual entropy [123]. However it is clear that a full analogue to spin ice with four equal spins per vertex requires a 3D arrangement of the spins. One possibility of realizing a three dimensional version is through self assembly [124]. Unfortunately this allows for little control over the system and its symmetry. Another approach is to start from the two dimensional lithographic patterns and add the third

dimension by stacking multiple layers [125]. This however involves technical problems in the lithographic nano-fabrication process which makes the experimental realization challenging [43]. Recently there were nonetheless some first samples realized with this difficult technique [126].

In section 4.7 I present a new approach to restore the degeneracy in our two dimensional colloidal model system. It preserves the square geometry and the four coordinated vertices and nonetheless allows to stick to two dimension. The latter should pave the way for a fast experimental realization.

4.5 Artificial colloidal ice

Artificial spin ice allows us to probe and manipulate single spins and to observe the statistics of its ground state. It is for example possible to visualize the location of defects in response to different external magnetic fields [127]. A central aspect however remains elusive. Due to the extremely fast spin flipping processes all the dynamics of artificial spin ices are hardly experimentally accessible.

Artificial colloidal ice overcomes this limitation. In this system the nanomagnetic islands are replaced by interacting colloids that are confined in double well traps. As I will show in the following, such a system can exhibit a collective behavior similar to artificial spin ice. The use of micron sized colloidal particles has the major advantage that they can be directly observed with video microscopy and that their timescales are easily experimentally accessible. Also the particles as well as their interactions can be manipulated in real time.

The first proposal to realize such a colloidal system came from Libal et.al. [128]. It is based on electrostatically interacting colloids that are confined in a lattice of bistable optical traps. However, the experimental realization of optically based colloidal ice turned out to be challenging. On the one hand, it is difficult to stabilize and control the electric charges of the colloids. On the other hand, the huge number of optical traps would require a very high laser power.

Antonio Ortiz and Pietro Tierno succeeded to experimentally realize an alternative system [129]. Instead of optical traps they used soft lithography to create gravitational double well structures (Figure 4.8). These are elliptic cavities ($21 \mu\text{m}$ by $11 \mu\text{m}$) with a small hill in the center (figure 4.8a-c). A colloidal particle placed in these traps has two possible stable positions, one in each side of the hill. The depth of the trap is chosen such that the interaction with the other colloids can push the particle over the central hill but the particles can never escape the trap. Thermal fluctuation cannot induce a jump over the hill which makes the system athermal like artificial spin ice.

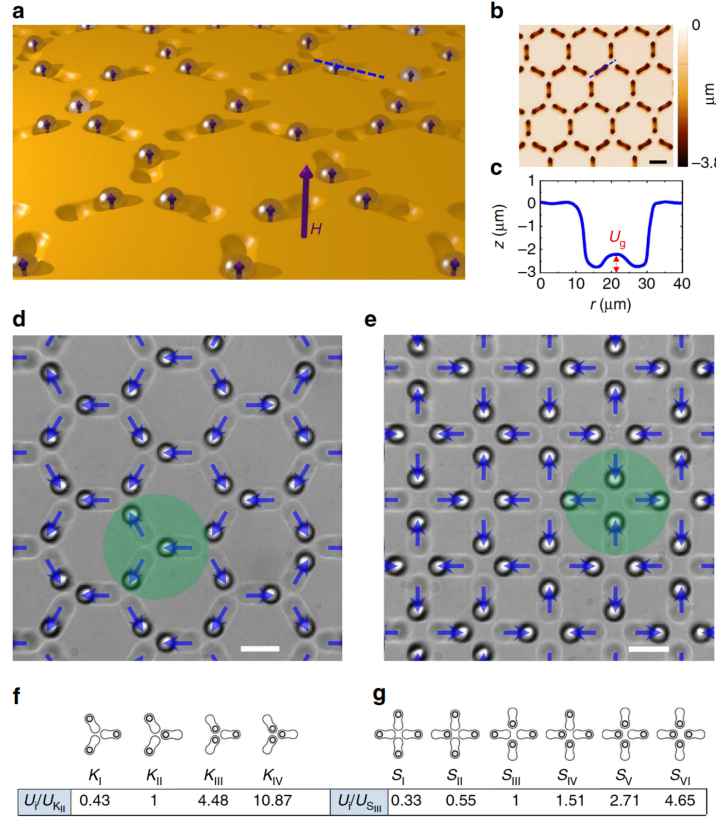


Figure 4.8: **a)** Scheme of colloidal spin ice in honeycomb geometry. The external magnetic field \mathbf{B} (purple arrow) induces magnetic moments in the paramagnetic colloids. **b)** Profilometer measurement of the soft lithographic structure. **c)** Cross section of the profile along a double well trap (along the blue line in (a) and (b)). The two stable positions and the central hill are clearly visible. **d,e)** Spin configurations of honeycomb ice (lattice constant $a = 44 \mu\text{m}$) and square ice ($a = 33 \mu\text{m}$). Blue arrows denote the assigned spin direction. A ground state vertex is highlighted in both cases. **f,g)** Vertex configuration for honeycomb and square ice sorted according to the corresponding energy. Scale bar for all images is $20 \mu\text{m}$. Picture adapted from [129].

The double well traps are then arranged either in a square (figure 4.8e) or a honeycomb lattice (figure 4.8d). The colloidal ice can be compared to conventional artificial spin ice by simply assigning arrows to each trap pointing from the vacant to the filled site (figure 4.8d,e). The system can also be described by the dumbbell model introduced in section 4. In this picture a particle close to the vertex would be a positive elementary

charge and a particle on the remote position a negative charge¹.

The interaction between the colloids is introduced by using paramagnetic colloids (diameter $2r = 10.3 \mu\text{m}$). Under application of an external magnetic field \mathbf{B} the particles acquire magnetic moments $\mathbf{m} = V\chi\mathbf{B}/\mu_0$, where V is the particle volume and $\chi \sim 0.1$ the volume susceptibility. The magnetic field is applied perpendicular to the crystal plane (figure 4.8a). The particles will therefore interact via a repulsive isotropic dipolar potential

$$U = \frac{\mu_0 m^2}{4\pi r_{ij}^3} \propto B^2. \quad (4.3)$$

The advantage in comparison to artificial spin ice is obvious, changing the interaction strength no longer requires changing the lithographic pattern but can be easily done by varying the applied magnetic field.

The pairwise repulsion gives rise to four energetically different vertex configuration in the honeycomb lattice (fig. 4.8f) and 6 different configuration in the square lattice (fig. 4.8g). On a single vertex level the repulsive interaction tries to maximize the distance between the particles and therefore negatively charged vertices are energetically favorable. Considering the whole lattice this is no longer true. In contrast to artificial spin ice the overall ground state cannot be derived from a single vertex consideration but arises from a collective effect of all interacting particles. The reason is that the colloidal particles move in contrast to the spins, which results in a higher energy for positive charges than for negative ones. Both are though topologically connected. To maintain overall charge neutrality a negatively charged vertex always has to be balanced by a positive one. In consequence the ground state is not made of the lowest energy vertices but of uncharged S_{III} and S_{IV} vertices (K_{II} and K_{III} for the honeycomb lattice), that obey the (pseudo) ice rule.

In [129] this was experimentally verified. The results are shown in figure 4.9. In the square ice the S_{III} type vertices dominate as the interaction between the particles is increased. The reason for the suppression of S_{IV} vertices is the artifact of the two dimensional projection, which was discussed in the previous section. In the honeycomb colloidal ice K_{II} and K_{III} vertices dominate in agreement with the pseudo ice rule.

In summary colloidal ice also follows the (pseudo) ice rule. Like conventional artificial spin ice it is a suitable two dimensional model system for spin ice, which additionally has access to the dynamics of the system.

¹Since the underlying degrees of freedom in this case are not magnetic moments or spins, the elementary charges introduced here are not magnetic monopoles. Hence also excited vertices will not carry an overall magnetic charge and are therefore not magnetic monopoles. They can be considered as topological charges or monopoles. Nonetheless, publication [P6] shows that these charges closely resemble the behavior of magnetic monopoles.

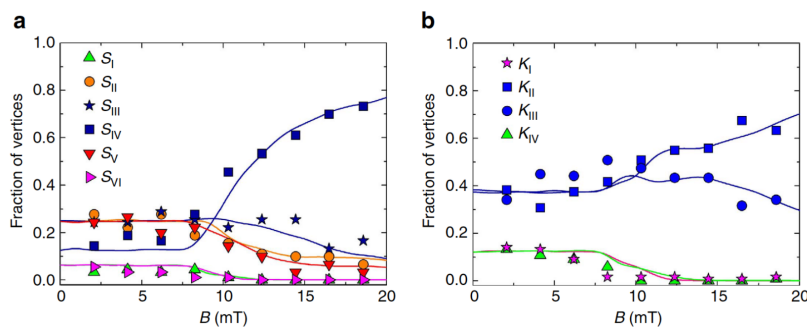


Figure 4.9: Measurement and simulation (line) of the fraction of vertex types as a function of the external magnetic field for square ice (a) and honeycomb ice (b). At low field strengths the distribution is random but with increasing field the ground state dominates. It is made of S_{III} vertices in square ice and of K_{II} and K_{III} vertices in the honeycomb ice. The fraction of K_{III} is only lower due to finite size effects of the system. Picture adapted from Ref. [129]. Note that the fraction of S_{III} and S_{IV} vertices is confused. In fact the vertices S_{III} are dominating the ground state of square colloidal ice.

4.6 Defect dynamics in artificial colloidal ice

So far the descriptions were mainly focused on the ground states properties of spin ice and its model system. An intriguing aspect in spin ice are of course the magnetic monopole excitations and in particular their dynamics. A lot of theoretical and numerical work based on artificial spin ice was invested in this topic [130, 131]. However the spin flipping processes in artificial spin ice are too fast and therefore experimentally accessible. Hence the experimental confirmation of the theoretical predictions remain elusive. It is only with colloidal ice that the dynamics in the system becomes accessible in real time.

In [P6], I use colloidal square ice to experimentally examine the dynamics and the interaction of charged defects². This work confirms former theoretical findings and proves that defects in the system in fact behave like bound magnetic monopoles. Furthermore I demonstrate how the system can be manipulated with external magnetic fields and gradients and how they were used to build a logic gate based on magneticity.

One of the major differences between three dimensional spin ice and two dimensional artificial spin ice is the interaction of defects. Two charged defects are linked by a Dirac string (compare figure 4.4). In 3D the Dirac string is energetically unimportant and charged defects interact only through a magnetic Coulomb law [42]. In the two dimensional projection this is no longer true. The string is made of S_{IV} vertices which have a higher energy than the ground state S_{III} vertices. This gives rise to an additional interaction energy in form of a line tension [130], that is a contribution that grows linearly with the distance of the defects. Therefore monopoles are bound, as opposed to

²Details on the experimental setup are described in the appendix A.2.

the unbound monopoles in three dimensional spin ice.

In the experiments I used an arrangement of two oppositely charged defects embedded in a lattice of ground state vertices. The initial configuration was set with the help of the optical tweezers. Once this is done the magnetic field is switched on. The two defects start to attract through Coulombic interaction and line tension. Both defects approach each other until they finally meet and neutralize.

The real-time observation of this process is then used to determine, the Coulombic as well as the line tension contribution of the interaction potential between the two defects. With the contraction speed as a function of the defect distance, and assuming an overdamped motion, a value for the charge of monopole defects in our system could be extracted³. The integrated equation of motion is fitted to the experimental data. The good agreement proves that defects in colloidal ice interact via Coulomb potential and line tension. This result was further validated with numerical simulations following the scheme presented in the supplementary material of [P6].

Unfortunately the Coulombic contribution is small compared to the line tension. To further illustrate the Coulombic interaction I used a different setup of biased vertices. All colloids are biased towards the left upper corner. Hence this metastable configuration is made up of S_{IV} vertices. This setup has the advantage that defect lines with positive or negative line tension can be created.

To extract the Coulombic contribution the dynamics of a defect line with both interactions is compared to the motion of a single defect that is only driven by line tension. To better visualize the Coulomb contribution I took advantage of the cleanliness of the simulation environment. This helped to clearly demonstrate that charged defects in colloidal ice obey the Coulomb law. All experimental and numerical results are in good agreement to the theoretical assumptions.

In addition I showed how the system and its defects can be manipulated by external magnetic fields and gradients. I used this to implement a 'NOR' gate. It is a complete logical function, which means every logical operation can be constructed in terms of a 'NOR' gate. The novelty is that it is based on the motion of monopole defects instead of electric charges. Our results should be transferable to artificial spin ice or maybe even real spin ice. The possibility to control monopoles in spin ice systems might stimulate the realization of a new class of computing devices based on magnetism, the motion of magnetic charges (magnetic current), instead of electricity.

4.7 Restoring the residual entropy in artificial colloidal ice

Artificial spin ice and especially colloidal spin ice offer a lot of new opportunities compared to real three dimensional spin ice. They allow for direct observation and manipulation of the single spin degrees of freedom and even open up the possibility to directly observe the dynamics of monopole defects. However, as discussed two dimensional model

³It is clear that due to their low Reynolds numbers ($Re \sim 10^{-6}$) the colloidal motion is overdamped, that is inertia is negligible. This suggests that defects in colloidal ice follow the same dynamics. In the supplementary material of [P6] we validated this assumptions with the help of numerical simulations

systems have one major drawback. As discussed in the chapter on artificial spin ice (section 4.4) they do not reproduce one of the most intriguing features of 3D spin ice, its residual entropy.

In this chapter I will present a new approach to restore residual entropy in colloidal ice. In contrast to previous attempts based on artificial spin ice this truly two dimensional approach should be easier to realize in experiments. The idea is to combine two particles of different magnetic moments with two types of traps with different lengths. In the following I will theoretically show that there are combinations of lengths and moments that result in equal energies for all ice rule vertex configurations and hence gives rise to residual entropy. I validate the theoretical result with numerical simulations. This gives strong indications that our approach in fact shows the ground state degeneracy of 3D spin ice.

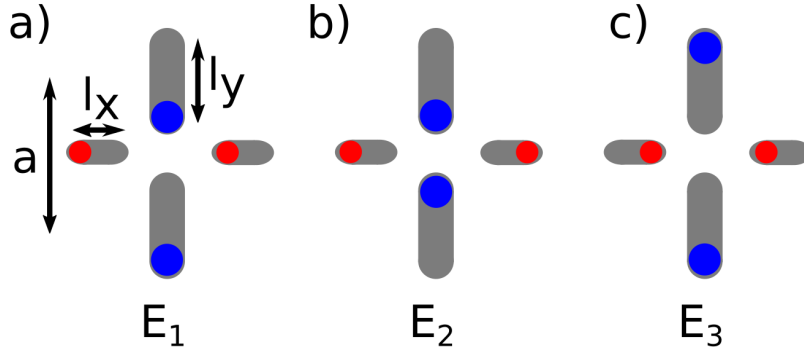


Figure 4.10: Vertex geometry of the modified spin ice. The horizontal traps are shorter than the vertical traps. The two different types of traps contain particles of different magnetic moments (red and blue). **a)** All four S_{IV} type vertices have equal energy E_1 . **b,c)** The two former ground state configuration (S_{III}) now have different energies $E_2 \neq E_3$

A vertex of the modified system is shown in figure 4.10. It consists of traps of different lengths l_x along the x -direction and l_y along the y -direction. The length of the trap is defined as the distance between the two stable positions on both sides of the central hill. The vertices thereby remain in their original square configuration with a lattice constant a .

The different types of traps are occupied by two different types of particles with magnetic moments \mathbf{m}_x and \mathbf{m}_y . Here again a perpendicular magnetic field \mathbf{B} is used to induce dipolar interactions between the paramagnetic colloids. The two magnetic moments $\mathbf{m}_i = \chi_i V_i \mathbf{B}$ can be realized by either using particles of different volume susceptibility χ_i or with colloids of different diameter and therefore different volume V_i .

The sum of the 6 pairwise dipolar interaction energies

$$U_{ij} = \frac{\mu_0 m_i m_j}{4\pi r_{ij}^3} \quad (4.4)$$

of the 4 particles per vertex gives the total vertex energy

$$E = \sum_{\substack{i,j=1 \\ j>i}}^4 U_{ij} \quad (4.5)$$

where r_{ij} is the distance between the particles i and j . All 4 possible S_{IV} vertices have the same energy E_1 (figure 4.10a). But the two former ground state S_{III} can now have different energies $E_2 \neq E_3$ (figure 4.10b,c). The requirement for residual entropy is, that all 6 configurations that fulfill the ice rule must have the same energy. Thus the set of equations

$$E_1 = E_2 = E_3 \quad (4.6)$$

has to be solved, where each of the energies $E = E(l_x, l_y, \frac{m_y}{m_x})$ is a nonlinear function of the system parameters. Note that the two magnetic moment degrees of freedom can be reduced to the ratio since the total moment is anyways scaled by the magnitude of the external field. I used a self made maple program to numerically determine parameters that solve equation (4.6). I obtained several sets of parameters that physically possible solutions to the problem. Although a lot of them contain values that are difficult to be realized in experiments there are still solution that lie in the experimentally accessible range.

I then performed numerical simulations with these solutions. The parameter set that yields the best results in simulations is

$$l_x = 0.291 \cdot a; l_y = 0.835 \cdot a; \frac{m_y}{m_x} = 0.082. \quad (4.7)$$

The simulations scheme is the same that I also used in [P6]. The particles have the same size $2r = 10.3 \mu\text{m}$, but different susceptibility with $\chi_x = 0.08$ for the higher value. The system of 15 by 15 vertices is bigger than the in experiments accessible size. Only the central 4 by 4 vertices are used to determine the statistics of the ground state. In the beginning the system is in a disordered state. The simulations runs for 30s (time step $\Delta t = 0.01$ s) with the magnetic field switched. After that the vertex distribution is measured. All results are averaged over 100 simulation runs.

The result is shown in figure 4.11. At high magnetic fields the ground state is dominated by S_{III} and S_{IV} vertices that obey the ice rule. But in contrast to the normal colloidal ice (compare figure 4.9) the S_{IV} are no longer suppressed and instead now have approximately twice the fraction of the S_{III} sites. This is expected from the different numbers of possible configurations (4 and 2). Note that the system used for simulation is bigger than the experimental system. But the behavior in a smaller, experimentally accessible system is basically the same except for a slightly higher fraction of non ground state S_{II} vertices due to finite size effects. To increase the number of ice rule vertices and to get

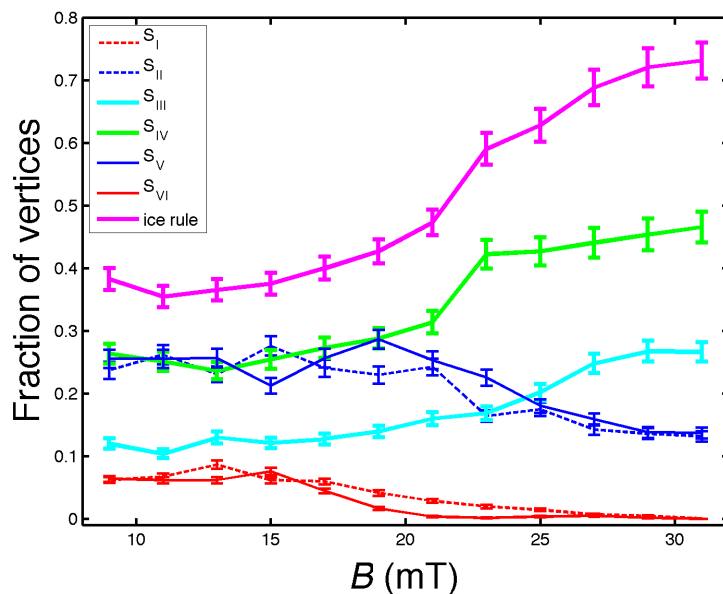


Figure 4.11: Fraction of vertices in the ground state of modified spin ice for various magnetic fields. Ice rule vertices are S_{III} and S_{IV} type vertices. For low fields the distribution of vertices is random while at higher fields ice rule vertices dominate with up to 75%. The S_{IV} vertices are approximately twice as frequent as S_{III} ones.

rid of remaining defects one could think of further modifications to the system, such as for example a improved shape of the gravitational traps. Another approach could be to introduce some equilibration scheme instead of instantaneously switching the field from zero to its maximum value.

In summary I could show that it is possible to modify the colloidal ice system in a way that it recuperates its residual entropy. Numerical simulations prove that our theoretical idea works. This system thus overcomes the biggest drawback of two dimensional spin ice model systems and could pave the way for the study of countless interesting properties of spin ice that are related to its residual entropy.

4.8 Summary and outlook

Spin ice is a interesting class of magnetic materials. Despite the ferromagnetic coupling between the single spin degrees of freedom they are highly frustrated. This frustration results in a multi fold degenerate ground state configuration of the spins that causes the residual entropy. To examine the configuration of the spins, which is normally hidden in the bulk of the spin ice, a two dimensional model system, so-called artificial spin ices, proved helpful.

My work presented in this chapter and in publication [P6] is based on colloidal artificial

ice which has the advantage of accessible dynamics. I used it to experimentally examine the interaction potential between charged defects. something that was only done in theory and simulations before. I could verify that they behave like bound magnetic monopoles. That is they obey a Coulomb law with an additional line tension, an artifact of the two dimensional projection.

The second major result is a proposal for restoring the residual entropy in colloidal ice. The colloidal system is modified by using gravitational traps of two different lengths and colloids of two different susceptibilities. By carefully choosing these parameters it is possible to adjust the energy of all 6 ice rule vertices to be equal. The system therefore shows the same ground state behavior as 3D spin ice. This could pave the way for a lot of interesting future studies. The dynamics of monopoles for example would not be governed by line tension and excitations would therefore behave like the free emergent monopoles in real spin ice.

Another interesting aspect of [P6] is the realization of a universal logic gate in colloidal ice. It is not based an electric current but on the motion of monopole defects. In [129] a storage device based on colloidal ice was already proposed. Together this could foster the development of new generation of computing devices. Probably it is not desirable to realize this in colloidal ice but it would be interesting to transfer these ideas to artificial or even real spin ice. This could open the possibility to build computing units at the scale of only a few atomic building blocks.

Beyond that, there are a lot of interesting topics to continue the work on artificial colloidal ice. The most promising thing is probably the experimental realization of colloidal ice with residual entropy. It is work that is already in progress by Pietro Tierno and his group in Barcelona. Another thing where colloidal ice could prove superior to artificial spin ice is the thermalization of the system. A topic that despite intensive effort remains difficult in artificial spin ice [43]. In colloidal ice this could be reached by simply downscaling the system. Using smaller particles of diameters around one micron and equally smaller lithographic patterns could introduce considerable thermal fluctuations to the system. Colloidal ice would offer the possibility to follow the dynamics, e.g. of monopole defects, related to thermal activity in the system.

Appendix A

Materials and Methods

In this section I outline the details of the setups and methods necessary to prepare and to perform the experiments presented in this thesis. For the topological protection (chapter 2) as well as for the work on the bacteria (chapter 3) the experimental setup is built around a commercial polarization microscope. It is equipped with coils to generate external magnetic fields. For the colloidal ice experiments (chapter 4), however, I used a more sophisticated magneto optical setup. It is composed of a homemade microscope equipped with optical tweezers to prepare the initial configuration of the colloidal ice.

A.1 Topologically protected transport and magnetic guidance of bacteria

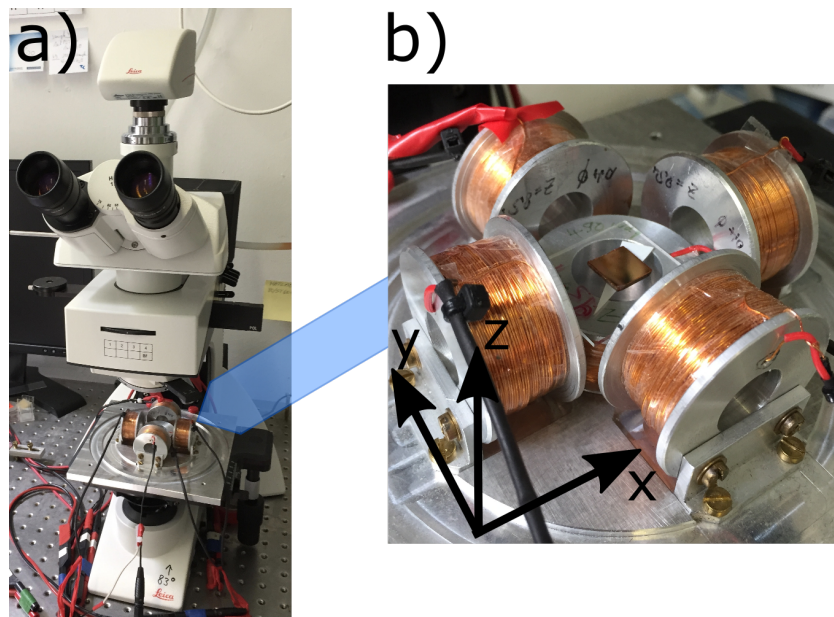


Figure A.1: a) Picture of the experimental setup. The polarization microscope is equipped with a CCD camera on top and a set of coils on the slide table. b) Close up on the arrangement of coils. There are two coils each for the x and the y direction and one for the z direction. The magnetic patterns (with the samples) are placed on top of the z coil.

Figure A.1a shows the heart of the experimental setup, the polarization microscope *DM2500P* from *Leica*. It is used to simultaneously visualize the particles and the magnetic structures. Five coils are mounted on top of the slide table to generate the external magnetic fields (fig. A.1b). The magnetic structures were placed directly on top of the z -coil. The respective samples (colloids or bacteria) are then put on top of structures with a pipette. In the following I will present the single components and their functionality.

Recovery of particle trajectories: A CCD-camera (*Leica DFC360 FX*) was attached on top of the microscope (fig. A.1a). Together with the commercial software *StreamPix* the dynamics could be recorded with a resolution of 1392×1040 at 20 frames per second. The particle trajectories were extracted from the videos using tracking routines that I implemented in *Matlab*. To measure distances and velocities of the particles the camera was calibrated with an object micrometer.

External magnetic fields To superpose time-dependent, homogeneous external magnetic field to the heterogeneous field of the magnetic structures, the arrangement of coils shown in figure A.1b is used. It consists of five coils, two each for the x and y direction and one for the z direction¹. Due to the macroscopic dimension of the coils we can in good approximation assume, that the magnetic fields are constant on the observed mesoscopic length scale. To generate the time-dependent fields the coils are connected to a wave generator (*Aim-TTi TGA 1244*) via a bi-polar amplifier (*Kepeco BOP 20-50GL*). The wave generator is capable of playing arbitrary wave forms that were beforehand created with a *Matlab* program. To convert the applied voltage into a defined field strength the coils are calibrated with a Gauss meter (*LakeShore 410*). Like this it is possible to apply any desired, time-dependent modulation of the external magnetic field.

Magnetic structures The most important ingredient in the experimental setup were magnetic structures generating the desired magnetic potentials. For stripe patterns as well as for hexagonal patterns we could use magnetic garnet films. All other symmetries required custom designed lithographic magnetic patterns.

Garnet films Ferrite garnet films (FGF) are a few micrometer thin layers that are deposited on a substrate (Gadolinium-Gallium-Granat) by *Liquid-phase-epitaxy* [132, 133]. The chemical composition of the films is $\text{Y}_{2.5}\text{Bi}_{0.5}\text{Fe}_{5.7q}\text{Ga}_q\text{O}_{12}$ ($q = 0.5 - 1$). This results in ferrimagnetic materials with uniaxial anisotropy. Ferrimagnetic materials have a vanishing macroscopic magnetization but nonetheless possess mesoscopic magnetic domains. These domains have the saturation magnetization M_S which is oriented perpendicular to the film, pointing either in the positive or the negative z -direction. The saturation

¹An earlier design used in [P2] and [P5] only had one coil each for the x and the y directions. But in experiments with ferrofluid drops on top of the lithographic magnetic patterns it turned out that the gradients in the $x - y$ -plane caused by this arrangement of coils were too strong. To reduce the in-plane gradient the experimental setup was enhanced with two additional coils for the $x - y$ -plane.

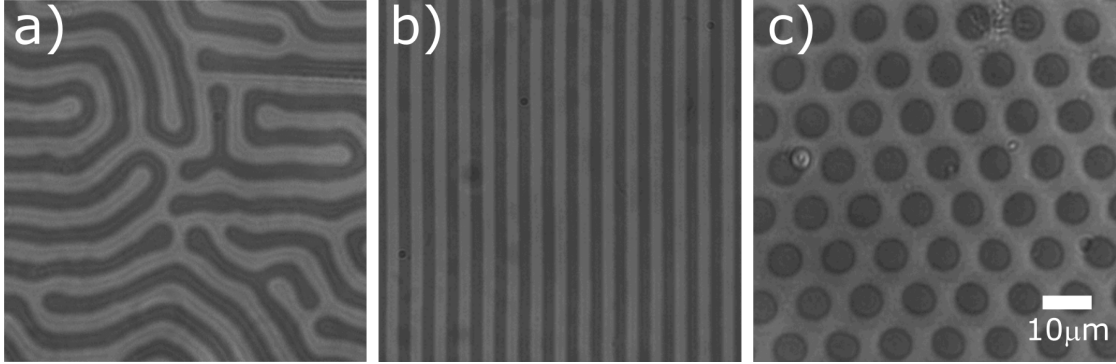


Figure A.2: Polarization microscopy images of the domain structures of ferrite garnet films. Bright and dark areas are oppositely magnetized domains. **a)** Disordered, stable labyrinth pattern. **b)** Metastable regular stripe and **c)** hexagonal bubble lattice.

magnetization is of the order of $M_S \approx 10 \text{ kA/m}$. If an external magnetic field is applied perpendicular to the film, the domains magnetized parallel to the field grow on the expense of the anti parallel domains. The domains can be observed with the polarization microscope in transmission mode via the Faraday effect [134, 135]. The oppositely magnetized domains have a different brightness in the microscope image (compare fig. A.2).

Figure A.2a shows the stable configuration which is a labyrinth pattern of stripe domains with a typical wavelength $\lambda \approx 10 \mu\text{m}$. Using a suitable external modulation this disordered pattern can be transformed into metastable states with higher symmetries. It is possible to create a regular stripe pattern (fig. A.2b) or a hexagonal bubble lattice (fig. A.2c). The necessary modulation consists of a strong perpendicular field $H_z \approx 0.7 \cdot M_S$ that is very slowly (within some minutes) reduced to zero. If an oscillating in plane field $H = H_0 \cos(2\pi ft)$ with a magnitude $H_0 \approx 0.7 \cdot M_S$ and a frequency $f \approx 20 \text{ Hz}$ is simultaneously applied the pattern tends to form stripes along the field direction. An in plane rotating field with equal magnitude and frequency will favor the formation of a hexagonal bubble lattice. The derivation of the magnetic field of the patterns is shown in detail in Ref. [136] for the stripe pattern and in Ref. [135] for hexagonal bubble lattice. Applying a field $H_{ext} \geq 0.7 \cdot M_S$ destroys the metastable states and leads back to the unordered labyrinth pattern.

Lithographic magnetic patterns The lithographic process presented in this section allowed for the creation of magnetic structures with any desired domain pattern. The starting point are [Co/Au] multilayer structures with perpendicular magnetic anisotropy. The pattern is imposed by the bombardment of the material with He-ions through a shadow mask. The mask has the pattern of the desired domain structures. The He-ions will only hit the areas that are not covered in the mask. This results in a local decrease of the materials coercive field. Applying a field with a field strength between the initial

and the new coercive field will invert the magnetization in the bombarded areas and therefore result in the formation of up and down magnetized domains. The domain pattern will coincide with the geometry that was imposed on the shadow mask. Unfortunately the used lattice constant $a = 7 \mu\text{m}$ is close to the lower end of the lithographic resolution. Therefore some smaller details of the structures are lost and also the overall magnetization did not vanish as theoretically assumed. This gave rise to some of the experimental problems discussed in publication [P1]. Details of the production process are described in the appendix of [P1].

Despite the higher saturation magnetization $M_S = 1420 \text{kA/m}$ the field strength H_p on top of the pattern is lower than on top of garnets. This is because of the layer thickness $t \approx 3.5 \text{ nm}$ which is orders of magnitude smaller than the lattice constant a . Therefore the magnetic field on top of the pattern is given by $H_p = M_S \cdot t \cdot Q \approx 3 \text{ kA/m}$. In contrast the thickness of the garnet films is of the order of the lattice constant and thus the field is given by $H_p = M_S$. This lower field strength prohibited the visualization of the domain pattern via the Faraday effect. The ion bombardment also slightly changed the color of the multilayer surface. This weak contrast is enough to identify the patterns in direct view. In the recorded videos, especially with ferrofluid on top of the structure, the domains are nonetheless hardly visible. Due to the non transparent substrate, the magnetic structures and the particles had to be observed in reflection mode.

Samples

Colloids on garnet films The garnet films were used for the experiments presented in [P2] and for the experiments on the 2 fold symmetric pattern in [P1]. The colloidal suspension is placed directly on top of the film. It contains nonmagnetic polystyrene particles (*FluoroMax*, *ThermoScientific*) of diameter $2r = 3.1 \mu\text{m}$ and polystyrene particles that are doped with iron and thus superparamagnetic ($2r = 2.8 \mu\text{m}$, *Dynabeads M-270*) with an effective susceptibility $\chi_{p,eff} \approx 0.4$ [137]. Beyond that the suspension contains nonmagnetic spacer particles (*FluoroMax*, *ThermoScientific*) with a bigger diameter $2r = 4.8 \mu\text{m}$. Together with a top cover slip this ensures a constant layer thickness $d = 4.8 \mu\text{m}$.

The colloidal particles are immersed in diluted aqueous ferrofluid (*EMG707*, *FerroTec*) of susceptibility $\chi_f \approx 0.1$ ². On the one hand, this renormalizes the susceptibility of the nonmagnetic particles such that it becomes negative and the particles behave effectively diamagnetic while the paramagnetic particles do not change their behavior. On the other hand, the boundary conditions at the transition from the ferrofluid to the top cover glass and to the garnet film cause the formation of virtual image dipoles outside of the ferrofluid. These push the particles in the mid-film plane at a constant elevation $d/2 = 2.4 \mu\text{m}$ above the surface of the garnet film. This height turned out to be a good compromise of achieving a sufficiently universal potential and keeping the magnetic fields

²In [P2] we state that the susceptibility is $\chi = 0.6$. Later on it turned out that this measurement was wrong. Apart from the total value all results presented in [P2] remain qualitatively correct.

of the patterns strong enough. A picture of the setup is shown in [P2]. A more detailed description of the magnetic levitation mechanisms can be found in Ref. [135].

The different elevations d studied for the two fold symmetric stripe pattern in [P1] are realized by two different sizes of spacers, $2r = 10 \mu\text{m}$ ($d = 5 \mu\text{m}$) and $2r = 4.8 \mu\text{m}$ ($d = 2.4 \mu\text{m}$). For even lower elevations the ferrofluid was replaced by water causing the paramagnetic colloids to sediment onto the surface of the garnet film. We approximated the elevation $d = 1.4 \mu\text{m}$ with the particle radius. Using smaller paramagnetic particles of diameter $2r = 1 \mu\text{m}$ (*Dynabeads MyOne*, $\chi_{p,eff} \approx 1$ [138]) enables the exploration of an even lower elevation $d = 0.5 \mu\text{m}$.

To realize the hybridization reaction presented in [P2] I functionalized streptavidin coated colloidal particles with complementary strands of single stranded DNA (ssDNA). The particles are first separately washed and redispersed into a 20mM NaCl TE-buffer solution (pH 8.0). Then the DNA sequences are added to the two separate particles suspensions: 5'-/5Bio/TCA CTC AGT ACG ATA TGC GGC ACA G-3' to the paramagnetic particles (*Dynabeads M270*) and its complementary strand 5'-/5Bio/CTG TGC CGC ATA TCG TAC TGA GTG A-3' to the diamagnetic particles (*SpheroTech*, $2r \approx 3 \mu\text{m}$). To allow the binding of the biotinylated ends of the DNA to the streptavidin of the particles, the suspensions are equilibrated for 30 minutes under continuous shaking (to avoid particle sedimentation). Afterwards the particles were washed again to get rid of unbound sequences of DNA. The different batches of particles were only mixed directly prior to putting the sample on the garnet film to be sure of having unbound particles in the beginning. During the hybridization experiment the linkage between a paramagnetic and a diamagnetic particle can now take place once they meet above a bubble of the magnetic pattern.

Colloids on lithographic magnetic structures All experiments in [P4] and [P1], except for those on the two fold symmetric pattern, were based on lithographic magnetic structures. Since their magnetic fields are significantly weaker magnetic levitation of colloidal particles did not reliably work. To nonetheless ensure the universal elevation of the particles the structures were coated with a photo resist (AZ-1512HS, *Microchem, Newton, MA*) of defined thickness $1.6 \mu\text{m}$. It was deposited using spin coating at a speed of 3000 rpm for 30 s, with an acceleration of 300 rpm/s. After the spin coating the resist was baked for 1 min at 115°C on a heat-plate.

A drop of the colloidal suspension is then placed on top of the photo resist layer. This time the sample is not closed with a cover slip and the objective is immersed into the liquid from above. The negligible magnetic levitation on top of the photo layer will cause the particles to sediment (due to their higher density). Like this, they are again moving at a fixed, sufficiently universal, elevation.

Magnetotactic bacteria on garnet films The work presented in [P5] is based on a wild type strain of the magnetotactic bacteria *Magnetospirillum gryphiswaldense*. The bacteria are grown in a flask standard growth medium following the procedure described in [139]. The growing process was handled by Dr. Daniel Pfeiffer at the chair of microbi-

ology on the university of Bayreuth. The result were bacteria of average length $l \approx 3 \mu\text{m}$ and average diameter $d \approx 1 \mu\text{m}$. The magnetic moment of the magnetosome chain is of the order of $m \approx 1.5 \cdot 10^{-15} \text{Am}^2$ [91, 92].

For performing the experiments, a drop of the growth medium containing the right concentration of bacteria, was put on top of the garnet films. The three different relative fitnesses presented in [P5] are obtained by using garnet films with different saturation magnetizations M_S and different elevations of the bacteria above the film surface. The strongest Magnetization is achieved by using a garnet with $M_S = 20 \text{kA/m}$ and a wavelength $\lambda = 4.8 \mu\text{m}$ of the stripe pattern. The medium magnetization corresponds to a garnet with a weaker saturation magnetization $M_S = 10 \text{kA/m}$ ($\lambda = 6.3 \mu\text{m}$). The weakest magnetic field is obtained by again using the high magnetization garnet. In this case, however, the bacteria are not deposited right on top of the garnet, but are elevated at a height $z = 1.2 \mu\text{m}$ above it, which results in a lower field strength. The elevation is again realized by depositing a photo resist layer on top of the garnet film (a higher speed of 6000 rpm results in a thinner layer). To fit experimental data and theoretical predictions, an effective magnetization, which was roughly 40 times smaller than the saturation magnetization, is used³. This value arises, among other things, since we reduce the magnetic field of the pattern to its leading Fourier component.

An issue when dealing with living bacteria is of course that their properties, such as size, magnetic moment and motility, underlie natural fluctuations. These were especially significant between bacteria from different samples. To minimize these effects as far as possible, all experiments shown in [P5] were performed with the same batch of bacteria.

A.2 Artificial colloidal ice

The experiments on the artificial colloidal ice in [P6] are based on the setup shown in figure A.3. It is a homemade inverted optical microscope provided with optical tweezers and magnetic coils. The samples are illuminated from above with a white light LED. The colloids as well as the double well pattern is observed from below with a 100X achromatic microscope objective with a high numerical aperture $NA = 1.2$ (*Nikon*). The dynamics are captured by a CCD camera (*Basler A311f*). The objective fits through the center of the z -coil that is used to introduce the repulsive interaction between the paramagnetic colloids. The optical tweezers are realized with a Butterfly Laser Diode (*Thorlabs*) with a wavelength $\lambda = 975 \text{nm}$ and a power $P = 330 \text{mW}$. The laser beam is coupled in by an optical fiber and a dichroitic mirror and is tightly focused by the same objective that is used for observation. The coils are mounted onto a motorized slide table. Therefore it is possible to move the sample with respect to the fixed objective and the laser beam. Hence an optically trapped particle can be moved across the lithographic structures.

The heart of the setup are the soft lithographic double well structures. The traps are realized by etching elliptical inlets with small hills in the middle into a photo resist. The single traps are arranged to form a square lattice. Details of the production process are

³In [P5] we state that the effective magnetization is 20 times smaller than the saturation magnetization. Unfortunately an error slipped in there, it is actually 40 times smaller.

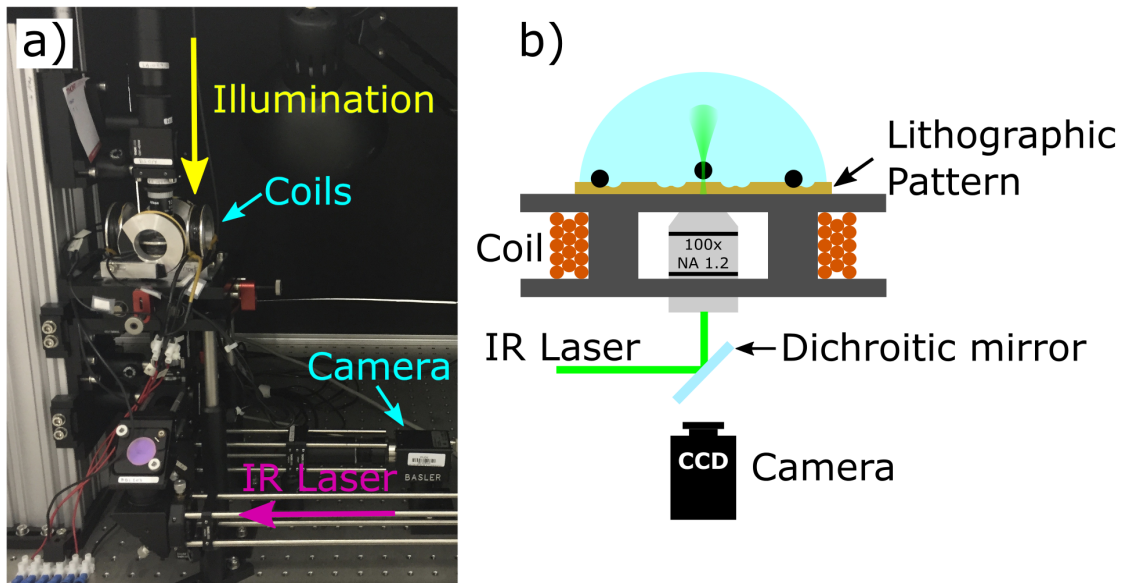


Figure A.3: **a)** Picture of the inverted optical microscope and its single components. It is equipped with a set of five coils of which only the central z -coil is used here. **b)** Schematic of the setup. The IR-laser is coupled in via a dichroitic mirror and tightly focused by the same objective that is also used for observation. The soft lithographic structures are placed directly on top of the z -coil. A drop of the colloidal suspension is put on top of the lithographic pattern.

given in the supporting information of [P6]. To avoid sticking of the colloidal particles to the surface of the structures, they are functionalized with negative charges. This is done by coating them with polysodium 4-styrene sulfonate, a negatively charged polyelectrolyte, following the procedure described in [129]. The particles are also negatively charged due to the dissociation of COOH groups and are therefore repelled from the surface.

The structures are placed on top of the z -coil. A drop of the colloidal suspension is put right on top of them. It contained paramagnetic particles (*Microparticles GmbH*) of diameter $d = 10.3 \mu\text{m}$ and susceptibility $\chi = 0.08$. The colloids are allowed to sediment onto the surface of the structure. The laser tweezers are then used to assure a filling ratio of one particle per double well trap and to prepare the desired initial configuration of the colloidal ice. Once this is done, the magnetic field is switched on and the relaxation process is recorded. All components are remotely controlled via a custom made *LabView* program which is simultaneously used for image recording.

Acknowledgments

It is my wish to sincerely thank a lot of people that supported me along the way. Without your help this thesis would not have been possible. I want to thank

- **Thomas Fischer.** It was a real honor and a big pleasure to have met you. Thank you so much for your continuous support, inspiration and for really stimulating discussions. It was an exciting journey getting into the details of topology and trying to unveil its secrets. I had a great time and a lot of fun working with you for the last four years. I also want to thank you for the chance to go to Barcelona.
- **Pietro Tierno** for the warm welcome in Barcelona. It was a great experience working with you. I could personally learn a lot from our collaboration. Many thank also to the whole group, especially **Antonio Ortiz** and **Fernando Martinez**, for the good time in Barcelona and for your support.
- All of my colleagues who spend this seven years at university with me and made it a time I will like to think back. Thanks **Jonas** and **Florian** for the good time together in the office and lab. Thanks **Fabian** and **Arne** for sharing the coffee breaks including the countless scientific problems we solved.
- **Daniel de las Heras** for our fruitful collaboration. It was our luck that we could excite you about our topological colloids. Many thanks also to **Michael Lönne** for supporting us to face the challenges of topology.
- **Dennis Holzinger** and his team from Kassel as well as the team from Poznan for you indispensable support in creating the magnetic structures. I also want to thank **Dirk Schüler** and **Daniel Pfeiffer** for handling the magnetotactic bacteria and for discussing their behavior.
- **Christine** for helping me with all administrative matters and **Klaus and Andreas** for the technical support.
- My whole family, especially my parents **Otto** and **Ria**. Without your never ending support in each and every aspect during these long years of studying, but also before, I would not have come so far. Dankeschön!
- **Carina** for your patience with me and my tales about physics, despite all those dangerous crocodiles and demons. But most importantly thank you for being on my side and for accompanying me along all the ways we are going.

HERZLICHEN DANK!

Thank you so much!

¡Muchas Gracias!

Gracie Mille!

Bibliography

- [1] P. D. Vogel: Natures design of nanomotors. *European Journal Of Pharma. and Biopharma.*, **60**, 267–277 (2005).
- [2] P. C. Hiemenz and R. Rajagopalan: Principles of Colloid and Surface Chemistry. 3rd edition, Dekker, New York (1997).
- [3] J. M. Brader: Nonlinear rheology of colloidal dispersions. *J. Phys: Condens. Matter* **22**, 363101 (2010).
- [4] M. Schmidt and J. M. Brader: Power functional theory for Brownian dynamics. *J. Chem. Phys.* **138**, 214101 (2013).
- [5] J. K. G. Dhont: An Introduction to Dynamics of Colloids, Elsevier, Amsterdam (1996).
- [6] T. M. Fischer and M. Löche: Pattern Formation in Langmuir Monolayers Due to Long-Range Electrostatic Interactions. Lecture Notes in Physics, Molecules in interaction with surface and interfaces, ed: R. Haberlandt, D. Michel, A. Pöpl and R. Stannarius, Springer Verlag **634**, 383-394 (2004).
- [7] P. Reimann: Brownian Motors: Noisy Transport far from Equilibrium. *Phys. Rep.* **361**, 57-265 (2002).
- [8] J. H. Spurk, N. Aksel: Strömungslehre. Springer, Berlin (2007).
- [9] J. Howard: Molecular motors: structural adaptations to cellular functions. *Nature* **389**, 561 (1997).
- [10] C. Bechinger, R. Di Leonardo, H. Löwen, C. Reichhardt, G. Volpe and G. Volpe: Active particles in complex and crowded environments. *Rev. Mod. Phys.* **88**, 045006 (2016).
- [11] B. J. Nelson, I. K. Kaliakatsos and J. J. Abbott: Microrobots for minimally invasive medicine. *Annu. Rev. Biomed. Eng.* **12**, 55–85 (2010).
- [12] J. Wang and W. Gao: Nano/microscale motors: Biomedical opportunities and challenges. *ACS Nano* **6**, 5745–5751 (2012).
- [13] D. Mark, S. Haeberle, G. Roth, F. von Stetten, R. Zengerle: Microfluidic lab-on-a-chip platforms: requirements, characteristics and applications. *Chem. Soc. Rev.* **39**, 1153-1182 (2010).
- [14] R. P. Feynman: There’s plenty of room at the bottom. *Engineering and Science* **23**, 22 (1960).

- [15] G. M. Whitesides: The origins and the future of microfluidics. *Nature* **442**, 368–373 (2006).
- [16] Y. Hiratsuka, T. Tada, K. Oiwa, T. Kanayama, T. Q. P. Uyeda: Controlling the Direction of Kinesin-Driven Microtubule Movements along Microlithographic Tracks. *Biophys. Jour.* **81**, 1555-1561 (2001).
- [17] J. Sauvage: Transition Metal-Containing Rotaxanes and Catenanes in Motion: Toward Molecular Machines and Motors. *Acc. Chem. Res.* **31**, 611-619 (1998).
- [18] V. I. Furdai, J. K. Kariuki and D. J. J. Harrison: Paramagnetic Structures within a Microfluidic Channel for Enhanced Immunomagnetic Isolation and Surface Patterning of Cells. *Micromech. Microeng.* **13**, 164-170 (2003).
- [19] R. H. Liu, J. N. Yang, R. Lenigk, J. Bonanno and P. Grodzinski: Self-contained, fully integrated biochip for sample preparation, polymerase chain reaction amplification, and DNA microarray detection. *Anal. Chem.* **76**, 1824-1831 (2004).
- [20] I. Hilger, K. Früauf, W. Andra, R. Hiergeist, R. Hergt and W. A. Kaiser: Antitumor effects of inductive hyperthermia using magnetic ferucarbotran nanoparticles on human lung cancer xenografts in nude mice. *Acad. Radiology* **9**, 198-202 (2002).
- [21] A. Terray, J. Oakey and D. W. M. Marr: Microfluidic Control Using Colloidal Devices *Science* **296**, 1841-1844 (2002).
- [22] P. Tierno, S. V. Reddy, M. G. Roper, T. H. Johansen, T. M. Fischer: Transport and Separation of Biomolecular Cargo on Paramagnetic Colloidal Particles in a Magnetic Ratchet. *J. Phys. Chem. B* **112**, 3833-3837 (2008).
- [23] H. Massana-Cid, F. Martinez-Pedrero, E. Navarro-Argemí, I. Pagonabarraga and P. Tierno: Propulsion and hydrodynamic particle transport of magnetically twisted colloidal ribbons. *New J. Phys.* **19**, 103031 (2017).
- [24] F. Martinez-Pedrero, A. Cebers and P. Tierno: Dipolar Rings of Microscopic Ellipsoids: Magnetic Manipulation and Cell Entrapment *Phys. Rev. Applied* **6**, 034002 (2016).
- [25] P. Tierno, F. Sagués, T. H. Johansen, Th. M. Fischer: Colloidal Transport on magnetic garnet films. *Phys. Chem. Chem. Phys.* **11**, 9615-9625 (2009).
- [26] A. Erbe, M. Zientara, L. Baraban, C. Kreidler and P. Leiderer: Various driving mechanisms for generating motion of colloidal particles. *J. Phys.: Condens. Matter* **20**, 404215 (2008).
- [27] T. Turiv, I. Lazo, A. Brodin, B. I. Lev, V. Reiffenrath, V. G. Nazarenko and O. D. Lavrentovich: Effect of collective molecular reorientations on Brownian motion of colloids in nematic liquid crystal. *Science* **342**, 1351 (2013).

-
- [28] A. Engel, H. W. Müller, P. Reimann and A. Jung: Ferrofluids as Thermal Ratchets. *Phys. Rev. Lett.* **91**, 060602 (2003).
- [29] P. Reimann, P. Hänggi: Introduction to the physics of Brownian motors, *Applied Physics A* **75** 169-178 (2002).
- [30] C. R. Doering, W. Horsthemke, J. Riordan: Nonequilibrium Fluctuation Induced Transport, *Phys. Rev. Lett.* **72**, 2984-2987 (1994).
- [31] F. Marchesoni: Transport properties in disordered ratchet potentials, *Phys. Rev. E* **56**, 2492-2495 (1997).
- [32] S. Savel'ev, F. Marchesoni, F. Nori: Stochastic transport of interacting particles in periodically driven ratchets, *Phys. Rev. E* **70**, 061107 (2004).
- [33] E. M. Purcell: Life at low Reynolds number. *Am. Jour. Phys.* **45**, (1), 3-11 (1977).
- [34] H. C. Berg: *E. coli in Motion*. Springer-Verlag, Heidelberg (2004).
- [35] D. J. Thouless, M. Kohmoto, M. P. Nightingale and M. den Nijs: Quantized Hall Conductance in a Two-Dimensional Periodic Potential. *Phys. Rev. Lett.* **49**, 405 (1982).
- [36] M. Z. Hasan and C. L. Kane: Colloquium: Topological insulators. *Rev. Mod. Phys.* **82**, 3045 (2010).
- [37] W. Poon: Colloids as Big Atoms. *Science* **304**, 830-831 (2004).
- [38] S. C. Glotzer and M. J. Solomon: Anisotropy of building blocks and their assembly into complex structures. *Nat. Mat.* **6**, 557-562 (2007).
- [39] M. Chaudhuri, E. Allahyarov, H. Löwen, S. U. Egelhaaf and D. A. Weitz: Triple Junction at the Triple Point Resolved on the Individual Particle Level. *Phys. Rev. Lett.* **119**, 128001 (2017).
- [40] P. Tierno, T. M. Fischer: Excluded Volume Causes Integer and Fractional Plateaus in Colloidal Ratchet Currents., *Phys. Rev. Lett.* **112**, 048302 (2014).
- [41] S. T. Bramwell and M. J. P. Gingras: Spin Ice State in Frustrated Magnetic Pyrochlore Materials. *Science* **294**, 5546 (2001).
- [42] C. Castelnovo, R. Moessner and S. L. Sondhi: Magnetic monopoles in spin ice. *Nature* **451**, 42 (2008).
- [43] C. Nisoli, R. Moessner and P. Schiffer: Colloquium: Artificial spin ice: Designing and imaging magnetic frustration. *Rev. Mod. Phys.* **85**, 1473 (2013).
- [44] S. Kumar: Fundamental Limits to Moore's Law. *arXiv* **1511.05956** (2015).

- [45] X.-L. Qi and S.-C. Zhang: Topological insulators and superconductors. *Rev. Mod. Phys.* **83**, 1057 (2011).
- [46] A. Kitaev: Fault-tolerant quantum computation by anyons. *Ann. Phys.* **303**, 2 (2003).
- [47] S. D. Huber: Topological mechanics. *Nat. Phys.* **12**, 621-623 (2016).
- [48] M. Nakahara: Geometry, Topology and Physics. Adam Hilger, Bristol and New York (1990).
- [49] E. H. Hall: On a New Action of the Magnet on Electric Currents. *Am. J. Math.* **2**, 287 (1879).
- [50] K. von Klitzing, G. Dorda, M. Pepper: New Method for High-Accuracy Determination of the Fine-Structure Constant Based on Quantized Hall Resistance. *Phys. Rev. Lett.* **45**, 494 (1980).
- [51] S.-Q. Shen: Topological insulators: Dirac equation in condensed matters, Springer Science, and Business Media, Berlin (2013).
- [52] F. D. M. Haldane: Model for a Quantum Hall Effect without Landau Levels: Condensed-Matter Realization of the "Parity Anomaly". *Phys. Rev. Lett.* **61**, 2055 (1988).
- [53] C.-Z. Chang *et al.*: Experimental Observation of the Quantum Anomalous Hall Effect in a Magnetic Topological Insulator. *Science* **340**, 167 (2013).
- [54] C. L. Kane and E. J. Mele: Z₂ Topological Order and the Quantum Spin Hall Effect. *Phys. Rev. Lett.* **95**, 146802 (2005).
- [55] C. L. Kane and E. J. Mele: Quantum Spin Hall Effect in Graphene. *Phys. Rev. Lett.* **95**, 226801 (2005).
- [56] M. König, S. Wiedmann, C. Brüne, A. Roth, H. Buhmann, L. W. Molenkamp, X.-L. Qi and S.-C. Zhang: Quantum Spin Hall Insulator State in HgTe Quantum Wells. *Science* **318**, 766 (2007).
- [57] L. Fu, C. L. Kane and E. J. Mele: Topological Insulators in Three Dimensions. *Phys. Rev. Lett.* **98**, 106803 (2007).
- [58] D. Hsieh, D. Qian, L. Wray, Y. Xia, Y. S. Hor, R. J. Cava and M. Z. Hasan: A topological Dirac insulator in a quantum spin Hall phase. *Nature* **452**, 970 (2008).
- [59] A. R. Mellnik, J. S. Lee, A. Richardella, J. L. Grab, P. J. Mintun, M. H. Fischer, A. Vaezi, A. Manchon, E.-A. Kim, N. Samarth and D. C. Ralph: Spin-transfer torque generated by a topological insulator. *Nature* **511**, 449 (2014).

-
- [60] T. Kitagawa, E. Berg, M. Rudner, E. Demler: Topological Characterization of periodically driven quantum systems. *Phys. Rev. B* **82**, 235114 (2010).
- [61] M. S. Rudner, N. H. Lindner, E. Berg, M. Levin: Anomalous Edge States and the Bulk-Edge Correspondence for Periodically Driven Two-Dimensional Systems. *Phys. Rev. X* **3**, 031005 (2013).
- [62] A. Alù: Topological order gets active. *Nat. Phys.*, 4216 (2017).
- [63] R. Süsstrunk and S. D. Huber: Observation of phononic helical edge states in a mechanical topological insulator. *Science* **349**, 47 (2015).
- [64] L. M. Nash, D. Kleckner, A. Read, V. Vitelli, A. M. Turner and W. T. M. Irvine: Topological mechanics of gyroscopic metamaterials. *Proc. Natl Acad. Sci. USA* **112**, 14495 (2015).
- [65] A. B. Khanikaev, R. Fleury, S. H. Mousavi and A. Alù: Topologically robust sound propagation in an angular-momentum-biased graphene-like resonator lattice. *Nat. Comm.* **6**, 8260 (2015).
- [66] M. C. Rechtsman, J. M. Zeuner, Y. Plotnik, Y. Lumer, D. Podolsky, F. Dreisow, S. Nolte, M. Segev and A. Szameit: Photonic Floquet topological insulators. *Nature* **496**, 196 (2013).
- [67] V. Peano, C. Brendel, M. Schmidt and F. Marquardt: Topological Phases of Sound and Light. *Phys. Rev. X* **5**, 031011 (2015).
- [68] S. Kashiwaya, H. Kashiwaya, H. Kambara, T. Furuta, H. Yaguchi, Y. Tanaka and Y. Maeno: Edge States of Sr₂RuO₄ Detected by In-Plane Tunneling Spectroscopy. *Phys. Rev. Lett.* **107**, 077003 (2011).
- [69] R.-J. Slager, A. Mesaros, V. Juricic and J. Zaanen: The space group classification of topological band-insulators. *Nat. Phys.* **9**, 98 (2013).
- [70] L. Fu: Topological crystalline insulators. *Phys. Rev. Lett.* **106**, 106802 (2011).
- [71] S. Diehl, E. Rico, M. A. Baranov and Peter Zoller: Topology by dissipation in atomic quantum wires. *Nat. Phys.* **7**, 971-977 (2011).
- [72] A. M. E. B. Rossi, J. Bugase and T. M. Fischer: Macroscopic Floquet topological crystalline steel and superconductor pump. *Euro. Phys. Lett.* **119**, 40001 (2017).
- [73] A. Einstein: Über die von der molekularkinetischen Theorie der Wärme geforderte Bewegung von in ruhenden Flüssigkeiten suspendierten Teilchen. *Ann. Phys.* **17**, 549–60 (1905).
- [74] U. Erdmann, W. Ebeling, L. Schimansky-Geier and F. Schweitzer: Brownian particles far from equilibrium. *Eur. Phys. J. B* **15**, 105–113 (2000).

- [75] C. W. Reynolds: Flocks, herds and schools: A distributed behavioral model. *ACM Siggraph Computer Graphics* **21**, 25 (1987).
- [76] F. Schweitzer: Brownian agents and active particles: Collective dynamics in the natural and social sciences. Springer-Verlag, Heidelberg (2007).
- [77] J. Palacci, S. Sacanna, A. P. Steinberg, D. J. Pine and P. M. Chaikin: Living crystals of light-activated colloidal surfers. *Science* **339**, 936 (2013).
- [78] N. H. Mendelson, A. Bourque, K. Wilkening, K. R. Anderson and J. C. Watkins: Organized cell swimming motions in *Bacillus subtilis* colonies: Patterns of short-lived whirls and jets. *J. Bacteriol.* **181**, 600 (1999).
- [79] M. E. Cates: Diffusive transport without detailed balance: Does microbiology need statistical physics? *Rep. Prog. Phys.* **75**, 042601 (2012).
- [80] G. M. Viswanathan, M. G. E. da Luz, E. P. Raposo and H. E. Stanley: The physics of foraging: An introduction to random searches and biological encounters. Cambridge University Press, Cambridge (2011).
- [81] N. Vladimirov and V. Sourjik: Chemotaxis: how bacteria use memory. *Biol. Chem.* **390** (11), 1097 (2009).
- [82] J. R. Howse, R. A. L. Jones, A. J. Ryan, T. Gough, R. Vafabakhsh and R. Golestanian: Self-motile colloidal particles: From directed propulsion to random walk. *Phys. Rev. Lett.* **99**, 048102 (2007).
- [83] A. Ghosh and P. Fischer: Controlled propulsion of artificial magnetic nanostructured propellers. *Nano Lett.* **9**, 2243–2245 (2009).
- [84] F. Martinez-Pedrero, A. Ortiz-Ambriz, I. Pagonabarraga and P. Tierno: Colloidal microworms propelling via a cooperative hydrodynamic conveyor belt. *Phys. Rev. Lett.* **115**, 138301 (2015).
- [85] F. J. Maier, T. Lachner, A. Vilfan, T. O. Tasci, K. B. Neeves, D. W. M. Marr and T. M. Fischer: Non reciprocal skewed rolling of a colloidal wheel due to induced chirality. *Soft Matter* **12**, 9314–9320 (2016).
- [86] D. A. Bazylinski and R. B. Frankel: Magnetosome formation in prokaryotes. *Nat. Rev. Micro.* **2**, 217 (2004).
- [87] D. Faivre and D. Schüler: Magnetotactic Bacteria and Magnetosomes. *Chem. Rev.* **108**, 4875 (2008).
- [88] R. P. Blakemore: Magnetotactic Bacteria. *Science* **190**, 377–379 (1975).

-
- [89] K.-H. Schleifer, D. Schüler, S. Spring, M. Weizenegger, R. Amann, W. Ludwig, M. Köhler: The Genus *Magnetospirillum* gen. nov. Description of *Magnetospirillum gryphiswaldense* sp. nov. and Transfer of *Aquaspirillum magnetotacticum* to *Magnetospirillum magnetotacticum* comb. nov.1. *Syst. Appl. Microbiol.* **14**, 379 (1991).
- [90] D. Murat, M.H'erisse, L. Espinosa, A. Bossa, F. Alberto and L.-F. Wu: Opposite and Coordinated Rotation of Amphitrichous Flagella Governs Oriented Swimming and Reversals in a Magnetotactic Spirillum. *J. Bacteriol.* **197**, 3275 (2015).
- [91] E. Wajnberg, L. H. Salvo de Souza, H. G. P. Lins de Barros, D. M. S. Esquivel: A Study of Magnetic Properties of Magnetotactic Bacteria. *Biophys. J.* **50**, 451-455 (1986).
- [92] P. Dhar, Y. Cao, T. Kline, P. Pal, C. Swayne, T. M. Fischer, B. Miller, T. E. Mallouk, A. Sen and T. H. Johansen: Autonomously moving local nano probes in heterogeneous magnetic fields. *J. Phys. Chem. C*, **111**, 3607 (2007).
- [93] S. Klumpp and D. Faivre: Magnetotactic Bacteria. *Eur. Phys. J. Spec. Topics* **225**, 2173 (2016).
- [94] F. Popp, J. P. Armitage, D. Schüler: Polarity of bacterial magnetotaxis is controlled by aerotaxis through a common sensory pathway, *Nat. Comm.* **5**, 5398 (2014).
- [95] A. J. Kalmijn and R. P. Blakemore: The Magnetic Behavior of Mud Bacteria. In: K. Schmidt-Koenig, W. T. Keeton (eds): *Animal Migration, Navigation, and Homing. Proceedings in Life Sciences.* Springer, Berlin, Heidelberg (1978).
- [96] T. Matsunaga and A. Arakaki: Molecular Bioengineering of Bacterial Magnetic Particles for Biotechnological Applications. In: D. Schüler: *Magnetoreception and Magnetosomes in Bacteria.* Springer, Berlin (2007)
- [97] X. Zhu, X. Ge, N. Li, L. Wu, C. Luo, Q. Ouyang, Y. Tu and G. Chen: Angle sensing in magnetotaxis of *Magnetospirillum magneticum* AMB-1. *Integrative Biology* **6** 706-713 (2014).
- [98] L. M. Gonzalez, W. C. Ruder, A. P. Mitchell, W. C. Messner and P. LeDuc: Sudden motility reversal indicates sensing of magnetic field gradients in *Magnetospirillum magneticum* AMB-1 strain. *ISME Journal* 1-11 (2014).
- [99] K. A. Milton: Theoretical and experimental status of magnetic monopoles. *Rep. Prog. Phys.* **69**, 1637-1712 (2006).
- [100] M. W. Ray, E. Ruokokoski, S. Kandel, M. Möttönen and D. S. Hall: Observation of Dirac monopoles in a synthetic magnetic field. *Nature* **505**, 657-660 (2014).

- [101] D. J. P. Morris, D. A. Tennant, S. A. Grigera, B. Klemke, C. Castelnovo, R. Moessner, C. Czternasty, M. Meissner, K. C. Rule, J.-U. Hoffmann, K. Kiefer, S. Gerischer, D. Slobinsky and R. S. Perry: Dirac Strings and Magnetic Monopoles in the Spin Ice $\text{Dy}_2\text{Ti}_2\text{O}_7$. *Science* **326**, 411 (2009).
- [102] J. F. Sadoc: Geometrical Frustration. Cambridge University Press, Cambridge (1999).
- [103] A. P. Ramirez: Geometric frustration: magnetic moments. *Nature* **421**, 483 (2003).
- [104] P. W. Anderson: The resonating valence bond state in La_2CuO_4 and superconductivity. *Science* **235**, 1196-1198 (1987).
- [105] D. Bryngelson and P. G. Wolynes: Spin glasses and the statistical mechanics of protein folding. *Proc. Natl. Acad. Sci. USA* **84**, 7524-7528 (1987).
- [106] S. N. Dorogovtsev, A. V. Goltsev and J. F. Mendes: Critical phenomena in complex networks. *Rev. Mod. Phys.* **80**, 1275-1335 (2008).
- [107] R. Moessner and A. P. Ramirez: Geometrical Frustration. *Phys. Today* **59**, 24-29 (2006).
- [108] W. Giauque and M. F. Ashley: Molecular Rotation in Ice at 10°K . Free Energy of Formation and Entropy of Water. *Phys. Rev.* **43**, 81 (1933).
- [109] M. J. Harris, S. T. Bramwell, D. F. Mc Morrow, T. Zeiske and K. W. Godfrey: Geometrical frustration in the ferromagnetic pyrochlore $\text{Ho}_2\text{Ti}_2\text{O}_7$. *Phys. Rev. Lett.* **79**, 2554 (1997).
- [110] G. H. Wannier: Antiferromagnetism; The triangular ising net. *Phys. Rev.* **79**, 357-364 (1950).
- [111] L. Pauling: The Structure and Entropy of Ice and of Other Crystals with Some Randomness of Atomic Arrangement. *J. Am. Chem. Soc.* **57**, 2680 (1935).
- [112] D. Bernal and R. H. Fowler: A Theory of Water and Ionic Solution, with Particular Reference to Hydrogen and Hydroxyl Ions. *J. Chem. Phys.* **1**, 515 (1933).
- [113] P. W. Anderson: Ordering and Antiferromagnetism in Ferrites. *Phys. Rev.* **102**, 1008 (1956).
- [114] A. P. Ramirez, A. Hayashi, R. J. Cava, R. Siddharthan and B. S. Shastry: Zero-point entropy in 'spin ice'. *Nature* **399**, 333 (1999).
- [115] P. A. M. Dirac: Quantised singularities in the electromagnetic field. *Proc. R. Soc. A* **133**, 60-72 (1931).
- [116] H. Aoki, T. Sakakibara, K. Matsuhira and Z. Hiroi: Magnetocaloric effect study on the pyrochlore spin ice compound $\text{Dy}_2\text{Ti}_2\text{O}_7$ in a [111] magnetic field. *J. Phys. Soc. Jpn* **73**, 2851-2856 (2004).

-
- [117] R. Higashinaka, H. Fukazawa, K. Deguchi and Y. Maeno: Low temperature specific heat of $\text{Dy}_2\text{Ti}_2\text{O}_7$ in the kagome ice state. *J. Phys. Soc. Jpn* **73**, 2845–2850 (2004).
- [118] T. Fennell, P. P. Deen, A. R. Wildes, K. Schmalzl, D. Prabhakaran, A. T. Boothroyd, R. J. Aldus, D. F. McMorrow and S. T. Bramwell: Magnetic Coulomb Phase in the Spin Ice $\text{Ho}_2\text{Ti}_2\text{O}_7$. *Science* **326**, 415 (2009).
- [119] A. P. Ramirez, A. Hayashi, R. J. Cava, R. Siddharthan and B. S. Shastry: Zero-point entropy in 'spin ice'. *Nature* **399**, 333–335 (1999).
- [120] R. F. Wang, C. Nisoli, R. S. Freitas, J. Li, W. McConville, B. J. Cooley, M. S. Lund, N. Samarth, C. Leighton, V. H. Crespi and P. Schiffer: Artificial 'spin ice' in a geometrically frustrated lattice of nanoscale ferromagnetic islands. *Nature* **439**, 303 (2006).
- [121] M. Tanaka, E. Saitoh and H. Miyajima: Magnetic interactions in a ferromagnetic honeycomb nanoscale network. *Phys. Rev. B* **73**, 052411 (2006).
- [122] W. R. Branford, S. Ladak, D. E. Read, K. Zeissler and L. F. Cohen: Emerging Chirality in Artificial Spin Ice. *Science* **335**, 6076 (2012).
- [123] G-W Chern, M. J. Morrison and C. Nisoli: Degeneracy and Criticality from Emergent Frustration in Artificial Spin Ice, *Phys. Rev. Lett.* **111**, 177201 (2013).
- [124] A. A. Mistonov, N. A. Grigoryeva, A. V. Chumakova, H. Eckerlebe, N. A. Sapoletova, K. S. Napolskii, A. A. Eliseev, D. Menzel and S. V. Grigoriev: Three-dimensional artificial spin ice in nanostructured Co on an inverse opal-like lattice. *Phys. Rev. B* **87**, 220408 (2013).
- [125] G.-W. Chern, C. Reichhardt and C. Nisoli: Realizing three-dimensional artificial spin ice by stacking planar nano-arrays. *Appl. Phys. Lett.* **104**, 013101 (2014).
- [126] Y. Perrin, B. Canals and N. Rougemaille: Extensive degeneracy, Coulomb phase and magnetic monopoles in artificial square ice. *Nature* **540**, 410 (2016).
- [127] E. Mengotti, L. J. Heyderman, A. F. Rodríguez, F. Nolting, R. V. Hügli and H.-B Braun: Real-space observation of emergent magnetic monopoles and associated Dirac strings in artificial kagome spin ice. *Nat. Phys* **7**, 68-74 (2011).
- [128] A. Libál, C. Reichhardt and C. J. O. Reichhardt: Realizing colloidal artificial ice on arrays of optical traps. *Phys. Rev. Lett.* **97**, 228302 (2006).
- [129] A. Ortiz-Ambriz and P. Tierno: Engineering of frustration in colloidal artificial ices on microfeatured grooved lattices. *Nat. Commun.* **7**, 10575 (2016).
- [130] L. A. Mól, R. L. Silva, R. C. Silva, A. R. Pereira, W. A. Moura-Melo and B. V. Costa: Magnetic monopole and string excitations in two-dimensional spin ice. *J. Appl. Phys.* **106**, 063913 (2009).

- [131] E. Y. Vedmedenko: Dynamics of Bound Monopoles in Artificial Spin Ice: How to Store Energy in Dirac Strings. *Phys. Rev. Lett.* **116**, 077202 (2016).
- [132] A. H. Bobeck, P. I. Bonyhard and J. E. Geusic: Magnetic bubbles -emerging new memory technology. *Proc. IEEE* **63** 1176- 1195 (1975).
- [133] J. M. Robertson: Liquid Phase Epitaxy of Garnets. *Journal of Crystal Growth* **45**, 233-242 (1978).
- [134] L. D. Landau and E. M. Lifschitz: Elektrodynamik der Kontinua. 5. Auflage, Akademie Verlag, Berlin (1990).
- [135] J. Löhr: Bewegung von Mikroobjekten in Magnetfeldern. Universität Bayreuth, Masterrarbeit (2015).
- [136] P. Dahr, Y. Cao, T. Kline, P. Pal, C. Swayne, T. M. Fischer, B. Miller, Th. M. Mallouk, A. Sen and T. H. Johansen: Autonomously Moving Local Nanoprobes in Heterogeneous Magnetic Fields. *J. Phys. Chem. C* **111** 3607-3613 (2007).
- [137] L. E. Helseth: Paramagnetic particles as sensitive force detectors in liquids. *J. Phys. D: Appl. Phys.*, **40**, 3030-3037 (2007).
- [138] L. Clime, B. L. Drogoff and T. Veres: Dynamics of Superparamagnetic and Ferromagnetic Nano-Objects in Continuous-Flow Microfluidic Devices. *IEEE Trans. Magn.*, **43**, 2929-2931 (2007).
- [139] U. Heyen and D. Schüler: Growth and magnetosome formation by microaerophilic Magnetospirillum strains in an oxygen-controlled fermentor. *Appl. Microbiol. Biotechnol.* **61** , 536-544 (2003).

Part II

Publications

Publication 1

Lattice symmetries and the topologically protected transport of colloidal particles

Soft Matter, **13**, 5044 (2017)

Johannes Loehr^{a1}, Daniel de las Heras^{a2}, Michael Loenne^{a3},
Jonas Bugase^{a1}, Adam Jarosz^b, Maciej Urbaniak^b, Feliks Stobiecki^b,
Andreea Tomita^c, Rico Huhnstock^c, Iris Koch^c, Arno Ehresmann^c,
Dennis Holzinger^c and Thomas M. Fischer^{a1}

^{a1} Experimental Physics, ^{a2} Theoretical Physics, and ^{a3} Mathematics, Faculty of Physics, Mathematics and Computer Science, University of Bayreuth, 95447 Bayreuth, Germany.

^b Institute of Molecular Physics, Polish Academy of Sciences, ul. M. Smoluchowskiego 17, 60-179 Poznań, Poland.

^c Institute of Physics and Center for Interdisciplinary Nanostructure Science and Technology (CINSA-T), University of Kassel, Heinrich-Plett-Strasse 40, D-34132 Kassel, Germany.

My Contribution

I designed, performed and analyzed all experiments, except for those on the four fold symmetric patterns. I also developed the theoretical description together with Daniel de las Heras, Michael Lönne and Thomas Fischer and wrote the manuscript together with Daniel de las Heras and Thomas Fischer.


 Cite this: *Soft Matter*, 2017,
13, 5044

Lattice symmetries and the topologically protected transport of colloidal particles†

 Johannes Loehr,^a Daniel de las Heras,^{ib} Michael Loenne,^c Jonas Bugase,^a Adam Jarosz,^d Maciej Urbaniak,^d Feliks Stobiecki,^d Andreea Tomita,^e Rico Huhnstock,^e Iris Koch,^e Arno Ehresmann,^e Dennis Holzinger^e and Thomas M. Fischer^{ib}*^a

The topologically protected transport of colloidal particles on top of periodic magnetic patterns is studied experimentally, theoretically, and with computer simulations. To uncover the interplay between topology and symmetry we use patterns of all possible two dimensional magnetic point group symmetries with equal lengths lattice vectors. Transport of colloids is achieved by modulating the potential with external, homogeneous but time dependent magnetic fields. The modulation loops can be classified into topologically distinct classes. All loops falling into the same class cause motion in the same direction, making the transport robust against internal and external perturbations. We show that the lattice symmetry has a profound influence on the transport modes, the accessibility of transport networks, and the individual transport directions of paramagnetic and diamagnetic colloidal particles. We show how the transport of colloidal particles above a two fold symmetric stripe pattern changes from universal adiabatic transport at large elevations *via* a topologically protected ratchet motion at intermediate elevations toward a non-transport regime at low elevations. Transport above four-fold symmetric patterns is closely related to the two-fold symmetric case. The three-fold symmetric case however consists of a whole family of patterns that continuously vary with a phase variable. We show how this family can be divided into two topologically distinct classes supporting different transport modes and being protected by proper and improper six fold symmetries. We discuss and experimentally demonstrate the topological transition between both classes. All three-fold symmetric patterns support independent transport directions of paramagnetic and diamagnetic particles. The similarities and the differences in the lattice symmetry protected transport of classical over-damped colloidal particles *versus* the topologically protected transport in quantum mechanical systems are emphasized.

 Received 17th May 2017,
Accepted 5th July 2017

DOI: 10.1039/c7sm00983f

rsc.li/soft-matter-journal

1 Introduction

The theoretical description of topological insulators highlighted the connection between symmetry and topology in quantum phases of matter.^{1,2} Symmetries and the topology of quantum matter are deeply intertwined. The exploration of the

role of symmetry in topological phases has led to a topological classification of phases of matter.³ The complex quantum wave function of an excitation in a lattice can be considered as a two dimensional vector with real and imaginary part components that lives in the first Brillouin zone of the reciprocal lattice. When one identifies the borders of the first Brillouin zone it is topologically a torus. Attaching the quantum wave function vector to this torus mathematically defines a vector bundle that can be characterized by Chern classes. These classes must be compatible with the symmetries of the Hamiltonian. Chern classes are symmetry protected against perturbations compatible with the symmetry. Amongst the most prominent symmetries protecting topological insulators are the time reversal symmetry, the particle hole symmetry, but also the point symmetry of the lattice.^{4–6} Different constraints of the lattice symmetries cause physical distinct effects on lattices of different symmetry.^{7,8} In topological nontrivial systems Dirac cones play a crucial role. The number of these Dirac cones in a

^a Experimental Physics, Universität Bayreuth, 95440 Bayreuth, Germany.
E-mail: Thomas.Fischer@uni-bayreuth.de

^b Theoretical Physics, Universität Bayreuth, 95440 Bayreuth, Germany

^c Mathematics, Institute of Physics and Mathematics, Universität Bayreuth,
95440 Bayreuth, Germany

^d Institute of Molecular Physics, Polish Academy of Sciences,
ul. M. Smoluchowskiego 17, 60-179 Poznań, Poland

^e Institute of Physics and Center for Interdisciplinary Nanostructure Science and
Technology (CINSaT), University of Kassel, Heinrich-Plett-Strasse 40,
D-34132 Kassel, Germany

† Electronic supplementary information (ESI) available. See DOI: 10.1039/c7sm00983f

hexagonal and a square lattice differ and their robustness against perturbations is different if they are located at a high symmetry point, a high symmetry line or a generic location of the Brillouin zone.⁹

The variety of phenomena enriches when considering time dependent periodically driven systems. In such systems the frequency or energy of an excitation is conserved only modulo the frequency of the driving field and the first frequency zone can be folded into a circle in the same spirit as folding the first Brillouin zone into a torus.^{10,11} Floquet topological insulators are one example of topologically non trivial systems arising from periodic driving.

The discreteness of spectra of quantum phenomena is one ingredient shared also with spectra of bound classical waves and with the nature of topological invariants. The quantum Hall effect is one important example, where transport coefficients increase in discrete steps that contain only fundamental constants of nature including Planck's constant. The discreteness of the steps are caused by topology.¹²

The topological classification of phases is not restricted to quantum systems. There are other non-quantum vector waves in lattices^{13–18} that can be characterized in just the same way. Hence the topological discreteness also appears in many classical wave like systems. The topological characterization is not restricted to classical vector bundles. It has been applied to non-equilibrium stochastic systems that describe biochemical reactions.¹⁹ We applied the concept of topological protection to the dissipative transport of magnetic colloidal particles on top of a modulated periodic magnetic potential.^{20,21} There the transport of the point particle is fully characterized by the topology of the mathematical manifold on which it moves. The manifold does not carry any vector property. It can be characterized by its genus, a topological invariant somewhat more descriptive than the Chern class. We have shown that the driven transport of paramagnetic or diamagnetic colloidal particles above a two dimensional lattice is topologically protected by topological invariants of the modulation loops used to drive the transport.^{20,21} Non-topological transport of particles in a dissipative environment is usually vulnerable because of a spreading of the driven motion with the distribution of properties of the classical particles^{22–28} as well as due to the abundance of possible hydrodynamic instabilities^{29,30} that limit the control over their motion. Topologically protected particle transport in contrast is robust against sufficiently small continuous modifications of the external modulation. Only when the modulation loops are changed drastically they will fall into another topological class, and the direction of the transport changes in a discrete step.

In this work we investigate how the topological classes of modulation loops are affected by the lattice symmetry. We use experiments, theory and simulations to study transport above lattices of all possible two dimensional magnetic point symmetry groups and examine the impact of the symmetry on the number of transport modes, the number of topological invariants and on the type (adiabatic or ratchet) of transport. We show that lattice symmetry, as in topological crystalline insulators,^{4–9} has a profound influence on the topologically protected transport modes.

Applying periodic boundary conditions the unit cell of each lattice is a torus, which defines the action space. That is, the space in which the colloids move. The colloids are driven with periodic modulation loops of an external magnetic field, the direction of which defines the control parameter space. As a result of the interplay between the external magnetic field and the static magnetic field of the pattern, action space is divided into accessible and forbidden regions for the colloidal particles. For every point in an accessible region there exist a direction of the external magnetic field such that the magnetic potential has a minimum at that point. The borders between different regions in action space are characterized by special objects in control space. Modulation loops of the external field that wind around these special objects in control space cause colloidal transport along lattice vectors in action space.

In ref. 20 and 21 we studied the motion of colloids above hexagonal and square patterns, respectively. Here, we extend our previous studies in several ways. We corroborate the theory developed in ref. 20 and 21 with experiments on four-fold symmetric patterns and prove experimentally the existence of ratchet modes in the six-fold symmetric patterns. We also develop a theory for two- and three-fold patterns and prove their validity with experiments. Moreover, we find theoretically two new topological transitions, one in the non-universal stripe pattern, and one in the family of three-fold patterns. All theoretical predictions are tested experimentally.

2 Colloidal transport system

In this section we introduce a soft matter system for Floquet crystalline symmetry protected driven transport of colloidal particles on top of two dimensional magnetic lattices of different symmetry.

2.1 Magnetic colloids on magnetic lattices

Our system consists of a two dimensional periodic magnetic film having domains magnetized in the z -direction normal to the film (Fig. 1a). We consider a film that has as much area

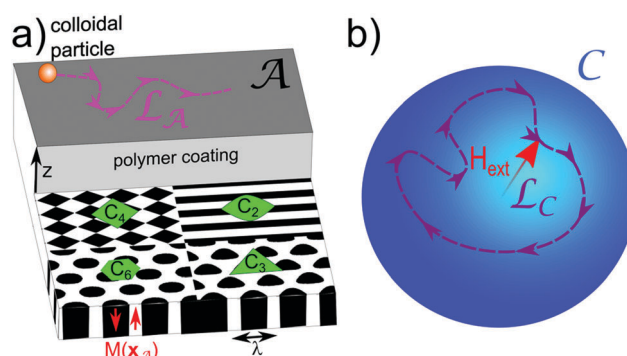


Fig. 1 (a) Magnetic pattern of symmetry C_2 , C_3 , C_4 , and C_6 with wavelength $\lambda = 2\pi/Q$ and magnetization $M(\mathbf{x}_A)$. The magnetic colloidal particles move in the two dimensional action space \mathcal{A} on top of the film at fixed elevation $z > \lambda$. (b) A modulation loop \mathcal{L}_C of the external magnetic field \mathbf{H}_{ext} in the control space \mathcal{C} causes a transport loop \mathcal{L}_A of the colloidal particle.

magnetized in the $+z$ as in the $-z$ direction. The magnetic field \mathbf{H}^p of the pattern can be derived from a scalar magnetic potential

$$\mathbf{H}^p = -\nabla\psi \quad (1)$$

that satisfies the Laplace equation and can be written as

$$\psi = \sum_{\mathbf{Q}} \psi_{\mathbf{Q}} e^{-Qz} e^{i\mathbf{Q}\cdot\mathbf{x}_A} \quad (2)$$

where the sum is taken over the reciprocal lattice vectors \mathbf{Q} ($Q = 2\pi/\lambda$ for the smallest non-zero reciprocal lattice vector) of the two dimensional lattice and \mathbf{x}_A is a two dimensional vector in the lattice plane. Lower Fourier modes dominate the sum (2) at higher elevation z .

Magnetic colloids can be confined in a liquid at a fixed elevation z that is larger than the wavelength of the pattern λ by coating the magnetic film with a polymer film of defined thickness or by immersing the colloids into a ferrofluid that causes magnetic levitation of the colloids.²⁰ We call the two-dimensional space in which the particles move the action space \mathcal{A} . We will use a number of geometric spaces and objects. Their definitions are listed in Appendix A.3. The positions of the particles are described by the vector \mathbf{x}_A .

Magnetic fields induce magnetic moments

$$\mathbf{m} = \chi_{\text{eff}} V \mathbf{H} \quad (3)$$

of the colloids of effective susceptibility χ_{eff} and volume V . We define the colloidal potential $U = H^2$. The colloids thus acquire a potential energy $E = -\chi_{\text{eff}} V U$. This depends on the square of the total magnetic field $\mathbf{H} = \mathbf{H}^p + \mathbf{H}_{\text{ext}}$ which is the superposition of a homogeneous time dependent external field to the heterogeneous pattern field. The potential energy E has a different sign for paramagnetic and diamagnetic colloids. Hence, paramagnetic particles move to positions that are maxima of U while diamagnetic colloids move to the minima.

We are particularly interested in the motion of paramagnetic and diamagnetic colloids at an elevation $z > \lambda$ above the magnetic film such that only the contributions of the lowest non zero reciprocal lattice vectors to eqn (2) are relevant. At this elevation the response of the colloidal particles moving in action space \mathcal{A} becomes universal, *i.e.* independent of the details of the pattern. The symmetry of the pattern becomes the only important property. If the lattice has a proper C_N rotation symmetry or an improper S_N symmetry there are N reciprocal lattice vectors of lowest absolute value contributing to the universal scalar magnetic potential ψ^* and we find

$$\psi^* = \tilde{\psi} e^{-Qz} \sum_{n=0}^{N-1} \det(\mathcal{R}_N^n) e^{i[\mathcal{R}_N^n \cdot \mathbf{Q}] \cdot \mathbf{x}_A} \quad (4)$$

where \mathbf{Q} is one of the lowest absolute value reciprocal unit vectors and \mathcal{R}_N denotes a proper rotation matrix by $2\pi/N$ ($\det(\mathcal{R}_N) = +1$) or an improper rotation consisting of a rotation by $2\pi/N$ and a reflection at the film plane ($\det(\mathcal{R}_N) = -1$). The universal scalar magnetic potential is determined only by the symmetry of the lattice and a prefactor carrying a phase ϕ

and an amplitude, $\tilde{\psi} = |\tilde{\psi}| \exp(i\phi)$. The amplitude is irrelevant and the phase ϕ is only important in the $N = 3$ case. The scalar magnetic potential will be the same for all lattices sharing the same point symmetry.

Magnetization patterns generating such universal magnetic potentials are shown in Fig. 2. The magnetization is given by

$$\mathbf{M}(\mathbf{x}_A) = M_s \mathbf{e}_z \text{sign} \left(t(\phi) + \sum_{n=0}^{N-1} \cos([\mathcal{R}_N^n \cdot \mathbf{Q}] \cdot \mathbf{x}_A - \phi) \right) \quad (5)$$

with $t(\phi) \approx \frac{1}{2} \cos(3\phi) \delta_{N,3}$ chosen such that the magnetic moment of a unit cell (UC) vanishes,

$$\int_{\text{UC}} \mathbf{M}(\mathbf{x}_A) d\mathbf{x}_A = 0. \quad (6)$$

The colloidal potential can now be reduced to the leading non-constant term, which is described by the universal colloidal potential:

$$U^* = e^{Qz} \mathbf{H}_{\text{ext}} \cdot \mathbf{H}^p(\mathbf{x}_A). \quad (7)$$

Note that the prefactor e^{Qz} rescales the potential such that it is independent of z , see eqn (4).

As we will see, adiabatic transport where the colloids adiabatically follow the maximum/minimum of the potential is possible along the crystallographic directions of the lattices when the potential is modulated with external fields. We call the space of the external field that may alter the colloidal potential the control space \mathcal{C} . Following eqn (7) we see that in the universal case changing the magnitude of \mathbf{H}_{ext} does not alter the position of the extrema of the colloidal potential. Control space \mathcal{C} , is thus a sphere of the external fields of constant magnitude. Each direction of the external field, which is a point in \mathcal{C} , produces a different colloidal potential (see Fig. 1b).

2.2 Lattice symmetries and topology

In Fig. 2 we depict the Wigner Seitz unit cells (with lattice vectors \mathbf{a}_1 and \mathbf{a}_2) of the periodic magnetic patterns defined by eqn (5) for $N = 2, 3, 4$ and $N = 6$ and show the points of these patterns having C_N (green) or S_2, S_4 or S_6 (red) symmetry. The patterns in Fig. 2 exhaust all possible single lattice constant ($a_1 = a_2$) magnetic point groups in 2D. White areas of the unit cell are magnetized in the positive z -direction and black areas in the negative z -direction. There are other patterns creating the same universal potential, the field of which differs from the field of the patterns of Fig. 2 if experienced at lower $Qz < 1$ (non-universal) elevation. Patterns having both C_N (green) and S_N (red) symmetries ($N = 2$ or $N = 4$) can be generated by using either proper or improper rotations. $N = 3$ can be generated only with proper rotations. The C_6 and S_6 symmetries arise if we chose $N = 3$ in eqn (5) and $\phi = 0$ ($\phi = \pi/6$). They can equally well be produced with $N = 6$ and using proper (improper) rotations.

Let us start with the topological characterization of action space. For a lattice with two-fold symmetry there is only one relevant reciprocal lattice vector and therefore the lattice is

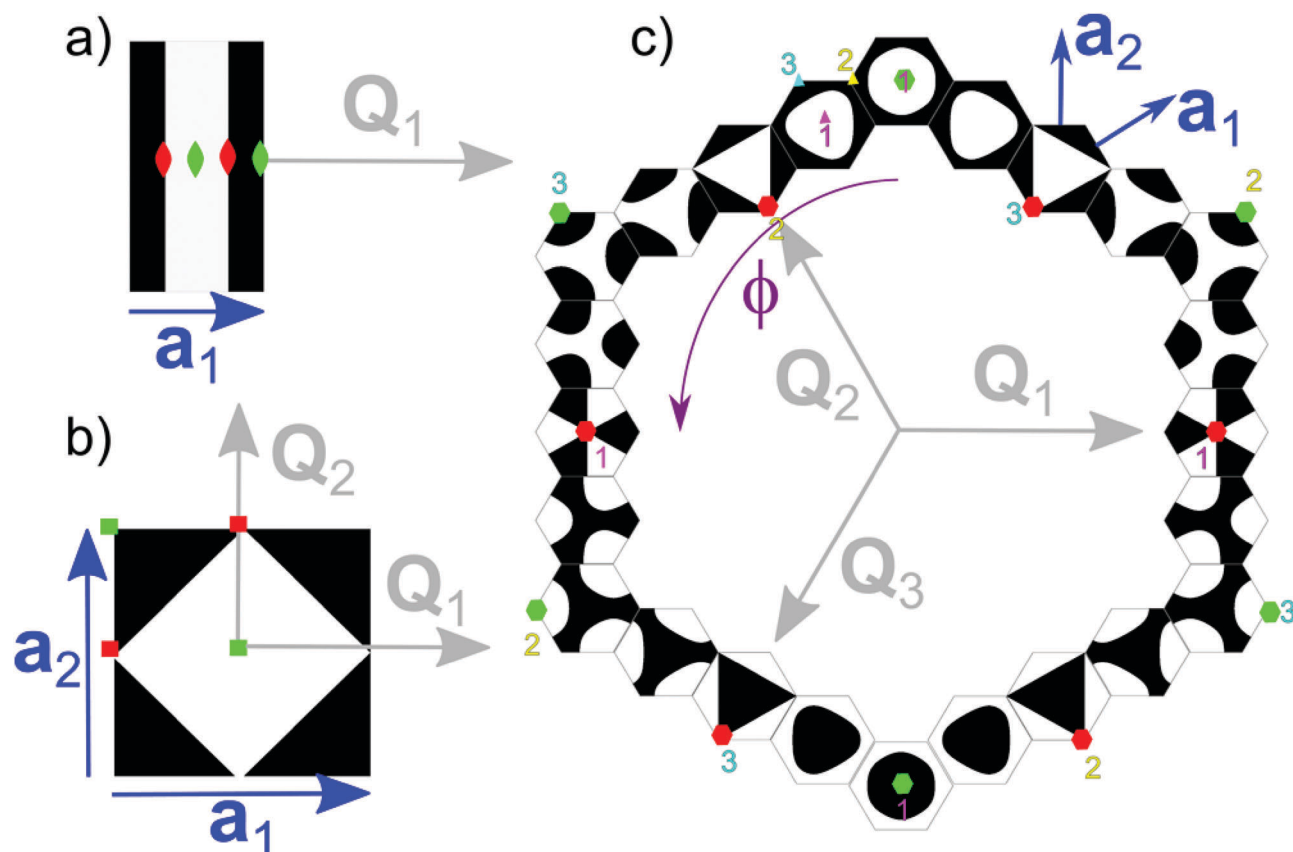


Fig. 2 Wigner Seitz cells, unit vectors (blue), and reciprocal lattice vectors (gray) of all possible two dimensional single lattice constant magnetic point groups generating lattices. Black and white indicate the discrete down and up magnetized pattern according to eqn (5) that creates a universal colloidal potential at an elevation $z > \lambda$ above the pattern. The \mathbf{Q}_1 vector is always pointing to the right in the x -direction. In (a) we show the unit cell of the two-fold and in (b) of the four-fold symmetric pattern, and in (c) 24 smaller three-fold symmetric unit cells. The magnetic pattern of these three-fold symmetric unit cells continuously varies with the phase ϕ of eqn (5). We show a sequence of such cells in steps of $\Delta\phi = \pi/12$ starting at $\phi = 0$ at the top. For each case there are 3 symmetry points with C_3 symmetry per unit cell. They are shown in 3 different colors (pink, yellow, cyan) in the unit cell next to $\phi = 0$. For special values of ϕ one of these three points acquires a proper or improper six-fold symmetry. N -Fold symmetric points of all unit cells are marked in green for proper rotation symmetries C_N and in red for improper rotation symmetries S_N .

quasi one dimensional (see Fig. 2a). Since the lattice is periodic, we can deform the Wigner Seitz cell to merge the opposite borders. For $N = 2$ the Wigner Seitz cell is a one dimensional segment, and hence action space \mathcal{A}_2 becomes topologically a circle. For all other symmetries, action space \mathcal{A}_N , with $N > 2$, is a torus.

Action space is topologically nontrivial for both $N = 2$ and $N > 2$ since both a circle and a torus have a hole. For $N = 2$ there is one winding number around the hole, while for a torus there are two winding numbers. The winding number of action space \mathcal{A} has a very simple meaning in the underlying lattice. A winding around the circle (torus) corresponds to a translation by one unit vector in the lattice.

As we already mentioned, control space \mathcal{C} is a sphere of radius H_{ext} . The two-fold symmetric colloidal potential is independent of the in-plane external field component perpendicular to \mathbf{Q}_1 . Therefore, in the two dimensional problem we only need a reduced control space \mathcal{C}_2^r , which is the intersection of \mathcal{C} with the plane spanned by \mathbf{Q}_1 and the vector normal to the film $\mathbf{n} = \mathbf{e}_z$. Like action space \mathcal{A}_2 the reduced control space \mathcal{C}_2^r is a circle.

The topology of the reduced control space \mathcal{C}_2^r is fundamentally different from the full control space \mathcal{C} . The latter is a genus zero spherical surface that has no holes. For this reason we can continuously deform any closed loop of the external field \mathcal{L}_C into any other loop \mathcal{L}_C' . This is not the case if we restrict the modulation loops to lie on the reduced control space \mathcal{C}_2^r , which is a circle with a hole. Modulation loops in \mathcal{C}_2^r can be characterized by their winding number around the hole $w(\mathcal{L}_C^r)$. The winding number is a topological invariant and we cannot continuously deform a modulation loop \mathcal{L}_C^r with one winding number w into another modulation loop \mathcal{L}_C^r with a different winding number $w' \neq w$.

2.3 Classification of modulation loops

The fundamental question that we address in this work is, what are the topological requirements for a modulation loop \mathcal{L}_C in control space to cause action loops \mathcal{L}_A with different, non vanishing winding numbers in action space and hence induce transport of the colloidal particles.

For $N = 2$ the answer is simple in reduced control space \mathcal{C}_2^r but less obvious in full control space \mathcal{C} . Reduced control and

action space are non trivial. One might guess that the non-trivial topological classification of modulation loops in reduced control space directly translates into the same topological classification of induced action-loops, *i.e.*

$$w(\mathcal{L}_A) = w(\mathcal{L}_C), \quad \text{for } N = 2. \quad (8)$$

We will show that this indeed is the correct answer to the question for the universal case. But there are other, non-universal answers to this question. At low elevation the transport in the two-fold symmetric potential differs from this simple answer.

Eqn (8) does not hold in full control space, *i.e.* there are loops with $w(\mathcal{L}_A) \neq w(\mathcal{L}_C)$ for any N . Otherwise there would not be transport since $w(\mathcal{L}_C) = 0$ for any loop. Full control space \mathcal{C} becomes nontrivial if we puncture it at specific points or introduce even more complicated objects on it. The result is a constrained control space $\tilde{\mathcal{C}}$, for which the simple answer

$$w(\mathcal{L}_A) = w(\mathcal{L}_{\tilde{\mathcal{C}}}) \quad (9)$$

with $w(\mathcal{L}_{\tilde{\mathcal{C}}})$ the winding numbers around the objects of $\tilde{\mathcal{C}}$ holds. The task is to find the objects that we need to project onto full control space and figure out how winding around those objects allows for a classification of the modulation loops into classes that induce topologically different transport of colloids in action space.

2.4 Computer simulations

We use Brownian dynamics to simulate the motion of a single point paramagnetic colloid above the different patterns. The motion of the particle is described by the stochastic differential Langevin equation

$$\gamma \frac{d\mathbf{x}_A(t)}{dt} = -\nabla_A E(\mathbf{x}_A, \mathbf{H}_{\text{ext}}(t)) + \mathbf{f}(t),$$

with t the time, γ the friction coefficient, and \mathbf{f} a Gaussian random force. The variance of the random force is determined by the fluctuation-dissipation theorem. As usual, we integrate the equation of motion in time using a standard Euler algorithm. We always equilibrate the system before the modulation loop in control space starts, such that the colloidal particles always start in the minimum of the potential energy E at $t = 0$.

The phase diagrams of the transport modes that we present in the next sections were initially obtained with computer simulations and can now also be predicted theoretically.

2.5 Outline

The rest of the paper is organized as follows. In Section 3 we treat the case $N = 2$. The simplicity of \mathcal{C}_2^r allows us to visualize many concepts that cannot be visualized for $N > 2$ such as the full dynamics in phase space. We also study the non-universal transport for $N = 2$, and the connection to previous works.^{32–35} We outline the concept of topologically protected ratchets with this very simple example. We then extend the treatment of $N = 2$ to the full control space, introducing the concept of the constrained control space $\tilde{\mathcal{C}}$. The case $N = 4$ is related to the case $N = 2$ and is treated in Section 4. In Section 5 we analyze the case $N = 3$

that consists of a whole family of patterns continuously varying with the phase ϕ of the pattern. This includes the two special cases, C_6 symmetry ($\phi = 0$) and S_6 symmetry ($\phi = \pi/6$). We find a new topological transition between C_6 - and S_6 -like three-fold symmetric lattices. Section 6 contains a discussion of the experiments, a comparison to the theoretical and numerical predictions, and a discussion of the results in comparison to quantum systems. Finally Section 7 summarizes the main conclusions concerning transport.

3 Two-fold symmetry

In this section we study the transport on top of a two-fold symmetric pattern. We start with the universal case and subsequently reduce the elevation of the colloids towards non universal cases. This allows us to first study the transition from topologically protected adiabatic motion towards ratchet motion, and then to a non transporting regime.

3.1 Theory

A stripe pattern is a magnetic pattern with two-fold symmetry (see Fig. 2a). The magnetic field of a thick ($tQ > 1$, t being the thickness of the magnetic film) pattern of stripes of opposite magnetization $\pm M$ alternating along the x direction reads:

$$\begin{aligned} H_x^p + iH_z^p &= \frac{2M}{\pi} \ln[\tan(Q(x + iz))] \\ &= \sum_{n=0}^{\infty} \frac{8M}{(2n+1)^2} e^{i(2n+1)Q(x+iz)}, \end{aligned} \quad (10)$$

where H_x^p are the (real) components of the pattern magnetic field, and in the last part of eqn (10) we have decomposed the field into its Fourier-components. The non-universal colloidal potential valid at any height z reads:

$$U = (H_x^p + H_{\text{ext}} \cos \varphi_{\text{ext}})^2 + (H_z^p + H_{\text{ext}} \sin \varphi_{\text{ext}})^2, \quad (11)$$

where

$$\mathbf{H}_{\text{ext}} = H_{\text{ext}} \begin{pmatrix} \sin \varphi_{\text{ext}} \\ \cos \varphi_{\text{ext}} \end{pmatrix}, \quad \varphi_{\text{ext}} \in [0, 2\pi] \quad (12)$$

denotes the external magnetic field lying in the reduced control space \mathcal{C}_2^r . In the limit $Qz > 1$ the pattern field is well described by

$$\mathbf{H}^p(Qz > 1) = 8Me^{-Qz} \begin{pmatrix} \sin Qx \\ \cos Qx \end{pmatrix}, \quad Qx \in [0, 2\pi] \quad (13)$$

and the universal potential reads, *cf.* (7)

$$U^* = 8MH_{\text{ext}} \cos(Qx - \varphi_{\text{ext}}). \quad (14)$$

The over-damped Brownian motion of a colloidal particle in the x -direction is given by

$$\gamma \dot{x} = \zeta_{\text{eff}} V \frac{\partial U(x, \varphi_{\text{ext}})}{\partial x} + f_{\text{Brown}} \quad (15)$$

where f_{Brown} is a zero average random force fulfilling the fluctuation dissipation theorem, $\gamma \propto \eta$ the friction coefficient

of the colloid in the liquid of viscosity η , and the effective magnetic susceptibility χ_{eff} has a different sign for the paramagnets and diamagnets. Since our colloidal potential is sufficiently strong we can neglect the random force.

There are two kinds of colloidal dynamics that occur on separate time scales, when we adiabatically modulate the direction of the external field, which is described by $\varphi_{\text{ext}}(t)$. One is the intrinsic dynamics of the colloids on an intrinsic short time scale t_{int}

$$\gamma \dot{x}(t_{\text{int}}) = \chi_{\text{eff}} V \frac{\partial U(x(t_{\text{int}}), \varphi_{\text{ext}}(t_{\text{fixed}}))}{\partial x} \quad (16)$$

with which the colloids follow the path of steepest descent along the slope of the colloidal potential along the x -direction towards an extremum in U . The typical angular speed of this intrinsic motion is of the order $\omega_{\text{int}} = Q\dot{x} \propto e^{-Qz} \chi_{\text{eff}} \mu_0 M H_{\text{ext}} (QV^{1/3})^2 / \eta$; (the intrinsic angular frequency renormalizes by an additional factor $tQ < 1$ for

thin magnetic films). Since the external modulation frequency $\omega_{\text{ext}} \ll \omega_{\text{int}}$ is significantly slower this happens at fixed external field ($\varphi_{\text{ext}}(t) = \varphi_{\text{ext}}(t_{\text{fixed}})$). The other timescale is an adiabatic creeping of the colloid with the maximum/minimum of the colloidal potential,

$$0 = \pm \frac{\partial U(x(t_{\text{ext}}), \varphi_{\text{ext}}(t_{\text{ext}}))}{\partial x}, \quad (17)$$

with a small velocity dictated by the much slower time scale t_{ext} of the external field modulation. Making use of the periodicity of the pattern we wrap the Qx -coordinate into a circle of circumference 2π such that action space \mathcal{A} is a circle. Reduced control space \mathcal{C}_2^r is also a circle with radius H_{ext} and coordinate φ_{ext} . The full dynamics occurs in phase space $\mathcal{C}_2^r \otimes \mathcal{A}$, which is the product space of the reduced control and action space and thus a torus.

In Fig. 3a we depict the reduced phase space $\mathcal{C}_2^r \otimes \mathcal{A}$, together with the directions Qx of action space and φ_{ext} of the reduced

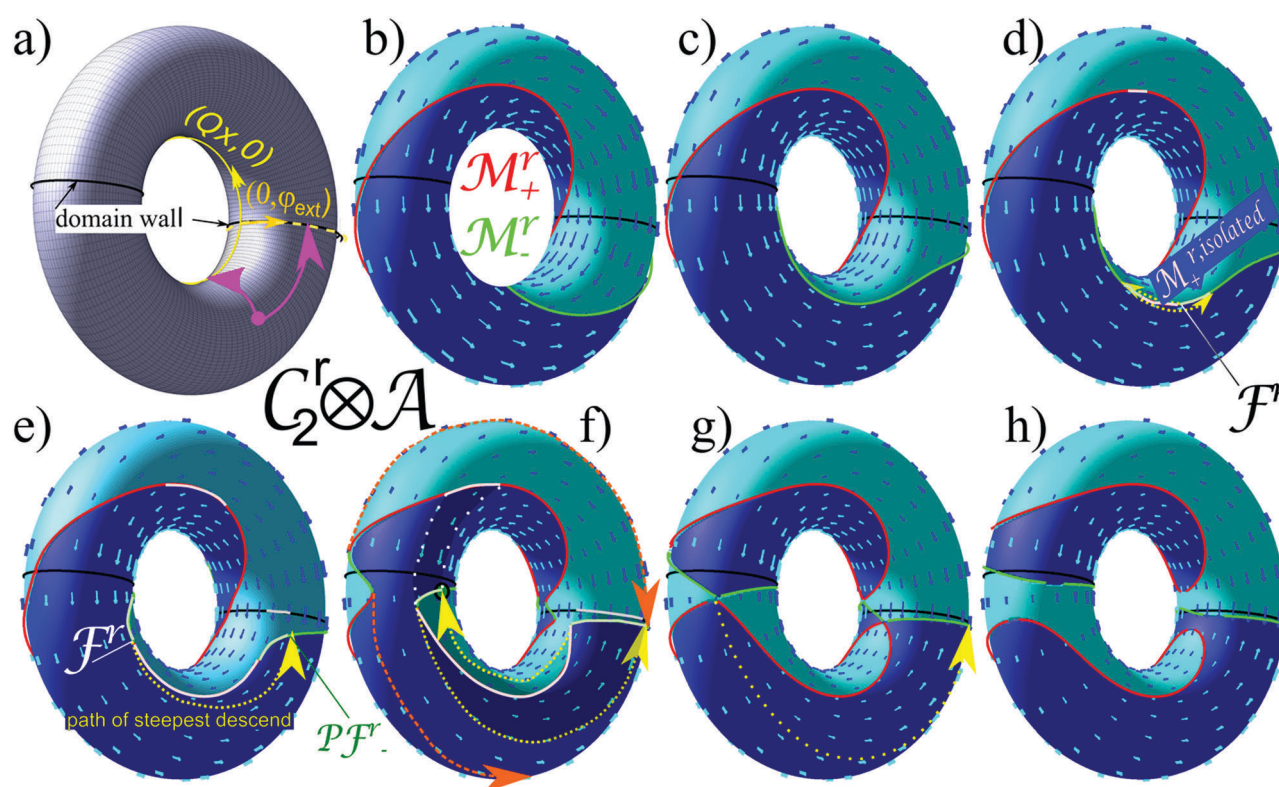


Fig. 3 Reduced phase space of the two-fold symmetric system: (a) the black lines depict the locations of the domain walls separating regions of opposite magnetization in phase space, which are two copies of control space at $x = 0, \pi$. We may use the first one as reduced control space \mathcal{C}^r (orange). Equally a level curve at fixed angle φ (yellow) is a copy of action space. A point in phase space may be projected onto either control or action space, see an example in panel (a) pink arrows. (b) Reduced phase space and intrinsic dynamics of paramagnetic colloids for the universal potential in the limit $Qz > 1$. The stationary manifolds \mathcal{M}_-^r and \mathcal{M}_+^r are depicted in green and red. The intrinsic dynamics is shown as a vector field of generalized velocities with cyan arrows (pointing in positive x -direction) and blue arrows (pointing in negative $-x$ -direction). Adiabatic motion of colloidal particles occurs on the stable stationary manifold via the external modulation. (c) At a lower non universal elevation $Qz = 0.4$. The topology is still the same as in the universal case. As in all the following cases we choose $H_{\text{ext}} = M$. (d) Development of fences in \mathcal{M}_-^r at $Qz = 0.34$ and the transition towards topological protected ratchet jumps (yellow) from the fence (border between pink and green color on \mathcal{M}^r) toward the pseudo fence (border between green and light green color on \mathcal{M}^r) for paramagnetic particles (see Appendix A.3 for a concise definition of fence and pseudo fence). Both fence and pseudo fences on \mathcal{M} are projected into the same fence points in control space (border between gray and black on the domain wall). Preimages of the gray ($m = 4$) excess line of control space are the two pink and two bright green lines. Preimages of the black ($m = 2$) part of control space are the full red and full green colored lines. (e) Dynamics at an elevation $Qz = 0.2$. (f) At $Qz = 0.1$ fences also start to develop in \mathcal{M}_+^r causing ratchet jumps for the diamagnets (not shown) and additional feeder ratchet jumps (orange) starting from $\mathcal{M}_-^r, \text{isolated}$ for the paramagnets. (g) Dynamics at the transition elevation $Qz = 0.09$ toward a non transporting regime. (h) Phase space and dynamics at low $Qz = 0.07$ elevation. There are now four disconnected stationary manifolds (two of each kind) which all have zero winding number in action space.

control space. As indicated by the pink arrows in Fig. 3a each point $(x, \varphi_{\text{ext}})$ can be projected into the copy $x = 0$ of reduced control space $(0, \varphi_{\text{ext}}) = P_{C_2^r}(Qx, \varphi_{\text{ext}})$ as well as into the copy $\varphi_{\text{ext}} = 0$ of action space $(Qx, 0) = P_A(Qx, \varphi_{\text{ext}})$.

Fig. 3b–h are plots of the phase space $C_2^r \otimes \mathcal{A}$ at different elevations Qz above the pattern and for an external field-strength of $H_{\text{ext}} = M$. As we will see in the non-universal case the magnitude of H_{ext} matters. The intrinsic dynamics, see eqn (16), is shown as a vector field on the torus. According to eqn (16) the trajectories move along lines of constant external field direction $\varphi_{\text{ext}}(t_{\text{fixed}}) = \text{const}$, either in Qx or $-Qx$ direction. Regions of phase space with one sense of motion are colored in blue, regions of phase space with opposite sense in cyan. Both regions are separated from each other by the reduced stationary manifold \mathcal{M}^r , a line consisting of all points for which the potential is stationary $\partial_x U = 0$. A stationary point is either a minimum $(Qx, \varphi_{\text{ext}}) \in \mathcal{M}_+^r$ (red) or a maximum $(Qx, \varphi_{\text{ext}}) \in \mathcal{M}_-^r$ (green). The intrinsic dynamics of the paramagnetic colloids starts at the red minimum line \mathcal{M}_+^r and ends at the green maximum line \mathcal{M}_-^r .

The reduced stationary manifold \mathcal{M}^r of the universal potential (Fig. 3b) consists of two lines: the line $\varphi_{\text{ext}} = Qx$ (red) is the set of minima \mathcal{M}_+^r and the line $\varphi_{\text{ext}} = Qx + \pi$ (green) is the set of maxima \mathcal{M}_-^r . Following eqn (17) the adiabatic creeping of the particles has to happen along the stationary manifolds. Paramagnetic colloids will adiabatically follow the green \mathcal{M}_-^r line while diamagnetic ones will follow \mathcal{M}_+^r (red). The simplicity of the universal stationary manifold (Fig. 3b) thereby converts any motion in control space into similar motion in action space. If we loop around the control circle we also loop around the action circle and thus induce transport by one unit vector. Both, paramagnetic and diamagnetic particles move at a fixed distance $\lambda/2$. A general modulation loop \mathcal{L}_C^r in reduced control space causes an action loop \mathcal{L}_A in action space with similar winding number $w_A = w_C^r$. The particles can stay on the corresponding manifold during the entire modulation. Therefore the dynamics is completely adiabatic and thus dominated by the external modulation.

When we lower the colloidal plane to $Qz = 0.4$ the manifold \mathcal{M}^r deforms (Fig. 3c). Eventually at $Qz = 0.34$, \mathcal{M}_-^r becomes parallel to the tangent vector of action space \mathbf{e}_x in one critical point of \mathcal{M}_-^r . At this critical point $\partial_x U = \partial_x^2 U = \partial_x^3 U = 0$ and therefore the point is no longer a maximum. As one further lowers Qz an isolated section $\mathcal{M}_+^{r,\text{isolated}}$ (pink) interrupts \mathcal{M}_-^r .

Two fence points $\mathcal{F}^r = \{(x, \varphi_{\text{ext}}) | \partial_x U = \partial_x^2 U = 0\}$ as common borders between $\mathcal{M}_+^{r,\text{isolated}}$ (pink) and \mathcal{M}_-^r (bright green) develop from the formerly closed \mathcal{M}_-^r loop (Fig. 3d). When a paramagnetic colloid adiabatically creeps along \mathcal{M}_-^r via the externally induced dynamics and reaches the fence \mathcal{F}^r it must leave the stationary manifold, follows the intrinsic dynamics and jumps (yellow arrow) toward a new maximum that we call the pseudo fence $\mathcal{P}\mathcal{F}_-^r$ (border between the bright and full green in Fig. 3e). A pseudo fence is a point on \mathcal{M} different from the fence that has the same projection onto reduced control space (border between the black and gray line) as the fence but different projections onto action space.

The intrinsic dynamics is irreversible, *i.e.* one can move along the path of steepest descent only in one direction. When we are at the critical elevation the $\mathcal{M}_+^{r,\text{isolated}}$ interruption has zero length, fence and pseudo fence fall on top of each other. Like this the path of steepest descent has zero length. When we decrease the elevation Qz the path of steepest descent continuously grows. Although it is no longer on \mathcal{M}^r it falls into the same homotopy class as the section of \mathcal{M}^r that it bypasses. That is, both are topologically equivalent and transport by one unit vector can still be achieved by winding around the control space. The dynamics of the colloids, however, undergoes a phase transition from adiabatic toward a ratchet motion.^{36–42} The ratchet jumps occur along the path of steepest descent with jump times short compared to the external modulation dynamics. The result of a ratchet transport is the same as the adiabatic motion at higher elevations because of the homotopy between the avoided section of \mathcal{M}^r and the path of steepest descent. Like this the transport is topologically protected at the adiabatic to ratchet transition.

If we further decrease the elevation to $Qz = 0.1$ the same thing happens to the other sub-manifold \mathcal{M}_+^r . It is now interrupted by a $\mathcal{M}_-^{r,\text{isolated}}$ section resulting in irreversible jumps for the diamagnetic colloids (Fig. 3f). This section also opens up a new possible ratchet jump of paramagnetic particles initially located on $\mathcal{M}_-^{r,\text{isolated}}$ onto the disconnected other parts of \mathcal{M}_-^r . The special thing about these feeder jumps is, that once a colloidal particle leaves the isolated section it will never return due to the absence of pseudo fences in $\mathcal{M}_-^{r,\text{isolated}}$.

The projection of a point in $C^r \otimes \mathcal{A}$ onto a point in C^r defines a mapping from \mathcal{M}^r onto C^r . The inverse of this map is not a map because the projection maps several points of \mathcal{M}^r onto the same point in C^r . We call the number of preimages of the projection on \mathcal{M}^r the multiplicity. Note that, the two (bright green) sections between pseudo fence and fence, the (pink) $\mathcal{M}_+^{r,\text{isolated}}$ insertion as well as a non isolated section (pink) of \mathcal{M}_+^r are projected onto the same (gray) excess segment of control space. Consequently the (gray) excess segment has multiplicity $m = 4$ (it has four preimages on the manifold \mathcal{M}^r). The rest of \mathcal{M}^r is projected twice on the remaining (black, multiplicity $m = 2$) section of C_2^r . Like this there are sections of control space with different multiplicity. When we move from the $m = 2$ -region of control space to the $m = 4$ region a maximum minimum pair is created in \mathcal{M}^r .

The topology of \mathcal{M}^r does not change at the adiabatic to ratchet transition. It is only the distribution of points on \mathcal{M}^r into the subsets \mathcal{M}_-^r and \mathcal{M}_+^r that changes. A transition of the topology of \mathcal{M}^r occurs at $Qz = 0.09$ when the formerly disconnected parts of \mathcal{M}^r touch each other in four fence points (Fig. 3g) and then separate into four disconnected parts (Fig. 3h). Two of the new disconnected parts after the disjoining are entirely of type \mathcal{M}_-^r and two are of type \mathcal{M}_+^r . The \mathcal{M}_-^r parts are localized near the domain walls, while the \mathcal{M}_+^r parts lie on top of a domain. All four parts of \mathcal{M}^r have non vanishing winding number around the reduced control space but vanishing winding numbers around action space. Any control loop will thus only

create periodic motion in action space that is associated with no net transport over a period.

We have given a description of the dynamics of paramagnets. The dynamics of diamagnets is the reversed intrinsic dynamics coupled with the external dynamics on \mathcal{M}_+^r . For the universal case at high elevations both types of particles move exactly the same way however they are separated by half the wavelength $\Delta Qx = \pi$ of the pattern. At lower elevation the transitions to a ratchet motion occurs for different elevations $Qz = 0.34$ (Fig. 3d) for the paramagnets and $Qz = 0.1$ (Fig. 3f) for the diamagnets. The transition from transport to no transport happens for both particles simultaneously at an elevation of $Qz = 0.09$ (Fig. 3g). Paramagnets are then confined to the domain walls and diamagnets to the domains.

3.2 Experiments

We have performed experiments with paramagnetic colloids above the stripe pattern of wavelength $\lambda = 7.2 \mu\text{m}$, and magnetization $M \approx 20 \text{ kA m}^{-1}$ of a magnetic garnet film.^{43,44} We covered the garnet film with a ferrofluid of defined thickness d . Magnetic levitation lifts the colloids to the mid plane of the film at a fixed elevation z . Since we were limited in the variation of the thickness d we used the amplitude H_{ext} of the external field as a second control parameter. Both, decreasing the field or decreasing the elevation renders the transport behavior non-universal. The modulation of the external magnetic field that drove the dynamics was generated by three coils arranged along the x , y , and z axes.³¹ We applied a palindrome modulation loop $\mathcal{L}_{\text{cr}} = \tilde{\mathcal{L}}_{\text{cr}} \tilde{\mathcal{L}}_{\text{cr}}^{-1}$, i.e. a combination of a forward loop $\tilde{\mathcal{L}}_{\text{cr}}$ of winding number $w(\tilde{\mathcal{L}}_{\text{cr}}) = 1$ followed by the time reversed backward loop $\tilde{\mathcal{L}}_{\text{cr}}^{-1}$ with winding number $w(\tilde{\mathcal{L}}_{\text{cr}}^{-1}) = -1$, each subloop has a duration of $\Delta t = 5 \text{ s}$.

We measured the corresponding trajectories in reduced phase space $\mathcal{C}_2^r \otimes \mathcal{A}$ at different heights. By video tracking we obtained the coordinate $x_{\mathcal{A}}(t)$ of the trajectory in action space. Simultaneously we determine $\varphi_{\text{ext}}(t)$ by measuring the width of an up magnetized stripe that periodically varies with the external field and is visualized in the same video (see ref. 45) *via* the polar Faraday effect.

At the universal elevation (Fig. 4a) the colloids creep adiabatically along the stationary manifold \mathcal{M}_-^r . Forward (green) and backward (olive) trajectories fall almost on top of each other. If we lower the elevation we can observe ratchet motion (Fig. 4b). There we can identify the sections of the trajectories that lie on \mathcal{M}_-^r as those where the speed of the colloids on the trajectories is slow (adiabatic) (see green data in Fig. 4b). The paths of steepest descent are the regions where the velocity is high (intrinsic dynamics). In the forward loop the adiabatic motion passes the pseudo fence and the particle jumps when it reaches the fence. The path of steepest descent reunites with the backward trajectory at the pseudo fence. The two sections on \mathcal{M}_-^r between fence and pseudo fence together with the paths of steepest descent connecting fence and pseudo fence define the hysteresis between forward and backward ratchet loops. A fully adiabatic motion has negligible hysteresis.

At even lower elevations, below the topological transition height, we no longer observe transport. The paramagnetic particles are attached to the domain walls (Fig. 4c).

In a ratchet motion the path of steepest descent, and therefore the hysteresis, develops continuously from the critical point. The winding number $w(\tilde{\mathcal{L}}_{\mathcal{A}}) = -w(\tilde{\mathcal{L}}_{\mathcal{A}}^{-1})$ of the forward loop does not change across this continuous transition. In contrast, the topological transition towards the non transporting regime is discontinuous.

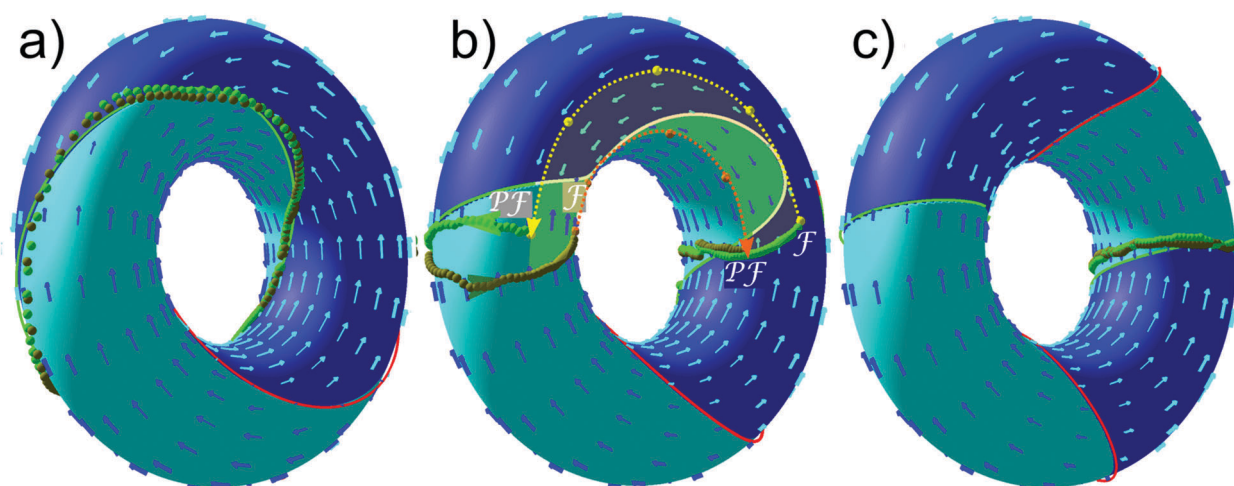


Fig. 4 Reduced phase space (torus), intrinsic dynamics (vector field), stationary manifolds (green and red solid lines), and experimental trajectories (green, olive, yellow and orange) for three different non-universal elevations. (a) Adiabatic motion in a nearly universal potential $Qz = 4.34$, $H_{\text{ext}} = 0.2M$. (b) Ratchet motion at an elevation $Qz = 0.43$, $H_{\text{ext}} = 0.2M$. (c) No motion at a elevation $Qz = 0.43$, $H_{\text{ext}} = 0.1M$ below the topological transition. Experimentally measured data for a forward (backward) modulation loop with $w_{\text{c}} = 1(-1)$ is shown as green (olive) spheres for adiabatic, i.e. slow, motion and in yellow (orange) for the fast ratchet jumps. The ratchet motion in (b) exhibits hysteresis between forward and backward motion (yellow shaded area). The experimental data does not perfectly match the theory (solid green line) since the changes of the stripe pattern of the garnet film with the external field (relevant at non-universal elevation) have not been included into the theory. Both experimental data and theory however fall into the same homotopy class. A video clip of the adiabatic motion of the paramagnetic colloidal particle in (a) is provided in ref. 45.

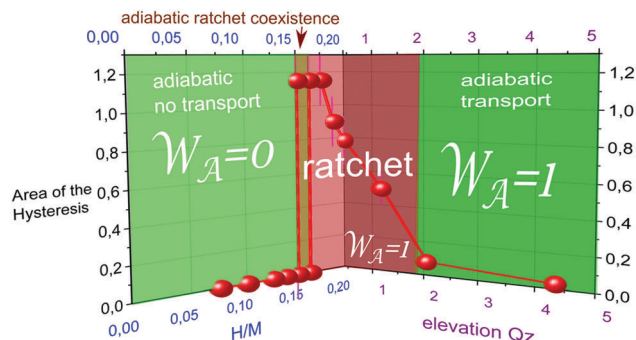


Fig. 5 Experimentally measured area of the hysteresis of the transport. The area of the hysteresis is measured on the surface of the torus $\mathcal{C}_2^r \otimes \mathcal{A}$. The total area of a torus is $(2\pi)^2 \approx 40$. On the right we lowered the elevation Qz . This reveals the continuous transition from adiabatic transport toward ratchet motion. On the left side we decrease the external field amplitude at constant elevation. This reveals the discontinuous topological transition towards no transport.

In Fig. 5 we plot the area of the hysteresis *versus* the non-universality parameters (external field H_{ext} and elevation Qz). Both the continuous adiabatic toward ratchet transition as well as the discontinuous ratchet to adiabatic non-transport transition can be clearly identified from the figure.

3.3 Constrained control space

In Section 4 we will discuss the universal potential of a four-fold symmetric pattern. It is useful to first reiterate the universal case of the two-fold symmetric problem, using full control space \mathcal{C} .

In the Section 3.2 we reduced the control space of the stripe system to fields that are lying in the plane spanned by the normal vector \mathbf{n} to the pattern and by the unique reciprocal unit vector \mathbf{Q} . We just dropped the physically possible external field component along the indifferent $\pm\mathbf{n} \times \mathbf{Q}$ direction. Here we do not ignore this component. Hence, since the magnitude of the external field H_{ext} does not play a role for the universal case, full control space is a sphere. The constrained control space $\tilde{\mathcal{C}}_2$ of the stripe pattern is a two punctured sphere. The two points along the $\pm\mathbf{n} \times \mathbf{Q}$ direction are removed from the sphere of the full control space \mathcal{C} since these points produce an indifferent constant potential in action space.

Topologically, the two punctured sphere $\tilde{\mathcal{C}}_2$ and the circle \mathcal{C}_2^r are equivalent. Since only the topology of control space is important we may expand \mathcal{C}_2^r to the constrained control space $\tilde{\mathcal{C}}_2$. Note that the winding number of a modulation loop in \mathcal{C}_2^r becomes the winding number of a modulation loop around the indifferent $\pm\mathbf{n} \times \mathbf{Q}$ axis through the two removed points of the punctured sphere in $\tilde{\mathcal{C}}_2$. The reduced control space is just the grand circle on the sphere around this axis. We can predict the result of modulation loops in the constrained control space $\tilde{\mathcal{C}}_2$: winding around the punctured points induces transport in action space.

To make the connection to the topologically trivial full control spaces of lattices with higher point symmetries, we can

reinsert the removed points into the punctured sphere $\tilde{\mathcal{C}}_2$. That is, we recover the topologically trivial full control space \mathcal{C} allowing fields pointing into the indifferent direction. This enables us to continuously deform a modulation loop with one winding number around the axis into a modulation loop with different winding number. The transition in winding number occurs when the modulation loop passes through the reinserted point.

Note that the indifferent direction satisfies

$$\nabla_{\mathcal{A}} U^* = 0, \quad (18)$$

and

$$\det(\nabla_{\mathcal{A}} \nabla_{\mathcal{A}} U^*) = 0, \quad (19)$$

for any point $\mathbf{x}_{\mathcal{A}} \in \mathcal{A}$. We call points in $\mathcal{C} \otimes \mathcal{A}$ that fulfill eqn (18) and (19) the fences \mathcal{F} on \mathcal{M} . For the stripe pattern and the universal case fence points only exist in $\mathcal{C} \otimes \mathcal{A}$, not in $\mathcal{C}_1^r \otimes \mathcal{A}$. In the stationary manifold of the reduced control space \mathcal{M}^r the sub-manifolds are two disconnected lines (maximum and minimum) without fences (Fig. 3b). On the full stationary manifold \mathcal{M} the fence consists of two copies (one for each of the opposite indifferent points in \mathcal{C}) of the one dimensional action space and thus consists of two disconnected circles.

The fences separate the maxima of the stationary manifold from the minima (Fig. 6). Hence using the constrained control space the stationary manifold \mathcal{M} is a two dimensional manifold that is not disconnected. \mathcal{M}_- and \mathcal{M}_+ are both copies of the punctured sphere, with the puncture point enlarged to a circular fence and there joined to one closed surface. Fig. 6 shows the topology of the universal stationary manifold \mathcal{M} for the full control space. \mathcal{M}_+ is depicted in red and \mathcal{M}_- in green.

The constrained control space $\tilde{\mathcal{C}}_2$ can be subdivided into two hemispheres, the northern hemisphere for which $H_{\text{ext},z} > 0$ and the southern hemisphere ($H_{\text{ext},z} < 0$). Both hemispheres are simply connected areas, *i.e.* areas where every loop is zero

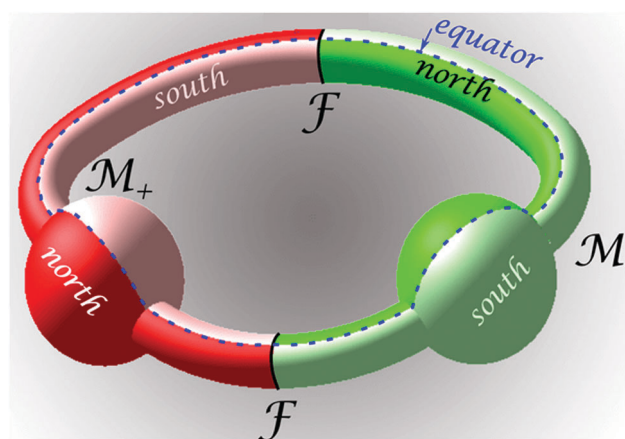


Fig. 6 The stationary manifold for the universal potential of the stripe pattern for the full control space \mathcal{C} . \mathcal{M}_+ is depicted in red and \mathcal{M}_- in green. Both are connected by two circular fences \mathcal{F} . Copies of the northern hemispheres of \mathcal{C} are shown in full colors, while the southern ones are shown in light colors. (See Appendix A.3 for a concise definition of the hemispheres and the equator.)

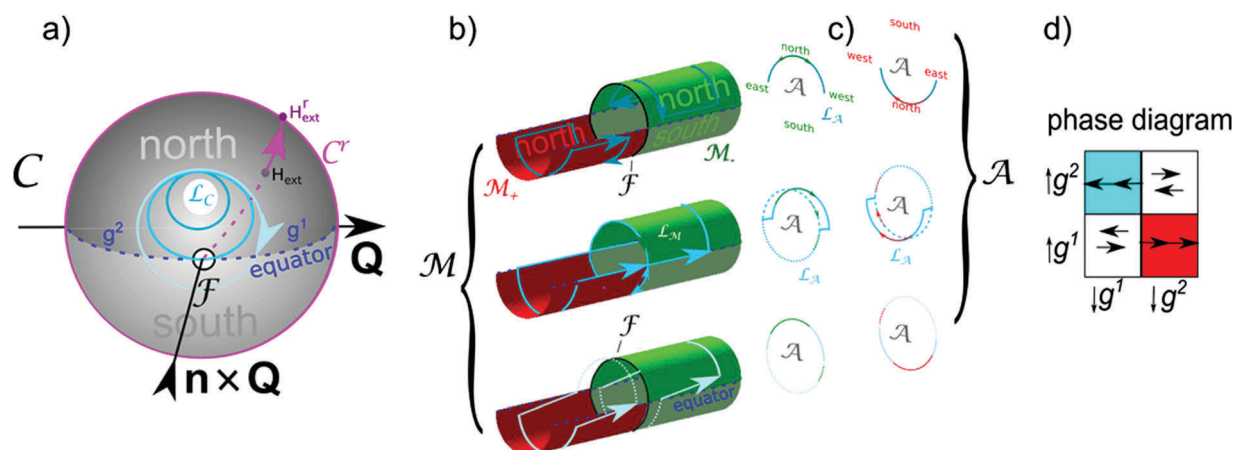


Fig. 7 (a) Full control space of the stripe pattern. (b) Section of the stationary manifold \mathcal{M} and (c) its projection into action space. Several modulation loops \mathcal{L}_C in \mathcal{C} and their preimages \mathcal{L}_M on \mathcal{M} and the further projections \mathcal{L}_A into \mathcal{A} are shown. In (a) the reduced control space is shown in pink together with a projection of a full external field \mathbf{H}_{ext} into the reduced external field $\mathbf{H}_{\text{ext}}^r$ is also shown. (d) Phase diagram of the transport modes for the fundamental loops $\mathcal{L}_C = \downarrow g^i \uparrow g^j$. Colored squares indicate transport, white squares indicate no transport.

homotopic. The areas are glued together at the two sections g^1 and g^2 of the equator between the puncture points. In Fig. 6 we show the simply connected areas of the stationary manifold that are projected into both hemispheres of $\tilde{\mathcal{C}}_2$.

Two lines circle the stationary manifold, see Fig. 6. We call these lines the equator since they are projected onto the equator of $\tilde{\mathcal{C}}_2$, see Fig. 7a. When the equator hits the puncture point in $\tilde{\mathcal{C}}_2$ the two equators of the stationary manifold cross the fences in \mathcal{M} . Topologically \mathcal{M} is a genus one surface with two winding numbers. The winding numbers of the fences are different from the winding numbers of the equator.

Fig. 7 shows the topological transition of the transport modes on \mathcal{M} and \mathcal{A} due to the continuous deformation of a control loop in \mathcal{C} . We start with a control loop (dark blue loop) that is entirely in the north and hence does not wind around the indifferent point. The loop has two preimages on \mathcal{M} , one on \mathcal{M}_- and one on \mathcal{M}_+ . Both are zero homotopic. Now we further deform the modulation loop such that it crosses the fence point (blue loop). The preimage on \mathcal{M} is the union of the two formerly disconnected loops and the fence itself. Mathematically the preimage is not a loop but a lemniscate.⁴⁶ When we slightly enlarge the loop (cyan), such that it is now winding around the fence point in \mathcal{C} , the lemniscate on \mathcal{M} disjoins again into two loops on \mathcal{M}_- and \mathcal{M}_+ . Now, both loops have non vanishing winding numbers. The projection of the loop in \mathcal{M}_- (\mathcal{M}_+) corresponds to a maximum (minimum) of the potential in \mathcal{A} that adiabatically moves around with a winding number similar to the winding number around the indifferent axis in \mathcal{C} , $w_A = w_C$.

We now understand how to produce a topological transition of the transport modes by continuously deforming the loop in control space. The transport direction in action space is topologically protected for any deformation of the modulation loop that does not alter the winding number around the fence points. A topological transition occurs when we move the loop across one of the fence points.

We can characterize the simplest modulation loops by the two segments of the equator that they cross. We define $\downarrow g^i$, $i = 1, 2$ as a south traveling path that passes the equator segment g^i between the two fence points. We complete the loop with an analogous north traveling path, $\uparrow g^j$. In Fig. 7d we depict a phase diagram of the transport for the fundamental loops $\mathcal{L}_C = \downarrow g^i \uparrow g^j$. Modulation loops that do not cross the equator, as well as those passing the same equator segment south and north, cause no transport. Modulation loops passing one segment south and the other one north induce transport.

4 Four fold symmetry

In ref. 21 we study in detail theoretically and with computer simulations four-fold symmetric patterns. Here we summarize the theoretical results, present experimental data, and show the connection to the two-fold symmetric system.

4.1 Theory

The four-fold symmetric magnetic potential

$$\psi_4(z, x, y) = \psi_2(z, x) + \psi_2(z, y) \quad (20)$$

is closely related to the two-fold symmetric potential ψ_2 , where \mathbf{e}_x points along \mathbf{Q}_1 and \mathbf{e}_y points along \mathbf{Q}_2 . Action space $\mathcal{A}_4 = \mathcal{A}_2 \otimes \mathcal{A}_2$ is the product space of two circles and thus a torus with both Qx and Qy varying from 0 to 2π . There is no indifferent direction and hence it is simpler to use full control space \mathcal{C} . However there exist fence-points satisfying eqn (18) and (19). These fence points play the same role as in $N = 2$ -case in generating transport.

The universal scalar magnetic potential is the superposition of two stripe potentials that separate the variables x and y in action space. Therefore, we have four fence points on the equator of the control space sitting in the $\pm \mathbf{e}_x$ and $\pm \mathbf{e}_y$ directions (Fig. 8a).

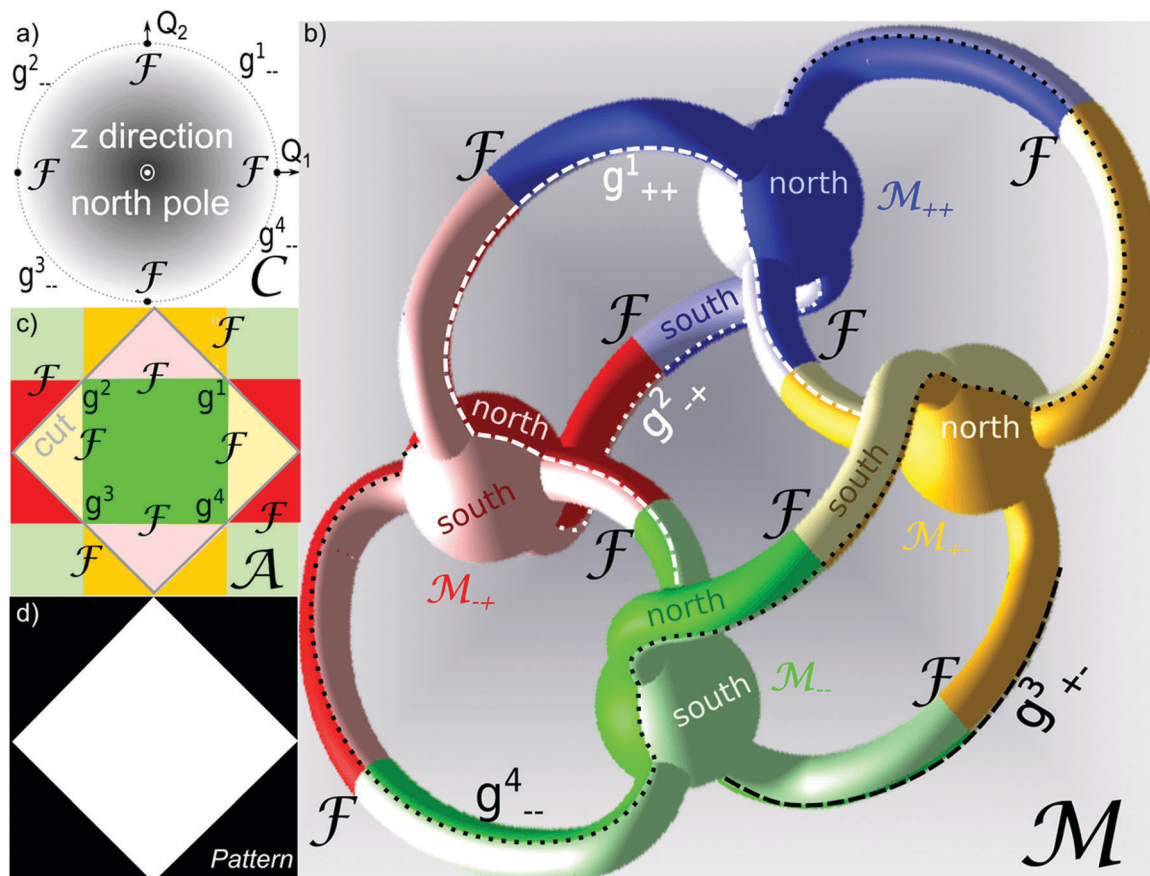


Fig. 8 (a) Top view of the four-fold symmetric control space including the fence points and the maximum segments g^i_{\pm} , $i = 1, 2, 3, 4$ of the four gates. (b) Genus five stationary manifold \mathcal{M} . Blue colors correspond to minima (\mathcal{M}_{++}), green to maxima (\mathcal{M}_{--}), red and yellow to saddle points. (c) Projection of the half of \mathcal{M} lying closer to \mathcal{M}_{--} into action space. The cut in \mathcal{A} is the projection of the points in \mathcal{M} separating both halves. (d) Magnetic pattern generating the four-fold symmetric universal potential. (see Appendix A.3 for a concise definition of the gates).

We define the unit vectors

$$\mathbf{e}_1(\mathbf{x}_A) = \frac{\partial_1 \mathbf{H}^P}{|\partial_1 \mathbf{H}^P|}, \quad \mathbf{e}_2(\mathbf{x}_A) = \frac{\partial_2 \mathbf{H}^P}{|\partial_2 \mathbf{H}^P|}, \quad (21)$$

where $\partial_{1,2}$ denote the partial derivatives with respect to the two coordinates in \mathcal{A} . Points in \mathcal{A} with $\mathbf{e}_1 \times \mathbf{e}_2 \neq 0$ are made stationary by two opposite external fields^{20,21}

$$\mathbf{H}_{\text{ext}}^{(s)} = \pm \frac{\mathbf{e}_1 \times \mathbf{e}_2}{|\mathbf{e}_1 \times \mathbf{e}_2|}. \quad (22)$$

The two signs in (22) cause opposite curvature of U^* and thus each point in \mathcal{A} can be made either an extremum (maximum or minimum) or a saddle point. Hence, we can split action space into forbidden and accessible regions (see Fig. 8c). Allowed regions are regions of extrema and they are colored green, while forbidden regions are regions of saddle points and are colored red and yellow.

Each field in control space renders 4 points in action space stationary, a maximum a minimum and two saddle-points. Hence our stationary manifold consists of four copies of control space (instead of two for the case $N = 2$). The indices of the four sub-manifolds \mathcal{M}_{++} , \mathcal{M}_{+-} , \mathcal{M}_{-+} , and \mathcal{M}_{--} correspond to a minimum (index +) or a maximum (index -) along the

x (first index) and y (second index) coordinates. The four fence points in control space deform into circular fences in \mathcal{M} . The four sub-manifolds are glued together at eight fences to form the full stationary manifold, see Fig. 8b. The stationary manifold is a genus five surface.

The fences in \mathcal{M} are projected onto lines in action space that are the borders between the forbidden and allowed regions. The fences do not intersect on \mathcal{M} but they do in \mathcal{A} . This is possible because the fences meet at special points in \mathcal{A} with $\mathbf{e}_1 \times \mathbf{e}_2 = 0$, that we call the gates. As we will show below, the gates are the only points that connect two consecutive allowed regions. From eqn (7), (21) and (22) we conclude that the gates are rendered stationary by the whole grand circle on \mathcal{C} around $\mathbf{e}_1 = \mathbf{e}_2$. For the four-fold symmetric pattern there are four coinciding gates g^i , $i = 1, 2, 3, 4$ in \mathcal{C} that run across the equator right through the four fence points, see Fig. 8a. In $\mathcal{C} \otimes \mathcal{A}$ each gate is a line on \mathcal{M} that lies in a single copy of the equator of control space and that is projected into the gate in \mathcal{A} . Since one gate in \mathcal{C} cuts through all four fences the gate in \mathcal{A} must be the same as the intersection of fences in \mathcal{A} .

In \mathcal{C} the fence points cut each gate into 4 segments g^i_{++} , g^i_{+-} , g^i_{-+} , g^i_{--} , that are projections of the gates in the corresponding sub-manifolds of \mathcal{M} . Each gate crosses four of the eight fences

in \mathcal{M} and passes over all four sub-manifolds. Each fence crosses two of the four gates. The gate $g_{\alpha\beta}^{i+1}$ in \mathcal{C} coincides with the gate $g_{\alpha\beta}^i$ rotated by $\pi/2$. Therefore the maximum segments of the gates g_{-}^i , $i = 1, 2, 3, 4$ fill the whole equator and subdivide \mathcal{C} as well as all sub-manifolds $\mathcal{M}_{\alpha,\beta}$ and their projections on \mathcal{A} into simply connected northern and southern hemispheres. Northern and southern allowed regions touch each other in \mathcal{A} only at the gates. Nontrivial adiabatic transport therefore must pass these singular points.

In the following we will first deal with the transport of paramagnetic particles. Since these reside on the maxima of U^* , we are only interested in loops on \mathcal{M}_{--} . Modulation loops that remain in one hemisphere of control space are zero homotopic loops of the four punctured sphere and have zero homotopic preimage loops on \mathcal{M} . The simplest non trivial modulation loop must cross the equator twice. Such loop $\mathcal{L}_C = \downarrow g^i \uparrow g^j$ consists of two paths $\downarrow g^i$ and $\uparrow g^j$. $\downarrow g^i$ is a path from north to south passing the gate g_{-}^i and $\uparrow g^j$ is the reverse path passing through gate g_{-}^j from south to north. The winding numbers in control space around the fences cause similar winding in action space. Fig. 9 shows the phase diagram of the transport directions of the simplest gate crossing modulation loops. The topological transition between different transport

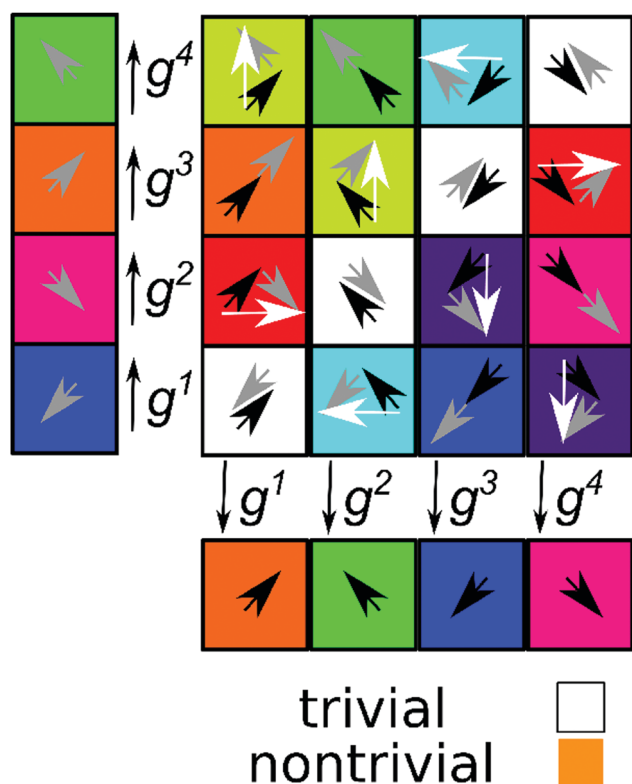


Fig. 9 Phase diagram of the transport modes in a four-fold symmetric system. Black arrows denote the traveling direction in the first, south heading part of the modulation, gray ones describe the transport direction of the second part, and white arrows describe the travel direction of the full loop. The colors of the squares indicate the traveling direction. Loops passing through the same gate twice do not induce transport (white). All other combinations induce transport in one of the eight neighboring unit cells.

modes is similar to the two-fold case. Modulation loops passing a fence cause topological transitions.

Diamagnetic particles move synchronously with the paramagnetic ones at a fixed distance $\mathbf{d} = 1/2(\mathbf{a}_1 + \mathbf{a}_2)$, to the paramagnets.

4.2 Experiments

Four fold symmetric patterns have been created by lithography.^{47–50} The lithographic magnetic patterns are designed to have the four-fold symmetric pattern of Fig. 2b with a period $a = 7 \mu\text{m}$. The strength of the pattern field directly on top of the surface of the thin $Qt < 1$ lithographic film is $H^p \approx 3 \text{ kA m}^{-1}$. Details on the production process are given in the Appendix A.2.

Lithographic edge effects of the pattern production process render white regions larger than the black regions such that the average magnetization of the film is non-zero. This breaks the S_4 -symmetry of the pattern, but it does not affect the S_4 -symmetry of the universal limit $Qz > 1$ and the C_4 symmetry is preserved for the pattern and the universal limit. We coat the patterned magnetic film with a photo-resist of thickness $1.6 \mu\text{m}$. The thickness is a compromise of achieving universality and keeping the magnetic field of the pattern sufficiently strong. Paramagnetic colloids (diameter $d = 2.7 \mu\text{m}$) immersed into deionized water are placed on top of the coating.

In Fig. 10a we apply fundamental modulation loops. They all fall in the class $\mathcal{L}_C = \downarrow g^1 \uparrow g^4$, but have different proximity to the fence point in the \mathbf{Q}_1 direction in \mathcal{C} . In Fig. 10b we plot the corresponding experimental trajectories of paramagnetic particles. No matter which particular modulation loop within the same homotopy class we choose, the global result after completing the loop is the transport of the particle by one unit vector \mathbf{a}_2 . Modulation loops closer to the encircled fence point

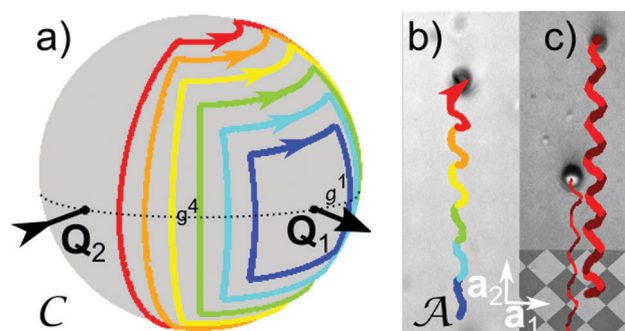


Fig. 10 (a) various modulation loops in control space of the type $\mathcal{L}_C = \downarrow g^1 \uparrow g^4$. (b) Resulting trajectories of paramagnetic colloids. All modulation loops induce transport into the same \mathbf{a}_2 -direction. (c) Trajectories of a paramagnetic (thick line) and a diamagnetic colloid (thin line) subjected to the large (red) modulation loop. Trajectories are colored in dark red for the $\downarrow g^1$ segment and in bright red for the $\uparrow g^4$ segment of the loop. Both types of particles are synchronously transported into the same direction. The trajectories however are shifted by $\mathbf{d} = 1/2(\mathbf{a}_1 + \mathbf{a}_2)$. The background in (b and c) are reflection microscopy images of the four-fold symmetric pattern. We have added the theoretical pattern to the lower part of (c) for clarity. The length of the arrows indicating the lattice vectors is equivalent to the lattice constant $a = 7 \mu\text{m}$. A video clip of the motion of the paramagnetic and the diamagnetic colloidal particle in (c) is provided in ref. 45.

have a straighter trajectory than loops passing the equator far from it (see Fig. 10b).

In Fig. 10c we repeat the experiment with paramagnetic and diamagnetic colloids using the largest modulation loop (red). We immerse paramagnetic and non magnetic (polystyrene $d = 4 \mu\text{m}$, susceptibility $\sim -10^{-5}$) particles in ferrofluid which renders the non magnetic particles effectively diamagnetic. The direction of the magnetic field inside the ferrofluid is used for the direction in control space. It has a higher tilt angle to the film normal than the tilt of the external field applied by the coils, because of refraction at the glass ferrofluid interface. All loops with colloids immersed in ferrofluids are corrected for this effect. Both particles are transported in \mathbf{a}_2 direction by the red loop and the predicted shift of both trajectories by $1/2(\mathbf{a}_1 + \mathbf{a}_2)$ is clearly visible.

In Fig. 11 we show the motion of a paramagnetic particle subject to a modulation poly-loop that consists of all sixteen fundamental loops $\downarrow g^i \uparrow g^j$ of the phase diagram of Fig. 9. We plot the fundamental sections of the trajectory of the particles

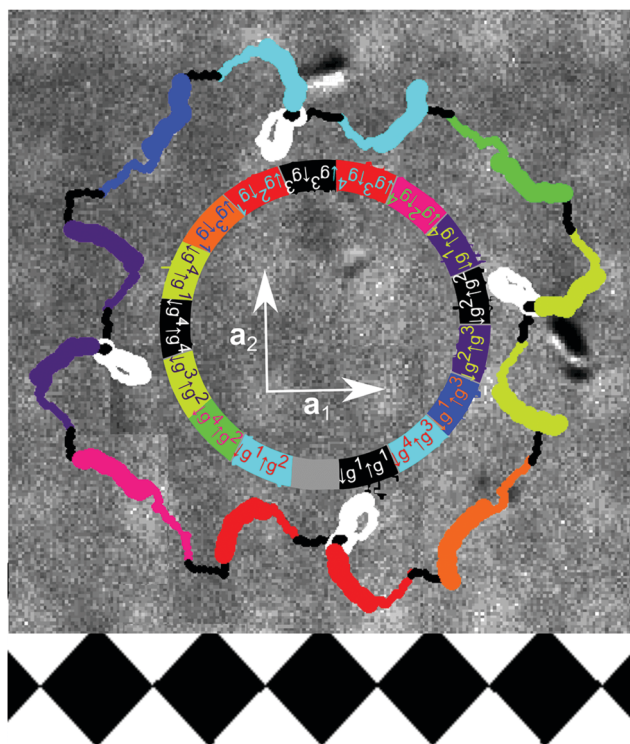


Fig. 11 Experimental trajectory of a paramagnetic colloidal particle in action space \mathcal{A} caused by a modulation poly-loop in \mathcal{C} . The poly-loop consists of a sequence of all fundamental modulation loops in the phase diagram of Fig. 9. The single fundamental loops are colored according to the color in the phase diagram in Fig. 9. South traveling segments are marked as thick lines while north traveling segments are marked as thin lines. Consecutive loops are connected by trivial constant latitude connections that remain in the north of \mathcal{C} (black trajectories). The type of the single loops is indicated inside the region surrounded by the trajectory. The background is the reflection microscopy image of the underlying square magnetic pattern. At the bottom we show a scheme of the theoretical pattern aligned and oriented to the weakly visible experimental pattern on the top. A video clip of the motion of the paramagnetic colloidal particle is provided in ref. 45.

in the colors of the corresponding fundamental loops in the phase diagram (Fig. 9). It can easily be seen that all fundamental loops induce the theoretically predicted transport. Due to the lack of S_4 -symmetry the lemniscates of the zero homotopic loops in \mathcal{A} (white) lose their inversion symmetry with respect to the gate in \mathcal{A} (the crossing point of the lemniscate) resulting in a big and a tiny white loop. We conclude that the experimental response of the particles to all modulation loops is in perfect agreement with the theoretical predictions.

5 Three-fold symmetry

In ref. 20 we studied the motion on a C_6 -symmetric pattern theoretically and provided experiments of the adiabatic motion on this pattern. The C_6 -symmetric pattern is part of the family of three-fold symmetric patterns. Here, we extend the theory to this entire family, explain a new topological transition within the family and corroborate the theory with experiments on adiabatic and ratchet transport for all family members. We also confirm experimentally the new topological transition from C_6 -like toward S_6 -like topology.

5.1 Control space, stationary manifold and action space

The transport on the three-fold symmetric pattern is more complex than on the two-fold and four-fold patterns. The increased complexity is related to the fact that the three reciprocal lattice vectors \mathbf{Q}_1 , \mathbf{Q}_2 and \mathbf{Q}_3 are linearly dependent. In Fig. 12 we show the control spaces, the stationary manifolds, and the action spaces of the three-fold symmetric system for various values of the phase ϕ of the pattern. The phase ϕ varies in an interval $0 \leq \phi \leq \pi/6$ which covers all possible three-fold symmetries including C_6 ($\phi = 0$) and S_6 ($\phi = \pi/6$). We call the range $\pi/9 < \phi \leq \pi/6$ the S_6 -like case and the range $0 \leq \phi < \pi/9$ the C_6 -like case. The range $\pi/6 < \phi < 2\pi$ repeats those patterns, however, centered around one of the other two three-fold symmetric points and/or interchanging up and down magnetized regions, see Fig. 2c. For each value of the phase ϕ of the pattern the stationary manifold \mathcal{M} in Fig. 12 is a genus seven surface. As in the two and four-fold cases there are fences of \mathcal{M} separating different sub-manifolds. We distinguish two different fences: (i) the maximum fence $\mathcal{F}_- = \mathcal{M}_- \cap \mathcal{M}_0$, which is the border between the regions of maxima of the colloidal potential (green colors) and the saddle point regions (red colors), and (ii) the minimum fence $\mathcal{F}_+ = \mathcal{M}_+ \cap \mathcal{M}_0$, which is the border between saddle points and minima (blue colors).

Due to the separability of the two-fold and four-fold problem the fences were projected onto single points in control space. For $N = 3$ the fences in control space \mathcal{C} are not points but closed lines. In Fig. 12a the maximum fences \mathcal{F}_- are shown as green lines and the minimum fences \mathcal{F}_+ as blue lines in control space. The fences in \mathcal{C} separate regions of different multiplicity of preimages in \mathcal{M} . For any value of ϕ there is one multiply connected area (gray) that we call the tropics. This area has multiplicity $m = 4$, that is, one external field renders 4 points in action space \mathcal{A} stationary: one maximum, one minimum and

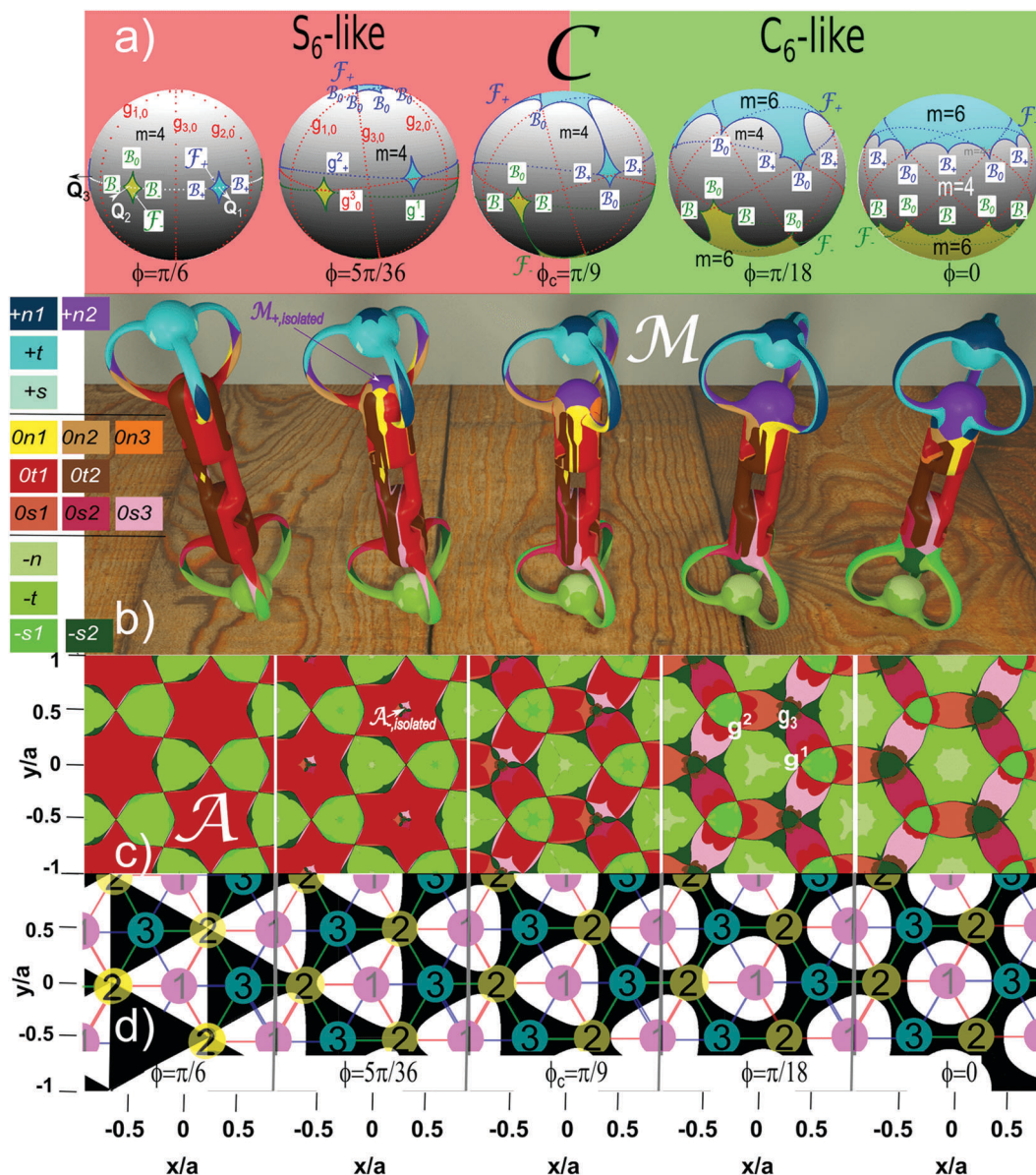


Fig. 12 Topology of the three-fold symmetric case as a function of the phase ϕ : (a) control spaces with areas of different multiplicity $m = 4$ (gray), $m = 6$ extra maximum areas (yellow) which are surrounded by the southern fence \mathcal{F}_- (green lines) and $m = 6$ extra minimum areas (cyan) surrounded by the northern fence \mathcal{F}_+ (blue lines). The gates g are colored according to their segments. (b) Genus seven stationary manifolds \mathcal{M} . Blue colors correspond to minima (M_+), red colors to saddle points (M_0) and green colors to maxima (M_-). Fences are the boundaries between the color families and pseudo fences are the boundaries between the colors of one family. Areas with labeled with a prefix (n) are projected into the northern area or the northern satellites in \mathcal{C} , with a prefix (s) to the south, with a prefix (t) to the tropical $m = 4$ area of \mathcal{C} . (c) Projection of the lower half of the stationary manifold into action space \mathcal{A} . The projection of the upper half exactly matches the lower projection, however, with the colors of the upper half replacing those of the lower half. The areas $0t1$ and $0t2$ contain cuts (not shown) that connect the shown projection of the southern half of \mathcal{M}_0 to its similar twin projection of the northern half. (d) Magnetic patterns corresponding to the different phases. Up magnetized regions shown in white and down magnetized regions in black. The pink, yellow and cyan circles mark the three high symmetry points of the lattice and the high symmetry lines connecting the points form the 12-, 23-, and 31-network. Higher resolution images of \mathcal{A} , \mathcal{C} , and \mathcal{M} for each of the phases with further details can be found in the Appendix A.1, definitions of the various geometrical objects in Appendix A.3.

two saddle points. In addition there are concave excess regions of multiplicity $m = 6$. In the yellow regions surrounded by \mathcal{F}_- there is an extra maximum and an extra saddle point, while in the cyan regions (surrounded by \mathcal{F}_+) there is an additional minimum and also a saddle point. The control space always shows the C_3 symmetry and the inversion symmetry $U^*(\mathbf{H}_{\text{ext}}) = -U^*(-\mathbf{H}_{\text{ext}})$,

see eqn (7). For this reason the cyan regions are the inverted yellow regions on the opposite side of control space. A rotation of control space by $2\pi/3$ leaves the control space invariant. Not all excess regions are visible in Fig. 12a. We can infer the location of hidden excess regions from the visible excess regions using these two symmetry operations.

The stationary manifold is formed from multiple copies (according to the multiplicity) of the areas in \mathcal{C} . As already mentioned the two fences separate the three sub-manifolds of \mathcal{M} . But on \mathcal{M} there are additional preimages of the fences in \mathcal{C} that are different from the fences in \mathcal{M} . As in the two-fold case we call these pseudo fences. The pseudo fences in \mathcal{M} and in \mathcal{A} (Fig. 12b and c) are the borders between the areas with different colors belonging to the same color family (red, green or blue).

In the three-fold case we have an additional type of point that we did not have in the two- and four- fold cases. They are bifurcation points,⁵¹ located on the fences on \mathcal{M} . These are the only points where more than two areas of different colors meet. We have \mathcal{B}_- (\mathcal{B}_+) bifurcation points where three areas on \mathcal{M}_- (\mathcal{M}_+) and one area on \mathcal{M}_0 meet, and \mathcal{B}_0 bifurcation points where three areas on \mathcal{M}_0 and one area in either \mathcal{M}_- or \mathcal{M}_+ meet. Both types of bifurcation points split the fences on \mathcal{M} , as well as their projection onto \mathcal{C} and onto \mathcal{A} , into single segments (Fig. 12a).

We now consider a control loop \mathcal{L}_C that passes through a multiplicity $m = 6$ excess region. When the loop crosses the fence towards this region the multiplicity increases by two. This happens *via* the creation of an extremum–saddle point pair at the fence on \mathcal{M} . At the same time the other preexisting stationary points pass a pseudo fence. When the modulation loop leaves the excess region the multiplicity returns to $m = 4$. Now a extremum–saddle point pair is annihilated at the fence. When the loop transports a paramagnetic colloidal particle, the particle is now either adiabatically transported through the pseudo fence or the colloid carrying maximum is annihilated at the fence resulting in ratchet motion.

The type of transport is directly related to the number of bifurcation points of each excess area enclosed by the modulation loop. When the modulation loop in \mathcal{C} encircles an even number of \mathcal{B}^- (\mathcal{B}^+) bifurcation points of one excess area, then the exit of the excess area corresponds to a pseudo fence on \mathcal{M}_- (\mathcal{M}_+) and the transport is adiabatic. If the number of encircled \mathcal{B}^- (\mathcal{B}^+) bifurcation points in an excess area is odd the exit of the excess area corresponds to the fence of \mathcal{M}_- and the loop induces a ratchet. This ratchet is time reversible if the number of encircled \mathcal{B}^0 bifurcation points is a multiple of 2 (3) for each excess area in the S_6 (C_6)-like case, and non-time reversible otherwise. A time reversal ratchet is a ratchet where the reversed modulation results in the reversed transport direction.

5.2 S_6 - C_6 -Topological transition

The topology of the S_6 -like (C_6 -like) systems is the same as the S_6 - (C_6) symmetric system. A topological transition between S_6 -like and C_6 -like occurs at a critical phase $\phi_c = \pi/9$ of the pattern. The topological transition can be easily seen in control space. Control space consists of areas with different multiplicity. The shape and location of the areas vary with the phase ϕ . The topology of these areas, however, only differs for the two situations $\pi/9 < \phi \leq \pi/6$ (S_6 -like) and $|\phi| < \pi/9$ (C_6 -like). Fig. 12a shows examples of the control spaces \mathcal{C} for these two cases as well as for the critical transition value $\phi_c = \pi/9$.

For any value of the phase ϕ there is one multiply connected area in control space \mathcal{C} , the tropics (gray) having four preimages ($m = 4$). In the S_6 -like case there are four areas (yellow) surrounded by a maximum fence \mathcal{F}_- (green) with multiplicity $m = 6$ housing an extra maximum–saddle point pair. One area is a (hidden) southern area (opposite to the visible cyan northern area) surrounded by a maximum fence \mathcal{F}_- with 6 segments joined at six \mathcal{B}_0 bifurcation points. The other three are southern satellites surrounded by a maximum fence \mathcal{F}_- with four segments joined at two \mathcal{B}_0 and two \mathcal{B}_- bifurcation points. We call these areas southern satellites since at the topological transition they merge with the southern area. The southern area shrinks to zero as the phase approaches $\phi = \pi/6$ (S_6 -symmetry). Four further areas of multiplicity $m = 6$ (cyan) housing an extra minimum-, saddle point pair are located opposite to the yellow ones.

The topological transition occurs at $\phi_c = \pi/9$ where the three southern satellites join with the corresponding southern area. Simultaneously the northern satellites join with the northern area. In each satellite one \mathcal{B}_0 bifurcation point merges with one \mathcal{B}_0 bifurcation point from the polar area. Thus the two polar fence segments of a satellite are both unified with two fence segments of the polar region. This results in a new topology with only two polar areas for the C_6 -like case. Both areas are surrounded by a fence with twelve segments that are separated by a sequence of bifurcation points alternating between \mathcal{B}_0 and \mathcal{B}_- (\mathcal{B}_+).

Due to the inversion symmetry $U^*(\mathbf{H}_{\text{ext}}) = -U^*(-\mathbf{H}_{\text{ext}})$ the transport of diamagnetic particles on \mathcal{M}_+ is the same as those of the transport of paramagnetic particles on \mathcal{M}_- at the inverted external magnetic field. In Fig. 12b we depict the topology of the stationary manifold for five different phases ϕ . The true stationary manifold is embedded in a four dimensional curved phase space and we can only show its topology by deforming it until it finally is embedded into three dimensions. The deformation partially breaks the three-fold C_3 -symmetry, however, the inversion symmetry shows up as a up-down mirror symmetry of the manifolds, accompanied by an inversion of the sign of the index of the submanifolds.

In the S_6 -like case there is a (hidden) preimage on \mathcal{M} of the southern excess area of \mathcal{C} that is entirely surrounded by \mathcal{M}_0 areas and therefore disconnected from the rest of \mathcal{M}_- . We call this region $\mathcal{M}_-^{\text{isolated}}$ and it lies opposite to the visible $\mathcal{M}_+^{\text{isolated}}$ region in Fig. 12b. This isolated area is surrounded by fences and does not contain pseudo fences. Therefore, all paths of steepest descend can only lead away from it since return points lie on pseudo fences. For this reason the isolated area $\mathcal{M}_-^{\text{isolated}}$ might be emptied once of a colloid but can never be refilled. Since we are interested in the motion occurring by the periodic repetition of modulation loops this area and hence its projection into \mathcal{C} is completely irrelevant. After the topological transition to the C_6 -like case the formerly irrelevant polar areas on \mathcal{C} incorporate the three corresponding satellites. Hence $\mathcal{M}_-^{\text{isolated}}$ is no longer disconnected from the rest of \mathcal{M}_- and becomes relevant for the motion.

For any ϕ the stationary manifold \mathcal{M} is a genus seven surface and there are thus 14 different winding numbers. In the S_6 -like case only two linear independent winding numbers correspond to loops $\mathcal{L}_{\mathcal{M}} \subset \mathcal{M}_-$ that are lying entirely in \mathcal{M}_- . Therefore there are only two ways of nontrivial adiabatic transport modes. When $\mathcal{M}_-^{\text{isolated}}$ joins with the other part of \mathcal{M}_- ($\phi = \pi/9$) two additional windings around holes of \mathcal{M}_- occur allowing two new transport routes through the formerly isolated region of \mathcal{A} .

Fig. 12c shows the projection of the lower half of the stationary manifold into action space \mathcal{A} . The projection of the upper half exactly matches the lower projection, however, with the colors of the upper half replacing those of the lower half. Fig. 12d shows possible magnetization patterns that generate the universal potentials U^* . We also show the three-fold symmetric points $\mathbf{x}_{\mathcal{A},1}$, $\mathbf{x}_{\mathcal{A},2}$, and $\mathbf{x}_{\mathcal{A},3}$ within the pattern. Their connections form a 12-, 23-, and 31-network which are the three kinds of high symmetry lines of the lattice.

5.3 Modulation loops in the S_6 -like case

As in the four-fold symmetric case, in the three-fold case two neighboring allowed regions in \mathcal{A} only touch each other at a single point, the gate. Hence modulation loops in \mathcal{C} causing adiabatic transport in \mathcal{A} have to pass through the grand circles of the gates in \mathcal{C} .

In the three-fold symmetric case there are six gates g^i , g_i , $i = 1, 2, 3$ of two different types g^i and g_i . All gates in \mathcal{M} are closed curves dissected twice by \mathcal{F}_+ and twice by \mathcal{F}_- (the gates on \mathcal{M} are shown in more detailed images of \mathcal{M} in the Appendix A.1 of this work). Hence, for the projection of each gate into \mathcal{C} there is one minimum gate segment g_+ (blue in Fig. 12a) projected from \mathcal{M}_+ , one maximum segment g_- (green) projected from \mathcal{M}_- , and two saddle point gate segments g_0 (red).

Whenever we cross a gate segment of type g_-^i or $g_{i,-}$ in the $m = 4$ (gray) region of \mathcal{C} the unique maximum in \mathcal{A} adiabatically passes from one allowed area through the gate g_-^i or $g_{i,-}$ in \mathcal{A} to the allowed area on the other side. For the S_6 -like case the maximum segments $g_{i,-}$ of the three gates g_i , $i = 1, 2, 3$ lie entirely in the irrelevant southern excess region of \mathcal{C} and are hence unimportant for transport. For the C_6 -like case all six gates cross both polar excess regions. Therefore all gates become important for transport. Eventually if we have C_6 -symmetry (at $\phi = 0$) the difference in character between both types of gates g^i and g_i completely vanishes. Gates cross each other in \mathcal{C} but in \mathcal{M} they do not cross. Only when we have a S_6 -symmetry ($\phi = \pi/6$) the three gates g_i of the isolated allowed region merge such that they touch each other in \mathcal{M} and are all projected into the one monkey saddle point in \mathcal{A} . Otherwise the gates are separated curves on \mathcal{M} much in the same way as in the four-fold case.

For the S_6 -like case we can characterize fundamental modulation loops $\mathcal{L}_{\mathcal{C}} = \downarrow s \uparrow s'$ in \mathcal{C} by two loop segments. One is a south heading path $\downarrow s$ and the other is a north heading path $\uparrow s'$. There are three possible types of south traveling paths. It is either of type $\downarrow g_-^i$, of type $\downarrow \mathcal{F}_{-l}^i$, or of type $\downarrow \mathcal{F}_{-r}^i$ with $i = 1, 2, 3$ in all cases.

Each gate segment g_-^i has two B_- bifurcation points close to it. A path of type $\downarrow g_-^i$ is a path that moves south between these two bifurcation points. It might thereby completely stay in the gray $m = 4$ area or eventually enter a southern satellite (yellow) and exit it again *via* the same southern fence segment. Examples of all types of paths are shown in Fig. 13a. A path of type $\downarrow \mathcal{F}_{-l}^i$ passes left of the two bifurcation points. It thereby has to enter the $m = 6$ satellite to the left of gate g_-^i through one of the two upper fence segments. The path exits the satellite *via* the lower right fence segment that is also crossed by the corresponding gate segment g_-^i . A path of type $\downarrow \mathcal{F}_{-r}^i$ is the equivalent path that passes right of the two bifurcation points and enters the satellite to the right of gate g_-^i . Since the paths $\downarrow \mathcal{F}_{-l}^i$ and $\downarrow \mathcal{F}_{-r}^i$ are fence crossing paths they induce ratchet motion and therefore they do not necessarily have to cross the gate. The paths $\downarrow \mathcal{F}_{-l}^i$ and $\downarrow \mathcal{F}_{-r}^i$ are topologically protected by the path $\downarrow g^i$ through the neighboring gate.

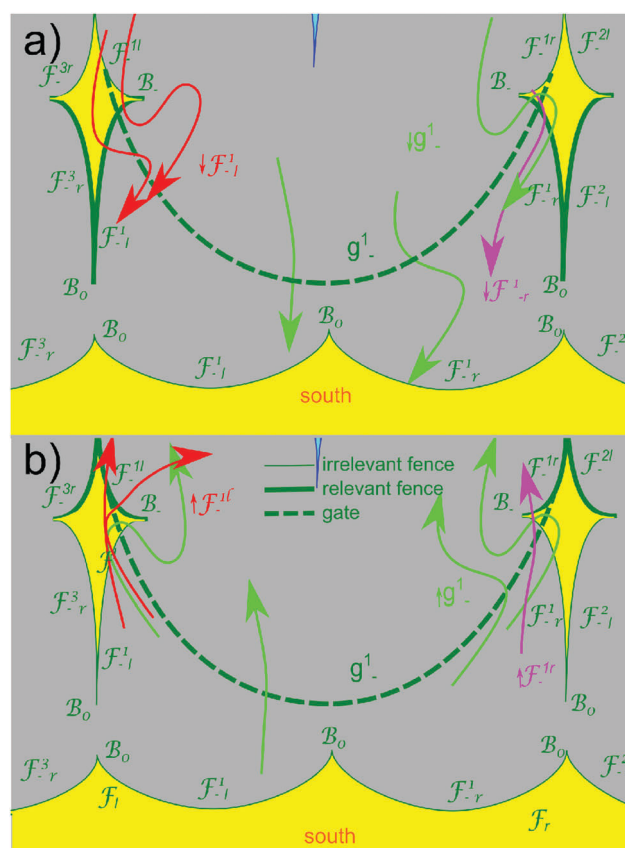


Fig. 13 Paths in the southern hemisphere of \mathcal{C} relevant for the loops in the S_6 -like case. Paths of type $\downarrow g_-^i$ and $\uparrow g_-^i$ are shown in green, $\downarrow \mathcal{F}_{-l}^i$ and $\uparrow \mathcal{F}_{-l}^i$ in red and $\downarrow \mathcal{F}_{-r}^i$ and $\uparrow \mathcal{F}_{-r}^i$ in purple. The fences of the satellites are enumerated according to the gate closest to them. The index l (r) indicates that the fences are left (right) of the corresponding gate and the position of the index (subscript or superscript) indicates the location of the fence segment in the satellite (up or down). The fence segments of the irrelevant polar fence share the names with those segments of the satellites with which they will join beyond the topological transition. (a) South traveling paths for which the lower fences (highlighted) are relevant. (b) North traveling paths for which the upper fence segments (highlighted) are relevant. See Appendix A.3 for definitions and terminology.

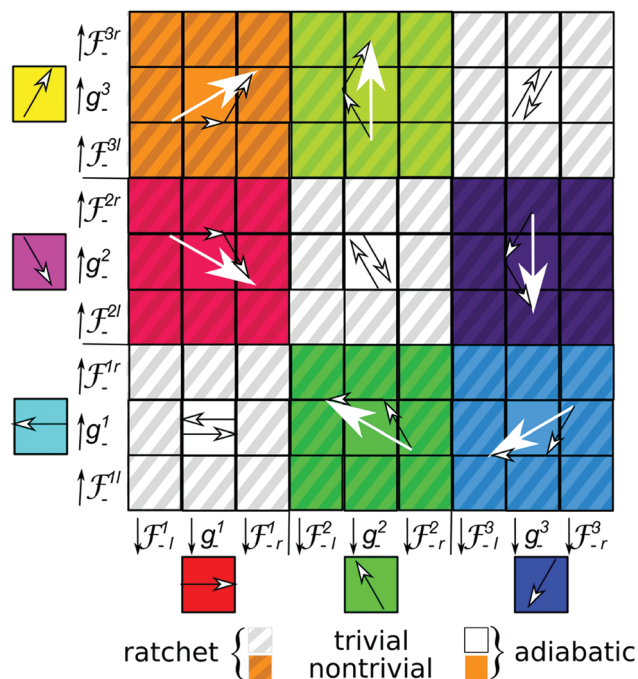


Fig. 14 Phase diagram of the transport of paramagnetic colloids for S_6 -like case. All paths (small arrows) occur on the 31-network. The terminology of the paths is explained in Section 5.3.

We complete the fundamental loop with a north traveling path of type $\uparrow g^i$, $\uparrow \mathcal{F}^{il}$ or $\uparrow \mathcal{F}^{ir}$. A path of type $\uparrow \mathcal{F}^{il}$ is a north traveling path that passes left of the two bifurcation points. It enters the satellite left of gate g^i and exits it *via* the upper right fence segment attached to the gate segment g^i (for examples see Fig. 13b).

In Fig. 14 we depict the phase diagram of the transport induced by the fundamental loops $\mathcal{L}_C = \downarrow s \uparrow s'$ for the S_6 -like case. Loops for which both paths are of type g are adiabatic, while loops containing at least one path of type \mathcal{F} are ratchets. Note that the transport direction is independent of how we enter an $m = 6$ satellite region. We therefore do not specify the point of entry in the phase diagram. The entry determines whether a ratchet loop is a time reversal or non time reversal loop. If the entry and the exit are attached to a different gate segment the modulation loop is predicted to cause a non-time reversal ratchet. In contrast, loops where paths enter and exit the satellites through the fence segments attached to the same gate are time reversal ratchet loops.

5.4 Modulation loops in the C_6 -like case

The C_6 -like case is easier than the S_6 -like case. There is one single southern fence. Non trivial transport of paramagnetic particles occurs for modulation loops that cross the southern fence. Fundamental loops $\mathcal{L}_C = \downarrow s \uparrow s'$ can be characterized by the south traveling path $\downarrow s$ through fence segment s and the path $\uparrow s'$ traveling north through fence segment s' . We abbreviate the fence segments for the C_6 -like case with the names of the segments for the S_6 -like case from which they developed. The type of transport as well as the direction can also be

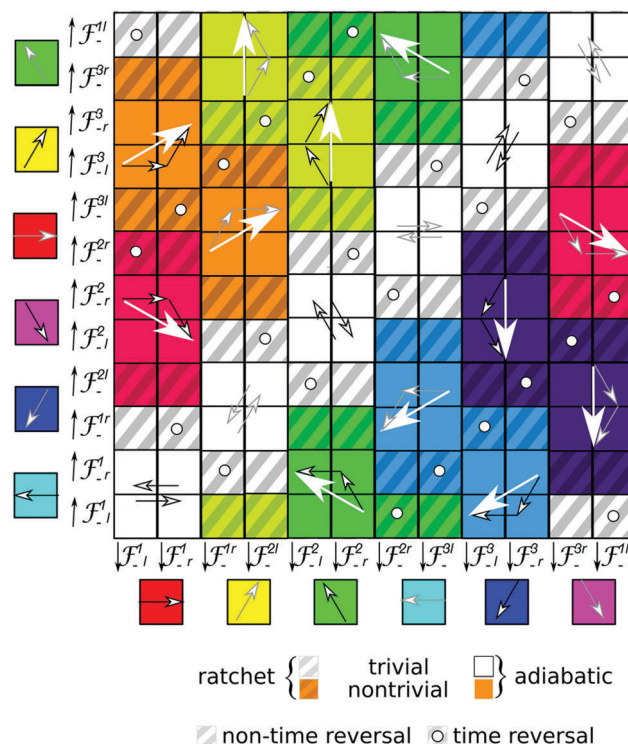


Fig. 15 Phase diagram of the transport for C_6 -like case. Ratchets are topologically protected by the adiabatic loop sharing the same south traveling path. Paths occur on the 31-network (black) or on the 12-network (gray arrows). The choice of network depends on the south heading path $\downarrow \mathcal{F}^i$. The terminology of the paths is explained in Sections 5.3 and 5.4.

explained by the bifurcation points the modulation loop encloses. The exact way the gates are crossed is still important. The gates, however, lie in such a way that crossing a fence segment dictates which gate the loop must pass. Hence, the fence segments passed by the loop fully determine the transport direction. Fig. 15 depicts the phase diagram of the transport directions of the C_6 -like case. It is a checker board of adiabatic and ratchet loops. Despite the topological transition the clustering of colors and therefore directions is quite similar to the phase diagram of the S_6 -like case (Fig. 14). Note that in contrast to the S_6 situation we use the same fence segments for both directions of the modulation loops.

Due to the symmetry of the universal potential U^* diamagnetic transport can be achieved in the same way by simply reversing the field $\mathbf{H}_{\text{ext}} \rightarrow -\mathbf{H}_{\text{ext}}$. In contrast to the four-fold case the transport in all three-fold cases is more versatile. Paramagnetic and diamagnetic colloids are no longer fixed to the same transport direction but can be transported fully independently, because \mathcal{F}_- and \mathcal{F}_+ are well separated in \mathcal{C} .

5.5 Three and six fold symmetry

Let us reconsider the symmetry of the three-fold lattice. As we have seen there are three points $\mathbf{x}_A^1 = 0$, $\mathbf{x}_A^2 = (\mathbf{a}_1 + \mathbf{a}_2)/3$ and $\mathbf{x}_A^3 = -(\mathbf{a}_1 + \mathbf{a}_2)/3$ in the unit cell of \mathcal{A} with three-fold symmetry (see Fig. 2c). As we vary ϕ one of these points acquires a higher C_6 symmetry at $\phi = n\pi/3$, with $n = 1, 2, 3, \dots$. The higher

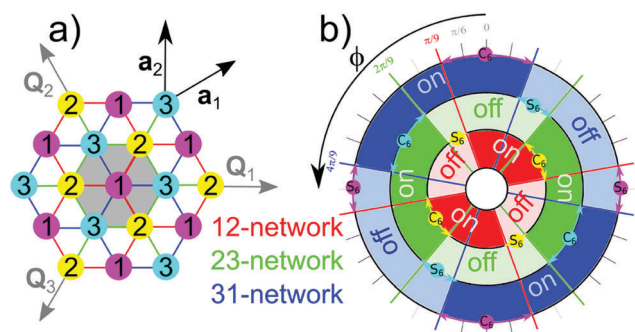


Fig. 16 (a) Threefold unit cell with the three possible symmetry points \mathbf{x}_1 (purple), \mathbf{x}_2 (yellow) and \mathbf{x}_3 (cyan). There are three networks along which transport is possible, the 12-network (red lines), the 31-network (blue) and the 23-network (green). (b) State of each network as a function of the phase of the pattern. Activated (on) networks have full colors while deactivated (off) networks have light colors. Phases ϕ , where one of the symmetry points acquires higher S_6 or C_6 symmetry are marked by circles of the color of the high symmetry point. Topological transitions between S_6 and C_6 symmetries are also marked with colored thick lines. The state of a network can only change at the topological transition. See Appendix A.3 for definitions and terminology.

symmetry permutes amongst the three points. Similarly, one of the points acquires a S_6 symmetry for $\phi = \pi/6 + n\pi/3$. Connections between two different points \mathbf{x}_i^A and \mathbf{x}_j^A define a ij -network that might enable transport between two unit cells. There are three possible networks: the 12-network, the 23-network, and the 31-network (see Fig. 16a).

For a polar orientation of the external field at least one of the three points is a minimum and at least one is a maximum. At the S_6 symmetry point the potential has a monkey saddle for a polar external field orientation and a normal saddle point otherwise. In any case the S_6 point lies in the forbidden region. Hence the S_6 symmetry shuts off all connections to the point with S_6 symmetry. Only the network between the remaining two symmetry points can be used for transport *via* appropriate modulation loops. In contrast when the pattern acquires C_6 symmetry the point with C_6 symmetry is connected to both other symmetry points *via* two networks. The network between the lower C_3 symmetry points is shut off.

As we vary ϕ from 0 to 2π each network is switched on and off twice. For any ϕ at least one network is on and at least one network is off. The exact number of active networks depends on whether ϕ is in the neighborhood of a C_6 or a S_6 symmetry. In Fig. 16b we plot the symmetry of the three points and the state of the three networks as a function of ϕ . Note the close relationship to an antiferromagnetic equilibrium Ising system in a triangular lattice.⁵² Both systems are geometrically frustrated, with not all possible connections between sites being turned on.

5.6 Experiments on the S_6 -like symmetry

Three fold symmetric patterns with lattice constant $a = 7 \mu\text{m}$ have been created in the same way as the four-fold patterns. Here again lithographic edge effects of the patterning process render white regions larger than the black regions such that the

average magnetization of the film is non-zero. This breaks the S_6 -symmetry and shifts the phase $\phi < \phi_{\text{mask}}$ of the patterns away from the phase ϕ_{mask} of the lithographic mask toward the C_6 -like symmetric direction.

To show the topological protection of the transport directions in the S_6 -like case we apply different fundamental modulation loops that all fall in the classes $\mathcal{L}_C = \downarrow \mathcal{F}_{-r}^2 \uparrow \mathcal{F}_{-r}^{3l}, \downarrow g^2 \uparrow g^3$, or $\downarrow \mathcal{F}_{-l}^2 \uparrow \mathcal{F}_{-l}^{3r}$, but have different proximity to the satellite centered at $-\mathbf{Q}_1$ in \mathcal{C} . In Fig. 17 we plot the corresponding trajectories of paramagnetic particles on a S_6 -like pattern. All loops induce transport in the \mathbf{a}_2 direction, which is in accordance with the predictions of Section 5.3. It does not matter which particular modulation loop within the same homotopy class we choose, the global result after completing the loop is the transport of the paramagnetic particle by one unit vector \mathbf{a}_2 . Modulation loops closer to the encircled satellite have a straighter trajectory than loops passing the equator far from it (see Fig. 17). For small as well as for large modulation loops passing the equator close to one of the southern (green) satellites, we observe the transition from adiabatic toward ratchet motion (dashed modulation loops in Fig. 17a). Therefore, ratchet loops are observed in a larger region than expected from the theoretically predicted positions of the B_- bifurcation points and the fences of the satellites. However their occurrence is topologically equivalent to the theoretical model. Note that passing the blue fences is irrelevant for the motion of paramagnetic particles. The difference between the adiabatic and ratchet motion will be shown in detail in Section 5.7.

In a second step we immersed the paramagnetic particles into a ferrofluid on top of the pattern and added effectively

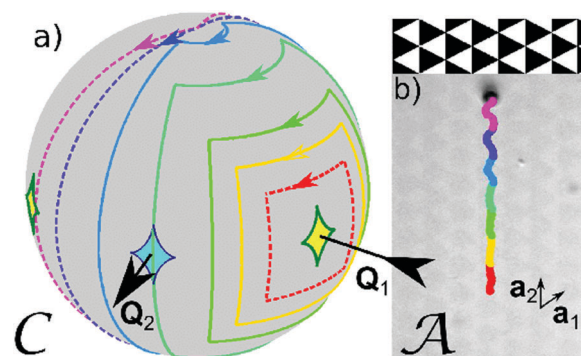


Fig. 17 (a) Different modulation loops in \mathcal{C} encircling the satellite around $-\mathbf{Q}_1$. The loops fall into the three classes $\mathcal{L}_C = \downarrow \mathcal{F}_{-r}^2 \uparrow \mathcal{F}_{-r}^{3l}$ (dashed red), $\mathcal{L}_C = \downarrow g^2 \uparrow g^3$ (solid yellow, green, light green, and blue) and $\mathcal{L}_C = \downarrow \mathcal{F}_{-l}^2 \uparrow \mathcal{F}_{-l}^{3r}$ (dashed purple and magenta), where dashed lines are indicating modulation loops that induce ratchets. (b) Corresponding experimental trajectories of a paramagnetic colloidal particle on top of the S_6 -pattern. The (dashed) ratchet loops fall into the same homotopy class as the (solid) adiabatic loops and therefore the travel direction (along \mathbf{a}_2) is topologically protected. Passing blue fences is irrelevant for the motion of the paramagnets. Note that some of the experimentally observed ratchet loops do not pass through the theoretical green fences of control space. The background in (b) is the reflection microscopy image of the underlying lithographic magnetic pattern. A video clip of the motion of the paramagnetic colloidal particle is provided in ref. 45.

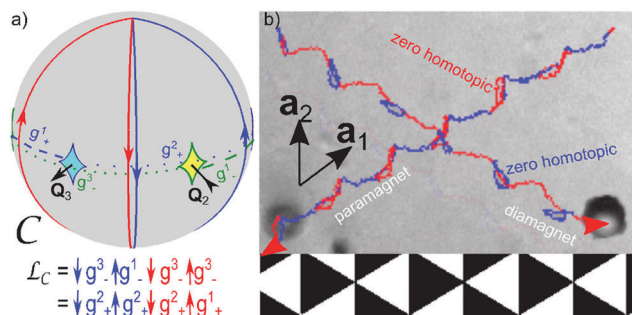


Fig. 18 (a) Control space \mathcal{C} with the applied modulation double loop $\mathcal{L}_C = \downarrow g^3 \uparrow g^1 \downarrow g^2 \uparrow g^3 = \downarrow g_+^3 \uparrow g_+^1 \downarrow g_+^2 \uparrow g_+^3$ consisting of two joint fundamental modulation loops. (b) Experimental trajectories of a paramagnetic and a diamagnetic colloidal particle in action space \mathcal{A} caused by this loop. The result is the transport of paramagnetic and diamagnetic particles in directions differing by an angle of $2\pi/3$. While the first (blue) fundamental loop transports the paramagnetic particles it is zero homotopic for the diamagnetic particles and vice versa for the second (red) loop. The background is the reflection microscopy image of the lithographic magnetic pattern. A video clip of the motion of the paramagnetic colloidal particle is provided in ref. 45.

diamagnetic particles. We subjected both types of particles to a double loop $\mathcal{L}_C = \mathcal{L}_C^1 \mathcal{L}_C^2$ consisting of two fundamental loops $\mathcal{L}_C^1 = \downarrow g^3 \uparrow g^1 = \downarrow g_+^3 \uparrow g_+^1$, and $\mathcal{L}_C^2 = \downarrow g^2 \uparrow g^2 = \downarrow g_+^2 \uparrow g_+^2$ (Fig. 18a). The first loop \mathcal{L}_C^1 (blue) transports the paramagnetic particles by the unit vector $-\mathbf{a}_1$. \mathcal{L}_C^1 is zero homotopic for the diamagnets since it is only crossing the same minimum segment g_+^2 twice. The second fundamental loop \mathcal{L}_C^2 (red) is zero homotopic for the paramagnets and transports the diamagnets in the different \mathbf{a}_1 - \mathbf{a}_2 direction. The resulting trajectories of paramagnetic and diamagnetic particles to the double loop \mathcal{L}_C are shown in Fig. 18b. The double loop \mathcal{L}_C is an example of a combination of two modulation loops that induces transport of paramagnetic and diamagnetic particles in two independent arbitrary directions on top of a S_6 -like pattern.

The experimental trajectories not only are in accordance with the theory for the previous loops, but for all possible fundamental loops. To experimentally show this we applied a poly-loop for paramagnetic particles that combines all the fundamental loops of the phase diagram of Fig. 14. In Fig. 19 we plot the experimental trajectory of paramagnetic particles with the fundamental sections colored with the color of the corresponding theoretical fundamental loop of Fig. 14. All fundamental loops transport into the theoretically predicted directions. In conclusion the experimental response of the particles on a S_6 -like pattern to all shown modulation loops is in topological agreement with the theoretical predictions. The only phenomenon that we could not observe in our experiments is a non time reversal ratchet. The reasons for this are discussed in Section 6.

5.7 Experiments on the C_6 -like symmetry

The experimental trajectories of the adiabatic modulation loops of the C_6 -like case are also in accordance with the theory.

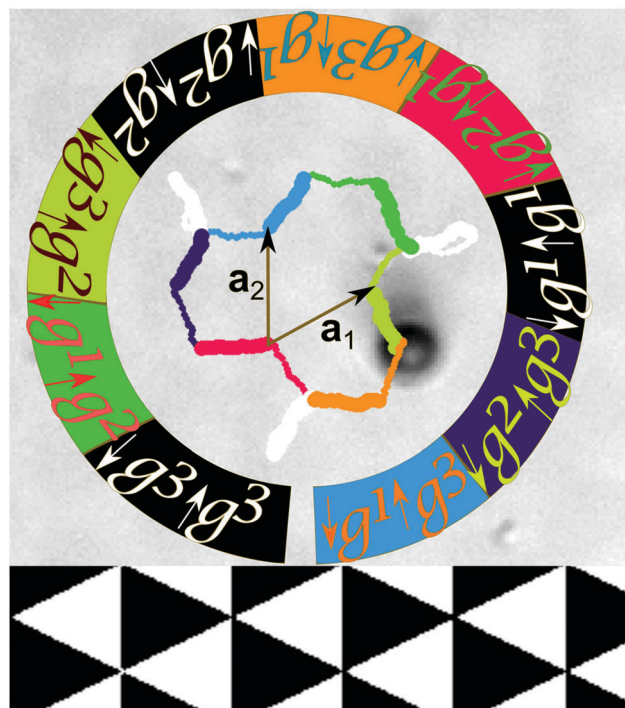


Fig. 19 Experimental trajectory of a paramagnetic colloidal particle on top of a S_6 pattern caused by a modulation poly-loop in \mathcal{C} consisting of a sequence of all fundamental modulation loops. The fundamental loops are colored according to the loops in the phase diagram in Fig. 14. South traveling segments are marked as thick lines. North traveling segments are marked as thin lines. A video clip of the motion of the paramagnetic colloidal particle is provided in ref. 45.

Fig. 20 shows the trajectory of a paramagnetic particle subject to an adiabatic poly-loop that consists of all different adiabatic right fence segment crossing fundamental loops of the phase diagram in Fig. 15 combined. We plot the trajectories of the particles in the color of the corresponding fundamental loops of the phase diagram. All adiabatic loops transport into the directions predicted by the theory.

In contrast to the universal two-fold and four-fold symmetric patterns the three and sixfold symmetric patterns not only support adiabatic motion but also ratchet type motion can be observed. To visualize the characteristics of the different types of motion we use palindrome modulation loops $\mathcal{L}_C = \tilde{\mathcal{L}}_C \tilde{\mathcal{L}}_C^{-1} = \downarrow \mathcal{F}^{3r} \uparrow s \downarrow s \uparrow \mathcal{F}^{3r} = \mathcal{L}_C^{-1}$. They consist of a loop $\tilde{\mathcal{L}}_C = \downarrow \mathcal{F}^{3r} \uparrow s$ that is first played in the forward direction and afterwards played again but this time reversed, *i.e.*, in the backward direction. While the first path $\downarrow \mathcal{F}^{3r}$ of $\tilde{\mathcal{L}}_C$ is kept the same, the second path $\uparrow s$ varies along the eleventh column of the phase diagram (Fig. 15). We start with (a) $s = \mathcal{F}^{11}$ which makes \mathcal{L}_C an adiabatic zero homotopic loop and then trace the transition towards adiabatic transport (d) ($s = \mathcal{F}^{21}$) via two different non time reversal ratchets (b) ($s = \mathcal{F}_1^1$) and (c) ($s = \mathcal{F}_r^1$). Afterwards we show the crossover toward another adiabatic transport direction (g) ($s = \mathcal{F}^{2r}$), this time by passing a time reversal ratchet (e) ($s = \mathcal{F}_1^2$) and another non time reversal ratchet (f) ($s = \mathcal{F}_r^2$). Trajectories of these motions are shown in Fig. 21.

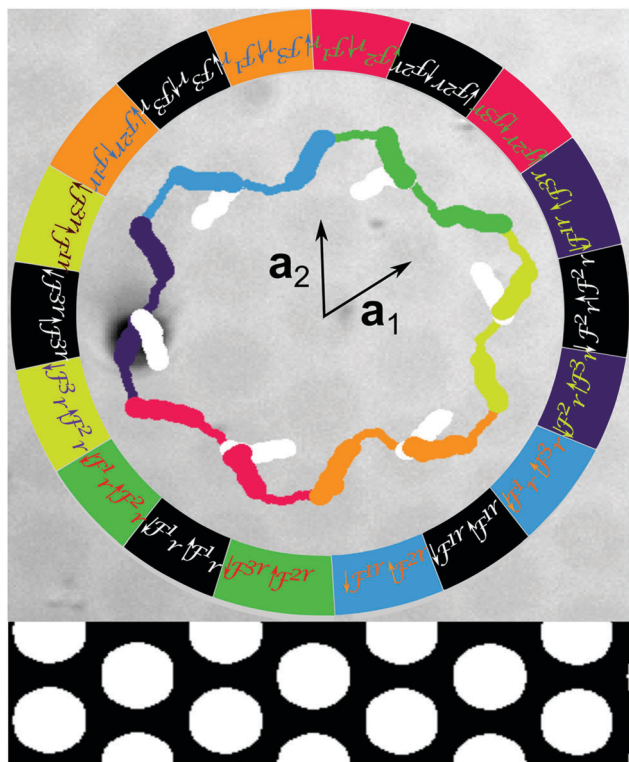


Fig. 20 Experimental trajectory of a paramagnetic colloidal particle on top of a C_6 -pattern. The colloidal particle is subjected to a modulation poly-loop in \mathcal{C} which is a combination of all adiabatic right fence crossing fundamental modulation loops. The single fundamental loops are colored according to the loops in the phase diagram in Fig. 15. South traveling segments are again marked as thick lines while north traveling segments are thin lines. Similar to the theory the circular bubble domains have positive magnetization. However the reflection microscopy image in the background has an inverted contrast such that the bubbles are dark. A video clip of the motion of the paramagnetic colloidal particle is provided in ref. 45.

Obviously, if the induced motion is adiabatic the colloidal particle is tracing some path in \mathcal{A} during the forward motion, and then returns to the initial position by tracing the exact same path in the backward direction. Three such adiabatic paths (a, d and g) are shown in Fig. 21. All adiabatic paths are caused by modulation loops making use of only upper type fence crossings and cause motion on the 12-network only. In contrast the irreversible nature of ratchet jumps causes the colloidal particles to move on a different path in \mathcal{A} during the forward and backward modulation loop. The reason for this is that the forward loop $\tilde{\mathcal{L}}_C$ uses a south traveling path crossing an upper type fence \mathcal{F}^{3r} and a north traveling path crossing a lower type fence. When $\tilde{\mathcal{L}}_C$ is played forward the colloid travels the first half adiabatically from $\mathbf{x}_{A,1}$ toward $\mathbf{x}_{A,2}$ since the modulation path enters the southern excess region and upper type fence crossings support motion on the 12-network. The second half of $\tilde{\mathcal{L}}_C$ must bring the particle back to $\mathbf{x}_{A,1}$. However, adiabatic motion with lower type fence crossing paths is possible only on the 31-network and our particle is currently at $\mathbf{x}_{A,2}$ that is not part of this network. Hence the particle performs a ratchet

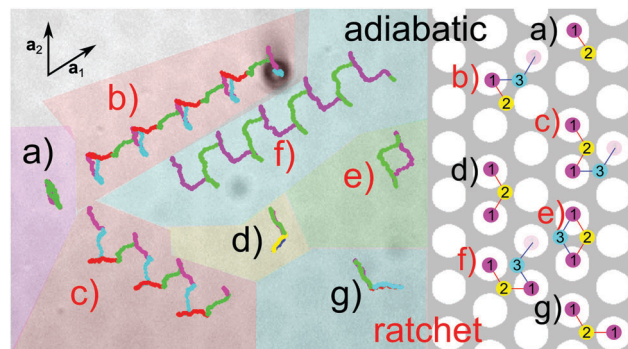


Fig. 21 Experimental trajectories of paramagnetic colloidal particles in action space \mathcal{A} above a C_6 -symmetric pattern. The trajectories are caused by various zero homotopic palindrome modulation loops $\mathcal{L}_C = \downarrow \mathcal{F}^{3r} \uparrow s \downarrow s \uparrow \mathcal{F}^{3r}$ with (a) $s = \mathcal{F}^{1l}$, (b) $s = \mathcal{F}_1^1$, (c) $s = \mathcal{F}_r^1$, (d) $s = \mathcal{F}^{2l}$, (e) $s = \mathcal{F}_i^2$, (f) $s = \mathcal{F}_r^2$, and (g) $s = \mathcal{F}^{2r}$. The paths in \mathcal{A} are colored according to the four paths of the modulation loop as indicated by the squares in the phase diagram Fig. 15. In the cases (a, d and g) the motion is adiabatic and the colloidal path in \mathcal{A} consists of two forward paths that coincide with the backward path. The case (e) corresponds to a time reversible ratchet with a zero homotopic path in \mathcal{A} . However the colloid is moving on different forward and backward paths that belong to two different networks indicated to the right. The other cases (b, c and f) are non time reversible ratchets where the zero homotopic modulation loops in \mathcal{C} induce non-zero homotopic (open) paths of the colloids in \mathcal{A} . The predicted paths between the high symmetry points for all loops are shown to the right. Video clips of the motion of the paramagnetic colloidal particle caused by the loops in (b, d and e), are provided in ref. 45.

jump back toward $\mathbf{x}_{A,1}$. When $\tilde{\mathcal{L}}_C$ is played backward the particle adiabatically moves from $\mathbf{x}_{A,1}$ toward $\mathbf{x}_{A,3}$ and jumps back *via* a ratchet jump. The full palindrome loop hence visits the high symmetry points in the sequence: $\mathbf{x}_{A,1}$, $\mathbf{x}_{A,2}$, $\mathbf{x}_{A,1}$, $\mathbf{x}_{A,3}$, $\mathbf{x}_{A,1}$. For time reversal ratchets the colloidal particle returns to its initial position after the full modulation loop \mathcal{L}_C , however by using a backward path in \mathcal{A} different from the forward path. Such a time reversible ratchet path is shown in Fig. 21e. In general palindrome modulation loops cause non-time reversal ratchet motion. The particle does not return to its initial position after a complete modulation loop but is transported by one unit vector. Three non-time reversible ratchet paths of this type are shown in Fig. 21b, c, and f.

The characteristics of the adiabatic and ratchet motion can also be inferred without looking at the differences between the forward and backward paths in \mathcal{A} . We measure the speed \dot{s}_A of the colloids in \mathcal{A} versus the normalized path length s_C of the modulation loop. We parametrize the forward modulation loop $\tilde{\mathcal{L}}_C$ from 0 to 2π and the backward loop $\tilde{\mathcal{L}}_C^{-1}$ from 2π to 0 such that the path length s_C in Fig. 22 runs back and forth between 0 and 2π . Ratchet loops can be distinguished from adiabatic loops by the ratchet jumps that have a significantly higher speed than the adiabatic motion. These jumps occur during the second half (magenta) of the forward and the second half (green) of the backward modulation when the modulation hits the fences and leaves the southern excess region in \mathcal{C} . There are also smaller maxima in the speed of the adiabatic motion when the beads pass the gates. The increased gate speed is a result of

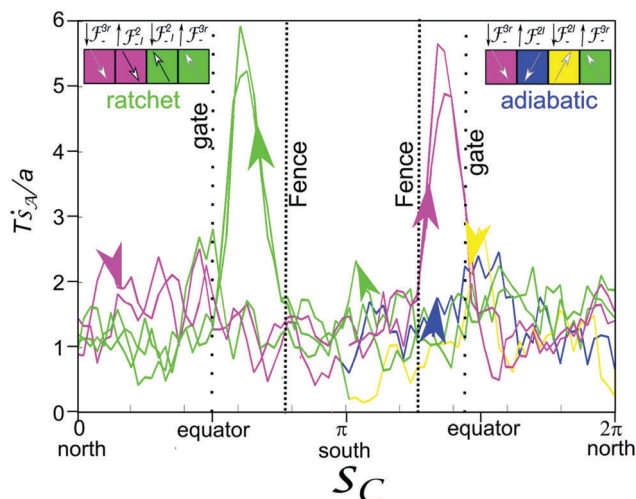


Fig. 22 Speed \dot{s}_A in \mathcal{A} of the colloidal motion induced by the palindrome modulation loop (d) and (e) of Fig. 21. The speed is normalized by the lattice constant a and the period T of one sub loop. It is plotted against the normalized path length s_C of the modulation in \mathcal{C} ranging from 0 to 2π for the forward modulation and from 2π to 0 for the backward modulation. Ratchet jumps in the ratchet modulation loop (maximum speed) occur in the second half of the forward (magenta maximum) and backward path (green maximum) when the modulation loop leaves the southern excess region in \mathcal{C} via the fence. Also the adiabatic speed profile (magenta/blue/yellow/green modulation, (d) in Fig. 21) exhibits maxima when the modulation crosses the gates. But they are clearly smaller than the maxima of the ratchet jumps.

the way that curves which are passing the gates in \mathcal{M} are projected into \mathcal{A} and \mathcal{C} . The projections are causing a maximum in the conversion of the speed in action space versus the speed in control space at the gate. In our special case the gates seem to be located less polar than the fences, which contradicts the theoretical predictions for the C_6 -symmetric case but is in accordance with theoretical predictions for weakly broken C_6 -symmetry.

We are hence able to independently characterize the type of motion and the particular path taken by the colloids. Both the experimentally determined types of motion as well as the directions are in perfect agreement with the theoretically predicted phase diagram (Fig. 15) for the C_6 -like case.

For the S_6 -like case we also observe adiabatic and ratchet motion in topological agreement to the theory. However, we did not succeed in finding palindrome loops causing non-time reversible ratchets as predicted by the theory and simulations. Instead, we observe that loops, which are supposed to induce non time reversal ratchets, cause the coexistence of time reversible ratchets with different directions above different unit cells. The directions thereby correspond to either the theoretically predicted forward or backward direction.

5.8 Experiments on the S_6 - C_6 -topological transition

To illustrate the S_6 - C_6 -topological transition we produced lithographic patterns with a slowly varying pattern phase $\phi(x)$. This continuously converts a C_6 pattern into a S_6 pattern within a spacial range of approximately 20 unit cells. In Fig. 23 we

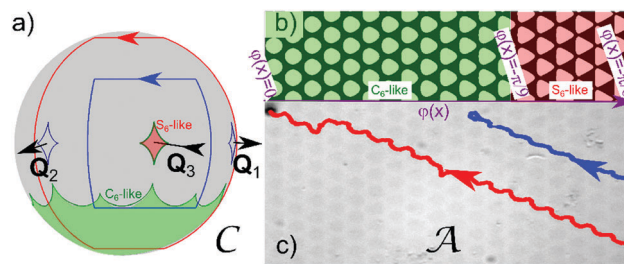


Fig. 23 Motion of colloids in a phase gradient pattern. (a) Control space with two modulation loops (blue and red) circulating around $-Q_3$. We have plotted the relevant excess satellite regions of the S_6 -symmetric case (red area) and the excess region of the C_6 -symmetric case (green area). (b) Scheme of the slowly varying phase pattern. The pattern is C_6 -like to the left and S_6 -like to the right. (c) Experimental trajectories of paramagnetic particles induced by the two modulation loops. Both loops encircle the S_6 -symmetric satellite excess region and thus induce transport on the S_6 -like pattern. The blue modulation loop barely touches the C_6 -like fence in \mathcal{C} which destroys the motion of the corresponding particle when it reaches C_6 -like territory. The red loop in contrast fully enters the southern C_6 -symmetric excess region in control space and leaves it only once. Therefore the red trajectory persists well in to the C_6 -like territory. A video clip of the motion of the paramagnetic colloidal particle is provided in ref. 45.

show the motion of paramagnetic particles on such a phase gradient pattern induced by two different modulation loops (blue and red) encircling the $-Q_3$ point. Both loops induce transport on the S_6 -like pattern. However as the phase of the pattern declines towards zero (the phase of the C_6 -pattern) the encircled satellite excess region of control space moves out of the blue loop such that the motion ceases beyond the critical phase $\phi < \phi_c = \pi/9$. The blue loop then touches the southern fence of the C_6 -symmetric pattern, which is no longer sufficient to induce transport on the C_6 -like pattern. The red loop fully crosses the southern fences of the C_6 -symmetric pattern. Therefore the motion of the particle persists as it enters C_6 -like territory in action space \mathcal{A} . The direction of transport is thereby topologically protected over the transition.

Upon the transition between S_6 and C_6 also the state of networks available for transport changes. While in the C_6 -like pattern the 12- and the 31-networks are active the first one is switched off in a S_6 -like pattern and only the 31-network is available for transport (see Fig. 16). To experimentally demonstrate this we apply a double loop of the type $\mathcal{L}_C = \mathcal{L}_C^{12} \mathcal{L}_C^{31}$ with $\mathcal{L}_C^{12} = \downarrow \mathcal{F}_{-r}^2 \uparrow \mathcal{F}_{-r}^1$ a fundamental loop passing through the lower fence segments (blue loop) and $\mathcal{L}_C^{31} = \downarrow \mathcal{F}_{-r}^2 \uparrow \mathcal{F}_{-r}^1$ (red loop) a fundamental loop passing through upper fence segments of the C_6 -symmetric case as shown in Fig. 24d. For the C_6 -like patterns the theory predicts an alternating use of the 12-network and the 31-network. The overall transport direction is the same for both fundamental loops. The same double loop converts into a $\mathcal{L}_C = \downarrow g_-^2 \uparrow g_-^1 \downarrow g_-^2 \uparrow g_-^1$ loop for the S_6 -like case where transport is only possible on the 31-network. In Fig. 24a and b we show the motion subject to this modulation loop on the C_6 -like and the S_6 -like patterns, respectively. Clearly the motion of the paramagnetic particle on the C_6 -like pattern makes use of the 12- and the 31-network. We observe an alternating

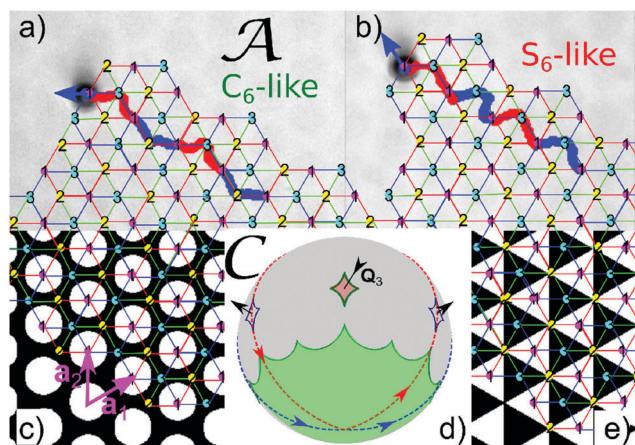


Fig. 24 Motion of paramagnetic colloids on (a) a C_6 symmetric pattern (scheme in (c)) and (b) a S_6 symmetric pattern (scheme in (e)). The particles are subject to a modulation double loop $\mathcal{L}_C = \mathcal{L}_C^{12} \mathcal{L}_C^{31}$ with $\mathcal{L}_C^{12} = \downarrow \mathcal{F}_{-r}^2 \uparrow \mathcal{F}_{-r}^1$ (blue loop) and $\mathcal{L}_C^{31} = \downarrow \mathcal{F}_{-r}^2 \uparrow \mathcal{F}_{-r}^1$ (red loop) crossing different segments of the C_6 -fence. (d) Control space with the combined modulation loop consisting of two fundamental loops (blue and red) which are both encircling the S_6 -symmetric excess region. We have plotted the relevant excess regions of the S_6 -symmetric ($\phi = -\pi/6$) case (red area) and the C_6 -symmetric case (green area). The induced motion on a C_6 -symmetric pattern is shown in (a). Both sub-loops induce motion on different networks resulting in a trajectory that alternately uses the 12 and the 31 network. In the S_6 -symmetric pattern only the 31-network is active. Therefore the induced motion shown in (b) has to use the 31-network during both sub-loops.

transport over these two networks. On the S_6 -like pattern transport happens *via* the 31-network only. The motion is again topologically protected in the direction, *i.e.* the modulation that before enforced the use the other network now also has to use the 31-network into the same direction.

6 Discussion

We have seen that most of the theoretically predicted features are experimentally robust. This ensures that colloids elevated only a few microns above the pattern behave pretty much the same way as predicted for universal potentials. The few deviations of experiment and theory can mostly be attributed to non-universal proximity effects. These arise from larger reciprocal lattice vectors contributing to the colloidal potential. We have shown, however, that higher reciprocal lattice vectors change the position of certain transport direction transitions, but not the topology of the problem as long as their influence is not too strong. Experimental proofs for proximity effects have been shown at different elevations for the two-fold symmetric problem. These effects will of course also play a role on lattices of higher symmetry and for non-symmetric magnetic lattices where such symmetry is broken by higher reciprocal lattice vector contributions. For the higher symmetric patterns we did not discuss these effects in detail and minimized them by performing experiments at sufficient elevation above the pattern. However, they are still visible in some experimental features. In the four-fold symmetric experiments for example the fence point is not a point but a finite area. Modulation loops must wind around this

larger area instead of winding around the theoretical point and hence modulation loops can not be chosen arbitrarily small to cause adiabatic transport.

The Bravais lattice of any periodic pattern has inversion symmetry and thus C_2 symmetry. Filling the unit cell of such a Bravais lattice with a magnetization pattern that has no net magnetic moment will generate a Fourier series that has contributions from Fourier coefficients at the non zero reciprocal lattice vectors. The contributions from the shortest reciprocal lattice vectors will always have one of the universal rotation symmetries. The symmetry can be broken by higher order reciprocal lattice vectors. The magnetic field contribution to a reciprocal lattice vector decays in the z -direction with the magnitude of the reciprocal lattice vectors, which is the reason why every transport at sufficient elevation of the order of the period will have exactly the characteristics of one of the patterns described in this paper. The transport remains topologically protected also for the symmetry broken case when the breaking of the symmetry is not too strong. There will be a topological transition to a non-transport regime for any type of pattern if one places the colloids close enough to the pattern. There might be other topological transport modes for symmetry broken patterns at intermediate elevation. These however are not universal as they will depend on all details of the pattern, field strength *etc.*

A difference between experiment and theory that cannot be explained with non universal proximity effects is the absence of non time reversible ratchets in the three-fold symmetric S_6 -like case. There instead of non time reversible ratchets we observed the coexistence of time reversible ratchets of different direction above different unit cells of the pattern. We attribute those effects to the noise of the magnetic patterns. Presumably the net magnetization of each unit cell does not vanish as required by eqn (6), but acquires values that might differ from one unit cell to the next. A non vanishing magnetization acts like an additional external field in the z -direction and therefore shifts the satellites to the north or to the south. We may see the effect of magnetization noise for the simple example of an additional staggered magnetization alternating between positive and negative values in neighboring unit cells. The staggered magnetization doubles the unit cell and therefore also doubles the length of the fence. Each satellite becomes a double satellite around which the fence circles twice. When we increase the magnitude of the staggered magnetization one half of the double satellite moves north while the other half moves south (see Fig. 25). Let us consider a modulation loop segment (red) that passes the unsplit double satellite on opposing segments. We expect this loop to induce a non time reversal ratchet. When the satellite splits the modulation loop segment will eventually pass the upper half of the double satellite south of the two \mathcal{B}_- bifurcation points and the lower half north of the other two \mathcal{B}_- bifurcation points. This, however, will now cause time reversible ratchets into different directions on one and the other half of the larger unit cell. This is exactly what we observe in the experiments, however, of course not in the simple staggered way predicted by our simplified period doubled theory.

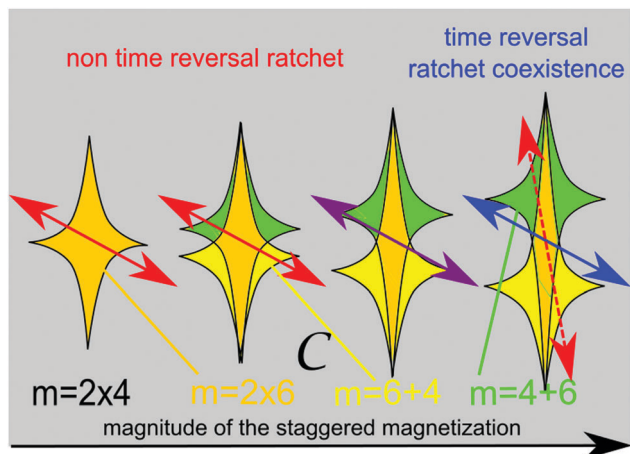


Fig. 25 Splitting of a satellite when switching on a staggered magnetization that doubles the period, doubles the fence and doubles the multiplicity m . The net magnetization of the two new different half unit cells shifts one half of the satellite fence to the north and the other half to the south. As a result a path that initially passed the fences on opposite sides of the satellites (red arrow) now cuts the northern (southern) half of the double satellites on the neighboring southern (northern) fence segments (blue arrow). Instead of a non time reversal ratchet this produces time reversible ratchets with different directions in one and the other new half unit cell.

In Fig. 22 we measured the speed of adiabatically moving colloidal particles. Gates in control space can then be identified by the location of the maximum speed in \mathcal{A} . The experiments measured the positions of the extremum segments of the gates to lie in the $m = 4$ region, while the theory of the C_6 symmetric case predicts that they lie inside of the excess area in \mathcal{C} . We have already mentioned that there might be a mismatch between the phase of the lithographic mask and the phase of the actual pattern. Indeed the lithographic writing process presumably produces a magnetization pattern with a phase that differs from the desired phase. A phase that is slightly different from the C_6 -symmetry would allow for gates in the tropics of \mathcal{C} and hence explain the observed deviation. Since the exact path of the gate on \mathcal{M} is a feature that is not topologically robust it is conceivable that either the phase shift or proximity effects might cause this discrepancy.

To achieve adiabatic transport our modulation loops in control space must be modulated at an angular frequency ω_{ext} that is significantly smaller than the intrinsic angular frequency $\omega_{\text{int}} \propto e^{-Qz}M$. For the lithographic magnetic patterns this restricts our modulation frequencies to $\omega_{\text{ext}} \approx 0.1$ Hz. For useful applications one would have to improve the saturation magnetization or the thickness of the lithographic patterns to increase the modulation frequency. The garnet films we used for the two-fold stripe pattern as well as for experiments on C_6 -like patterns in ref. 20 allowed for the use of up to two orders of magnitude higher modulation frequencies. The closer the particles are to the pattern the faster we might modulate the field, however, the less universal will be the behavior of the transport. An elevation of roughly half the lattice constant seems to be a good compromise that does not yet change the topology of the transport.

We describe our ratchet as a deterministic ratchet, *i.e.* thermal diffusion of particles only happens during very short and therefore irrelevant times when the colloidal particles sit right on the fence. This short diffusion will not lead to a broadening distribution of transport directions as long as we avoid the \mathcal{B}_0 points. When using modulation loops passing close to a \mathcal{B}_0 point the particles may access the two alternative paths of steepest descent also in the surroundings of this point. Thermal effects broaden the fences. A transition to a thermal ratchet will occur for temperatures where the broadened fences overlap. Some of the topological properties might persist even then and thus also explain the omni-directional transport observed in such thermal ratchets.²⁸

Comparing our system with topological crystalline insulators^{4–9} we note that the gates in our system are the analogues to the Dirac-cones in the quantum systems. Gates are lying on high symmetry points in the lattices with even C_4 , and C_6 symmetries, while they lie on the ij -network for the three-fold symmetric lattices. The situation is comparable to the position of Dirac-cones lying on high symmetry points and lines in the first Brillouin zone of the lattices of different symmetry. As in topological crystalline insulators their number and robustness varies based on the symmetry of the lattice.

Comparing our driven system with Floquet topological quantum systems^{10,11} we note that time dependent interactions of Floquet topological insulators usually must wind around the north–south axis to cause topologically non trivial behavior. This is because the unperturbed time independent Hamilton operator is diagonalized with respect to the z -component of the spin respectively pseudo spin operator. Different time dependent driving, such as THz-oscillating magnetic fields, stress modulation, or modest in plane electric field modulations⁵³ are experimental ways to achieve non trivial behavior. Only perturbations that have non commuting contributions of non-diagonalized spin components will couple the different bands and cause non trivial dynamics. Floquet topological insulators so far have been investigated mainly with respect to time reversal symmetry and particle hole symmetry protecting the topology. We are not aware of a crystalline Floquet topological insulator, which would be the quantum system in closest analogy to our system. Due to the lattice symmetry in our colloidal system we have a variety of different axes around which the perturbing external field may be wound. The reason for this is the multi-fold lattice symmetry that causes multiple stable points in the absence of a perturbing external field. In contrast to the quantum systems we have a richer variety of driving loops that can wind around alternative points of control space.

We should also mention that the dynamics of our colloidal system occurs in direct space not in reciprocal space. Direct space is an affine lattice having no natural origin. Each unit cell is equivalent to any other unit cell. Floquet topological quantum systems operate in reciprocal space where we can distinguish the first Brillouin zone from all the higher order Brillouin zones. For example in a hexagonal lattice the Γ -point in reciprocal space plays a different role than the K -points, while in our affine three-fold lattice all high symmetry points are equivalent and cause

lattice symmetries to have different effects in our colloidal system than in quantum systems.

Finally our system is dissipative causing irreversible relaxation processes to contribute to the dynamics. These irreversible processes can be rendered unimportant only on the stationary manifold *via* the adiabatic driving, but not on the paths of steepest descent. This is causing the non-time reversible ratchet processes that have no analogue in the topological quantum systems.

7 Conclusions

Paramagnetic and diamagnetic colloids above a magnetic pattern can be transported by modulating the potential with time dependent homogeneous external fields. If such modulation loops wind around specific points (fence points for the two- and four-fold symmetries, bifurcation points for the three- and six-fold symmetry) or pass through fence segments (three- and six-fold symmetry) in control space the topologically trivial modulation can be translated into non trivial motion of colloids. A summary of the relevant points and segments is shown as stereographic projection of control space for lattices of C_2 , C_4 , S_6 -like, and C_6 -like symmetry in Fig. 26. It shows the deep connection between symmetry and topology since all objects are completely different for the various symmetries. The lattice symmetry determines the transport modes, which are possible along the primitive lattice vectors.

Modulation loops can be sorted into topologically equivalent classes, according to their winding around those points and/or by the sequence of segment crossings. All modulation loops

belonging to the same class induce motion in the same direction, which makes the transport very robust against perturbations. Noise in the pattern only affects the less robust features of the transport while it doesn't alter its topological class.

On top of C_2 - and the C_4 -symmetric patterns para- and diamagnets are adiabatically transported into the same direction. In contrast above 3-fold and 6-fold symmetric patterns both types of particles can be transported into independent directions and the motion happens either adiabatically or *via* irreversible ratchets.

Classes of modulation loops causing transport modes into one direction cluster around the adiabatic paths. Ratchet modulation loops are topological protected by their neighboring adiabatic loops and hence transport into the same direction. The whole variety of possible transport is described by a set of topological invariants, which are winding numbers around the holes of the stationary surfaces \mathcal{M} .

The robustness of the topological transport can be used to transport a collection of colloids with a broad distribution of properties, such as size-polydispersity without dispersion. This is a clear advantage over other collective transport methods such as thermal ratchets, external gradients and active motion. The possibility of independent motion of paramagnets and diamagnets facilitates other applications such as guiding chemical reactions and assembly.²⁰

A Appendix

A.1 Three fold symmetric stationary manifolds

In Fig. 27–31 we give a high resolution view of \mathcal{C} , \mathcal{A} , and \mathcal{M} of the three-fold symmetric patterns at five different values of ϕ , where we explain specific details in one of the figures each. These details apply to all different phases if not stated otherwise. The positions of the six gates in each space is explained in Fig. 27 and remains the same throughout the rest of the figures. In Fig. 28 we show the color coding of the areas in \mathcal{C} as well as the color coding shared between \mathcal{M} and \mathcal{A} . The poles of \mathcal{C} have 2×6 preimages in \mathcal{M} that all lie on the central axis of \mathcal{M} either on a pole of a hemispherical cap or at the apex or base of the three central holes. When projecting \mathcal{M} into \mathcal{A} the poles on the hemispheres fall onto the three-fold symmetric points of \mathcal{A} , while the saddle point poles of \mathcal{M}_0 in the three central holes are expelled in the surroundings of $\mathbf{x}_{\mathcal{A},2}$. The topological transition happens in Fig. 27. Two \mathcal{B}_0 bifurcation points (pseudo bifurcation points) one from a satellite and one from a polar fence (polar pseudo fence) annihilate when the satellite excess area coalesces with the polar excess area at the ends of the full (dashed) arrows. Since only the lower half of \mathcal{M} is projected into \mathcal{A} there occur two cuts in the brown and red tropical regions of \mathcal{M}_0 . The cut in \mathcal{M} and its projection into \mathcal{A} is shown in Fig. 31. The cut in \mathcal{A} circles twice around $\mathbf{x}_{\mathcal{A},2}$ and around $\mathbf{x}_{\mathcal{A},3}$ and twists each of the six times it passes a gate thereby alternating between the lower half lying inside and outside the cut. The cuts in the other figures are topologically equivalent to those in Fig. 31. The projection of areas in \mathcal{M} into \mathcal{C} preserves the

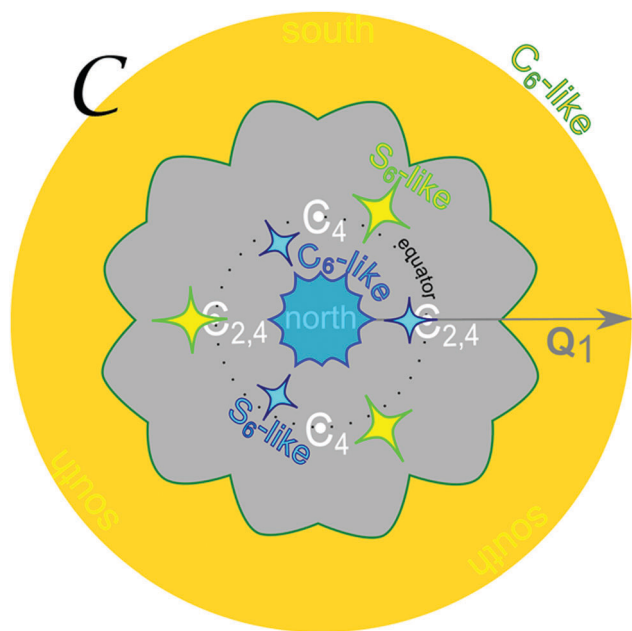


Fig. 26 Stereographic projection of control space with all relevant objects for the lattices of different symmetry. White circles are relevant for both paramagnets and diamagnets while green fences are relevant for the paramagnets only and blue fences are relevant for diamagnets only.

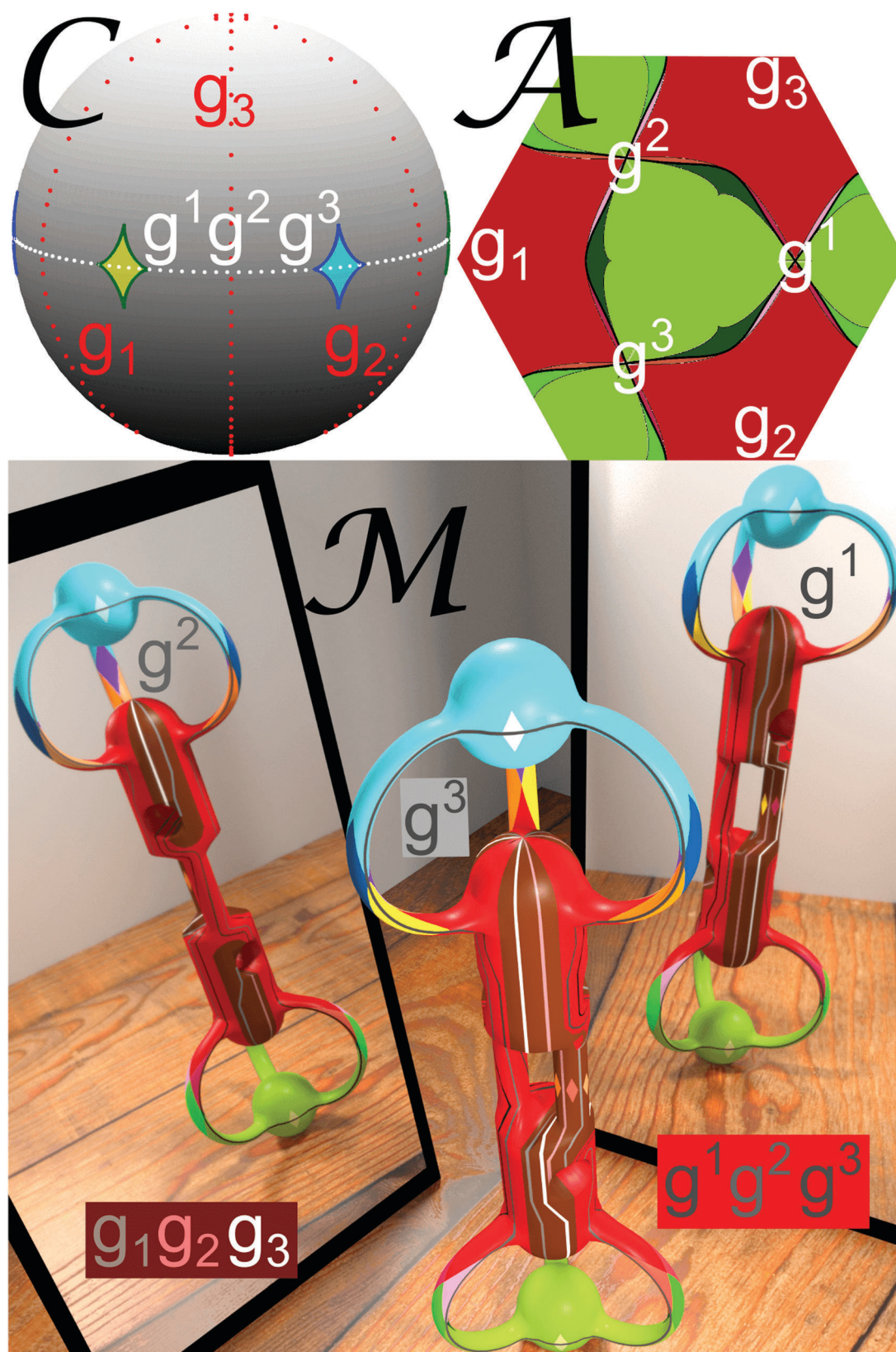


Fig. 27 Universal topology of \mathcal{C} , \mathcal{A} and \mathcal{M} for a pattern with S_6 symmetry ($\phi = \pi/6$). We have marked the six gates $g_1, g_2, g_3, g_1^1, g_2^1, g_3^1$ that are projected into the six gate points in \mathcal{A} . On \mathcal{M} the upper gates g_1^1, g_2^1, g_3^1 travel on the handles while the lower gates g_1, g_2, g_3 pass through polar regions that will become isolated in the S_6 -like case.

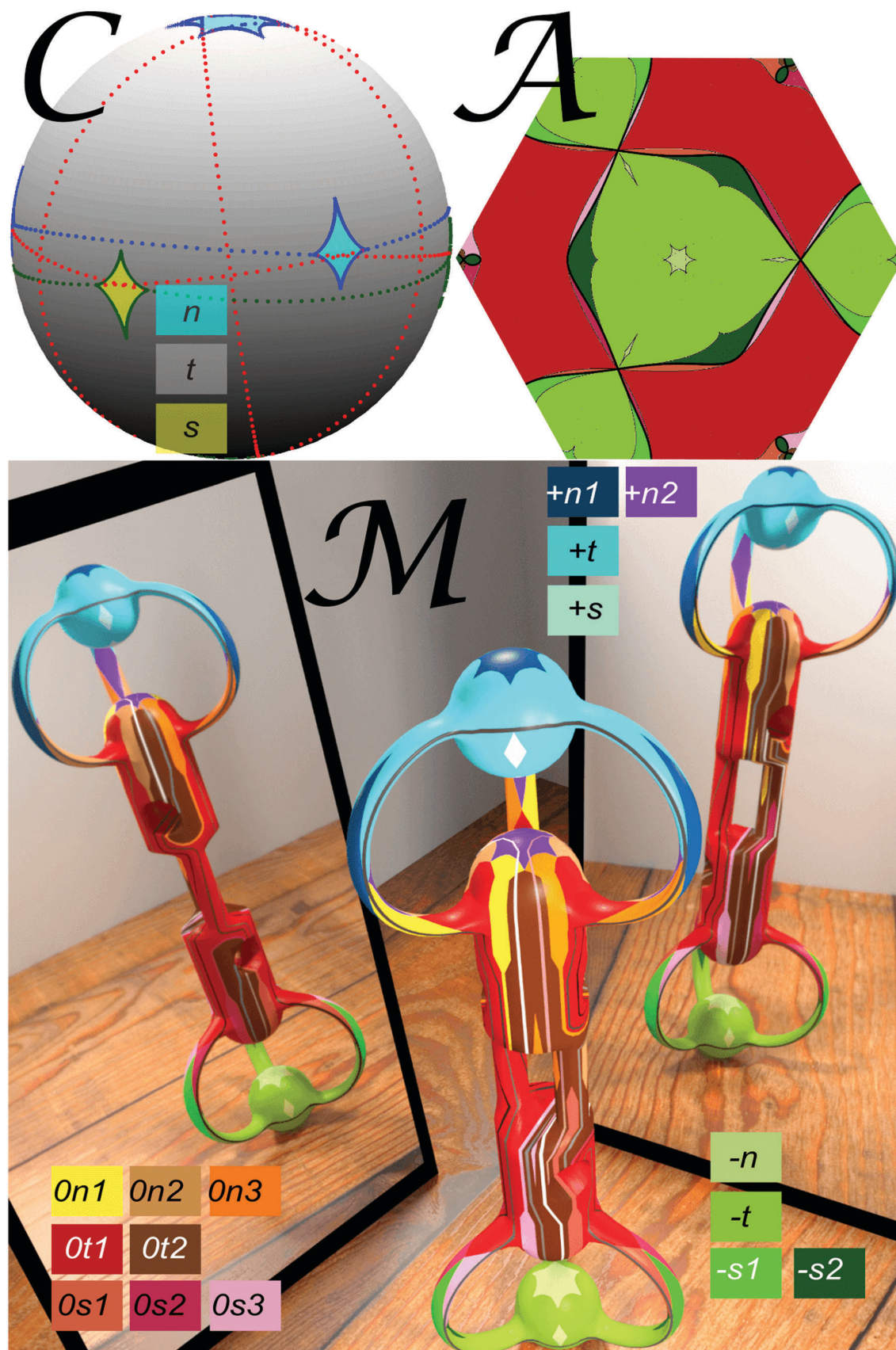


Fig. 28 Universal topology of \mathcal{C} , \mathcal{A} and \mathcal{M} for a pattern with S_6 -like symmetry ($\phi = 5\pi/36$) together with color codes for the areas of \mathcal{C} and the shared color codes of \mathcal{M} and \mathcal{A} . The coloring of the gates is the same as in Fig. 27.

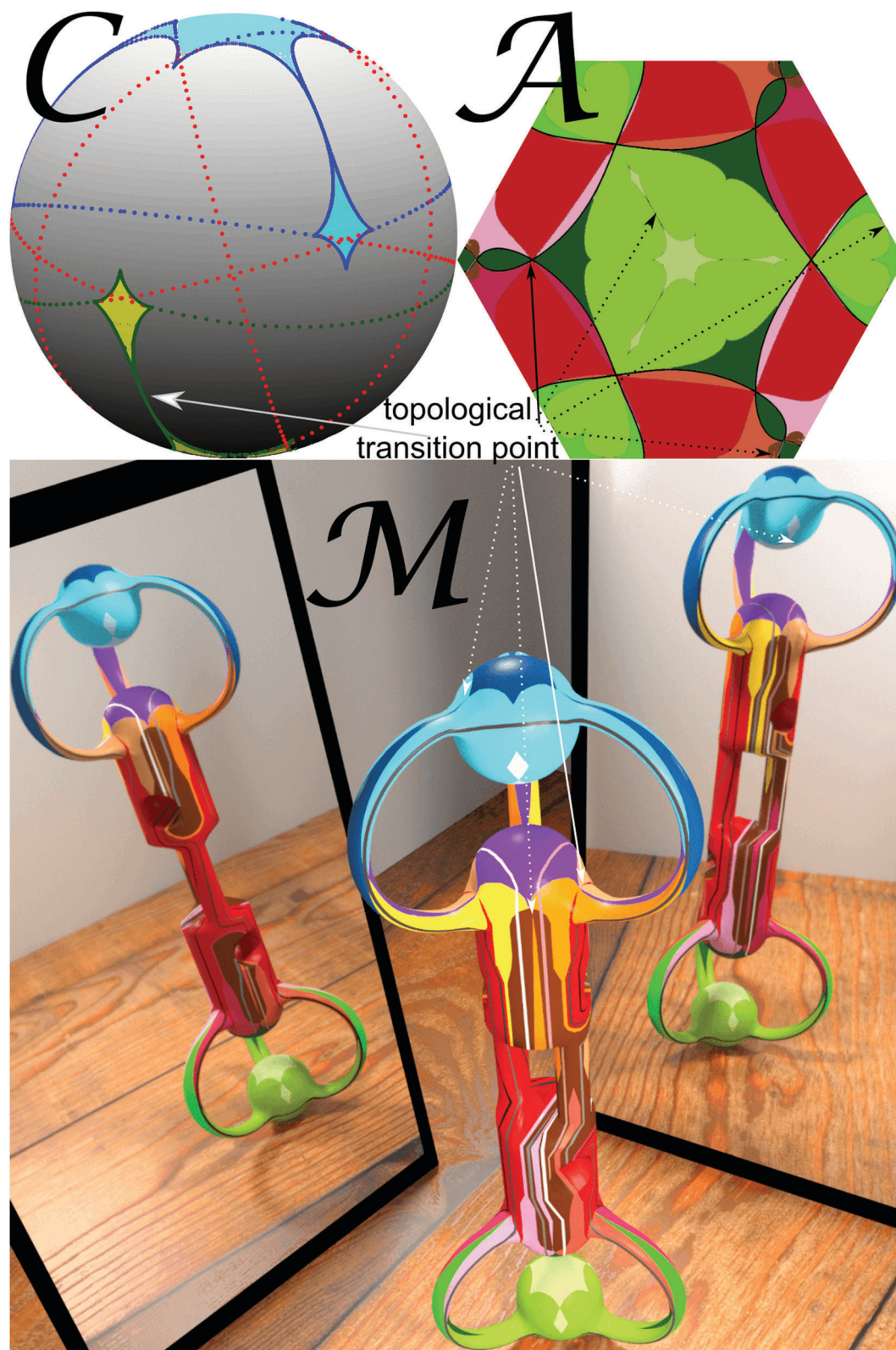


Fig. 29 Universal topology of \mathcal{C} , \mathcal{A} and \mathcal{M} for a pattern at the transition from S_6 -like to C_6 -like symmetry ($\phi_c = \pi/9$) with gates colored similar to Fig. 27. Two B_0 (pseudo) bifurcation points from two (pseudo) fences annihilate at the topological transition points at the solid (dashed) arrows where the satellites merge with the polar excess areas.

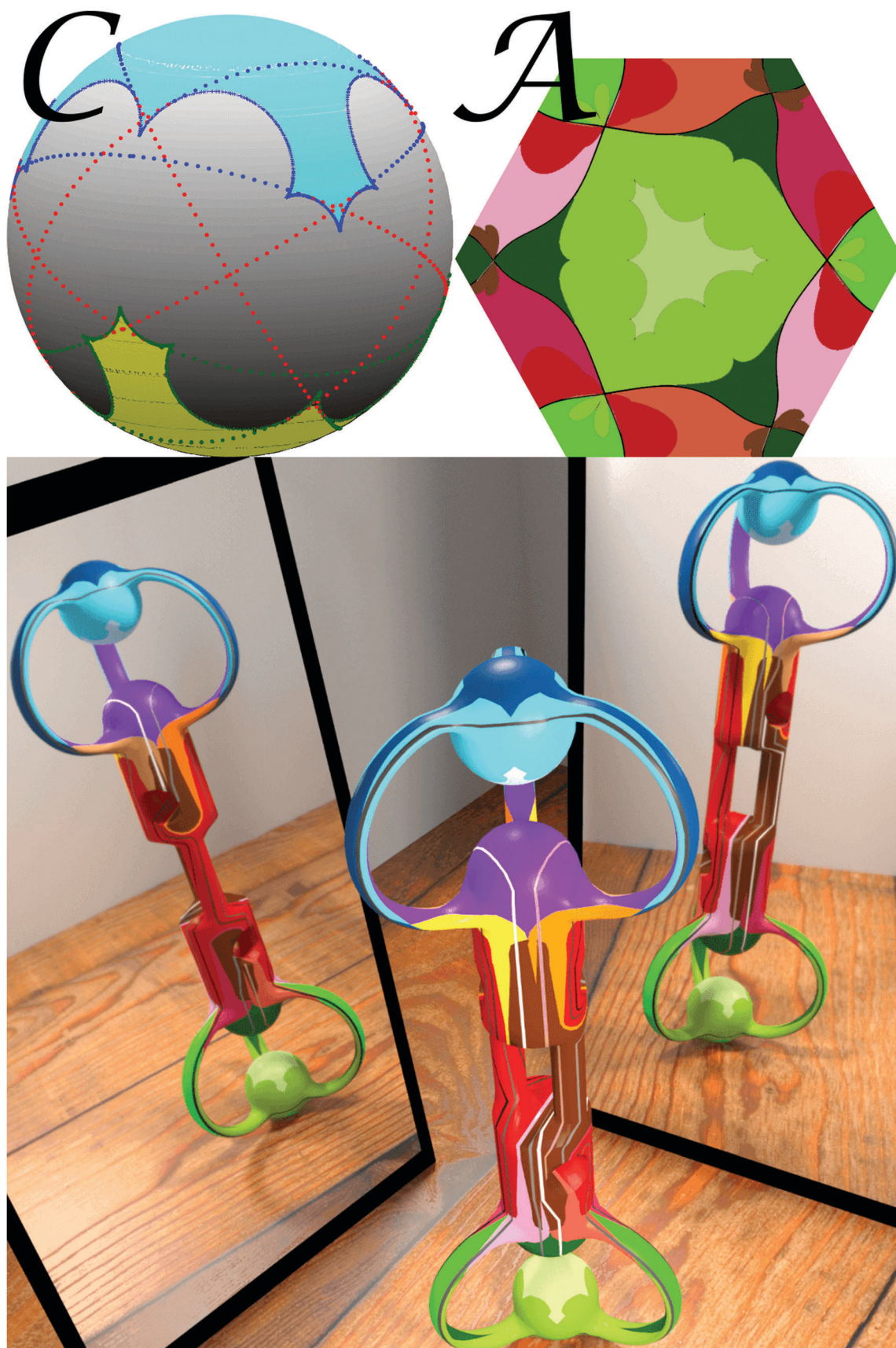


Fig. 30 Universal topology of \mathcal{C} , \mathcal{A} and \mathcal{M} for a pattern with C_6 -like symmetry ($\phi = \pi/18$).

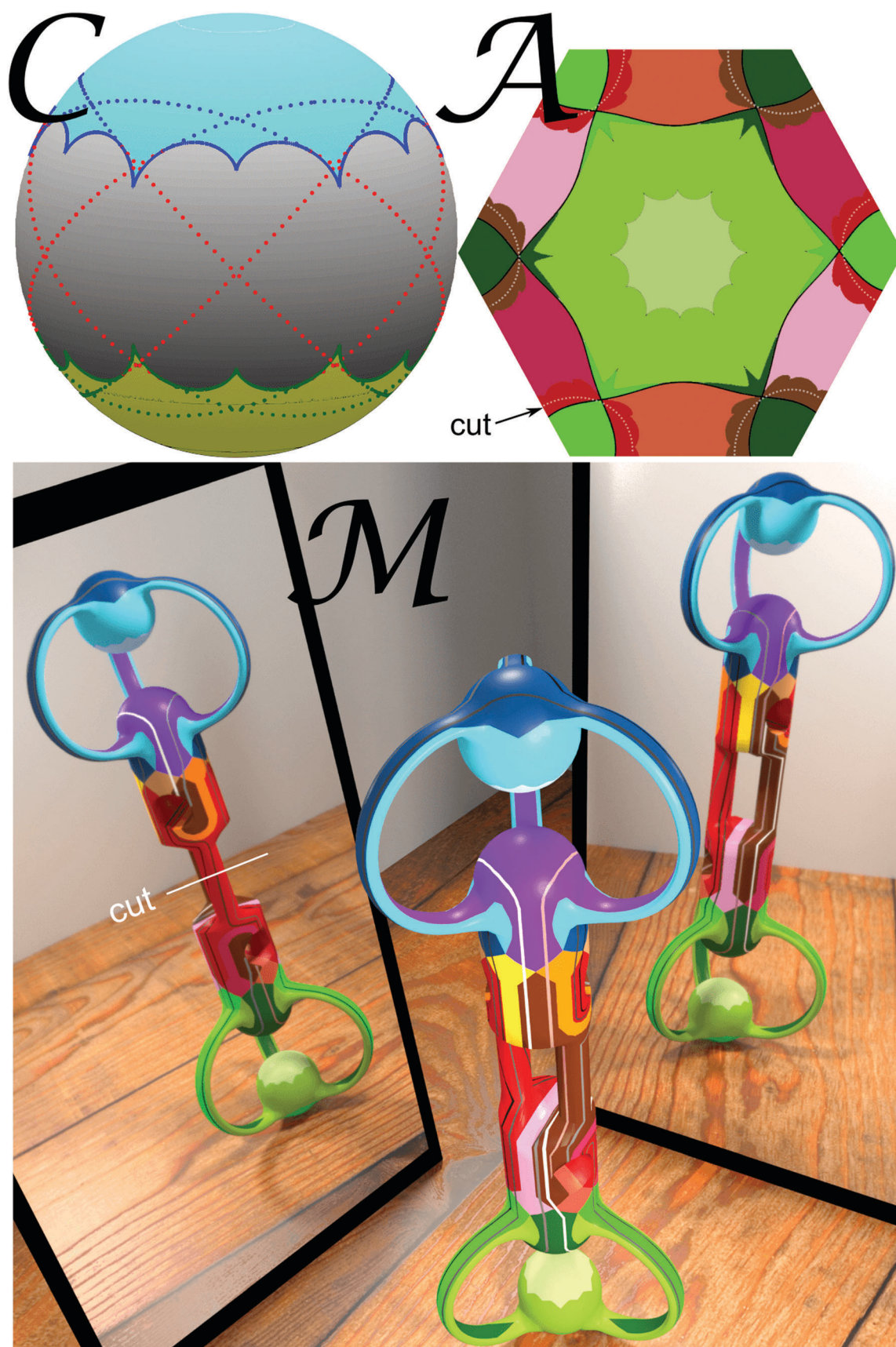


Fig. 31 Universal topology of \mathcal{C} , \mathcal{A} and \mathcal{M} for a pattern with C_6 symmetry ($\phi = 0$). We have marked the cut in \mathcal{A} that is the projection of the boundary between the projected lower half of \mathcal{M} and the upper half.

orientation of half the areas and switches sign for the others. Each time one passes a pseudo fence that is connected to a bifurcation point one switches the orientation of the projection in \mathcal{C} . The orientation of the projection from \mathcal{M} into \mathcal{A} switches sign when we pass from one side of the gate to the other side. The southern excess region south of the gates g_{i-}^j (g_{i-}) in \mathcal{C} switches orientation when its preimages in \mathcal{M}_- are mapped into the bright (dark) green regions around $\mathbf{x}_{A,3}$ (around $\mathbf{x}_{A,2}$) in \mathcal{A} .

A.2 Lithographic magnetic structures

Magnetic patterns with the desired symmetry have been created by 10 keV He-ion bombardment induced magnetic patterning of magnetic multilayer structures with perpendicular magnetic anisotropy^{49,54} using a home-built ion source for 5–30 keV He ions.⁵⁵ First, the layer system $\text{Ti}^{4\text{nm}}/\text{Au}^{60\text{nm}}/[\text{Co}^{0.7\text{nm}}/\text{Au}^{1\text{nm}}]_5$ with M_s of 1420 kA m^{-1} was fabricated by DC magnetron sputter deposition on a silicon substrate.^{56,57} The sample's magnetic properties were characterized by polar magneto-optical Kerr effect magnetometry, possessing an initial coercive field of $19.5 \pm 0.5 \text{ kA m}^{-1}$. The magnetic domain structure was introduced by a local change of the sample's coercive field *via* 10 keV He ion bombardment through a shadow mask with an ion fluency of 1×10^{15} Ions per cm^2 . Here, the geometry of the mask coincides with the desired four-fold symmetric, three-fold symmetric, or phase gradient pattern with a period length of $7 \mu\text{m}$ (Fig. 2). The mask locally prevents the He ions to penetrate into the layer system.⁵⁴ In the uncovered areas, however, ion bombardment leads to a decrease of the perpendicular magnetic anisotropy and hence, the coercive field, primarily due to defect creation at the interfaces of the [Co/Au] multilayer structure.^{48,50} In preliminary experiments, the decrease of the coercive field was characterized *via* polar magneto-optical Kerr effect magnetometry and determined to be $6.5 \pm 0.5 \text{ kA m}^{-1}$. The shadow mask was prepared *via* UV lithography on top of the sample. For this purpose, the sample was first spin coated with a photo-resist layer of AZ nLOF 2070 (MicroChemicals, AZ nLOF 2070 diluted with AZ EBR, ratio 4 : 1) with an average layer thickness of $2 \mu\text{m}$ as determined from atomic force microscopy measurements. The lithographic structure was introduced by UV exposure through a structured chromium hard mask and subsequent development in AZ 826 MIF (MicroChemicals) to remove the unexposed parts of the resist. After ion bombardment without external magnetic fields applied during the process, the sample was first treated with 1-methyl-2-pyrrolidone for 24 h at $80 \text{ }^\circ\text{C}$, than ultrasonicated for 1 minute and finally cleaned with acetone and isopropanol. Due to the thickness $t = 3.5 \text{ nm}$ of the magnetic layer, which is small in comparison to the wavelength of our structures ($tQ < 1$), the pattern magnetic field on top of the lithographic pattern is attenuated to $H^P = M_s \cdot t \cdot Q$ in comparison to the value $H^P = M_s$ of a thick ($tQ > 1$) garnet film.

A.3 Definitions

Action space: the plane $z = \text{const}$, where the colloidal particles move. Due to the periodicity different unit cells can be identified with each other which folds action space into a torus.

Adiabatic motion: a motion enslaved by the external modulation, possible when one preimage in \mathcal{M} of a modulation loop in \mathcal{C} lies in \mathcal{M}_- .

Allowed regions: projection of the minimum/maximum sections of \mathcal{M} into \mathcal{A} .

Bifurcation points: bifurcation points on \mathcal{M} and on \mathcal{A} are crossings of fences with pseudo fences. In \mathcal{C} the bifurcation points are cusps of the fence. Bifurcation points exist for the three- and six-fold pattern not for the two- and four-fold pattern.

Control space: the endpoints of the external magnetic field of constant magnitude, a sphere.

Equator: the boundary between the two hemispheres in control space excluding fence points. The equators in \mathcal{M} are the preimages of the equator in \mathcal{C} of the projection from \mathcal{M} onto \mathcal{C} . The equators are relevant for the two-fold pattern, where there are no gates.

Excess area: a connected set of points in \mathcal{C} with higher multiplicity.

Fence: the fence in \mathcal{M} is the boundary between minima (or maxima) and the saddle points on \mathcal{M} . We use the same names for its projection into control and action space. Fences on \mathcal{M} and on the torus \mathcal{A} are closed lines. Fences on \mathcal{C} are points for the two- and four-fold symmetric pattern and lines for the three- and six-fold symmetric pattern.

Forbidden regions: projection of the saddle point regions of \mathcal{M} into \mathcal{A} . Allowed and forbidden regions are disjunct areas in \mathcal{A} for all but the two-fold patterns.

Gates: a gate in \mathcal{A} is a crossing point of two fences in \mathcal{A} . Gates exist for the three-, four-, and six-fold pattern not for the two-fold pattern. The preimage in \mathcal{M} of a gate in \mathcal{A} of the projection from $\mathcal{C} \otimes \mathcal{A}$ onto \mathcal{A} is the gate (a closed line) on \mathcal{M} . The projection of the gate in \mathcal{M} onto \mathcal{C} is the gate in \mathcal{C} . A gate in \mathcal{C} is a grand circle.

Irrelevant fence: a fence that has no \mathcal{B}_+ and no \mathcal{B}_- bifurcation points.

Lemniscate: a preimage in \mathcal{M} of a modulation loop in \mathcal{C} that is not a set of loops in \mathcal{M} .

Modulation loop: a loop in \mathcal{C} .

Multiplicity: the multiplicity of a point $H_{\text{ext}} \in \mathcal{C}$ is the number of preimages $(H_{\text{ext}}, x_A) \in \mathcal{M} \subset \mathcal{C} \otimes \mathcal{A}$ mapped from \mathcal{M} onto $H_{\text{ext}} \in \mathcal{C}$ by the projection onto control space.

Non-time reversible ratchet: a ratchet motion that follows an open path when playing a palindrome modulation loop.

Northern hemisphere: the northern hemisphere are simply connected regions on \mathcal{C} and on \mathcal{M} with $H_{z,\text{ext}} > 0$. A similar definition holds for the southern hemisphere.

Palindrome modulation loop: a loop in \mathcal{C} consisting of two loops that are the inverse of each other.

Path: a path is a directed segment of a modulation loop.

Phase space the (multiply connected) product space of control space and action space and thus the product of a sphere and a torus.

Pseudo bifurcation points: pseudo bifurcation points in \mathcal{M} are preimages of the bifurcation points in \mathcal{C} that are not bifurcation points. Pseudo bifurcation points exist in three- and six-fold symmetric patterns. Pseudo bifurcation points in \mathcal{A} are

the projection of the pseudo bifurcation points in \mathcal{M} . Pseudo bifurcation points in \mathcal{M} and in \mathcal{A} are located at cusps of the pseudo fences.

Pseudo fence: a line in \mathcal{M} different from the fence in \mathcal{M} that is projected onto the fence in \mathcal{C} . Pseudo fences are closed lines in \mathcal{M} and \mathcal{A} that exist for the three- and six-fold symmetric pattern not the universal two- and four-fold symmetric pattern.

Ratchet motion: a motion where the adiabatic motion is interrupted by jumps following the intrinsic dynamics.

Reduced control space: the cut of control space with the space spanned by the single reciprocal lattice vector \mathbf{Q}_1 of the two-fold pattern and the normal vector \mathbf{n} .

Satellites: excess areas for the S_6 -like pattern that merge with their polar parent excess area upon the topological transition to a C_6 -like pattern.

Stationary manifold: a two dimensional manifold in phase space, where the action gradient of the colloidal potential vanishes.

Time reversible ratchet: a ratchet motion that follows a closed path when playing a palindrome modulation loop.

12-Network: the three-fold symmetric pattern has three different points per unit cell with three-fold rotation symmetry. The straight lines between the first two points define the 12-network. Similar definitions hold for the 23-network and the 31-network.

Acknowledgements

J. B and A. T. acknowledge support by a Ghana MOE – DAAD joined fellowship and a University of Kassel PhD fellowship respectively.

References

- M. Z. Hasan and C. L. Kane, Colloquium: topological insulators, *Rev. Mod. Phys.*, 2010, **82**, 3045–3067.
- S.-Q. Shen, *Topological insulators: Dirac equation in condensed matters*, Springer Science, and Business Media (2013).
- C.-K. Chiu, J. C. Y. Teo, A. P. Schnyder and S. Ryu, Classification of topological quantum matter with symmetries, *Rev. Mod. Phys.*, 2016, **88**, 035005.
- L. Fu, Topological crystalline insulators, *Phys. Rev. Lett.*, 2011, **106**, 106802.
- T. H. Hsieh, H. Lin, J. Liu, W. Duan, A. Bansil and L. Fu, Topological crystalline insulators in the SnTe material class, *Nat. Commun.*, 2012, **3**, 982.
- P. Dziawa, B. J. Kowalski, K. Dybko, R. Buczko, A. Szczerbakow, M. Szot, E. Lusakowska, T. Balasubramanian, B. M. Wojek, M. H. Berntsen, O. Tjernberg and T. Story, A topological crystalline insulator states in $\text{Pb}_{1-x}\text{Sn}_x\text{Se}$, *Nat. Mater.*, 2012, **11**, 1023–1027.
- R.-J. Slager, A. Mesaros, V. Juricic and J. Zaanen, The space group classification of topological band-insulators, *Nat. Phys.*, 2013, **9**, 98–102.
- X.-J. Liu, J. J. He and K. T. Law, Demonstrating lattice symmetry protection in topological crystalline superconductors, *Phys. Rev. B: Condens. Matter Mater. Phys.*, 2014, **90**, 235141.
- G. van Miert, C. M. Smith and C. Morai, Dirac cones beyond the honeycomb lattice: a symmetry-based approach, *Phys. Rev. B: Condens. Matter Mater. Phys.*, 2016, **93**, 035401.
- T. Kitagawa, E. Berg, M. S. Rudner and E. Demler, Topological characterization of periodically driven quantum systems, *Phys. Rev. B: Condens. Matter Mater. Phys.*, 2010, **82**, 235114.
- M. S. Rudner, N. H. Lindner, E. Berg and M. Levin, Anomalous Edge States and the Bulk-Edge Correspondence for Periodically Driven Two-Dimensional Systems, *Phys. Rev. X*, 2013, **3**, 031005.
- D. Thouless, M. Kohmoto, M. P. Nightingale and M. den Nijs, Quantized Hall Conductance in a Two-Dimensional Periodic Potential, *Phys. Rev. Lett.*, 1982, **49**, 405–408.
- C. L. Kane and T. C. Lubensky, Topological boundary modes in isostatic lattices, *Nat. Phys.*, 2014, **10**, 39–45.
- J. Paulose, B. G. Chen and V. Vitelli, Topological modes bound to dislocations in mechanical metamaterials, *Nat. Phys.*, 2015, **11**, 153–156.
- M. C. Rechtsman, J. M. Zeuner, Y. Plotnik, Y. Lumer, D. Podolsky, F. Dreisow, S. Nolte, M. Segev and A. Szameit, Photonic Floquet topological insulators, *Nature*, 2013, **496**, 196–200.
- L. M. Nash, D. Kleckner, A. Read, V. Vitelli, A. M. Turner and W. T. M. Irvine, Topological mechanics of gyroscopic metamaterials, *Proc. Natl. Acad. Sci. U. S. A.*, 2015, **112**, 14495–14500.
- M. Xiao, G. Ma, Z. Yang, P. Sheng, Z. Q. Zhang and C. T. Chan, Geometric phase and band inversion in periodic acoustic systems, *Nat. Phys.*, 2015, **11**, 240–244.
- S. D. Huber, Topological mechanics, *Nat. Phys.*, 2016, **12**, 621–623.
- A. Murugan and S. Vaikuntanathan, Topologically protected modes in non-equilibrium stochastic systems, *Nat. Commun.*, 2017, **8**, 13881.
- J. Loehr, M. Loenne, A. Ernst, D. de las Heras and Th. M. Fischer, Topological protection of multiparticle dissipative transport, *Nat. Commun.*, 2016, **7**, 11745.
- D. de las Heras, J. Loehr, M. Loenne and Th. M. Fischer, Topologically protected colloidal transport above a square magnetic lattice, *New J. Phys.*, 2016, **18**, 105009.
- C. J. Olson, C. Reichhardt and F. Nori, Nonequilibrium dynamic phase diagram for vortex lattices, *Phys. Rev. Lett.*, 1998, **81**, 3757–3760.
- C. Reichhardt and F. Nori, Phase locking, devil's staircases, Farey trees, and Arnold tongues in driven vortex lattices with periodic pinning, *Phys. Rev. Lett.*, 1999, **82**, 414–417.
- A. B. Kolton, D. Domínguez and N. Grønbech-Jensen, Mode locking in ac-driven vortex lattices with random pinning, *Phys. Rev. Lett.*, 2001, **86**, 4112–4115.
- P. T. Korda, M. B. Taylor and D. G. Grier, Kinetically locked-in colloidal transport in an array of optical tweezers, *Phys. Rev. Lett.*, 2002, **89**, 128301.

- 26 T. Bohlein, J. Mikhael and C. Bechinger, Observation of kinks and antikinks in colloidal monolayers driven across ordered surfaces, *Nat. Mater.*, 2012, **11**, 126–130.
- 27 M. Ghodbane, E. C. Stucky, T. J. Maguire, R. S. Schloss, D. I. Shreiber, J. D. Zahn and M. L. Yarmush, Development and validation of a microfluidic immunoassay capable of multiplexing parallel samples in microliter volumes, *Lab Chip*, 2015, **15**, 3211–3221.
- 28 A. V. Arzola, M. Villasante-Barahona, K. Volke-Sepúlveda, P. Jákl and P. Zemánek, Omnidirectional Transport in Fully Reconfigurable Two Dimensional Optical Ratchets, *Phys. Rev. Lett.*, 2017, **118**, 138002.
- 29 H. Loewen, Particle-resolved instabilities in colloidal dispersions, *Soft Matter*, 2010, **6**, 3133–3142.
- 30 M. Driscoll, B. Delmotte, M. Youssef, S. Sacanna, A. Donev and P. Chaikin, Unstable fronts and motile structures formed by microrollers, *Nat. Phys.*, 2017, **13**, 375–379.
- 31 J. E. Martin and K. J. Solis, Fully alternating, triaxial electric or magnetic fields offer new routes to fluid vorticity, *Soft Matter*, 2015, **11**, 241–254.
- 32 P. Tierno, T. H. Johansen and Th. M. Fischer, Localized and delocalized motion of colloidal particles on a magnetic bubble lattice, *Phys. Rev. Lett.*, 2007, **99**, 038303.
- 33 P. Tierno, S. V. Reddy, M. G. Roper, T. H. Johansen and Th. M. Fischer, Transport and separation of biomolecular cargo on paramagnetic colloidal particles in a magnetic ratchet, *J. Phys. Chem. B*, 2008, **112**, 3833–3837.
- 34 M. P. N. Juniper, A. V. Straube, R. Besseling, D. G. A. Aarts and R. P. A. Dullens, Microscopic dynamics of synchronization in driven colloids, *Nat. Commun.*, 2015, **6**, 7187.
- 35 P. Tierno and A. V. Straube, Transport and selective chaining of bidisperse particles in a travelling wave potential, *Eur. Phys. J. E: Soft Matter Biol. Phys.*, 2016, **39**, 54.
- 36 C. R. Doering, W. Horsthemke and J. Riordan, Nonequilibrium fluctuation-induced transport, *Phys. Rev. Lett.*, 1994, **72**, 2984–2987.
- 37 M. N. Popescu, C. M. Arizmendi, A. L. Salas-Brito and F. Family, Disorder induced diffusive transport in ratchets, *Phys. Rev. Lett.*, 2000, **85**, 3321–3324.
- 38 P. Reimann, Brownian motors: noisy transport far from equilibrium, *Phys. Rep.*, 2002, **361**, 57–265.
- 39 S. Savelév, F. Marchesoni and F. Nori, Stochastic transport of interacting particles in periodically driven ratchets, *Phys. Rev. E: Stat., Nonlinear, Soft Matter Phys.*, 2004, **70**, 061107.
- 40 S. Köhler, J. Lehmann and P. Hänggi, Driven quantum transport on the nanoscale, *Phys. Rep.*, 2005, **406**, 379–443.
- 41 N. A. Sinitsyn, The stochastic pump effect and geometric phases in dissipative and stochastic systems, *J. Phys. A: Math. Theor.*, 2009, **42**, 193001.
- 42 L. Gao, M. A. Tahir, L. N. Virgin and B. B. Yellen, Multiplexing superparamagnetic beads driven by multi-frequency ratchets, *Lab Chip*, 2011, **11**, 4214–4220.
- 43 A. H. Bobeck, P. I. Bonyhard and J. E. Geusic, Magnetic bubbles—an emerging new memory technology, *Proc. IEEE*, 1975, **63**, 1176–1195.
- 44 B. D. Terris and T. Thomson, Nanofabricated and self-assembled magnetic structures as data storage media, *J. Phys. D: Appl. Phys.*, 2005, **38**, R199–R222.
- 45 Videos adfigure4.avi, adfigure10c.avi, adfigure11.avi, adfigure17b.avi, adfigure18b.avi, adfigure19.avi, adfigure20.avi, adfigure21b.avi, adfigure21d.avi, adfigure21e.avi, adfigure23.avi and adfigure24.avi corresponding to Fig. 4, 10c, 11, 17b, 18b, 19, 20, 21b, d, e, 23 and 24 are shown free of charge in the ESI†.
- 46 I. Bauer and F. Catanese, Generic lemniscates of algebraic functions, *Math. Ann.*, 1997, **307**, 417–444.
- 47 A. Jarosz, D. Holzinger, M. Urbaniak, A. Ehresmann and F. Stobiecki, Manipulation of superparamagnetic beads on patterned Au/Co/Au multilayers with perpendicular magnetic anisotropy, *J. Appl. Phys.*, 2016, **120**, 084506.
- 48 C. Chappert, H. Bernas, J. Ferré, V. Kottler, J.-P. Jamet, Y. Chen, E. Cambril, T. De-volder, F. Rousseaux, V. Mathet and H. Launois, Planar patterned magnetic media obtained by ion irradiation, *Science*, 1998, **280**, 1919–1922.
- 49 P. Kuświk, A. Ehresmann, M. Tekielak, B. Szymański, I. Sveklo, P. Mazalski, D. Engel, J. Kisielewski, D. Lengemann, M. Urbaniak, C. Schmidt, A. Maziewski and F. Stobiecki, Colloidal domain lithography for regularly arranged artificial magnetic out-of-plane monodomains in Au/Co/Au layers, *Nanotechnology*, 2011, **22**, 095302.
- 50 M. Urbaniak, P. Kuświk, Z. Kurant, M. Tekielak, D. Engel, D. Lengemann, B. Szymański, M. Schmidt, J. Aleksiejew, A. Maziewski, A. Ehresmann and F. Stobiecki, Domain-Wall Movement Control in Co/Au Multilayers by He⁺-Ion-Bombardment-Induced Lateral Coercivity Gradients, *Phys. Rev. Lett.*, 2010, **105**, 067202.
- 51 Let \mathbf{v}_0 be an eigen vector of the Hesse matrix to the eigen value zero, i.e. $\nabla_{\mathcal{A}} \nabla_{\mathcal{A}} U^* \cdot \mathbf{v}_0 = 0$. Then a point on the fence in $\mathcal{C} \otimes \mathcal{A}$ is a bifurcation point if it fulfills eqn (18) and (19) and the condition $(\mathbf{v}_0 \cdot \nabla_{\mathcal{A}})^3 U^* = 0$.
- 52 A. P. Ramirez, Geometrical frustration in magnetism, *Annu. Rev. Mater. Sci.*, 1994, **24**, 453–480.
- 53 N. H. Lindner, G. Refael and V. Galitski, Floquet topological insulator in semiconductor quantum wells, *Nat. Phys.*, 2011, **7**, 490–495.
- 54 A. Ehresmann, I. Koch and D. Holzinger, Manipulation of Superparamagnetic Beads on Patterned Exchange-Bias Layer Systems for Biosensing Applications, *Sensors*, 2015, **15**, 28854.
- 55 D. Lengemann, D. Engel and A. Ehresmann, Plasma ion source for *in situ* ion bombardment in a soft X-ray magnetic scattering diffractometer, *Rev. Sci. Instrum.*, 2012, **83**, 053303.
- 56 M. Tekielak, R. Gieniusz, M. Kisielewski, P. Mazalski, A. Maziewski, V. Zablotkii, F. Stobiecki, B. Szymański and R. Schäfer, The effect of magnetostatic coupling on spin configurations in ultrathin multilayers, *J. Appl. Phys.*, 2011, **110**, 043924.
- 57 J. Quispe-Marcato, B. Pandey, W. Alayo, M. A. de Sousa, F. Pelegrini and E. Baggio Saitovitch, Preferential orientation of magnetization and interfacial disorder in Co/Au multilayers, *J. Magn. Magn. Mater.*, 2013, **344**, 176–181.

Publication 2

Topological protection of multiparticle dissipative transport

Nature Communications, **7**, 11745 (2016)

Johannes Loehr^{a1}, Daniel de las Heras^{a2}, Adrian Ernst^{a2}, Michael
Lönne^{a3} and Thomas M. Fischer^{a1}

^{a1} Experimental Physics, ^{a2} Theoretical Physics, and ^{a3} Mathematics, Faculty of Physics, Mathematics
and Computer Science, University of Bayreuth, 95447 Bayreuth, Germany.

My Contribution

I designed the modulation loops and performed and analyzed all experiments. Thomas Fischer and myself conducted the scientific discussion and developed the topological framework with the help of Michael Lönne. The manuscript was written by me, Daniel de las Heras and Thomas Fischer.

Note: The experiments on the independent transport directions of paramagnetic and diamagnetic particles and the measurement on the topological transition were already presented in my master thesis. However, all considerations were significantly extended by a new theoretical framework and further experiments.

ARTICLE

Received 24 Nov 2015 | Accepted 27 Apr 2016 | Published 1 Jun 2016

DOI: 10.1038/ncomms11745

OPEN

Topological protection of multiparticle dissipative transport

Johannes Loehr¹, Michael Loenne², Adrian Ernst³, Daniel de las Heras³ & Thomas M. Fischer¹

Topological protection allows robust transport of localized phenomena such as quantum information, solitons and dislocations. The transport can be either dissipative or non-dissipative. Here, we experimentally demonstrate and theoretically explain the topologically protected dissipative motion of colloidal particles above a periodic hexagonal magnetic pattern. By driving the system with periodic modulation loops of an external and spatially homogeneous magnetic field, we achieve total control over the motion of diamagnetic and paramagnetic colloids. We can transport simultaneously and independently each type of colloid along any of the six crystallographic directions of the pattern via adiabatic or deterministic ratchet motion. Both types of motion are topologically protected. As an application, we implement an automatic topologically protected quality control of a chemical reaction between functionalized colloids. Our results are relevant to other systems with the same symmetry.

¹Experimentalphysik, Institutes of Physics and Mathematics, Universität Bayreuth, Universitätsstraße 30, Bayreuth 95440, Germany. ²Mathematik, Institutes of Physics and Mathematics, Universität Bayreuth, Bayreuth 95440, Germany. ³Theoretische Physik, Institutes of Physics and Mathematics, Universität Bayreuth, Bayreuth 95440, Germany. Correspondence and requests for materials should be addressed to T.M.F. (email: thomas.fischer@uni-bayreuth.de).

Topological invariants are global properties of a system that remain unchanged by local perturbations. A property that depends only on topological invariants is topologically protected and is very robust against local changes. Topological protection is a promising approach to stabilize quantum computing¹ and is used to, for example, maintain robust transport in Hamiltonian systems. Topologically required edge states² in a bulk system can support transport of quantum mechanical excitations³, classical mechanical solitons⁴, dislocations⁵ and gyroscopic waves⁶. When the edge states are located in a gap of the bulk excitation spectrum, they are protected against scattering into bulk states. Conservation of the Chern number, which is a topological invariant, makes the edge states robust against perturbative interactions. Topological insulators⁷, which are based on this concept, conduct at the surface but insulate in bulk. In driven Hamiltonian systems, additional invariants, such as the winding number^{8,9} around quasi energy bands, add to the topological variety of possible transport phenomena.

Transport of a collection of classical particles with different properties, such as size, mobility and so on, usually generates a diffuse broadening of the trajectories. Topological protection might be used to transport a broad distribution of particles without dispersion, despite their different properties. High precision multiparticle transport is an important ingredient in, for example, multifunctional lab-on-a-chip devices^{10,11}.

Topological protection is also possible in driven dissipative (non-Hamiltonian) systems. The interplay between dissipation and topology has been studied in open quantum systems, see for example refs 12,13 for details. In driven dissipative lattices^{14–18}, transport typically involves the thermal ratchet effect^{19–22}, that is, biased irreversible jumps between neighbouring potential wells. Complicated correlations between the noise²³, disorder²⁴ and many particle interactions²⁵ cause a motion of astonishing complexity. The thermal ratchet mechanism is not robust when transporting simultaneously different types of particles. The complexity makes it hard to maintain control over the transport of one type of particles when adjusting the external drive to control the transport of another particle type.

Here, we show an example of topological protection in a driven dissipative colloidal system. We achieve predictable multiparticle transport of diamagnetic and paramagnetic colloids above a

hexagonal magnetic lattice. Using periodic boundary conditions, we describe the unit cell of the lattice as a torus, which defines the action space in which the colloids move. We drive the colloids with periodic modulation loops of an external magnetic field. The direction of the external field defines our control parameter space. The topological correspondence between control and action space is nontrivial, and enables robust, topologically protected, colloidal transport along the lattice vectors. The topological invariant in action space is the set of the two winding numbers around the torus, in close analogy with driven quantum systems^{8,9}. We demonstrate experimentally the robustness of the motion and implement a topologically protected quality control of a chemical reaction between functionalized colloids. We also develop a theoretical framework that fully describes the experimental findings. Our results apply to any hexagonal pattern.

Results

Colloidal model system. We use paramagnetic polystyrene core shell and solid polystyrene colloids of average diameters 2.8 and 3.1 μm , respectively, dispersed in a mixture of diluted water-based ferrofluid. The immersion of the colloids renormalizes their effective susceptibilities such that $\chi_{p,\text{eff}} > 0$ and $\chi_{d,\text{eff}} < 0$ for paramagnetic and diamagnetic colloids, respectively. The colloids immersed in the ferrofluid are placed on top of a magnetically patterned ferrite garnet film (FGF), see Fig. 1a. Spacer beads and a top glass plate create a ferrofluid film of thickness $d = 4.8 \mu\text{m}$. Magnetic boundary conditions at the garnet-ferrofluid and glass-ferrofluid interfaces distort the magnetic field lines (created by the magnetic moments of the colloids) to be parallel to both interfaces. Virtual image dipoles form in the garnet film and the top glass plate and generate a potential that levitates the colloids into the mid-film plane, far away from the FGF, see Fig. 1b. Without the ferrofluid the colloids sediment to the pattern^{26,27}. The FGF is characterized by a hexagonal lattice of magnetic bubble domains magnetized normal to the film (saturation magnetization $M_s = 17 \text{ kA m}^{-1}$). The bubbles are immersed in a continuous phase of opposite magnetization. In an external field H_{ext}^z normal to the film, the bubbles grow on the expense of the continuous phase if $H_{\text{ext}}^z > 0$ and shrink if $H_{\text{ext}}^z < 0$.

Control space. We use a homogeneous time-dependent magnetic external field $\mathbf{H}_{\text{ext}}(t)$ of constant magnitude, $H_{\text{ext}} = 5 \text{ kA m}^{-1}$,

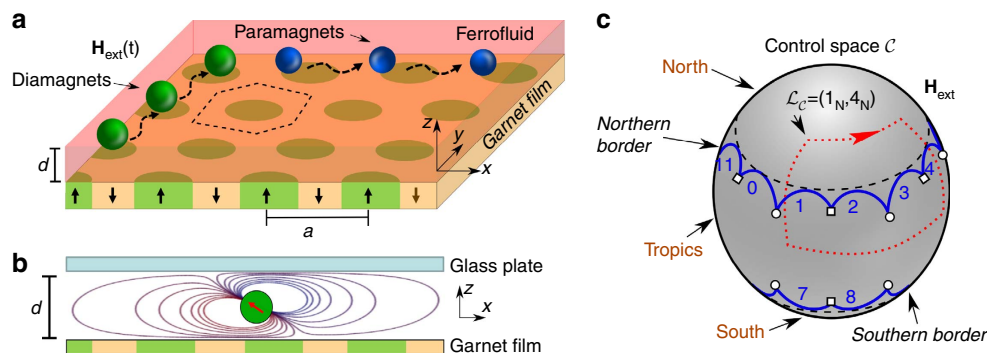


Figure 1 | Schematic of the system. (a) Hexagonal garnet film with lattice constant $a = 11.6 \mu\text{m}$ covered with ferrofluid of thickness $d = 4.8 \mu\text{m}$. One Wigner-Seitz unit cell is marked with a dashed line. By adjusting a closed modulation loop of a spatially homogeneous magnetic field $\mathbf{H}_{\text{ext}}(t)$, we have total control over the transport of paramagnetic (blue) and diamagnetic (green) colloids immersed into the ferrofluid. (b) Lateral view of the system showing the distortion of the dipolar magnetic field (the field of the garnet pattern is omitted here) of an individual particle immersed in ferrofluid. The field distortion pushes the colloidal particle into the midplane of the ferrofluid film. (c) The direction of \mathbf{H}_{ext} varies on the surface of a sphere, defining control space \mathcal{C} . Control space can be divided into three regions: the north, the tropics and the south. The northern and southern borders separate the tropics from the north and the south, respectively. Each border consists of 12 segments that we number from 0 to 11. The segments join at special points, indicated by empty circles and squares. \mathcal{L}_C is an example of a closed modulation loop of \mathbf{H}_{ext} that induces transport of diamagnetic particles along the lattice. The loop crosses the northern border through segments 1 and 4.

to drive the system. Hence, our control space \mathcal{C} is the surface of a sphere. Each point on \mathcal{C} corresponds to a direction of \mathbf{H}_{ext} . For reasons that will become clear later, we can divide \mathcal{C} in three regions: the north, the tropics and the south, see Fig. 1c. We call the interface between the tropics and the north (south) as the northern (southern) border. Each border is made of 12 segments. We experimentally perform periodic closed modulation loops \mathcal{L}_C of the external magnetic field. The period of the modulation is irrelevant provided that it is large enough such that the particles can follow the changes of the potential generated by \mathbf{H}_{ext} . There exist loops that induce intercellular colloidal transport. That is, when \mathcal{L}_C returns to its initial point, the colloids are not in their initial positions but on a different unit cell.

Experimental phase diagram. Only loops that cross the northern (southern) border of \mathcal{C} induce intercellular transport of the diamagnets (paramagnets). We discuss first the motion of the diamagnets. Let $\mathcal{L}_C = (i_N, j_N)$ be a loop in \mathcal{C} that crosses the i th segment of the northern border from the tropics to the north and returns to the tropics using the j th segment, see an example in Fig. 1c. The experimental phase diagram showing the motion of diamagnetic colloids for all possible modulation loops of type $\mathcal{L}_C = (i_N, j_N)$ is shown in Fig. 2a. The precise shape of the loop is irrelevant, a clear sign of the robustness of the transport. Only the segments of the northern border crossed by \mathcal{L}_C and their order is important. We can transport the diamagnets along the six fundamental lattice translations plus intracellular transport. Each direction is represented by a different colour in the phase diagram. The clustering of identical colours indicates the topological protection of the transport direction. A rotation of \mathcal{L}_C by $\pi/3$ around the polar axis, that is, from $\mathcal{L}_C = (i_N, j_N)$ to $\mathcal{L}_C = (i_N + 2, j_N + 2)$, is equivalent to rotate the sample by $-\pi/3$, and hence changes the transport direction by $\pi/3$. Therefore, the sixfold symmetry of the pattern guarantees that if transport is possible along one direction then it must also be possible in the other five directions.

There are two types of motion, adiabatic and deterministic ratchet moves. The phase diagram is a checkerboard of

alternating adiabatic- and ratchet-squares. In an adiabatic motion, the diamagnets always travel following the minimum generated by the magnetic potential. Hence, the speed of the modulation determines the speed of the colloids along the full trajectory. In contrast, the speed of the modulation loop does not fully determine the speed of the colloids in a ratchet. At some points during the modulation loop, the diamagnets hop between two minima of the magnetic potential at an intrinsic speed that is uncorrelated to the speed of the modulation.

The adiabatic motion is fully reversible. Reversing the modulation from $\mathcal{L}_C = (i_N, j_N)$ to $\mathcal{L}_C = (j_N, i_N)$ always reverts the direction of motion, and there is no hysteresis when comparing forward and backward trajectories of the colloids. For example, the loop $\mathcal{L}_C = (0_N, 4_N)$ transports the diamagnets adiabatically to the left, and the reverse loop $\mathcal{L}_C = (4_N, 0_N)$ to the right. In a deterministic ratchet motion, reversing the direction of the modulation loop does not usually revert the direction of the transported colloids. $\mathcal{L}_C = (0_N, 3_N)$, for example, induces a ratchet transporting the diamagnets to the left, but the reverse loop $\mathcal{L}_C = (3_N, 0_N)$ does not transport the particles to the right. Only some of the modulation loops induce a time reversal ratchet in which reversing the modulation also reverts the direction of motion. See for example, the loops $(0_N, 6_N)$ and $(6_N, 0_N)$ in Fig. 2a. There is always hysteresis in ratchet-like motion between forward and backward trajectories, even in the case of time reversal ratchets.

The dynamics we have discussed for the diamagnets on the northern border holds also for the paramagnets on the southern border of \mathcal{C} . The phase diagram of the paramagnets is the same as the one of the diamagnets, cf Fig. 2a, if instead of modulation loops of type $\mathcal{L}_C = (i_N, j_N)$ we perform modulation loops of type $\mathcal{L}_C = (i_S, j_S)$. That is, loops that cross the southern border of \mathcal{C} from the tropics to the south using segment i and back to the tropics through segment j . An implicit equation to compute the location of the borders is given in the Methods section, and the exact location of the borders is shown in Supplementary Fig. 1.

The northern and southern borders of \mathcal{C} are well separated. Hence, it is easy to transport the diamagnets and paramagnets

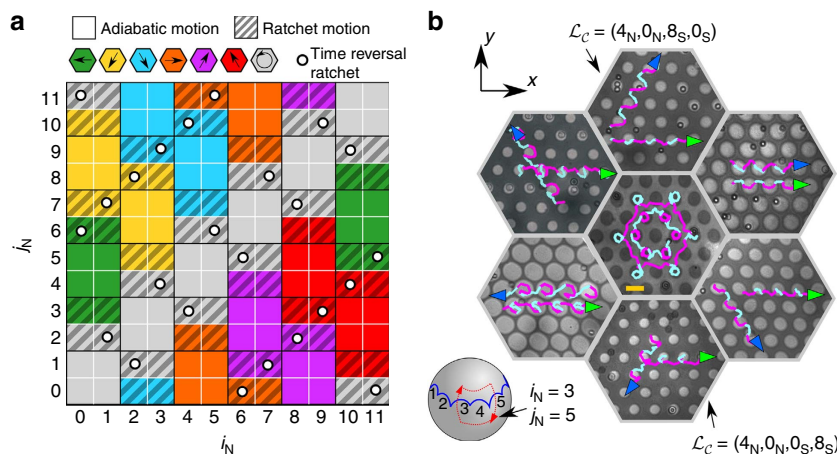


Figure 2 | Phase diagram and colloidal motion. (a) Experimental phase diagram showing the direction and type of motion of the diamagnets for the fundamental loops $\mathcal{L}_C = (i_N, j_N)$ crossing the northern border in \mathcal{C} . The same diagram holds for the paramagnets if the modulation loops cross the southern border: $\mathcal{L}_C = (i_S, j_S)$. Each colour corresponds to a direction of motion, as indicated. Non-textured squares indicate adiabatic motion, and striped textured squares indicate ratchet motion. Empty circles mark the time reversal ratchets. (b) Polarization microscopy images of the pattern and the diamagnetic and paramagnetic colloidal particles at the end of a transport process. Scale bar (yellow rectangle middle image), 10 μm . The path of one paramagnet (blue arrow) and one diamagnet (green arrow) in \mathcal{A} is depicted in the figure. The pink (cyan) segments of each path indicate the loop in \mathcal{C} is on the southern (northern) hemisphere. The outer images show the transport of diamagnets into the x direction and paramagnets into one of the six crystallographic directions, by using modulation loops of type $\mathcal{L}_C = (4_N, 0_N, i_S, j_S)$. The middle image is a Franconian folk dance performed by a paramagnetic and diamagnetic couple circulating around a central bubble in opposite sense and with different radius of the hexagon.

successively by using a loop $\mathcal{L}_C = (i_N, j_N, k_S, l_S)$. The loop starts on the tropics and goes to the north of \mathcal{C} crossing the segment i_N , then returns to the tropics (j_N) and moves to the south (k_S). It finally returns to the starting point on the tropics of \mathcal{C} crossing the segment l_S . In Fig. 2b, we show polarization microscopy images of the combined transport of six representative modulation loops of the form $\mathcal{L}_C = (4_N, 0_N, i_S, j_S)$. The loops induce adiabatic transport of diamagnets along the x -direction and adiabatic transport of paramagnets along the six possible lattice translations. The trajectories are coloured in pink (cyan) when \mathcal{L}_C travels on the northern (southern) hemisphere of \mathcal{C} .

We have total control over the colloidal motion, including the ability to programme complex trajectories. An example is given in the centre of Fig. 2b where we use a complex modulation loop such that the paramagnets and diamagnets perform a traditional Franconian folk dance. Videos showing the colloidal motion are provided in Supplementary Movies 1–7.

We next develop the theoretical framework needed to explain the experimental observations we have discussed above. An experimental application will be shown at the end of the Results section.

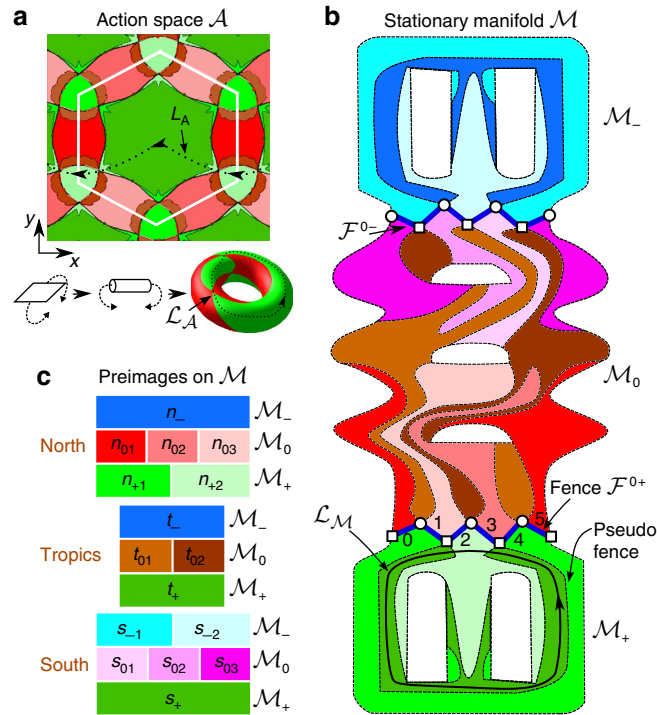


Figure 3 | Topology. (a) Action space \mathcal{A} is the space accessible to the colloids, a hexagonal lattice. Using periodic boundary conditions, action space is topologically a torus. (b) Two-dimensional projection of the stationary manifold \mathcal{M} , which has genus 7 and it is formed by 16 bijective areas indicated by different colours and listed in c. \mathcal{M}_+ , \mathcal{M}_0 and \mathcal{M}_- are the set of minima, saddle points and maxima of the magnetic potential, respectively. The fence \mathcal{F}^{0+} (\mathcal{F}^{0-}) separates \mathcal{M}_0 and \mathcal{M}_+ (\mathcal{M}_-), and it is projected onto the northern (southern) border of control space, cf. Fig. 1c. In b, empty squares (circles) on \mathcal{F}^{0+} are triple plus \mathcal{B}^+ (zero \mathcal{B}^0) bifurcation points, at which 4 bijective areas meet. Three out of these bijective areas lie on \mathcal{M}_+ (\mathcal{M}_0) in a \mathcal{B}^+ (\mathcal{B}^0) point. \mathcal{L}_M (b) is an example of a non-zero-homotopic loop that winds around the holes of \mathcal{M}_+ . The corresponding control loop is $\mathcal{L}_C = (1_N, 4_N)$. This loop in action space \mathcal{L}_A induces intercellular transport of the diamagnets along the $-x$ direction, black arrows in a. The colours in a show the projection of \mathcal{M}_+ and \mathcal{M}_0 onto action space.

Action space. We call the space accessible to the colloids the action space \mathcal{A} . Action space is a two-dimensional periodic hexagonal lattice at a fixed elevation above the FGF. Topologically \mathcal{A} is a torus if we use periodic boundary conditions at the edges of a unit cell of the lattice, see Fig. 3a. Intercellular transport from one unit cell to the next cell via one of the two lattice vectors in real space is the same as one of the two windings around the torus. Loops \mathcal{L}_A in \mathcal{A} that correspond to intercellular transport of colloids have non-zero winding numbers, and cannot be continuously deformed into a point. That is, lattice translation action loops are non-zero-homotopic. This is not the case in control space. Any modulation loop $\mathcal{L}_C \subset \mathcal{C}$ can be continuously deformed into any other desired modulation loop. For instance, we can continuously deform \mathcal{L}_C into a point on \mathcal{C} . Therefore, all loops in \mathcal{C} are zero-homotopic.

Here, we have demonstrated that there exist modulation loops \mathcal{L}_C in control space that induce either adiabatic or deterministic ratchet intercellular transport of the colloids. That is, there are zero-homotopic loops in \mathcal{C} that induce non-zero-homotopic action loops \mathcal{L}_A with non-vanishing winding number around the torus. To understand how this is possible, we study theoretically the motion of point dipoles in the magnetic potential generated by the garnet and the external field.

Stationary manifold. The full dynamics is described by a point $(\mathbf{H}_{\text{ext}}, x_A)$ moving in the product phase space $\mathcal{C} \otimes \mathcal{A}$, where $x_A \in \mathcal{A}$ is the position in action space. The energy landscape is given by the magnetic potential $V_m = -\chi_{\text{eff}}\mu_0\mathbf{H}^2$, with \mathbf{H} the total magnetic field and μ_0 the vacuum permeability. \mathbf{H} is the sum of the external field $\mathbf{H}_{\text{ext}} \in \mathcal{C}$ and the internal field $\mathbf{H}_g(\mathbf{x}_A)$ from the garnet film. The effective susceptibility χ_{eff} is positive for the paramagnets and negative for the diamagnets. Therefore, the unique scaled-potential $V = H^2$ is enough to qualitatively describe the motion of both types of colloids. The stable points for the diamagnetic (paramagnetic) colloids are the minima (maxima) of V . The colloids are far away from the garnet film. Hence, we can approximate the potential by its leading non-constant term at large elevations, which is given by:

$$V \propto \sum_{i=1}^6 \left(\frac{\mathbf{H}_{\text{ext}}^{\parallel}}{\tilde{H}_{\text{ext}}^z} \right) \cdot \left(\frac{\mathbf{q}_2 \sin(\mathbf{q}_2 \cdot \mathbf{x}_A)}{q_2 \cos(\mathbf{q}_2 \cdot \mathbf{x}_A)} \right), \quad (1)$$

where the sum runs only over the six reciprocal lattice vectors of the second Brillouin zone, \mathbf{q}_2 , all of which have magnitude q_2 . The full expression of V , at any elevation, is given in the Supplementary Note 1. $\mathbf{H}_{\text{ext}}^{\parallel}$ and $\tilde{H}_{\text{ext}}^z = H_{\text{ext}}^z/(1+\chi)$ are the components of the external magnetic field in the ferrofluid parallel and normal to the garnet film, respectively. χ is the magnetic susceptibility of the ferrofluid. V is independent of the details of the FGF, and hence the following theory can be transferred to other systems with the same symmetry. For each value of \mathbf{H}_{ext} , the stationary points $(\mathbf{H}_{\text{ext}}, \mathbf{x}_A)$ are those for which $\nabla_{\mathcal{A}}V=0$, where $\nabla_{\mathcal{A}}$ indicates the gradient in action space. The set of these points forms the stationary manifold \mathcal{M} , which is a two-dimensional manifold in $\mathcal{C} \otimes \mathcal{A}$. Only if \mathcal{M} contains non-zero-homotopic loops, we can achieve intercellular transport. \mathcal{M} can be viewed as the unification of three submanifolds: $\mathcal{M} = \mathcal{M}_+ \cup \mathcal{M}_0 \cup \mathcal{M}_-$. The Hessian matrix is positive definite in \mathcal{M}_+ (minima of V and hence stable points for the diamagnets), indefinite in \mathcal{M}_0 (unstable saddle points for both colloids) and negative definite in \mathcal{M}_- (maxima of V and hence stable points for the paramagnets). One can show that \mathcal{M} has genus 7 with 3 holes in \mathcal{M}_0 and 2 holes in each, \mathcal{M}_+ and \mathcal{M}_- , see Fig. 3b and Supplementary Fig. 2.

Let P_C be the projection that maps any point in $\mathcal{C} \otimes \mathcal{A}$ into control space. A key point is that P_C is multifold on \mathcal{M} , that is, several points $\mathbf{x}_{\mathcal{M}} = (\mathbf{H}_{\text{ext}}, \mathbf{x}_{\mathcal{A}})$ are mapped on the same point $\mathbf{H}_{\text{ext}} \in \mathcal{C}$. The north, the south and the tropics of \mathcal{C} , cf. Fig. 1c, have different multiplicity of preimages on \mathcal{M} . The multiplicity changes at the borders of \mathcal{C} via generation or annihilation of pairs involving one saddle point and one minimum or one maximum. We can divide $\mathcal{M}_{0,\pm}$ into a collection of bijective areas, $\{n_{+1}, n_{+2}, t_{+}, s_{+}\} \subset \mathcal{M}_{+}$, $\{n_{01}, n_{02}, n_{03}, t_{01}, t_{02}, s_{01}, s_{02}, s_{03}\} \subset \mathcal{M}_0$ and $\{n_{-}, t_{-}, s_{-1}, s_{-2}\} \subset \mathcal{M}_{-}$. Each area has exactly one preimage of either the north, the tropics or the south of \mathcal{C} . The letter indicates if the area is projected onto the north (n), the tropics (t) or the south (s) of \mathcal{C} . These areas are listed in Fig. 3c (with the colours corresponding to the colouring of \mathcal{M} , Fig. 3b). The first subindex (0, +, -) indicates if the area lies on \mathcal{M}_0 , \mathcal{M}_{+} or on \mathcal{M}_{-} . The second subindex labels the areas in case more than one area share the same letter and first subindex.

Fences and bifurcation points. We call the boundary between \mathcal{M}_0 and \mathcal{M}_{+} (\mathcal{M}_{-}) as the northern \mathcal{F}^{0+} (southern \mathcal{F}^{0-}) fence, see Fig. 3b. A segment of \mathcal{F}^{0+} separates a northern area on \mathcal{M}_{+} ($n_{+,1}$ or $n_{+,2}$) from a northern area on \mathcal{M}_0 ($n_{0,1}$, $n_{0,2}$ or $n_{0,3}$) and starts and ends at vertices that are bifurcation points. Four different bijective areas in \mathcal{M} meet at a bifurcation point, see Fig. 3b. There are three types of bifurcation points: triple zero bifurcation points \mathcal{B}^0 , where three out of the four areas meeting at the point are on \mathcal{M}_0 , and triple plus \mathcal{B}^+ (minus \mathcal{B}^-) bifurcation points, where three out of the four areas meeting at the point are on \mathcal{M}_{+} (\mathcal{M}_{-}). In total, each fence has 12 bifurcation points

that alternate between \mathcal{B}^0 and \mathcal{B}^+ or \mathcal{B}^- , depending on the fence. No further points where more than two areas meet on \mathcal{M} exist. The vertices on the fence are the only bifurcation points on \mathcal{M} . The projection P_C maps each of the 12 segments of \mathcal{F}^{0+} (\mathcal{F}^{0-}) onto one segment of the northern (southern) border of \mathcal{C} , see Fig. 1c. P_C also maps the bifurcation points on \mathcal{F}^{0+} (\mathcal{F}^{0-}) onto 12 points at the northern (southern) border of \mathcal{C} where two segments join. As P_C is multifold on \mathcal{M} , the preimage of the borders of \mathcal{C} are the fences and other lines that we call the pseudo fences. The preimage of the projection of the bifurcation points are the bifurcation points and other points that we call pseudo bifurcation points. The pseudo fences separate different bijective areas on \mathcal{M} , and are also divided in 12 segments, which are separated by pseudo bifurcation points. We label the segments of the borders of \mathcal{C} , and the segments of the fences and pseudo fences in \mathcal{M} from 0 to 11. A segment i on \mathcal{M} is projected onto the segment i on \mathcal{C} . Therefore, if we cross the i th segment of the border in \mathcal{C} , we cross several i th segments of fences and pseudo fences on \mathcal{M} .

Adiabatic motion. We next explain the adiabatic transport of diamagnets, similar arguments apply for the paramagnets. To achieve adiabatic transport of diamagnets, we need a modulation loop \mathcal{L}_C with a preimage loop \mathcal{L}_M in \mathcal{M} lying entirely in \mathcal{M}_{+} , such that the diamagnets can adiabatically follow the minimum of the magnetic potential. In addition, \mathcal{L}_M has to be non-zero-homotopic, that is, it has to wind around at least one of the two holes in \mathcal{M}_{+} . This non-zero-homotopic loop is then projected onto a loop in \mathcal{A} that can be non-zero-homotopic, and induce

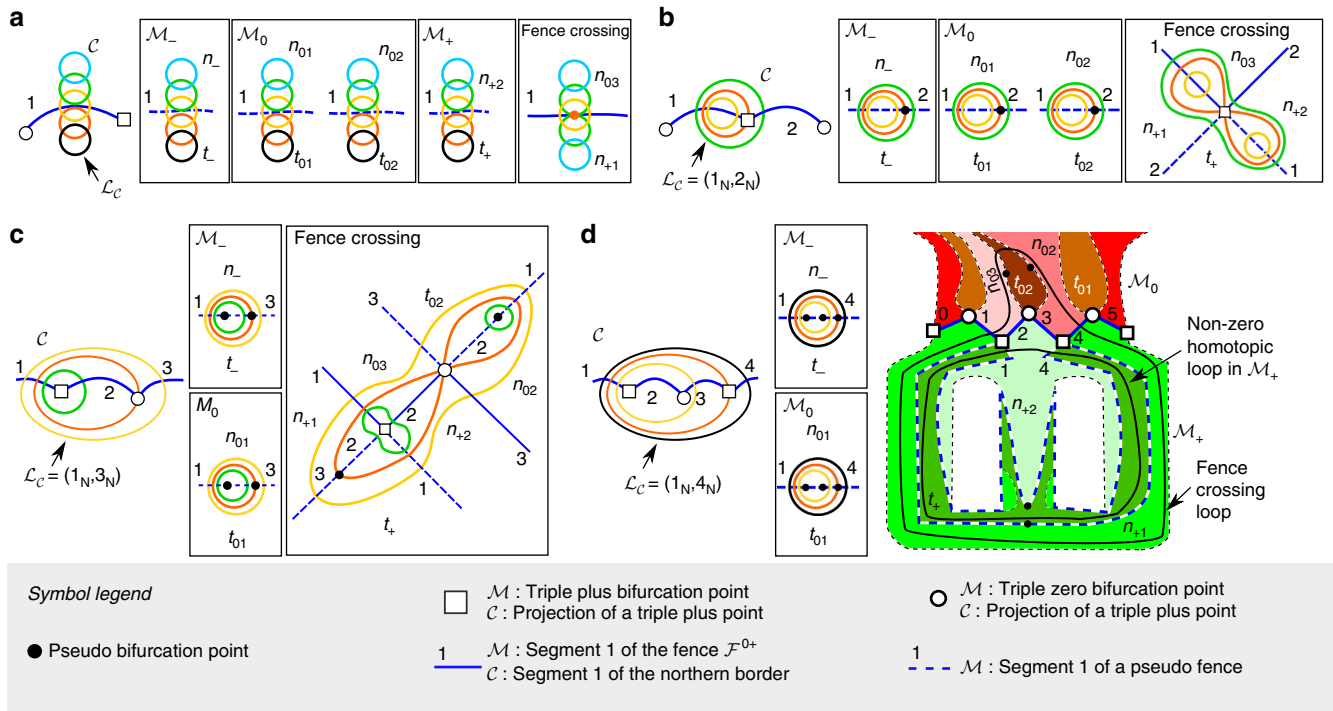


Figure 4 | Joining and disjoining loops in \mathcal{M} . Schematic of different modulation loops \mathcal{L}_C in control space \mathcal{C} and their corresponding preimage loops on the stationary surface \mathcal{M} . **(a)** \mathcal{L}_C crosses the first segment of the northern border of \mathcal{C} . When \mathcal{L}_C touches the border (red loop) a pair of a minimum and a saddle point is created in \mathcal{M} (red point). When \mathcal{L}_C crosses the border twice (yellow loop), a loop crossing the fence in \mathcal{M} (fence-crossing loop) is created (yellow loop). This fence-crossing loop lies in both \mathcal{M}_{+} and \mathcal{M}_0 . **(b)** We enlarge \mathcal{L}_C such that it encircles the projection of a triple plus bifurcation point. In \mathcal{M} , the fence-crossing loop joins with the loop in \mathcal{M}_{+} . No loop lies entirely in \mathcal{M}_{+} . **(c)** \mathcal{L}_C encircles the projection of two bifurcation points, one \mathcal{B}^+ and one \mathcal{B}^0 . The fence-crossing loop joins again with another loop that this time lies in \mathcal{M}_0 . **(d)** \mathcal{L}_C encircles now the projection of two \mathcal{B}^+ and one \mathcal{B}^0 bifurcation points. The four areas meeting at the second \mathcal{B}^+ point ($n_{+,1}$, $n_{+,2}$, t_{+} and n_{02}) were already joined in the fence-crossing loop. As a result, the fence-crossing loop disjoints into two loops, that in this case are non-zero homotopic with opposite winding numbers. One of the disjoint loops lies in \mathcal{M}_{+} and induces intercellular adiabatic motion. All loops in **a-c** are zero-homotopic.

intercellular transport. As we have already shown adiabatic motion along any lattice direction, $\mathbf{a} = w_1 \mathbf{a}_1 + w_2 \mathbf{a}_2$, with \mathbf{a}_i the basic lattice vectors in \mathcal{A} , is possible. Each transport direction corresponds to a value of the set of the two winding numbers $\{w_1, w_2\}$ around the hole in \mathcal{A} . Hence, our topological invariant is the set of winding numbers in \mathcal{A} . In \mathcal{M} there are 7 holes, and hence 14 winding numbers. The sum of any winding number in \mathcal{M} over all loops $\mathcal{L}_{\mathcal{M}}$ corresponding to a given loop in \mathcal{C} is zero since all loops in \mathcal{C} are zero-homotopic. We can only achieve a non-zero-homotopic loop in \mathcal{M} by first joining two zero-homotopic loops in \mathcal{M} , and next disjoining them into two loops with opposite winding numbers. The detailed explanation is shown next.

Consider the preimage in \mathcal{M} of the modulation loop $\mathcal{L}_{\mathcal{C}} = (1_{\mathcal{N}}, 1_{\mathcal{N}})$. We show a schematic of $\mathcal{L}_{\mathcal{C}}$ and all its preimage loops in \mathcal{M} in Fig. 4a. If $\mathcal{L}_{\mathcal{C}}$ is entirely in the tropics of \mathcal{C} (black loop) there are four zero-homotopic preimage loops on \mathcal{M} . One is in \mathcal{M}_- , two in \mathcal{M}_0 and another one in \mathcal{M}_+ . When $\mathcal{L}_{\mathcal{C}}$ touches the northern border of \mathcal{C} (red loop), a pair of a minimum and a saddle point is generated at the fence \mathcal{F}^{0+} . As $\mathcal{L}_{\mathcal{C}}$ crosses the northern border of \mathcal{C} (yellow loop), the minimum-saddle point pair deforms into a fifth (zero-homotopic) loop on \mathcal{M} that crosses the fence \mathcal{F}^{0+} . This new loop eventually disjoins into two new loops, one on \mathcal{M}_0 and one on \mathcal{M}_+ , when $\mathcal{L}_{\mathcal{C}}$ fully enters the north of \mathcal{C} (blue loop). At each stage in \mathcal{C} , the other four loops on \mathcal{M} smoothly pass through different pseudo fences on \mathcal{M} . All loops on \mathcal{M} produced with modulation loops $\mathcal{L}_{\mathcal{C}} = (i_{\mathcal{N}}, i_{\mathcal{N}})$ are zero-homotopic and therefore do not produce transport in \mathcal{A} . The specific bijective areas covered by the loops on \mathcal{M} depend on the segment of the border that we cross in \mathcal{C} . A figure showing the bijective areas that meet at each segment of fences and pseudo fences is given in Supplementary Fig. 3.

Let us now deform $\mathcal{L}_{\mathcal{C}}$ such that it finally encircles the projection of a triple plus bifurcation point, see Fig. 4b. The final loop is $\mathcal{L}_{\mathcal{C}} = (1_{\mathcal{N}}, 2_{\mathcal{N}})$. When $\mathcal{L}_{\mathcal{C}}$ crosses the projection of \mathcal{B}^+ , the corresponding loop $\mathcal{L}_{\mathcal{M}}$ crossing the fence on \mathcal{M} joins with the pseudo fence-crossing loop on \mathcal{M}_+ . The result is a new loop that crosses the fence and passes through four areas on \mathcal{M} . This loop lies in both \mathcal{M}_0 and \mathcal{M}_+ . As no other loop entirely lies on \mathcal{M}_+ , the diamagnets will follow a ratchet motion, leaving the stationary surface \mathcal{M} when the loop crosses the fence towards \mathcal{M}_0 . We will explain the ratchet motion later on. The winding number of the joint fence-crossing loop on \mathcal{M} is the sum of the winding numbers of the loops before the joining. In this case, the joining

loops are zero-homotopic and hence the joint loop is also zero-homotopic and induces no transport in \mathcal{A} .

In Fig. 4c, we further expand the modulation loop such that it encircles the following projection of a bifurcation point, a \mathcal{B}^0 . The final loop is $\mathcal{L}_{\mathcal{C}} = (1_{\mathcal{N}}, 3_{\mathcal{N}})$. In \mathcal{M} , we again join the fence-crossing loop with a pseudo fence-crossing loop that now lies in \mathcal{M}_0 . The result is, as in the previous case, a zero-homotopic fence-crossing loop.

We continue expanding the modulation loop such that it finally encircles the projection of two \mathcal{B}^+ points with $\mathcal{L}_{\mathcal{C}} = (1_{\mathcal{N}}, 4_{\mathcal{N}})$, see Fig. 4d. Now, all four areas that meet at the second \mathcal{B}^+ bifurcation point in \mathcal{M} are already joined in the fence-crossing loop. Therefore, crossing this bifurcation point disjoins the fence-crossing loops in two loops. The disjoint loops are no longer zero-homotopic. They have winding numbers with equal magnitude but opposite sign such that the sum is zero. One of the disjoint loops lies entirely in \mathcal{M}_+ , crosses the segments 1 and 4 of the pseudo fence between n_{+2} and t_+ and winds around the holes in \mathcal{M}_+ . This loop is projected into a non-zero-homotopic loop in \mathcal{A} that induces adiabatic transport of the diamagnets along the $-x$ direction.

Encircling the next projection of a \mathcal{B}^+ point, $\mathcal{L}_{\mathcal{C}} = (1_{\mathcal{N}}, 6_{\mathcal{N}})$, joins again the loop in \mathcal{M}_+ with a fence-crossing loop and creates a ratchet motion. The adiabatic transport is recovered by encircling a further projection of a \mathcal{B}^+ with $\mathcal{L}_{\mathcal{C}} = (1_{\mathcal{N}}, 8_{\mathcal{N}})$. This disjoins the fence-crossing loop and generates a new non-zero-homotopic loop in \mathcal{M}_+ . This new loop crosses segments and pseudo fences in \mathcal{M}_+ that are different than the previous non-zero-homotopic loop, and induces transport in a different lattice direction.

Deterministic ratchet motion. We next explain why the deterministic ratchet is topologically protected and its fundamental role in the phase diagram. A ratchet motion occurs if there is no loop that lies entirely on \mathcal{M}_+ . In this case, the minimum of the magnetic potential that transports the diamagnets disappears at the fence, and the particles leave the stationary manifold \mathcal{M} jumping to another minimum.

Our modulation is adiabatic, that is, the relaxation time of the colloids in the cage around the minimum is orders of magnitude faster than the period of the modulation. Hence, if the diamagnets are on \mathcal{M}_+ , they follow the minimum of the potential with a

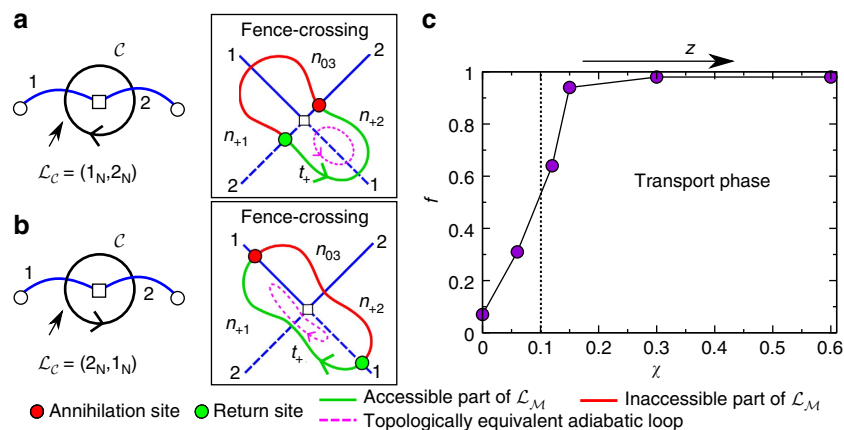


Figure 5 | Deterministic ratchet motion and elevation of the colloids. (a) A loop in \mathcal{C} encircling the projection of a triple plus bifurcation point and the corresponding fence-crossing loop in \mathcal{M} . (b) Same as in (a) but for a modulation loop in the opposite direction. The arrows in (a,b) indicate the starting points and the directions of the loops in \mathcal{C} and \mathcal{M} . The violet dashed line is an adiabatic loop topologically equivalent to the deterministic ratchet loop. It is formed by gluing the annihilation and return sites of the ratchet loop. (c) Fraction of transported colloids f as a function of the magnetic susceptibility χ of the ferrofluid. f is computed by counting how many colloids out of 100 have been successfully transported after a modulation loop. The vertical dotted line approximately marks the transition between transport and non-transport phases.

dynamics given by the modulation. If, on the contrary, the diamagnets are not on \mathcal{M}_+ , they move along the path of steepest descend of an effectively frozen potential in \mathcal{C} . This path brings the diamagnets back to \mathcal{M}_+ .

Consider again the modulation loop $\mathcal{L}_C = (1_N, 2_N)$ that encircles the projection of a \mathcal{B}^+ point and creates a ratchet. In Fig. 5a, we plot the loop in \mathcal{C} and the corresponding fence-crossing loop in \mathcal{M} . We start \mathcal{L}_C in the tropics of \mathcal{C} . In \mathcal{M} , the diamagnets follow the segment in t_+ of the loop. Next, \mathcal{L}_C crosses the first segment of the northern border, and the diamagnets cross the first segment of the pseudo fence between t_+ and n_{+2} in \mathcal{M} . Finally, \mathcal{L}_C crosses the second segment of the border. At this point, the loop in \mathcal{M} touches the fence. The minimum in n_{+2} that adiabatically transported the particles annihilates with a saddle point and disappears. The colloids leave the stationary surface \mathcal{M} at the annihilation site. Diamagnets follow now the path of steepest descend and are brought back to \mathcal{M}_+ through the return site, see Fig. 5a. Hence, the fence-crossing loop in \mathcal{M} can be divided into accessible and inaccessible parts. The particles can stay only in the accessible part. The path of steepest descend connecting the annihilation and the return sites is topologically trivial. It cannot change the homotopy class of the adiabatic loop that emerges by taking the accessible part of the loop and gluing both ends, annihilation and return sites, together, see Fig. 5a. The reason is that the path of steepest descend develops in a continuous manner from the bifurcation point \mathcal{B}^+ . To understand this, imagine we make \mathcal{L}_C smaller and smaller but always encircling the projection of \mathcal{B}^+ . Then, annihilation and return sites come closer and closer to each other, and eventually meet at the bifurcation point. This argument holds for any other ratchet motion in the system. A ratchet loop is always topologically protected by an adiabatic loop. Both loops have the same homotopy class, and therefore the same direction of motion.

Let us now revert the direction of \mathcal{L}_C , see Fig. 5b. The accessible part of the loop and the annihilation and return sites change. The forward and backward adiabatic loops that protect the ratchets are different, but induce transport in opposite directions. Therefore, the ratchet is time reversal. Reverting the modulation reverts the colloidal motion. There is, however, hysteresis since forward and backward loops differ in the path of steepest descend, and in the segments being crossed in \mathcal{M} . Usually, forward and backward loops are protected by adiabatic loops that induce transport in different, non-opposite, directions, resulting in a non-time reversal ratchet.

Ratchets play a fundamental role in the system. The homotopy class of an adiabatic loop, which lies on \mathcal{M}_+ , cannot be changed by continuous deformations. Therefore, the direction of transport cannot change if the motion remains adiabatic (note that all neighbouring adiabatic loops in the phase diagram of Fig. 2a induce transport in the same direction). It is only via ratchets that we can change the homotopy class of a loop and hence the transport direction. See, for example, in Fig. 2a, the ratchet loop $\mathcal{L}_C = (1_N, 2_N)$ (protected by the adiabatic loop $(1_N, 1_N)$) and the ratchet loop $(1_N, 3_N)$ (protected by $(1_N, 4_N)$). The topological transition that changes the transport direction occurs when \mathcal{L}_C encircles the projection of a \mathcal{B}^0 point (Supplementary Fig. 4).

Theory and experiments are in perfect agreement. The above theory predicts exactly the same phase diagram we have found experimentally, cf Fig. 2a. In addition, we have also performed Brownian dynamic simulations of paramagnetic and diamagnetic particles moving in the potential given by equation (1). The simulations are also in perfect agreement with the theory and the experiments. The simulation allows us to introduce thermal noise in the system. We have verified that the topological protection is very robust against thermal fluctuations. When the noise is very high, such that it erases the energy landscape, the topological

protection is lost. The degradation of the topological protection starts at both interfaces between different types of motion in the phase diagram: adiabatic-ratchet interface and the interface between deterministic ratchets along different directions.

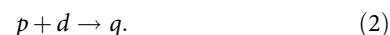
The transport direction is also robust against other perturbations, such as the precise shape and speed of the modulation loop, changes in size, mobility and magnetic susceptibility of the colloids, and changes in the pattern that do not affect its symmetry (for example, the shape of the bubbles). Most strikingly, the directions of the ratchets are protected, that is, the topology of the stationary surface determines not only the direction of the adiabatic motion but also of the non-equilibrium ratchet motion.

There are always operations that break the topological protection. In our system, we can break the protection by changing the topology of \mathcal{M} as we describe next.

Elevation above the garnet. We return now to the experiments. We have discussed the transport of colloids at elevations z far away from the garnet film so that the potential is given by equation (1). At low elevations, the field created by the garnet is very strong compared with the external magnetic field and the potential is given by that of the pattern alone. In this situation, the different parts of \mathcal{M} are disconnected manifolds and have a trivial topology (spheres) missing the requirements for topological transport.

Depending on the dilution of the ferrofluid, the image-dipole potential may or may not overcome the gravitational potential. Hence, controlling the ferrofluid susceptibility gives direct control over the colloidal elevation z above the garnet film. Consider a loop in \mathcal{C} that induces lattice translations if the colloids are at high elevations. By performing the same loop for different ferrofluid-water compositions, and hence varying the susceptibility χ , we can observe the transition from non-zero-homotopic loops in \mathcal{A} to zero-homotopic loops. The results are shown in Fig. 5c. The topological transition takes place at $\chi \approx 0.1$. For $\chi \lesssim 0.1$, the particles descend below a critical elevation z_c , and the transition to the non-transport phase occurs. Above z_c the effects of the hexagonal pattern are the same for any z , and topologically protected modulation loops work for any hexagonal pattern, independently of the fine details. By decreasing the elevation below z_c , we remove the holes of \mathcal{M} inducing a topological transition. This plays the role of gap closure in the dispersion relation of wave-like systems²⁸.

Application. We use the topological protection to implement an experimental internal quality control of a chemical reaction. We consider the hybridization reaction between two complementary single-stranded oligo nucleotides of DNA, which we attach to the paramagnetic and diamagnetic colloids. If the hybridization is successful, the paramagnet (p) and diamagnet (d) irreversibly bind to form a quadrupole (q)



We want to emulate the conditional command: if the reaction is successful, then transport the product q along a given direction a_q , otherwise transport the educts p and d along directions a_p and a_d , respectively.

We have already shown how to induce topologically protected transport of the educts (dipoles). The product of the reaction is a quadrupole that senses the quadrupolar potential $V_q = -(\nabla_A V)^2$. The modulation loops $\mathcal{T}_p \subset \mathcal{C}$ and $\mathcal{T}_d \subset \mathcal{C}$ for the transport of the educts can be chosen such that they do not affect the motion of the quadrupoles. We also find an appropriate

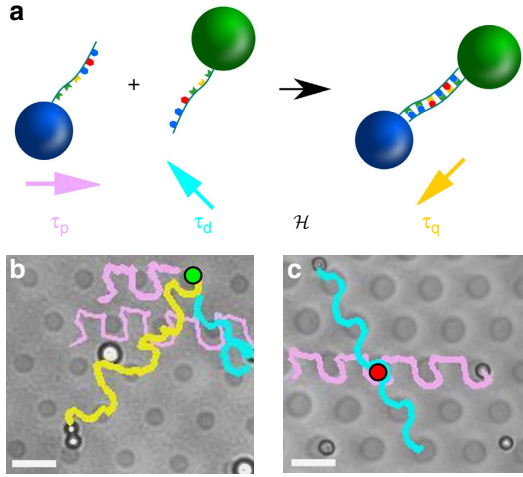


Figure 6 | Application. (a) Schematic of the hybridization reaction and the emulation of a conditional command that transport each type of particle in different directions. Polarization images of a successful and non-successful reaction are shown in **b,c**, respectively. The trajectories of the diamagnets, paramagnets and quadrupoles are highlighted in pink, cyan and yellow, respectively. The green (red) circle indicates the area where the dipoles meet and the hybridization takes place (fails). Scale bars (**b,c**), 10 μm .

modulation loop $\mathcal{T}_q \subset \mathcal{C}$ that transports the quadrupoles in the required direction without affecting the dipoles.

The paramagnets and diamagnets reside on opposite parts (\mathcal{M}_- and \mathcal{M}_+) of the stationary surface and, in the presence of the pattern, do not approach each other in \mathcal{A} to allow the hybridization. To bring the colloids together, we perform a non-adiabatic hybridization loop $\mathcal{H} \subset \mathcal{C}$ around the equator of \mathcal{C} with a very high angular frequency. Hence, the colloids cannot follow the instantaneous potential and feel an almost flat averaged potential. Effectively, we erase the potential of the pattern such that the weak dipolar attractive interaction is enough to bring paramagnets and diamagnets together. The colloids meet in a bubble and rotate around each other such that hybridization is possible. After hybridization, the bond is strong enough to resist the magnetic stress exerted by the potential of the next modulation loops such that the bond is irreversible. The particle pair remains inseparable and behaves like a stable quadrupole. The entire modulation is a loop of the type $\mathcal{T}_p \mathcal{T}_d \mathcal{H} \mathcal{T}_q$, see Fig. 6a. We show the transport of the colloids after a successful and a non-successful hybridization in Fig. 6b,c, respectively. Videos are provided in Supplementary Movies 8–9. This quality control is internal as we do not change the modulation loop after we have measured externally whether the reaction was successful. The quality control works without active intervention.

Discussion

When the modulation loop is in the north of \mathcal{C} , the magnetic potential presents two minima, one in n_{+1} and one in n_{+2} that are projected onto different points on \mathcal{A} . No colloidal transport between the minima exists as the potential barrier is too high. Phase space is hence divided into different nonergodic regions, and thermal equilibration only occurs over the cage around each minimum. The cage can only be left in a ratchet-like motion when the modulation loop touches the fence. Hence, our ratchet is associated with an ergodic-nonergodic transition, and might serve as a model for the cage effect in supercooled liquids²⁹ and glasses³⁰.

Dissipation has been used in open quantum systems¹² to isolate topologically protected edge modes from a bath. The final state of the edge modes is nevertheless dissipation free.

In contrast, our system must be driven to maintain the transport. Moreover, the ratchet effect (crucial to change the direction of motion) is intrinsically dissipative and cannot, in general, be described with an effective Hamiltonian.

In one-dimensional systems, one can prove that thermal ratchets³¹, in which the potential evolves in time adiabatically, are always time reversal ratchets. We have shown here an example in two dimensions of a non-time reversal ratchet in an adiabatically evolving potential.

The construction of the stationary surface \mathcal{M} and the mappings to action and control space is completely general and can be used for any potential. Other potentials might or might not support topologically protected transport, depending on the topological properties of \mathcal{M} . Our results are directly transferable to any system with hexagonal symmetry, and a potential proportional to the square of a field, which satisfies the Laplace equation.

High-quality magnetic bubbles lattices, like the one we have used here, have been studied extensively³² and hence the technology for its fabrication is well known. In addition, we note that any patterned substrates, such as lithographic magnetic patterns³³, will induce similar transport.

Methods

Experimental preparation and measurements. The FGF films were grown by Tom Johansen (Oslo) via liquid phase epitaxy. We use the water-based ferrofluid EMG 707 from FerroTec GmbH, Germany. We dilute the ferrofluid with water. The final magnetic susceptibility is $\chi \approx 0.6$. The time-dependent magnetic field is generated by three coils, following the ideas presented in ref. 34. Each coil controls the magnetic field along one of the three Cartesian axis. The current through the coils is provided by three phase-locked channels of programmable waveform generators (TTi TG1244) via three bipolar (KEPCO 20–50GL) amplifiers. The system is monitored via polarization microscopy. The pattern is visualized via the polar Faraday effect, and the colloids via ordinary transmission microscopy. Modulation loops in control space are programmed on a computer and transferred to the waveform generators.

For the hybridization reaction, we functionalize the colloids with streptavidin. The diamagnets and paramagnets are immersed separately into two solutions of biotinylated and complementary oligonucleotides. The complementary sequences are 5′-5Bio/TCACCTCAGTACGATATGCGGCACAG-3′ and 5′-5Bio/CTGTGC CGCATATCGTACTGAGTGA-3′.

Topology of the stationary manifold. We first find the projection of the bifurcation points and the fences onto action space. Next, we map action space into control space, so that we obtain the projection of the fences and bifurcation points in \mathcal{C} . With these projections we compute the vertices $v = 96$, edges $e = 124$ and areas $a = 16$ of \mathcal{M} . The Euler characteristic of \mathcal{M} is $\chi(\mathcal{M}) = v - e + a = -12$, and it has genus $g(\mathcal{M}) = 1 - \chi(\mathcal{M})/2 = 7$. The mapping of \mathcal{A} into \mathcal{C} also allows the determination of how the bijective areas are glued in \mathcal{M} . Further details are given below.

Projection of the fence. We use coordinates

$$\mathbf{x}_A = (x_1 \mathbf{a}_1, x_2 \mathbf{a}_2), \quad (3)$$

in action space \mathcal{A} , where \mathbf{a}_1 and \mathbf{a}_2 are the basic lattice vectors of the hexagonal lattice. In control space, we use coordinates

$$\mathbf{H}_{\text{ext}} = H_{\text{ext}} (\cos \phi \sin \theta, \sin \phi \sin \theta, \cos \theta), \quad (4)$$

where the azimuthal angle ϕ is measured with respect to the direction of \mathbf{a}_1 and the polar angle θ with respect to the z-direction. Consider the unit vectors $\hat{\mathbf{e}}_i(x_1, x_2) = \partial_i \mathbf{H}_g / |\partial_i \mathbf{H}_g|$, $i = 1, 2$, where \mathbf{H}_g is the magnetic field of the garnet film. As we have seen, the leading term of the magnetic potential is $V \propto \mathbf{H}_{\text{ext}} \cdot \mathbf{H}_g$ and the stationary points are those for which $\nabla_A V = 0$. Then, a point $(\mathbf{H}_{\text{ext}}, \mathbf{x}_A)$ in $\mathcal{C} \otimes \mathcal{A}$ is stationary, and hence lies on \mathcal{M} , if the direction of \mathbf{H}_{ext} is perpendicular to both $\hat{\mathbf{e}}_1$ and $\hat{\mathbf{e}}_2$. Therefore, a point in \mathcal{A} with coordinates (x_1, x_2) in the basis $(\mathbf{a}_1, \mathbf{a}_2)$ has two stationary preimages in \mathcal{M} that correspond to external magnetic fields $\mathbf{H}_{\text{ext}}^{(s)}(x_1, x_2) = \pm H_{\text{ext}} (\hat{\mathbf{e}}_1 \times \hat{\mathbf{e}}_2) / |\hat{\mathbf{e}}_1 \times \hat{\mathbf{e}}_2|$. The superscript (s) in $\mathbf{H}_{\text{ext}}^{(s)}(x_1, x_2)$ indicates that this field makes the point (x_1, x_2) in \mathcal{A} stationary. Consider now the Hessian matrix,

$$\nabla_A \nabla_A V = \begin{pmatrix} \mathbf{H}_{\text{ext}}^{(s)} \cdot \partial_1 \partial_1 \mathbf{H}_g & \mathbf{H}_{\text{ext}}^{(s)} \cdot \partial_1 \partial_2 \mathbf{H}_g \\ \mathbf{H}_{\text{ext}}^{(s)} \cdot \partial_2 \partial_1 \mathbf{H}_g & \mathbf{H}_{\text{ext}}^{(s)} \cdot \partial_2 \partial_2 \mathbf{H}_g \end{pmatrix}. \quad (5)$$

When crossing the fence on \mathcal{M} from \mathcal{M}_0 to \mathcal{M}_+ , a saddle point changes to a minimum. Hence, the determinant of the above Hessian matrix must vanish at the

fence, $\|\nabla_{\mathcal{A}} \nabla_{\mathcal{A}} V\|_{\text{fence}} = 0$. In this way, we find an implicit equation for the projection of the fences in action space. Both fences, \mathcal{F}^{0+} and \mathcal{F}^{0-} , are projected into the same region in \mathcal{A} with coordinates $(x_{1,f}, x_{2,f})$ given implicitly by:

$$0 = F^2 - 2SF - 3S^2 - 4(f_1f_2 + f_1f_3 + f_2f_3), \quad (6)$$

where

$$\begin{aligned} F &= f_1 + f_2 + f_3, \\ S &= c_1 + c_2 + c_3, \\ f_i &= 1 + c_i + c_i^2, \quad i = 1, 2, 3, \\ c_1 &= \cos(2\pi x_{1,f}), \\ c_2 &= \cos(2\pi x_{2,f}), \\ c_3 &= \cos(2\pi [x_{1,f} + x_{2,f}]). \end{aligned} \quad (7)$$

The projection of the fence \mathcal{F}^{0+} in control space, that is, the northern border on \mathcal{C} is given by:

$$\begin{aligned} \theta &= \text{atan} \left(\frac{\sqrt{H_1^2 + 2H_1H_2 \cos(\pi/3) + H_2^2}}{H_0 \sin(\pi/3)} \right), \\ \phi &= \text{atan} \left(\frac{\sin(\pi/3)}{H_1/H_2 + \cos(\pi/3)} \right), \end{aligned} \quad (8)$$

where

$$\begin{aligned} H_1 &= c_3(s_1 - s_2) + c_2(s_1 + s_3), \\ H_2 &= c_3(s_2 - s_1) + c_1(s_2 + s_3), \\ H_0 &= c_1c_2 + c_2c_3 + c_3c_1, \\ s_1 &= \sin(2\pi x_{1,f}), \\ s_2 &= \sin(2\pi x_{2,f}), \\ s_3 &= \sin(2\pi [x_{1,f} + x_{2,f}]). \end{aligned} \quad (9)$$

The coordinates of the southern border on \mathcal{C} are then obtained via the transformation $\theta \rightarrow \pi - \theta$ and $\phi \rightarrow \phi - \pi$. Supplementary Fig. 1 shows the projection of the fences in the $\phi - \theta$ plane of control space.

Projection of bifurcation points. Four bijective areas meet at a bifurcation point in \mathcal{M} . Four segments (two fence segments and two pseudo-fence segments) form the branches that bifurcate in a bifurcation point in \mathcal{M} . If we follow the fence \mathcal{F}^{0+} and cross a bifurcation point, then either the minimum or the saddle point that meet at the fence (depending on the type of bifurcation point) changes the bijective area to which it belongs. If we cross the projection of a triple plus bifurcation point in \mathcal{C} from the tropics to the north, then in \mathcal{A} a minimum undergoes a pitchfork bifurcation into two minima and one saddle point. An equivalent bifurcation happens if we cross the projection of a triple zero bifurcation point, in which case the roles of saddle points and minima are reversed.

The mathematical condition for a bifurcation point is as follows. Let \mathbf{v}_0 be the eigenvector of the Hessian matrix, cf. equation (5), at the fence with eigenvalue 0. Then, a bifurcation point is a fence point that satisfies

$$(\mathbf{v}_0 \cdot \nabla_{\mathcal{A}})^3 V = 0. \quad (10)$$

Solving the above equation, we find the projection in \mathcal{C} of a triple plus bifurcation point lying on the fence \mathcal{F}^{0+} at $(\theta, \phi) = (\pi/3, \pi)$. The coordinates in \mathcal{C} of the projection of a triple zero bifurcation point in \mathcal{F}^{0+} are $(\theta, \phi) = (0.381\pi, 7\pi/6)$. The other projections of bifurcation points belonging to the fence \mathcal{F}^{0+} are obtained, for symmetry reasons, via rotations around the z axis by multiples of $\pi/3$. Using the transformation $\theta \rightarrow \pi - \theta$ and $\phi \rightarrow \phi - \pi$, one finds the projection of the bifurcation points in \mathcal{F}^{0-} .

Bijective areas and the genus of \mathcal{M} . We can thus map each point in \mathcal{A} onto two opposing points in \mathcal{C} . The mapping of a point in \mathcal{A} onto the two points in \mathcal{C} will fall either in the north and the south (one point in each region), or both points fall into the tropics of \mathcal{C} . This gives the projections $\mathcal{P}_{\mathcal{A}}$ of the bijective areas of \mathcal{M} into action space. Hence, we can see how the bijective areas are glued together in \mathcal{A} and \mathcal{M} . A bijective area is a connected preimage of either the north, the south or the tropics of control space. That is, there is a one-to-one correspondence between the bijective area in \mathcal{M} and its corresponding region in \mathcal{C} . Any loop in \mathcal{M} lying entirely in a bijective area is projected onto a zero homotopic loop in \mathcal{A} . Hence, in order to achieve intercellular transport, a loop must cross different bijective areas. The neighbouring bijective areas in \mathcal{M} are shown in Supplementary Fig. 3. We can use it to construct the sequence of bijective areas for a given $\mathcal{L}_{\mathcal{C}}$. For example, consider the loop $\mathcal{L}_{\mathcal{C}} = (1_N, 4_N)$. We start in the tropics, where there is only one minimum which is located in t_+ . Segment 1_N connects t_+ to n_{+2} , and segment 4_N connects n_{+2} to t_+ , which closes the loop.

To compute the Euler characteristic of \mathcal{M} and hence its genus, we need to count the vertices, edges and bijective areas, as detailed next. Topologically, the north of \mathcal{C} is a simply connected area (that is, all loops are zero homotopic) with 12 edges (segments of the borders) and 12 vertices (projection of bifurcation points). Each point in the north of \mathcal{C} has 6 preimages on \mathcal{M} . Hence, the north of \mathcal{C}

contributes with 6 bijective areas, $12 \times 6 = 72$ edges and $12 \times 6 = 72$ vertices to \mathcal{M} . A similar contribution comes from the south of \mathcal{C} . The tropics of \mathcal{C} is a non-simply connected area, for example, the equator is zero homotopic in \mathcal{C} but not in the tropics of \mathcal{C} . To easily compute the Euler characteristic, we need simply connected areas. We make the tropics of \mathcal{C} simply connected by cutting it along a longitude that connects the projection of two bifurcation points, one in each border of \mathcal{C} . The total number of edges of the tropics is thus $12 + 12 + 2 = 26$ and the total number of vertices is $12 + 12 + 2 = 26$. There are 4 preimages of the tropics on \mathcal{M} . Hence, the total contribution of the tropics of \mathcal{C} to \mathcal{M} is 4 bijective areas, $4 \times 26 = 104$ edges and $4 \times 26 = 104$ vertices.

Next, we glue the bijective areas to form \mathcal{M} . Two unglued edges are glued to form a single edge such that the number of glued edges of \mathcal{M} is $(72 + 72 + 104)/2 = 124$. Regarding the vertices, we have $72 + 72 + 104 = 248$ before gluing them in \mathcal{M} . We have to subtract 8 vertices that were artificially produced by cutting the tropics of \mathcal{C} in order to have a simply connected area. We have then $248 - 8 = 240$ unglued vertices. There are two types of vertices on \mathcal{M} : bifurcation points where 4 bijective areas meet, and pseudo-bifurcation points where 2 bijective areas meet. There are 24 bifurcation points on \mathcal{M} . Hence, we need $4 \times 24 = 96$ unglued vertices to glue together the bijective areas at the bifurcation points. The remaining $240 - 96 = 144$ unglued vertices are glued in pairs to form $144/2 = 72$ pseudo bifurcation points. The total number of vertices on \mathcal{M} is the sum of the number of bifurcation and pseudo bifurcation points: $24 + 72 = 96$.

Finally, the Euler characteristic of \mathcal{M} is $\chi(\mathcal{M}) = 96 - 124 + 16 = -12$ and the genus of \mathcal{M} is $g(\mathcal{M}) = 1 - \chi(\mathcal{M})/2 = 7$. Similar arguments can be used to calculate the genus of the submanifolds that form \mathcal{M} , that is, \mathcal{M}_+ , \mathcal{M}_0 and \mathcal{M}_- . We show in Supplementary Fig. 2 a plaster model of \mathcal{M} .

Computer simulations. We simulate the motion of point dipoles moving in the potential given by equation (1) using Brownian dynamic simulations. The equation of motion is

$$\zeta \dot{\mathbf{x}}_{\mathcal{A}}(t) = \pm V(\mathbf{x}_{\mathcal{A}}, \mathbf{H}_{\text{ext}}(t)) + \eta(t), \quad (11)$$

where t is the time, $\mathbf{x}_{\mathcal{A}}$ is the position of the dipoles in \mathcal{A} , ζ is the friction coefficient and η is a Gaussian random force with a variance given by the fluctuation-dissipation theorem. The plus (minus) sign in front of the potential holds for the diamagnetic (paramagnetic) colloids. The equation of motion is integrated in time with a standard Euler algorithm. We use a time step $T/dt \approx 2 \cdot 10^5$ with T the period of a modulation loop $\mathcal{L}_{\mathcal{C}}$. Simulations fully reproduce the experimental phase diagram.

Data availability. The data that supports the findings of this study are available from the corresponding author upon request.

References

1. Freedman, M. H., Kitaev, A., Larsen, M. J. & Wang, Z. Topological quantum computation. *Bull. Amer. Math. Soc.* **40**, 31–38 (2003).
2. Kane, C. L. & Lubensky, T. C. Topological boundary modes in isostatic lattices. *Nat. Phys.* **10**, 39–45 (2014).
3. Hasan, M. Z. & Kane, C. L. Colloquium: topological insulators. *Rev. Mod. Phys.* **82**, 3045–3067 (2010).
4. Chen, B. G., Upadhyaya, N. & Vitelli, V. Nonlinear conduction via solitons in a topological mechanical insulator. *Proc. Natl Acad. Sci. USA* **111**, 13004–13009 (2014).
5. Paulose, J., Chen, B. G. & Vitelli, V. Topological modes bound to dislocations in mechanical metamaterials. *Nat. Phys.* **11**, 153–156 (2015).
6. Nash, L. M. *et al.* Topological mechanics of gyroscopic metamaterials. *Proc. Natl Acad. Sci. USA* **112**, 14495–14500 (2015).
7. Shen, S.-Q. *Topological Insulators: Dirac Equation in Condensed Matters* (Springer Science & Business Media, 2013).
8. Kitagawa, T., Berg, E., Rudner, M. & Demler, E. Topological characterization of periodically driven quantum systems. *Phys. Rev. B* **82**, 235114 (2010).
9. Rudner, M. S., Lindner, N. H., Berg, E. & Levin, M. Anomalous edge states and the bulk-edge correspondence for periodically driven two-dimensional systems. *Phys. Rev. X* **3**, 031005 (2013).
10. Ghodbane, M. *et al.* Development and validation of a microfluidic immunoassay capable of multiplexing parallel samples in microliter volumes. *Lab Chip* **15**, 3211–3221 (2015).
11. Gao, L., Tahir, M. A., Virgin, L. N. & Yellen, B. B. Multiplexing superparamagnetic beads driven by multi-frequency ratchets. *Lab Chip* **11**, 4214–4220 (2011).
12. Diehl, S., Rico, E., Baranov, M. A. & Zoller, P. Topology by dissipation in atomic quantum wires. *Nat. Phys.* **7**, 971–977 (2011).
13. Weimer, H., Müller, M., Lesanovsky, I., Zoller, P. & Büchler, H. P. A Rydberg quantum simulator. *Nat. Phys.* **6**, 382–388 (2010).
14. Olson, C. J., Reichardt, C. & Nori, F. Nonequilibrium dynamic phase diagram for vortex lattices. *Phys. Rev. Lett.* **81**, 3757–3760 (1998).
15. Korda, P. T., Taylor, M. B. & Grier, D. G. Kinetically locked-in colloidal transport in an array of optical tweezers. *Phys. Rev. Lett.* **89**, 128301 (2002).

16. Reichhardt, C. & Nori, F. Phase locking, devil's staircases, Farey trees, and Arnold tongues in driven vortex lattices with periodic pinning. *Phys. Rev. Lett.* **82**, 414–417 (1999).
17. Kolton, A. B., Dominguez, D. & Grønbech-Jensen, N. Mode locking in ac-driven vortex lattices with random pinning. *Phys. Rev. Lett.* **86**, 4112–4115 (2001).
18. Bohlein, T., Mikhael, J. & Bechinger, C. Observation of kinks and antikinks in colloidal monolayers driven across ordered surfaces. *Nat. Mater.* **11**, 126–130 (2012).
19. Reimann, P. Brownian motors: noisy transport far from equilibrium. *Phys. Rep. Rev. Phys. Lett.* **361**, 57–265 (2002).
20. Köhler, S., Lehmann, J. & Hänggi, P. Driven quantum transport on the nanoscale. *Phys. Rep. Rev. Phys. Lett.* **406**, 379–443 (2005).
21. Simon, S. M., Peskin, C. S. & Oster, G. F. What drives the translocation of proteins. *Proc. Natl Acad. Sci. USA* **89**, 3770–3774 (1992).
22. Jülicher, F., Ajdari, A. & Prost, J. Modeling molecular motors. *Rev. Mod. Phys.* **69**, 1269–1281 (1997).
23. Doering, C. R., Horsthemke, W. & Riordan, J. Nonequilibrium fluctuation-induced transport. *Phys. Rev. Lett.* **72**, 2984–2987 (1994).
24. Popescu, M. N., Arizmendi, C. M., Salas-Brito, A. L. & Family, F. Disorder induced diffusive transport in ratchets. *Phys. Rev. Lett.* **85**, 3321–3324 (2000).
25. Savel'ev, S., Marchesoni, F. & Nori, F. Stochastic transport of interacting particles in periodically driven ratchets. *Phys. Rev. E* **70**, 061107 (2004).
26. Tierno, P., Johansen, T. H. & Fischer, T. h. M. Localized and delocalized motion of colloidal particles on a magnetic bubble lattice. *Phys. Rev. Lett.* **99**, 038303 (2007).
27. Tierno, P., Reddy, S. V., Roper, M. G., Johansen, T. H. & Fischer, T. h. M. Transport and separation of biomolecular cargo on paramagnetic colloidal particles in a magnetic ratchet. *J. Phys. Chem. B.* **112**, 3833–3837 (2008).
28. Zhang, F., MacDonald, A. H. & Mele, E. J. Valley Chern numbers and boundary modes in gapped bilayer graphene. *Proc. Natl Acad. Sci. USA* **110**, 10546–10551 (2013).
29. Götze, W. & Sjögren, L. Relaxation processes in supercooled liquids. *Rep. Prog. Phys.* **55**, 241–376 (1992).
30. Doliwa, B. & Heuer, A. Cage effect, local anisotropies, and dynamic heterogeneities at the glass transition: A computer study of hard spheres. *Phys. Rev. Lett.* **80**, 4915–4918 (1998).
31. Sinitsyn, N. A. The stochastic pump effect and geometric phases in dissipative and stochastic systems. *J. Phys. A* **42**, 193001 (2009).
32. Bobeck, A. H., Bonyhard, P. I. & Geusic, J. E. Magnetic bubbles .-emerging new memory technology. *Proc. IEEE* **63**, 1176–1195 (1975).
33. Terris, B. D. & Thomson, T. Nanofabricated and self-assembled magnetic structures as data storage media. *J. Phys. D Appl. Phys.* **38**, R199–R222 (2005).
34. Martin, J. E. & Solis, K. J. Fully alternating, triaxial electric or magnetic fields offer new routes to fluid vorticity. *Soft Matter* **11**, 241–254 (2015).

Acknowledgements

We thank Ingrid Bauer, Matthias Schmidt, Pietro Tierno and Antonio Ortiz-Ambriz for illuminating discussions and critical reading of the manuscript. We thank Thomas Hauenstein and Konrad Stern for playing the Franconian Landler with Johannes Loehr. Publication costs have been partially funded by the Profildfeld Polymer- und Kolloid-forschung of the University of Bayreuth.

Author contributions

J.L. performed the experiments, designed the modulation loops and played the accordion in movie 'Franconian Landler.avi'. M.L. developed the topological relation between \mathcal{A} , \mathcal{C} and \mathcal{M} . D.de las H. had the idea to use Brownian dynamics to simulate the motion. Simulations were performed by A.E. and led to the discovery of the topological protection of the ratchet. T.M.F. had the idea of the experiments. J.L., D.de las H. and T.M.F. wrote the manuscript.

Additional information

Supplementary Information accompanies this paper at <http://www.nature.com/naturecommunications>

Competing financial interests: The authors declare no competing financial interests.

Reprints and permission information is available online at <http://npg.nature.com/reprintsandpermissions/>

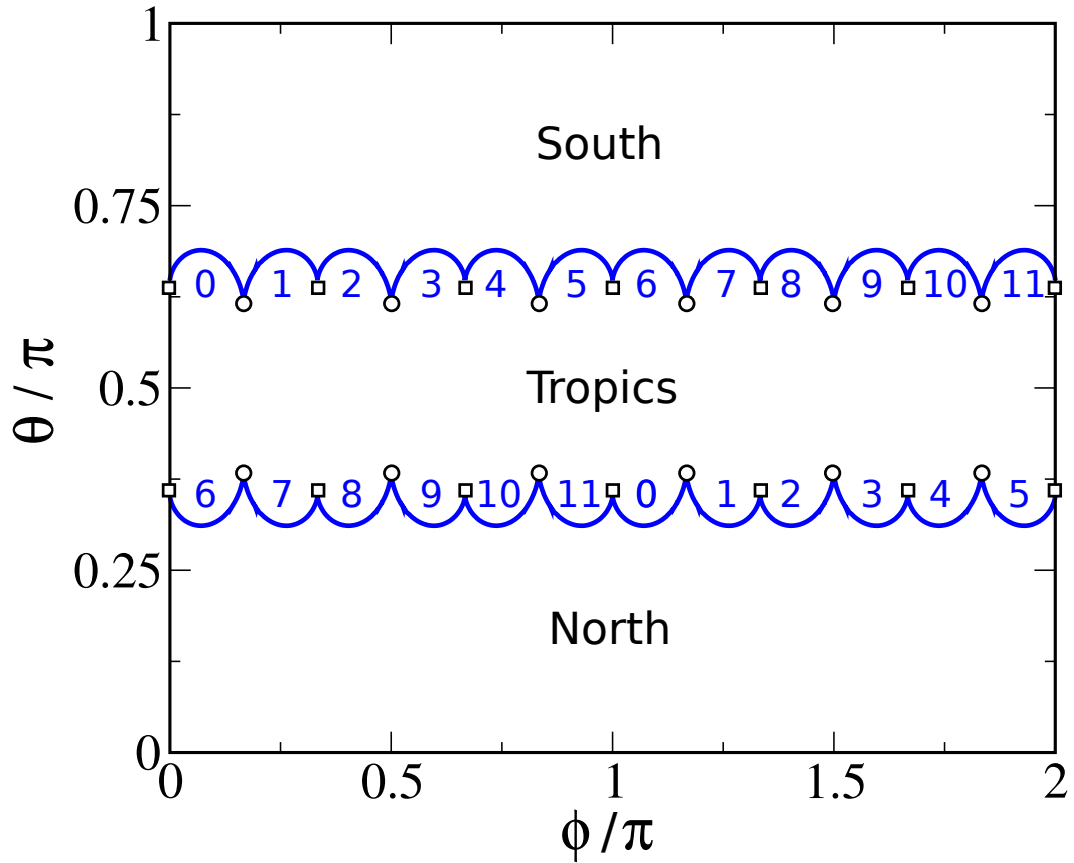
How to cite this article: Loehr, J. *et al.* Topological protection of multiparticle dissipative transport. *Nat. Commun.* **7**:11745 doi: 10.1038/ncomms11745 (2016).



This work is licensed under a Creative Commons Attribution 4.0 International License. The images or other third party material in this article are included in the article's Creative Commons license, unless indicated otherwise in the credit line; if the material is not included under the Creative Commons license, users will need to obtain permission from the license holder to reproduce the material. To view a copy of this license, visit <http://creativecommons.org/licenses/by/4.0/>

Publication 2

Supporting Information



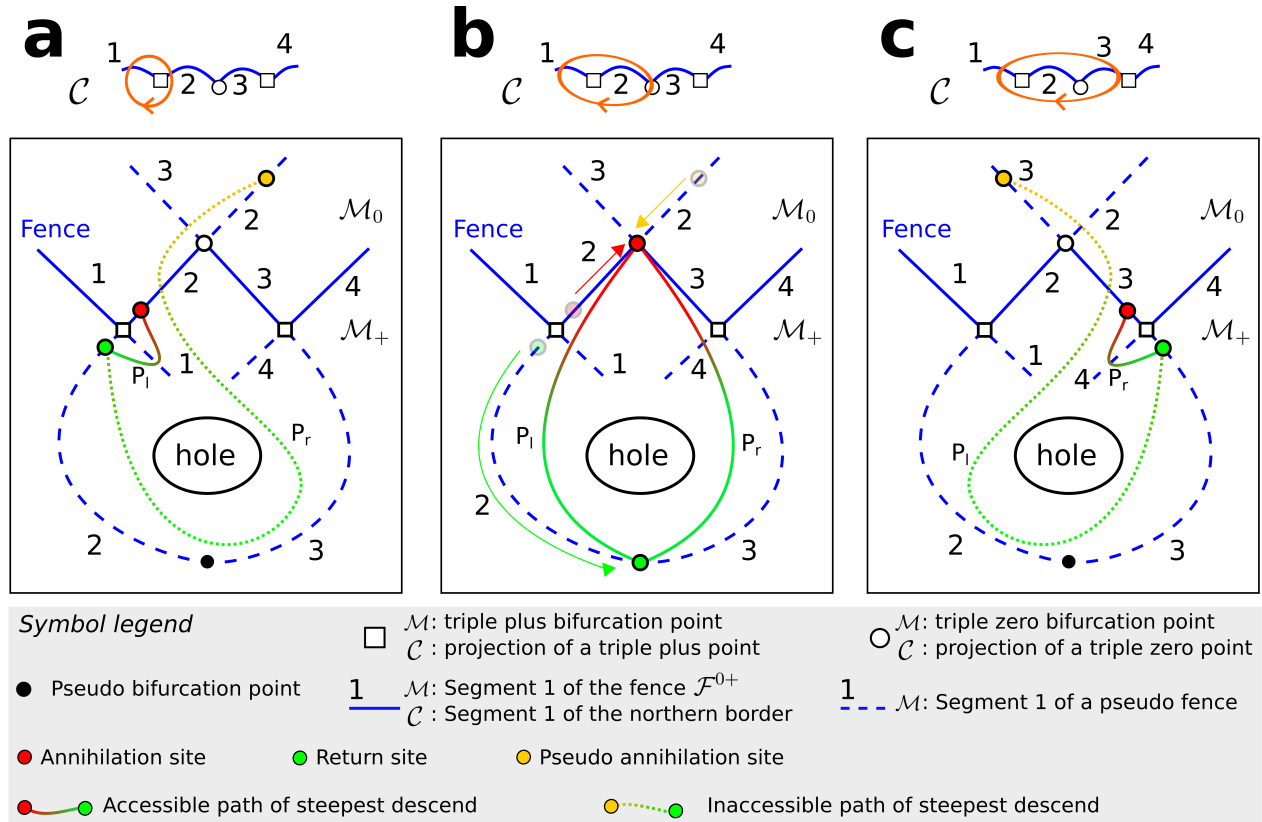
Supplementary Figure 1. **Borders of control space.** The borders of control space are the projections of the fences. Each border contains 12 segments that we label from 0 to 11 as indicated. The projection of \mathcal{F}^{0+} (\mathcal{F}^{0-}) is the northern (southern) border and separates the tropics from the north (south) of \mathcal{C} . Empty circles are projection of triple zero bifurcation points. Empty squares in the northern (southern) border indicate the projection of triple plus (minus) points.



Supplementary Figure 2. **Stationary surface \mathcal{M} .** A plaster model of the stationary surface \mathcal{M} . Each color is a bijective area. The green (blue) areas represent \mathcal{M}_+ (\mathcal{M}_-). The remaining areas (earth color tones) form \mathcal{M}_0 . The black and white lines separating two different areas represent segments of fences or pseudo fences. The color of the line indicates whether the segment is odd (white) or even (black). The stationary manifold \mathcal{M} is actually a two-dimensional surface in the four-dimensional curved space $\mathcal{C} \otimes \mathcal{A}$ that cannot be visualized. We can however embed \mathcal{M} in a Cartesian three-dimensional space, as the figure shows. Both, the real \mathcal{M} in $\mathcal{C} \otimes \mathcal{A}$ and the model shown in the figure are topologically equivalent. That is, both can be continuously deformed into each other.

	0	1	2	3	4	5	6	7	8	9	10	11
t_+	n_{+2}	n_{+2}	n_{+1}	n_{+1}	n_{+2}	n_{+2}	n_{+1}	n_{+1}	n_{+2}	n_{+2}	n_{+1}	n_{+1}
n_{+1}	n_{01}	n_{03}	t_+	t_+	n_{02}	n_{01}	t_+	t_+	n_{03}	n_{02}	t_+	t_+
n_{+2}	t_+	t_+	n_{03}	n_{02}	t_+	t_+	n_{01}	n_{03}	t_+	t_+	n_{02}	n_{01}
n_{01}	n_{+1}	t_{01}	t_{01}	t_{01}	t_{01}	n_{+1}	n_{+2}	t_{02}	t_{02}	t_{02}	t_{02}	n_{+2}
n_{02}	t_{02}	t_{02}	t_{02}	n_{+2}	n_{+1}	t_{01}	t_{01}	t_{01}	t_{01}	n_{+1}	n_{+2}	t_{02}
n_{03}	t_{01}	n_{+1}	n_{+2}	t_{02}	t_{02}	t_{02}	t_{02}	n_{+2}	n_{+1}	t_{01}	t_{01}	t_{01}
t_{01}	n_{03}	n_{01}	n_{01}	n_{01}	n_{01}	n_{02}	n_{02}	n_{02}	n_{02}	n_{03}	n_{03}	n_{03}
t_{02}	n_{02}	n_{02}	n_{02}	n_{03}	n_{03}	n_{03}	n_{03}	n_{01}	n_{01}	n_{01}	n_{01}	n_{02}
n_-	t_-											
t_-	n_-											

Supplementary Figure 3. **Neighbouring areas in \mathcal{M} .** The top-most row indicates a segment of a fence or a pseudo fence in \mathcal{M} . The left-most column is a list of the bijective areas involved in the motion of diamagnets. The inner cells indicate the neighbouring bijective areas. For example, the neighbour of t_+ in segment 1 is n_{+2} . This is a segment of a pseudo fence since both areas t_+ and n_{+2} are on \mathcal{M}_+ . The neighbour of n_{+1} in segment 9 is n_{02} . In this case the segment belongs to the fence \mathcal{F}^{0+} since it separates areas on \mathcal{M}_0 and \mathcal{M}_+ . A similar table can be constructed for the bijective areas involved in the motion of paramagnets.



Supplementary Figure 4. **Topological transition of the transport direction.** Ratchet modulation loop (a) $\mathcal{L}_C = (1_N, 2_N)$, (b) passing through the projection of a \mathcal{B}^0 bifurcation point, and (c) $\mathcal{L}_C = (1_N, 3_N)$ (top panels) and their corresponding path of steepest descend connecting points in \mathcal{M} (bottom panels). (a) The accessible path of steepest descend (P_l) connects the annihilation and return sites. The annihilation site is a preimage of the point where \mathcal{L}_C crosses from the north to the tropics in \mathcal{C} . Another preimage of the same point is the pseudo annihilation site, which is also connected to the return site through the path of steepest descend P_r . However, P_r is inaccessible because it develops from \mathcal{M}_0 . Both P_l and P_r are in $\mathcal{C} \otimes \mathcal{A}$, not in \mathcal{M} . They lie on opposite sides of the hole of $\mathcal{C} \otimes \mathcal{A}$, and hence induce transport in different directions. (b) The modulation loop passes through the projection of \mathcal{B}^0 . The annihilation site has moved (red arrow) along the segment 2 of the fence toward the \mathcal{B}^0 bifurcation point. The return site has moved (green arrow) along the segment 2 of the pseudo fence in \mathcal{M}^+ toward the pseudo bifurcation point. The pseudo annihilation site has moved (yellow arrow) along the segment 2 of the pseudo fence in \mathcal{M}^0 toward the \mathcal{B}^0 bifurcation point. Hence, the annihilation and the pseudo-annihilation site merge at the \mathcal{B}^0 bifurcation point. Both paths of steepest descend P_l and P_r are at this point accessible and they are topologically distinct. Following one path of steepest descend and returning in opposite direction via the other defines a non-zero homotopic loop that winds around a hole of $\mathcal{C} \otimes \mathcal{A}$. For this \mathcal{L}_C two ratchets with different directions coexist. (c) \mathcal{L}_C encircles the projection of \mathcal{B}^0 , and hence the former annihilation site in (a) has moved along the segment 3 of a pseudo fence in \mathcal{M}_0 , changing to a pseudo annihilation site. Its corresponding path of steepest descend P_l is now inaccessible. The other path P_r is now accessible, changing the transport direction.

SUPPLEMENTARY NOTE 1

Total external field. The pattern is a hexagonal lattice of bubbles with positive magnetization M immersed in an extended domain of negative magnetization $-M$. The domain walls between regions of opposite magnetization are very sharp. To obtain the total magnetic field \mathbf{H} we solve the Laplace equation $\Delta\mathbf{H} = 0$ subject to the boundary conditions:

$$\begin{aligned}\mathbf{H}(\mathbf{x}_A, z \rightarrow \infty) &= \mathbf{H}_{\text{ext}} \\ H_z(\mathbf{x}_A, z = 0) &= m(\mathbf{x}_A),\end{aligned}\tag{1}$$

where the local magnetization $m(\mathbf{x}_A)$ is given by

$$m(\mathbf{x}_A) = \begin{cases} +M & \text{if } \mathbf{x}_A \in \text{bubble} \\ -M & \text{if } \mathbf{x}_A \notin \text{bubble.} \end{cases}\tag{2}$$

The solution, given as a Fourier series, is:

$$\mathbf{H}(\mathbf{x}_A, z) = \begin{pmatrix} \mathbf{H}_{\text{ext}}^{\parallel} \\ \tilde{H}_{\text{ext}}^z \end{pmatrix} + 2(\tilde{M} + \tilde{H}_{\text{ext}}^z) \sum_{n=0}^{\infty} \sum_{m=0}^{n-1'} \frac{J_1(q_{nm}R)}{(q_{nm}R)^2} e^{-(q_{nm}z)} \sum_{j=1}^6 \begin{pmatrix} \mathbf{R}_{\pi/3}^j \cdot \mathbf{q}_{nm} R \sin(\mathbf{R}_{\pi/3}^j \cdot \mathbf{q}_{nm} \cdot \mathbf{x}_A) \\ q_{nm} R \cos(\mathbf{R}_{\pi/3}^j \cdot \mathbf{q}_{nm} \cdot \mathbf{x}_A) \end{pmatrix}\tag{3}$$

The presence of the ferrofluid renormalizes the magnetization and the z component of the external field, $\tilde{M} = M/(1 + \chi)$ and $\tilde{H}_{\text{ext}}^z = H_{\text{ext}}^z/(1 + \chi)$. In the above expression J_1 is the order one Bessel function of the first kind, $\mathbf{q}_{nm} = n\mathbf{q}^{(1)} + m\mathbf{q}^{(2)}$ is a reciprocal lattice vector with reciprocal unit vectors

$$\mathbf{q}^{(1)} = \frac{2\pi}{a \sin(\pi/3)} \begin{pmatrix} \cos(\pi/6) \\ -\sin(\pi/6) \end{pmatrix} \quad \mathbf{q}^{(2)} = \frac{2\pi}{a \sin(\pi/3)} \begin{pmatrix} 0 \\ 1 \end{pmatrix}.\tag{4}$$

q_{nm} denotes the magnitude of \mathbf{q}_{nm} . The radius of the magnetic bubbles can be found by matching the magnetic flux at $z = 0$ and $z \rightarrow \infty$, the result is $R = a\sqrt{(H_{\text{ext}}^z/M + 1)\sin(\pi/3)/(2\pi)}$, with a the period of the hexagonal lattice. The prime at the double sum in Supplementary Eq. (3) denotes the exclusion of the zero reciprocal vector ($n = m = 0$) of the first Brillouin zone from the sum. $\mathbf{R}_{\pi/3}$ is a rotation matrix that rotates all vectors by $\pi/3$ in the plane.

The Fourier modes decay exponentially as one moves away from the garnet film surface. At the elevation of the colloids only the leading order reciprocal lattice vectors of the second Brillouin zone ($n = 1, m = 0$) are needed for an accurate description of the field. The magnetic field at high elevations is therefore given by

$$\mathbf{H}(\mathbf{x}_A, z \gg 0) \approx \begin{pmatrix} \mathbf{H}_{\text{ext}}^{\parallel} \\ \tilde{H}_{\text{ext}}^z \end{pmatrix} + 2(\tilde{M} + \tilde{H}_{\text{ext}}^z) \frac{J_1(q_2 R)}{(q_2 R)^2} e^{-(q_2 z)} \sum_{i=1}^6 \begin{pmatrix} \mathbf{q}_{2i} \sin(\mathbf{q}_{2i} \cdot \mathbf{x}_A) \\ q_2 \cos(\mathbf{q}_{2i} \cdot \mathbf{x}_A) \end{pmatrix},\tag{5}$$

where the sum runs only over the six reciprocal lattice vectors of the second Brillouin zone

$$\mathbf{q}_{2i} = \frac{2\pi}{a} \begin{pmatrix} -\sin(2\pi i/6) \\ \cos(2\pi i/6) \end{pmatrix}, \quad i = 1, \dots, 6,\tag{6}$$

and $q_2 = 2\pi/a$. The colloids follow the magnetic potential $V_{\text{m}} = -\chi_{\text{eff}}\mu_0 H^2$. We use the unique scaled-potential $V = H^2$ to describe the motion of both diamagnets and paramagnets. At high elevations, the leading (not constant) term of V is given by

$$V \propto \sum_{i=1}^6 \begin{pmatrix} \mathbf{H}_{\text{ext}}^{\parallel} \\ \tilde{H}_{\text{ext}}^z \end{pmatrix} \cdot \begin{pmatrix} \mathbf{q}_{2i} \sin(\mathbf{q}_{2i} \cdot \mathbf{x}_A) \\ q_2 \cos(\mathbf{q}_{2i} \cdot \mathbf{x}_A) \end{pmatrix}.\tag{7}$$

Publication 3

Topologically protected colloidal transport above a square magnetic lattice

New Journal of Physics, **18**, 105009 (2016)

Daniel de las Heras^{a1}, **Johannes Loehr**^{a2}, Michael Lönne^{a3} and Thomas M. Fischer^{a2}

^{a1} Theoretical Physics, ^{a2} Experimental Physics and ^{a3} Mathematics, Faculty of Physics, Mathematics and Computer Science, University of Bayreuth, 95447 Bayreuth, Germany.

My Contribution

I contributed to the development of the theoretical description, to the interpretation of the simulation results and to the preparation of the manuscript.



PAPER

Topologically protected colloidal transport above a square magnetic lattice

OPEN ACCESS

RECEIVED

2 August 2016

REVISED

27 September 2016

ACCEPTED FOR PUBLICATION

13 October 2016

PUBLISHED

26 October 2016

Original content from this work may be used under the terms of the [Creative Commons Attribution 3.0 licence](#).

Any further distribution of this work must maintain attribution to the author(s) and the title of the work, journal citation and DOI.

Daniel de las Heras¹, Johannes Loehr², Michael Loenne³ and Thomas M Fischer²¹ Theoretische Physik, Institutes of Physics and Mathematics, Universität Bayreuth, D-95440 Bayreuth, Germany² Experimentalphysik, Institutes of Physics and Mathematics, Universität Bayreuth, D-95440 Bayreuth, Germany³ Mathematik, Institutes of Physics and Mathematics, Universität Bayreuth, D-95440 Bayreuth, GermanyE-mail: thomas.fischer@uni-bayreuth.de

Keywords: colloids, topology, transport, lattice, four-fold symmetry

Abstract

We theoretically study the motion of magnetic colloidal particles above a magnetic pattern and compare the predictions with Brownian dynamics simulations. The pattern consists of alternating square domains of positive and negative magnetization. The colloidal motion is driven by periodic modulation loops of an external magnetic field. There exist loops that induce topologically protected colloidal transport between two different unit cells of the pattern. The transport is very robust against internal and external perturbations. Theory and simulations are in perfect agreement. Our theory is applicable to other systems with the same symmetry.

1. Introduction

Controlling the transport of colloidal particles is a requisite in several applications such as lab-on-a-chip devices [1], drug delivery with colloidal carriers [2, 3], and computation with colloids [4].

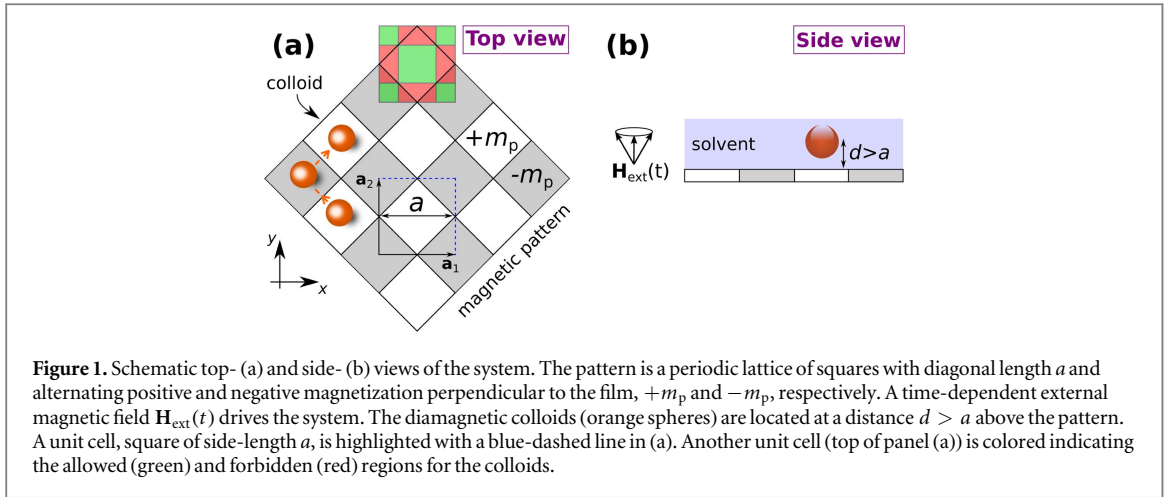
Techniques to control the motion of colloids include the use of gradient fields [5], thermal ratchets [6–8], liquid crystal-based solvents [9, 10], and active particles [11]. Colloidal particles are usually polydisperse in e.g. size, mass, etc. Therefore, the transport of a collection of colloids using the above techniques results always in a dispersion of the motion. One can avoid this by using optical tweezers [12] but at the expenses of having to move the colloids on a one-by-one basis.

Topological protection is a promising tool to overcome these problems. If the dynamics depends only on a topological invariant it is possible to have total control over the colloidal motion, independently of the intrinsic characteristics of the particles. Recently, we have studied the motion of magnetic colloids above a hexagonal magnetic pattern [13]. The system is driven by an external magnetic field. The positions of the colloids above the pattern are given by the minima of the magnetic potential which has contributions from the static field of the pattern and the time dependent external field. The set of stationary points of the potential form a surface in the full phase space whose topological properties fully determine the colloidal motion. There exist transport modes that are topologically protected and therefore extremely robust against perturbations.

The topology of the stationary surface, and hence the topologically protected transport modes, are unique for each type of lattice. Here, we theoretically study the transport of diamagnetic colloidal particles above a square magnetic lattice, and compare the results with computer simulations.

2. Theory

The colloids move in a plane at a distance $d > a$ above the pattern, with a the side-length of the unit cell of the pattern, see figure 1. A time-dependent external magnetic field $\mathbf{H}_{\text{ext}}(t)$ drives the system. The variation in time of $\mathbf{H}_{\text{ext}}(t)$ is slow enough such that the colloidal particles can adiabatically follow the minima of the magnetic potential at any time t . The magnetic potential is $V = -\chi_{\text{eff}} \mu_0 \mathbf{H} \cdot \mathbf{H}$, where \mathbf{H} is the total magnetic field with



contributions from the square pattern and the external potential, $\chi_{\text{eff}} < 0$ is the effective magnetic susceptibility of the diamagnets in the solvent, and μ_0 is the vacuum permeability.

\mathbf{H} can be expressed as a Fourier series with Fourier modes that decay exponentially with z . Hence, at high elevations, $z > a$, the potential is well approximated by $V \propto \mathbf{H}_{\text{ext}}(t) \cdot \mathbf{H}_p(\mathbf{x}_A)$, where

$$\mathbf{H}_p(\mathbf{x}_A) \propto \sum_{i=1}^4 \begin{pmatrix} q_{i,x} \sin(\mathbf{q}_i \cdot \mathbf{x}_A) \\ q_{i,y} \sin(\mathbf{q}_i \cdot \mathbf{x}_A) \\ q \cos(\mathbf{q}_i \cdot \mathbf{x}_A) \end{pmatrix}, \quad (1)$$

is, up to a multiplicative constant, the contribution from the magnetic pattern. Here,

$$\mathbf{q}_i = \frac{2\pi}{a} \begin{pmatrix} \sin(2\pi i/4) \\ -\cos(2\pi i/4) \end{pmatrix}, \quad i = 1, \dots, 4, \quad (2)$$

are the reciprocal lattice vectors of the second Brillouin zone with $q = 2\pi/a$ their common magnitude.

$\mathbf{x}_A = x_1 \mathbf{a}_1 + x_2 \mathbf{a}_2$ with \mathbf{a}_i the basic lattice vectors of the square pattern (see figure 1), are the coordinates in *action space* \mathcal{A} , i.e., the plane above the pattern in which the colloids move. We vary $\mathbf{H}_{\text{ext}}(t)$ on the surface of a sphere,

$$\mathbf{H}_{\text{ext}} = H_{\text{ext}} (\cos \phi_t \sin \theta_t, \sin \phi_t \sin \theta_t, \cos \theta_t). \quad (3)$$

The set (θ_t, ϕ_t) define our *control space*, \mathcal{C} , see figure 2(a). We measure θ_t with respect to the z axis and ϕ_t with respect to \mathbf{a}_1 . The system is driven with periodic closed loops of $\mathbf{H}_{\text{ext}}(t)$. There exist special loops that induce transport between different unit cells, i.e., when \mathbf{H}_{ext} returns to its initial position the particle is in a different unit cell.

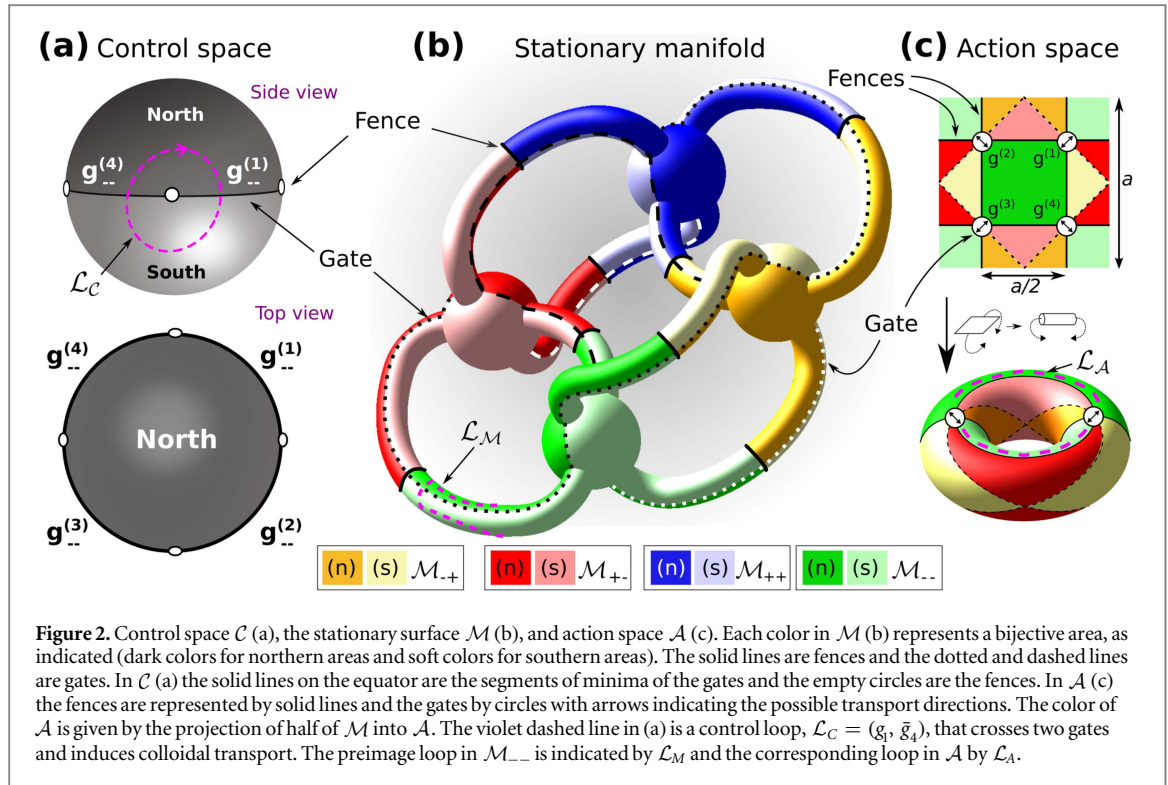
To understand the motion we need to look at the full phase space, i.e., the product space $\mathcal{C} \otimes \mathcal{A}$, with states given by $(\mathbf{H}_{\text{ext}}(t), \mathbf{x}_A)$. The stationary points satisfy $\nabla_{\mathcal{A}} V = 0$, with $\nabla_{\mathcal{A}}$ the gradient in \mathcal{A} . The set of all stationary points is a two-dimensional manifold in $\mathcal{C} \otimes \mathcal{A}$ that we call the *stationary manifold*, \mathcal{M} , see figure 2(b).

The correspondence between \mathcal{M} and \mathcal{C} is not bijective. Each direction of the external field is a point in \mathcal{C} . For each point in \mathcal{C} (with the exception of four special points that we discuss later) there are four points (preimages) in \mathcal{M} , the solutions of $\nabla_{\mathcal{A}} V = 0$. Two solutions are saddle points of V , one is a maximum, and the other one is a minimum. In \mathcal{A} the four points form a square of side $a/2$.

The correspondence between \mathcal{M} and \mathcal{A} is also not bijective. Consider the unit vectors $\hat{\mathbf{e}}_i(\mathbf{x}_A) = \partial_i \mathbf{H}_p / |\partial_i \mathbf{H}_p|$, $i = 1, 2$. Then, a point \mathbf{x}_A in \mathcal{A} is stationary if the external field points in a direction perpendicular to both $\hat{\mathbf{e}}_1$ and $\hat{\mathbf{e}}_2$, i.e.,

$$\mathbf{H}_{\text{ext}}^{(s)}(\mathbf{x}_A) = \pm H_{\text{ext}} \frac{\hat{\mathbf{e}}_1 \times \hat{\mathbf{e}}_2}{|\hat{\mathbf{e}}_1 \times \hat{\mathbf{e}}_2|}. \quad (4)$$

The subscript (s) stands for stationary. That is, each point in \mathcal{A} has two preimages $(\mathbf{H}_{\text{ext}}^{(s)}, \mathbf{x}_A)$ in \mathcal{M} (except for special points that we describe later).



Consider now the matrix of the second derivatives of V evaluated at the stationary field

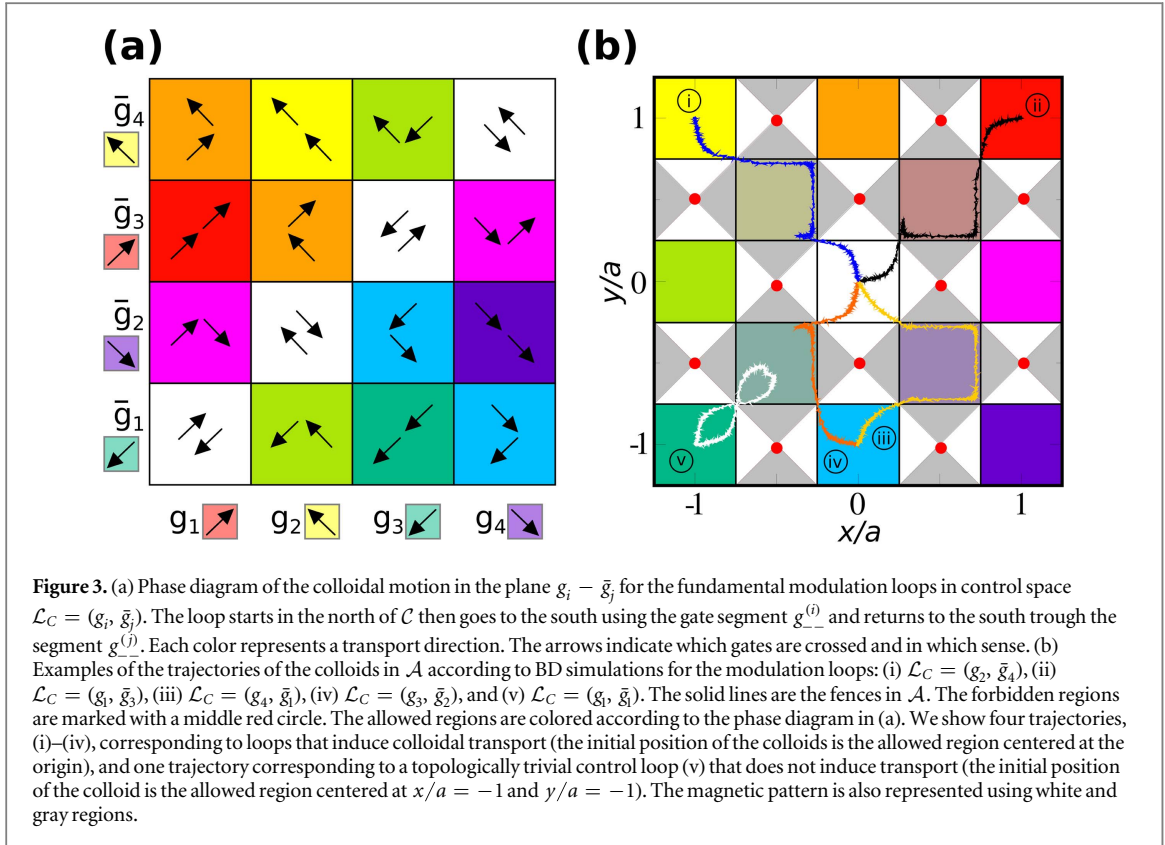
$$\nabla_{\mathcal{A}} \nabla_{\mathcal{A}} V|_{\mathbf{H}_{\text{ext}}^{(s)}} = \begin{pmatrix} \mathbf{H}_{\text{ext}}^{(s)} \cdot \partial_1 \partial_1 \mathbf{H}_p & \mathbf{H}_{\text{ext}}^{(s)} \cdot \partial_1 \partial_2 \mathbf{H}_p \\ \mathbf{H}_{\text{ext}}^{(s)} \cdot \partial_2 \partial_1 \mathbf{H}_p & \mathbf{H}_{\text{ext}}^{(s)} \cdot \partial_2 \partial_2 \mathbf{H}_p \end{pmatrix}, \quad (5)$$

which is diagonal since the mixed derivatives vanish, see (1). The stationary manifold \mathcal{M} is the union of submanifolds $\mathcal{M}_{\alpha\beta}$, where α (β) is the opposite sign of the eigenvalue of (5) with eigenvector pointing in the \mathbf{a}_1 (\mathbf{a}_2) direction. That is, $\mathcal{M} = \mathcal{M}_{++} \cup \mathcal{M}_{+-} \cup \mathcal{M}_{-+} \cup \mathcal{M}_{--}$. Hence the stable trajectories for the colloids reside in \mathcal{M}_{--} (minima of V). \mathcal{M}_{++} are maxima of V , and both \mathcal{M}_{+-} and \mathcal{M}_{-+} are saddle points. All the submanifolds are topologically equivalent since each point in \mathcal{C} has one preimage in each of the submanifolds.

The submanifolds share common borders in \mathcal{M} that we call the *fences*. Any two submanifolds with one common sign of one of the eigenvalues are glued together in \mathcal{M} through two fences. At the fences one eigenvalue changes its sign, i.e., the determinant of (5) vanishes. For example, \mathcal{M}_{++} and \mathcal{M}_{-+} share two fences. At both fences the eigenvalue of the eigenvector pointing along the \mathbf{a}_1 direction changes its sign. The stationary field, equation (4), points along $+\mathbf{a}_2$ in one fence and along $-\mathbf{a}_2$ in the other fence. Hence, in \mathcal{M} we have four submanifolds, and each one is double-joined to other two submanifolds. In other words, \mathcal{M} is a genus 5 surface, see figure 2(b).

Solving $\|\nabla_{\mathcal{A}} \nabla_{\mathcal{A}} V\| = 0$ we can see the fences in action and control space. In \mathcal{C} the fences are four equispaced points along the equator, corresponding to external fields pointing along $\pm\mathbf{a}_1$ and $\pm\mathbf{a}_2$, see figure 2(a). The fences divide action space in a square lattice (length $a/2$) of alternating allowed and forbidden regions, see figure 2(c) and figure 1(a). Using periodic boundary conditions \mathcal{A} is a torus. The allowed regions are areas of minima of V (projection of the submanifold \mathcal{M}_{--} into \mathcal{A}). In the forbidden areas all the stationary points are saddle points. As we have seen, a point in \mathcal{A} can be made stationary with two opposite external fields. Therefore \mathcal{M}_{++} and \mathcal{M}_{--} are projected into the same regions in \mathcal{A} . In other words, if there is a minimum of the potential in a given point in \mathcal{A} we can turn it into a maximum by just pointing the external field in the opposite direction. \mathcal{M}_{+-} and \mathcal{M}_{-+} are also projected into the same areas in \mathcal{A} . In figure 2(c) we show the projection of half of \mathcal{M} into \mathcal{A} (the half that contains all points closer to \mathcal{M}_{--} than to \mathcal{M}_{++}) such that each area has a unique meaning. That is, the projection of this half of \mathcal{M} into \mathcal{A} is bijective.

The fences cross in \mathcal{A} at points that we call the *gates* since they connect two allowed regions in \mathcal{A} . There are four gates $g^{(i)}$, $i = 1, \dots, 4$, see figure 2(c). The gates play a vital role for the colloidal motion. To find the gates in \mathcal{C} we note that the fences do not cross in \mathcal{M} but they do cross in \mathcal{A} . Hence, $\mathbf{H}_{\text{ext}}^{(s)}$ cannot be unique at the gates in \mathcal{A} (crossing points between fences in \mathcal{A}). The only possibility is that $\hat{\mathbf{e}}_1$ is parallel to $\hat{\mathbf{e}}_2$, see equation (4), at the gates. Therefore, as $\mathbf{H}_{\text{ext}}^{(s)} \perp \hat{\mathbf{e}}_1$, $\hat{\mathbf{e}}_2$, the gates in \mathcal{C} are great circles. For the present square lattice the gates in \mathcal{C} are located on the equator. Each gate is divided in four segments, $g_{\alpha\beta}^{(i)}$ where $\alpha, \beta = \pm$ are again the opposite signs



of the eigenvalues of (5). Although all gates in \mathcal{C} are in the equator, they are rotated such that the union of four segments with identical signs of the eigenvalues form a full equator, see figure 2(a).

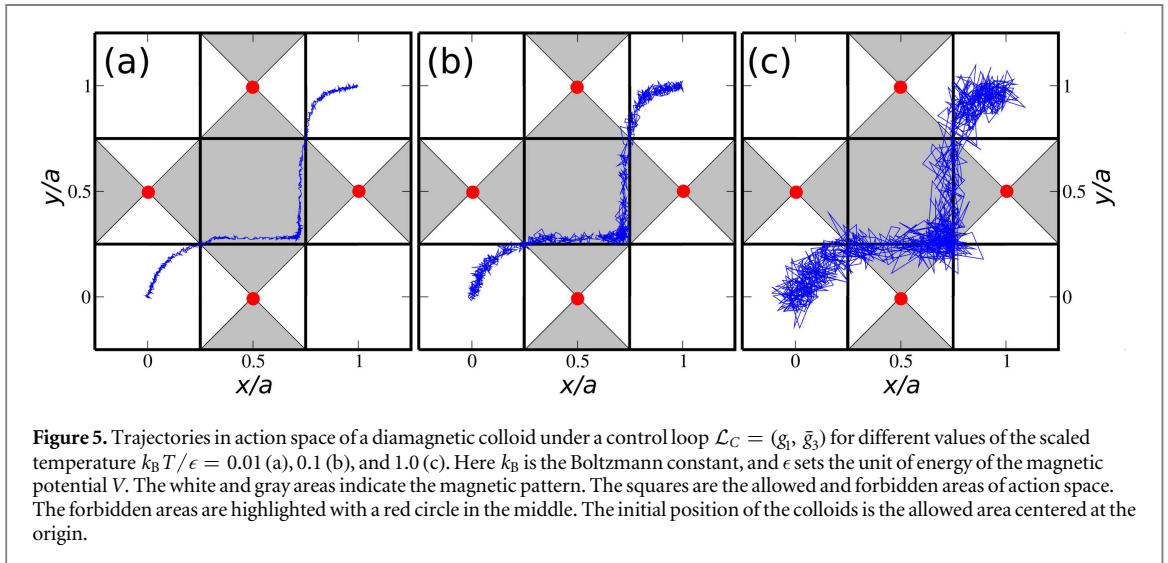
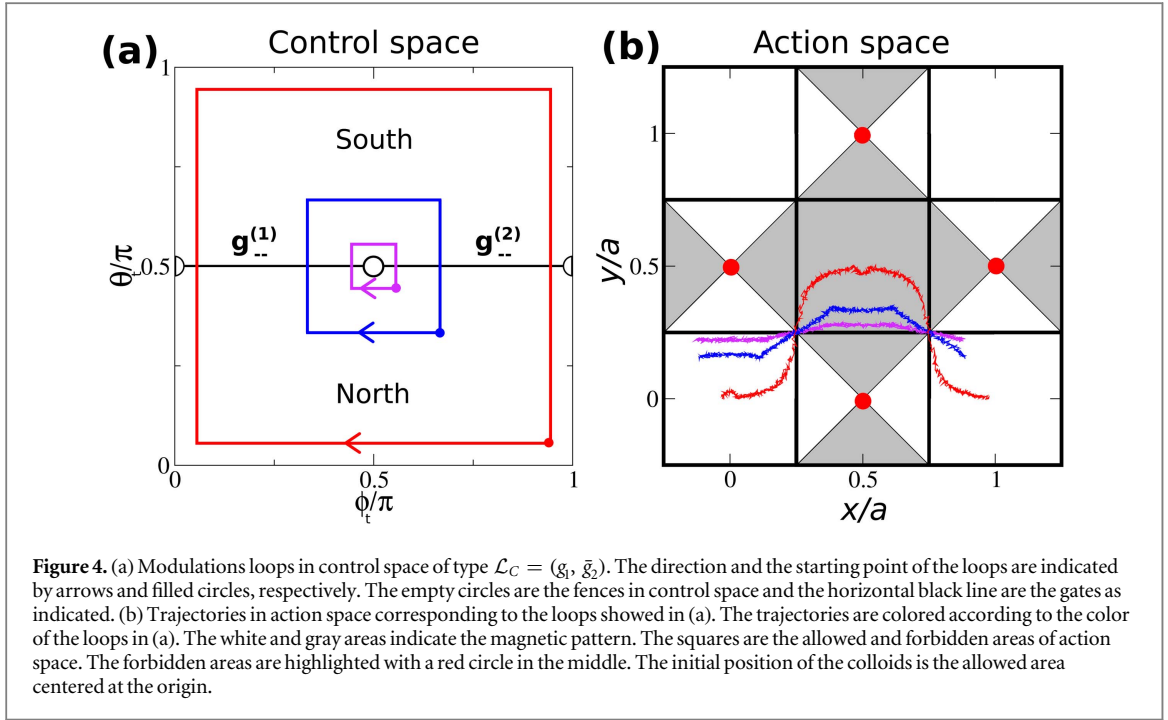
The gates split \mathcal{C} in two parts, the south (s) and the north (n), see figure 2(a). They also split each submanifold of \mathcal{M} in two parts $\mathcal{M}_{\alpha\beta} = \mathcal{M}_{\alpha\beta}^{(n)} \cup \mathcal{M}_{\alpha\beta}^{(s)}$, see figure 2(b). This splitting is very convenient since the resulting regions $\mathcal{M}_{\alpha\beta}^{(\nu)}$ with $\nu = n, s$ are simply connected bijective areas. That is, there are no holes in $\mathcal{M}_{\alpha\beta}^{(\nu)}$ and the correspondences between $\mathcal{M}_{\alpha\beta}^{(\nu)}$ and the other spaces (\mathcal{C} and \mathcal{A}) are unique.

3. Results

We are now in a position to understand the colloidal motion. Let \mathcal{L}_C be a closed modulation loop of the external field in \mathcal{C} . \mathcal{L}_C has four preimage loops in \mathcal{M} , one in each submanifold $\mathcal{M}_{\alpha\beta}$. Only the loop lying in \mathcal{M}_{--} is populated with colloids. This populated loop can be then projected into \mathcal{A} where we can read the actual trajectory of the colloids. Loops \mathcal{L}_C that induce colloidal transport from one unit cell to another in \mathcal{A} are only those that cross at least two different gates in control space, which is equivalent to enclosing at least one fence in \mathcal{C} . When \mathcal{L}_C crosses the segment $g_{-}^{(i)}$ in \mathcal{C} , the corresponding loop that transport the colloids in \mathcal{A} also crosses the gate $g^{(i)}$. Each gate in \mathcal{C} can be crossed from the north to the south or from the south to the north, which in \mathcal{A} results in opposite senses. Let $\mathcal{L}_C = (g_i, \bar{g}_j)$ be a loop of the external field that starts on the north of \mathcal{C} , then goes to the south of \mathcal{C} crossing the segment of minima of the potential of the gate i ($g_{-}^{(i)}$) and returns to the initial point in the north of \mathcal{C} using the segment of minima of the gate j . An example of such a loop is represented in figure 2(a). The phase diagram of the colloidal motion in the $g_i - \bar{g}_j$ plane is depicted in figure 3(a). It has been obtained (i) theoretically by translating loops in \mathcal{C} into loops in \mathcal{A} using the stationary surface \mathcal{M} and (ii) with standard Brownian dynamics simulations. Details of the simulations are provided in the appendix. The agreement between theory and simulations is perfect.

Loops that cross the same gate twice, i.e. $\mathcal{L}_C = (g_i, \bar{g}_i)$, do not induce transport between different unit cells (the initial and the final positions are the same). Loops that cross different gates induce transport between nearest or second nearest unit cells. There are two possible routes for each of the nearest unit cells (see e.g. $\mathcal{L}_C = (g_1, \bar{g}_4)$ and (g_2, \bar{g}_3)) and only one in the case of second nearest unit cells (e.g. $\mathcal{L}_C = (g_1, \bar{g}_3)$). In figure 3(b) we show Brownian dynamics trajectories for selected modulation loops.

The colloidal transport is very robust against internal and external perturbations. The shape of \mathcal{L}_C , for example, is completely irrelevant. Only the gates that \mathcal{L}_C crosses are important. In figure 4 we show the



trajectories in action space for three modulation loops that cross the same two gates, $\mathcal{L}_C = (\underline{g}_1, \underline{g}_2)$, yet following different paths. The trajectories in \mathcal{A} differ but the starting and ending allowed regions are the same. The motion is also robust against changes in the speed of the modulation, the thermal noise, and properties of the colloidal particles such as size, mass, effective susceptibility, etc (see an example in figure 5). Therefore we can transport in a dispersion-free and precise way a collection of particles with a broad distribution of masses, sizes, etc.

The reason behind this robustness is that the transport direction depends only on a topological invariant, and hence it is topologically protected. For each loop in \mathcal{M} we can define a set of 10 winding numbers, two for each hole of \mathcal{M} . $S_{\mathcal{M}}$, the set of winding numbers of the loop in \mathcal{M}_{--} , is the topological invariant. In each of the regions of the phase diagram $S_{\mathcal{M}}$ does not vary. Alternatively we can define the topological invariant of loops in \mathcal{A} and \mathcal{C} . The loop that lies in \mathcal{M}_{--} is projected into a loop in \mathcal{A} and \mathcal{C} . Since \mathcal{M}_{--} is topologically equivalent to control space without the fences, \mathcal{C}' , the correspondence between loops in \mathcal{M}_{--} and \mathcal{C}' is bijective. $S_{\mathcal{C}}$, the set of winding numbers of loops around the fences in \mathcal{C}' induce corresponding winding numbers of loops around the torus in action space ($S_{\mathcal{A}} = \{w_1, w_2\}$ with $w_i = 0, \pm 1$) via the loops in \mathcal{M}_{--} . Each of the eight non-zero values of $S_{\mathcal{A}}$ corresponds to a type of transport in \mathcal{A} . $S_{\mathcal{A}}$ and $S_{\mathcal{C}}$ are also topological invariants, they remain unchanged for each type of transport, i.e, in each region of the phase diagram of figure 3(a).

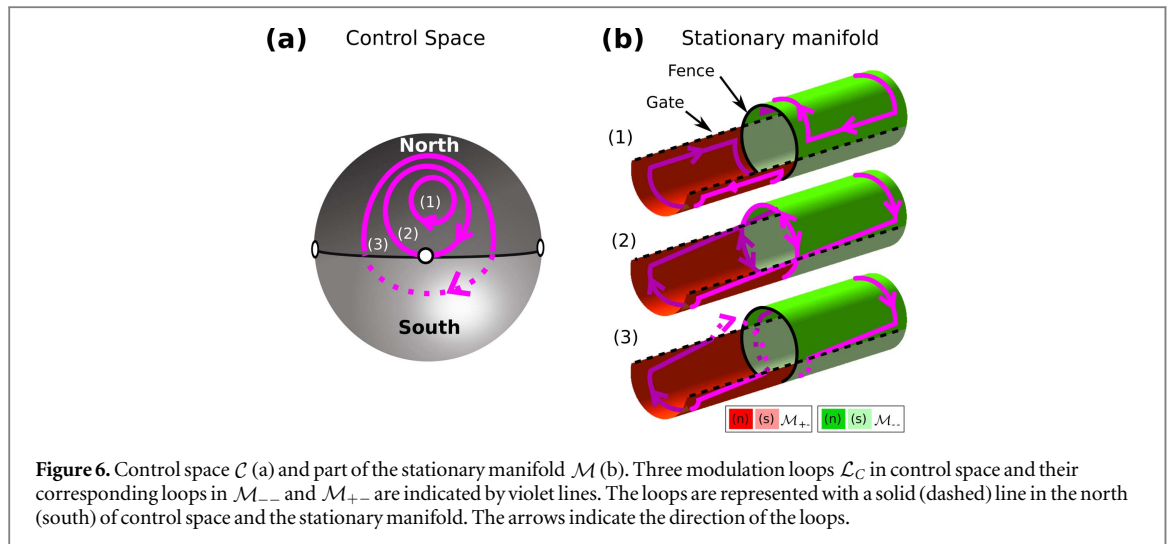


Figure 6. Control space \mathcal{C} (a) and part of the stationary manifold \mathcal{M} (b). Three modulation loops \mathcal{L}_C in control space and their corresponding loops in \mathcal{M}_{--} and \mathcal{M}_{+-} are indicated by violet lines. The loops are represented with a solid (dashed) line in the north (south) of control space and the stationary manifold. The arrows indicate the direction of the loops.

How is it possible to change the direction of transport if it is topologically protected? There are always operations that break the topological protection. This is precisely what happens at the interface between two transport directions in the phase diagram, see figure 3(a). At the interfaces between two different transport modes the topological protection is lost allowing for a change in the transport mode. This occurs for modulation loops that cross at least one of the fences in control space. In figure 6 we show an example of this process. The loop labeled as (1) lies entirely on the north of \mathcal{C} . That is, it does not cross gates and hence does not induce transport between different unit cells. The corresponding loops in \mathcal{M} lie on the northern areas of \mathcal{M} . There is one loop in each of the submanifolds of \mathcal{M} . Figure 6 shows only the loops in \mathcal{M}_{--} and \mathcal{M}_{+-} . When the loop in \mathcal{C} touches one of the fences (see loop (2) in figure 6) the loops in \mathcal{M}_{--} and \mathcal{M}_{+-} join at the fence (the loops in \mathcal{M}_{++} and \mathcal{M}_{-+} also join at a different fence). At this point the colloids, which follow the loop in \mathcal{M}_{--} , have two alternative paths: (i) a loop that resides entirely in the north of \mathcal{M}_{--} and (ii) a loop that lies in both the north and the south of \mathcal{M}_{--} and hence induce colloidal transport between different cells. The motion is not topologically protected in the sense that two different trajectories are possible. Next, we expand the loop in \mathcal{C} such that it encloses one fence in \mathcal{C} and hence crosses two gates, see loop (3) in figure 6. In \mathcal{M} the loops in \mathcal{M}_{--} and \mathcal{M}_{+-} are now disjointed and have interchanged a segment at the fence. The result is two loops that no longer reside in the northern areas of \mathcal{M} . The loop in \mathcal{M}_{--} winds around the holes of \mathcal{M} inducing colloidal transport. The direction of transport has changed with respect to the initial loop (1).

Due to the thermal noise in Brownian dynamics simulations the particles fluctuate around the minima of the potential, exploring the neighborhood of \mathcal{M}_{--} in $\mathcal{C} \otimes \mathcal{A}$. Hence, modulation loops in control space that do not cross a fence, but pass close enough to it, might also be topologically unprotected, leading to two differing transport modes in \mathcal{A} . How close the control loop has to be to the fence in order to be deprotected depends on the magnitude of the thermal noise. The thermal noise effectively expand the fences in \mathcal{C} into the surrounding areas, and broaden the topological transition in \mathcal{A} .

4. Discussion

We have explained the motion of diamagnetic colloids for which the effective susceptibility is negative. Paramagnetic colloids have a positive effective susceptibility, and hence will follow the maxima of V . The minima and the maxima of V always comove in \mathcal{A} separated by $\mathbf{r} = (a/2, a/2)$. Therefore, paramagnetic colloids perform the same motion as diamagnets but displaced by \mathbf{r} .

From an experimental view point, it is possible to use magnetic bubble lattices [14] or lithographic patterns [15] to generate the pattern. Possible methods to levitate the colloids above the pattern consists of using a ferrofluid solvent [13] and the deposition of a polymer layer [16] on the magnetic pattern.

The colloidal transport is fully determined by the topology of the manifold \mathcal{M} , which is unique for each type of magnetic pattern. For example, the stationary manifold of a hexagonal pattern is a genus 7 surface [13]. There, the modulation loops in \mathcal{C} that induce transport of colloids must cross the fences in \mathcal{C} , which are lines instead of points as in the present study. As a result, transport modes of hexagonal and square patterns are completely different. In both, hexagonal and square lattices, the topological invariant in \mathcal{A} is the set of two winding numbers around the hole in \mathcal{A} . This is just a consequence of the dimension of \mathcal{A} . Control space \mathcal{C} neither contains all the information. For example, in square lattices the transition between transport modes occurs for

those loops that cross a fence. However, in hexagonal lattices, a fence crossing loop in \mathcal{C} is a necessary but not sufficient condition to change the transport mode. What fully determines the transport modes is the stationary manifold \mathcal{M} (the topology, the fences, and how \mathcal{M} is projected into \mathcal{A} and \mathcal{C}). In \mathcal{M} the topological invariant is the set of winding numbers around the holes, which is very different in square (\mathcal{M} has genus 5) and hexagonal (\mathcal{M} has genus 7) lattices.

The topologically protected transport modes we have shown here can be understood as bulk modes sustained (driven) by an external field. The transport occurs in the bulk of the periodic system. Other forms of topologically protected motion occur at the edges of a periodic system, such as e.g., the motion of electrons in topological insulators [17], mechanical solitons [18–20], phonons [21], and photons [22, 23] among others. There, a perturbation populates an edge state that cannot scatter into the bulk due to the topology of the system. Our theory is transferable to other systems with the same symmetry. Hence, topological bulk states might exist in e.g. excitons in superlattices [24, 25], tight-binding models [26], and cold atoms in optical lattices [27]. Topologically protected edge states might also occur at the borders of finite magnetic lattices. Their topological properties might be substantially different from those of bulk states. How the edge states in our particle system compare to other edge states in wave systems is a very interesting subject for future studies.

In wave systems, such as e.g. topological insulators, the topology of the band structure is characterized by the Chern numbers of the bands. Each Chern number can be computed as an integral over the Berry curvature of the band [28]. In our particle system we describe the topological protection in terms of the stationary manifold. Both descriptions are probably equivalent in some form.

Acknowledgments

This publication was funded by the German Research Foundation (DFG) and the University of Bayreuth in the funding programme Open Access Publishing.

Appendix. Brownian dynamics simulations

We use Brownian dynamics to simulate the motion of a diamagnetic colloid above the pattern. The coordinates in action space are \mathbf{x}_A , and the equation of motion is given by

$$\xi \frac{d\mathbf{x}_A(t)}{dt} = -\nabla_A V(\mathbf{x}_A, \mathbf{H}_{\text{ext}}(t)) + \boldsymbol{\eta}(t),$$

where t is the time, ξ is the friction coefficient, and $\boldsymbol{\eta}$ is a Gaussian random force with a variance given by the fluctuation-dissipation theorem. The magnetic potential V has contributions from the external field \mathbf{H}_{ext} and the magnetic pattern (see the main text).

The equation of motion is integrated in time with a standard Euler algorithm:

$$\mathbf{x}_A(t + \Delta t) = \mathbf{x}_A(t) - \nabla_A V \Delta t + \boldsymbol{\delta}\mathbf{r}, \quad (\text{A1})$$

where Δt is the time step, and $\boldsymbol{\delta}\mathbf{r}$ is a random displacement sampled from a gaussian distribution with standard deviation $\sqrt{2\Delta t k_B T / \xi}$. Here k_B is the Boltzmann constant, and T is absolute temperature. Before starting the modulation loop in \mathcal{C} we first equilibrate the system by running 10^4 time steps such that the colloids find the minimum of the magnetic potential at $t = 0$.

References

- [1] Gao L, Tahir M A, Virgin L N and Yellen B B 2011 *Lab Chip* **11** 4214
- [2] Kataoka K, Harada A and Nagasaki Y 2001 *Adv. Drug Deliv. Rev.* **47** 113
- [3] Müller R H 1991 *Colloidal Carriers for Controlled Drug Delivery and Targeting: Modification, Characterization and In Vivo Distribution* (London: Taylor and Francis)
- [4] Phillips C L, Jankowski E, Krishnatreya B J, Edmond K V, Sacanna S, Grier D G, Pine D J and Glotzer S C 2014 *Soft Matter* **10** 7468
- [5] Erbe A, Zientara M, Baraban L, Kreidler C and Leiderer P 2008 *J. Phys.: Condens. Matter* **20** 404215
- [6] Matthias S and Müller F 2003 *Nature* **424** 53
- [7] Engel A, Müller H W, Reimann P and Jung A 2003 *Phys. Rev. Lett.* **91** 060602
- [8] Tierno P, Sagues F, Johansen T H and Fischer T M 2009 *Phys. Chem. Chem. Phys.* **11** 9615
- [9] Stark H and Venzki D 2001 *Phys. Rev. E* **64** 031711
- [10] Turiv T, Lazo I, Brodin A, Lev B I, Reiffenrath V, Nazarenko V G and Lavrentovich O D 2013 *Science* **342** 1351
- [11] Jiang H-R, Yoshinaga N and Sano M 2010 *Phys. Rev. Lett.* **105** 268302
- [12] Grier D G 2003 *Nature* **424** 810
- [13] Loehr J, Loenne M, Ernst A, de las Heras D and Fischer T M 2016 *Nat. Commun.* **7** 11745
- [14] Bobeck A H, Bonyhard P I and Geusic J E 1975 *Proc. IEEE* **63** 1176
- [15] Terris B D and Thomson T 2005 *J. Phys. D: Appl. Phys.* **38** R199
- [16] Tierno P and Fischer T M 2014 *Phys. Rev. Lett.* **112** 048302

- [17] Hasan M Z and Kane C L 2010 *Rev. Mod. Phys.* **82** 3045
- [18] Kane C and Lubensky T 2014 *Nat. Phys.* **10** 39
- [19] Chen B G-G, Upadhyaya N and Vitelli V 2014 *Proc. Natl Acad. Soc.* **111** 13004
- [20] Paulose J, Chen B G and Vitelli V 2015 *Nat. Phys.* **11** 153
- [21] Huber S D 2016 *Nat. Phys.* **12** 621
- [22] Rechtsman M C, Zeuner J M, Plotnik Y, Lumer Y, Podolsky D, Dreisow F, Nolte S, Segev M and Szameit A 2013 *Nature* **496** 196
- [23] Lu L, Joannopoulos J D and Soljačić M 2016 *Nat. Phys.* **12** 626
- [24] Agulló-Rueda F, Mendez E E and Hong J M 1989 *Phys. Rev. B* **40** 1357
- [25] Kim N Y, Kusudo K, Wu C, Masumoto N, Löffler A, Höfling S, Kumada N, Worschech L, Forchel A and Yamamoto Y 2011 *Nat. Phys.* **7** 681
- [26] Sun K, Gu Z, Katsura H and Das Sarma S 2011 *Phys. Rev. Lett* **106** 236803
- [27] Chern G-W, Chien C-C and Di Ventra M 2014 *Phys. Rev. A* **90** 013609
- [28] Shen S-Q 2013 *Topological Insulators: Dirac Equation in Condensed Matters* (Berlin: Springer)

Publication 4

Colloidal topological insulators

Communications Physics, 1, 4 (2018)

Johannes Loehr^{a1}, Daniel de las Heras^{a2}, Adam Jarosz^b, Maciej Urbaniak^b, Feliks Stobiecki^b, Andreea Tomita^c, Rico Huhnstock^c, Iris Koch^c, Arno Ehresmann^c, Dennis Holzinger^c and Thomas M. Fischer^{a1}

^{a1} Experimental Physics and ^{a2} Theoretical Physics, Faculty of Physics, Mathematics and Computer Science, University of Bayreuth, 95447 Bayreuth, Germany.

^b Institute of Molecular Physics, Polish Academy of Sciences, ul. M. Smoluchowskiego 17, 60-179 Poznań, Poland.

^c Institute of Physics and Center for Interdisciplinary Nanostructure Science and Technology (CINSaT), University of Kassel, Heinrich-Plett-Strasse 40, D-34132 Kassel, Germany.

My Contribution

I had the idea for the conceptual design of the magnetic structures and designed the modulation of the particle orbits. I performed, analyzed and interpreted the experiments and wrote the manuscript with the help of Daniel de las Heras and Thomas Fischer.



COMMUNICATIONS PHYSICS

ARTICLE

DOI: 10.1038/s42005-017-0004-1

OPEN

Colloidal topological insulators

Johannes Loehr¹, Daniel de las Heras ¹, Adam Jarosz², Maciej Urbaniak², Feliks Stobiecki², Andreea Tomita³, Rico Huhnstock³, Iris Koch³, Arno Ehresmann³, Dennis Holzinger³ & Thomas M. Fischer ¹

Topological insulators insulate in the bulk but exhibit robust conducting edge states protected by the topology of the bulk material. Here, we design a colloidal topological insulator and demonstrate experimentally the occurrence of edge states in a classical particle system. Magnetic colloidal particles travel along the edge of two distinct magnetic lattices. We drive the colloids with a uniform external magnetic field that performs a topologically non-trivial modulation loop. The loop induces closed orbits in the bulk of the magnetic lattices. At the edge, where both lattices merge, the colloids perform skipping orbits trajectories and hence edge-transport. We also observe paramagnetic and diamagnetic colloids moving in opposite directions along the edge between two inverted patterns; the analogue of a quantum spin Hall effect in topological insulators. We present a robust and versatile way of transporting colloidal particles, enabling new pathways towards lab on a chip applications.

¹Institute of Physics and Mathematics, Universität Bayreuth, D-95440 Bayreuth, Germany. ²Institute of Molecular Physics, Polish Academy of Sciences, ul. M. Smoluchowskiego 17, 60-179 Poznan, Poland. ³Institute of Physics and Centre for Interdisciplinary Nanostructure Science and Technology (CINSaT), Universität Kassel, Heinrich-Plett-Strasse 40, D-34132 Kassel, Germany. Correspondence and requests for materials should be addressed to T.M.F. (email: thomas.fischer@uni-bayreuth.de)

Topologically protected quantum edge states arise from the non trivial topology (non-vanishing Chern number) of the bulk band structure¹. If the Fermi energy is located in the gap of the bulk band structure, like in an ordinary insulator, edge currents might propagate along the edges of the bulk material. The edge currents are protected as long as perturbations to the system do not cause a band gap closure. The topological mechanism at work is not limited to quantum systems but has been shown to work equally well for classical photonic^{2,3}, phononic^{4,5}, solitonic⁶, gyroscopic⁷, coupled pendulums⁸, and stochastic⁹ waves. It is also known that the topological properties survive the particle limit when the particle size is small compared to the width of the edge. In the semi-classical picture of the quantum Hall effect, the magnetic field enforces the electrons to perform closed cyclotron orbits in the bulk of the material. Near the edge, the electrons can only perform skipping orbits, i.e., open trajectories that allow electronic transport along the edge¹⁰. Considerable effort to simulate such semi-classical trajectories has been undertaken^{10–13}. Their experimental observation, however, is quite difficult. So far, skipping orbits were only observed in two dimensional electron gas driven by microwaves¹⁴ and with neutral atomic fermions in synthetic Hall ribbons¹⁵.

We present here the experimental observation in a colloidal system of skipping orbits and hence edge states. These edge states allow for a robust transport of colloids along the edges and also the corners of the underlying magnetic lattice.

Results

We use a thin cobalt-based magnetic film lithographically patterned via ion bombardment^{16–18}. The pattern consists of a patch of hexagonally arranged circular domains (mesoscopic pattern lattice constant $a \approx 7 \mu\text{m}$) surrounded by a stripe pattern, see Fig. 1a. Both magnetic regions consist of alternating domains magnetized in the $\pm z$ -direction normal to the film. Paramagnetic colloidal particles of diameter $2.8 \mu\text{m}$ are immersed in water (or aqueous ferrofluid) and move at a fixed elevation above the pattern. Hence, the particles move in a two-dimensional plane that we refer to as action space, \mathcal{A} . A uniform time-dependent external magnetic field $\mathbf{H}_{\text{ext}}(t)$ of constant magnitude ($H_{\text{ext}} = 4\text{kAm}^{-1}$) is superimposed to the non-uniform and time-independent magnetic field of the pattern \mathbf{H}_p . We vary $\mathbf{H}_{\text{ext}}(t)$ on the surface of a sphere that we call the control space \mathcal{C} (Fig. 1b).

In Refs. 18–20, we demonstrate how bulk transport of colloids above different magnetic lattices can be topologically protected.

For each lattice symmetry there exist special modulation loops of \mathbf{H}_{ext} in \mathcal{C} that induce transport of colloids in \mathcal{A} . These loops share a common feature, they wind around special objects in \mathcal{C} ^{18–20}. For a hexagonal, six-fold symmetric lattice, the control space of paramagnetic colloids is characterized by twelve points connected by six pairs of segments (Fig. 1b). A modulation loop encircling one pair of segments in \mathcal{C} transports the colloids in \mathcal{A} one unit cell along one of the six possible directions of the hexagonal lattice $\pm \mathbf{a}_1^h, \mathbf{a}_2^h, \pm (\mathbf{a}_1^h - \mathbf{a}_2^h)$, with \mathbf{a}_1^h , and \mathbf{a}_2^h the lattice vectors. For example, encircling the red segments in Fig. 1b transports the paramagnetic particles into the $(\mathbf{a}_1^h - \mathbf{a}_2^h)$ -direction. If we now rotate the modulation loop such that it encircles the yellow segments, the transport occurs along \mathbf{a}_1^h , i.e., the transport direction rotates $\pi/3$ with respect to the previous $(\mathbf{a}_1^h - \mathbf{a}_2^h)$ -direction. Using these results we construct a hexagonal cyclotron orbit of hexagonal side length na^h , $n=1,2,3,\dots$ of a paramagnetic particle above the bulk of a hexagonal lattice. The corresponding cyclotron modulation loop in \mathcal{C} consists of six connected parts. Each of the six parts of the loop winds n times around a different pair of segments of \mathcal{C} , and therefore transports a particle n unit cells along one of the hexagonal directions in \mathcal{A} . In Fig. 1b we show a $n=2$ cyclotron modulation loop in \mathcal{C} . The corresponding colloidal trajectory in \mathcal{A} is depicted in Fig. 2a, b. Colloidal particles above the bulk of the hexagonal pattern perform closed hexagonal cyclotron orbits of the desired side length. The cyclotron modulation loop does not wind around the special objects in \mathcal{C} for a stripe pattern (located on the equator of \mathcal{C} ¹⁸). Hence, the colloids above the stripes are not transported. For the current modulation loops, the edge between the hexagonal and the stripe pattern is an edge between topologically non-trivial and trivial patterns, and allows for the existence of edge states, as it is the case in quantum topological insulators. Edge states are possible for those particles close to the edge between both patterns. The paramagnetic particles perform skipping orbits, see Fig. 2a, b and Supplementary Movie 1. That is, the particles do not follow all six directions of the closed cyclotron orbit but skip one of the hexagonal directions. The skipping direction is different for different orientations of the edge. A successive series of these skipping orbits results in an open trajectory along the edge direction. The skipping orbits allow for robust transport in armchair edges, i.e., edges oriented along one of the six directions of the hexagonal lattice, and also around the corners where two edges join.

The skipping of single directions can be explained by taking a closer look at the bulk transport mechanism, explained in detail in Refs. 18–20. Here, we just summarize the main concepts. For a

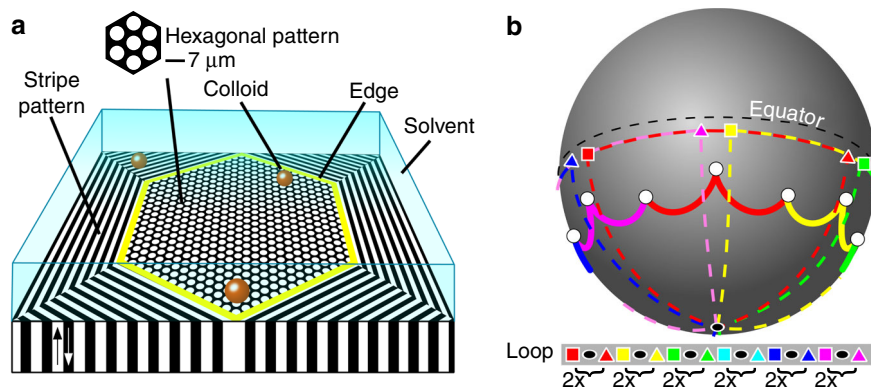


Fig. 1 Colloidal topological insulator. **a** Paramagnetic colloids are confined at a constant distance above a magnetically structured film of thickness 3.5 nm with regions of positive (white) and negative (black) magnetization perpendicular to the film. The film is a hexagonal lattice embedded into a stripe pattern. **b** Control space \mathcal{C} for a hexagonal lattice: twelve bifurcation points (empty circles) connected by segments (solid lines). Winding around a pair of equal color segments moves the colloids one unit cell along one of the hexagonal directions. The modulation loop used here is indicated by dashed lines and also in the legend. The loop starts at the red square and winds anticlockwise twice around each pair of equal color segments

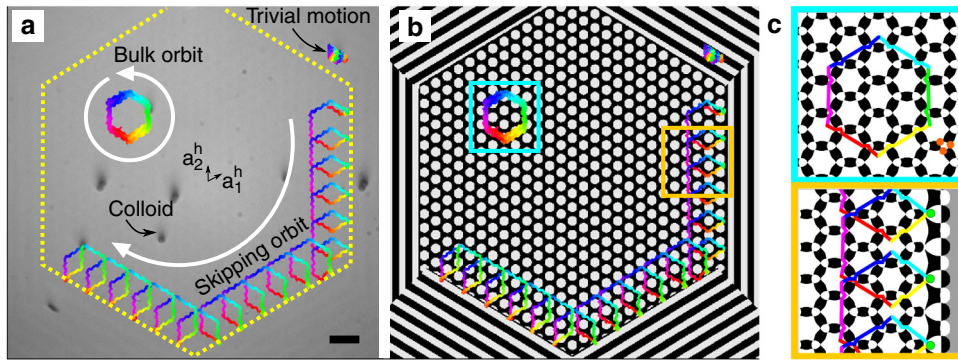


Fig. 2 Skipping and bulk orbits. **a** Microscopy images of paramagnetic colloidal particles at the end of a transport process. Scale bar $15\mu\text{m}$. Three trajectories are shown and indicated: a bulk orbit on top of the hexagonal pattern, a skipping orbit at the edge, and the trivial motion of a particle above the stripe pattern. The color of the trajectories matches that of the modulation loop (Fig. 1b). The edge between the hexagonal and the stripe patterns is indicated by a dashed yellow line. The colloidal motion can be seen in the Supplementary Movie 1. **b** Colloidal trajectories superimposed on the actual magnetic pattern. **c** Bulk (top) and skipping (bottom) orbits superimposed on action space, \mathcal{A} . The white (black) areas are allowed (forbidden) regions for the colloids. The grey area is the indifferent region on top of the stripe pattern. In the skipping orbits the colloids skip the green section of the bulk-trajectory. Three gates connecting adjacent allowed regions are highlighted with orange circles in the top panel

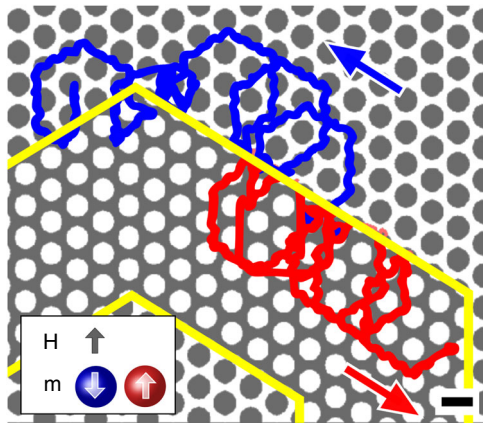


Fig. 3 Colloidal spin Hall effect. Trajectories followed by a paramagnetic (red) and a diamagnetic (blue) particle along the edge (yellow lines) of two hexagonal magnetic patterns with opposite magnetization. The scale bar is $7\mu\text{m}$. The particles are driven by the modulation loop shown in Fig. 1b. The magnetic moment \mathbf{m} of the paramagnets (diamagnets) is parallel (antiparallel) to the total magnetic field \mathbf{H} . A video of the colloidal motion is provided in the Supplementary Movie 2

fixed external field there are stationary points of the magnetic potential in each unit cell of the magnetic lattice. The colloids are transported by following the minima of the magnetic potential. Action space can be split into allowed, forbidden, and indifferent regions. In the allowed regions the stationary points are minima, whereas in the forbidden regions the only possible stationary points are saddle points. No extrema of the total magnetic potential exist in the indifferent regions, which are present only in stripe patterns. Therefore, the colloids can occupy only allowed and indifferent regions. We show in Fig. 2c the split of \mathcal{A} into the different types of regions for the current pattern. Two adjacent allowed regions touch each other at special points in \mathcal{A} that we refer to as the gates. To achieve transport between adjacent unit cells, a colloid has to pass through two gates. In the bulk of the hexagonal lattice transport is possible along all six crystallographic directions¹⁹. However, close to the edge this is no longer true. The necessary gates to transport the particle into the edge or parallel to it are no longer available. In consequence those particles close to the edge have to perform skipping orbits.

Transport above an infinite lattice remains unchanged if the magnetization of both the pattern and the colloidal particles is inverted. Thus, diamagnetic particles (magnetic holes) on a pattern respond to the external field in the same way as paramagnetic particles on an inverted pattern. In Fig. 3 and Supplementary Movie 2 we show the chiral response of paramagnetic and diamagnetic particles at the edge between two hexagonal patterns with inverted magnetization. The susceptibility of the ferrofluid-based solvent is set to a value in between the effective particle susceptibilities. We use the same cyclotron modulation loop as before. The loop induces anticlockwise cyclotron orbits of paramagnets on the bulk of one lattice and of diamagnets on the bulk of the inverted lattice. Near the edge, both types of colloids perform skipping orbits above the pattern that is non-trivial for them. Since the edge between both patterns is located in opposite directions from the center of the corresponding orbits, the skipping directions are antiparallel. Hence, this results in skipping orbits along the edge where both types of particles move on opposite sides of the edge in opposite directions. This represents the colloidal analogue of the quantum spin Hall effect²¹, in which electrons of opposite spins move in different directions along the same edge.

Discussion

A nontrivial topology of the shape of colloidal particles can be used to control the formation of topological defects in a nematic host^{22,23}. Here we have used topology in a dynamic way to control the motion of colloidal particles. We experimentally demonstrated how to realize a colloidal topological insulator. Like in the semi-classical picture of the quantum Hall effect, particles above the bulk of the material move following closed orbits, and particles close to the edge perform skipping orbits giving rise to robust edge states. The fine details of the pattern are irrelevant to determine the bulk transport properties¹⁸. At the edges, however, transport does depend on the details of the pattern. For example the exact positions of the stripes with respect to the circular domains and the orientation of the edges influence the edge states. Similar effects are also observed in graphene, where only certain edges support edge states. The versatility of our robust colloidal transport opens the possibility to transport multiple particles along multiple different edges into different directions using just a unique external modulation.

Our skipping orbits are an example of a purely geometric trajectory. As long as the modulation period T is slow enough, i.e.,

$T \geq 10s$, and the external magnetic field is sufficiently strong, $H_{\text{ext}} \geq 0.5 \text{ kAm}^{-1}$, the transport of the colloids does neither depend on the period, nor does it depend on the absolute value of the external field. Under those conditions only a small fraction of the colloidal particles, which adhere to the surface of the magnetic film, is not transported. The displacement over one period of the mobile particles, however, does only depend on the initial position of the particles with respect to the edge of the hexagonal pattern: particles in the bulk show no displacement over one period, while particles close to the edge are displaced parallel to the edge. The strongest limitation is therefore the period of the modulation, which is solely imposed by the magnetization of the pattern. Modulation periods orders of magnitude faster can be achieved by using e.g., garnet films^{19,24}.

Here we have worked at a low particle density: less than one particle per unit cell. New phenomenology will arise at high densities due to excluded volume effects. We expect for example quantized particle edge currents, as have been observed in the hexagonal bulk²⁵.

Colloids can be used to mimic aspects of molecules²⁶ and atoms²⁷. Our colloidal topological insulator goes a step further and mimics the behaviour of electrons in a colloidal system.

Data availability. The datasets generated during and/or analyzed during the current study are available from the corresponding author on reasonable request.

Received: 19 September 2017 Accepted: 18 December 2017

Published online: 22 February 2018

References

- Hasan, M. Z. & Kane, C. L. Colloquium: topological insulators. *Rev. Mod. Phys.* **82**, 3045–3067 (2010).
- Rechtsman, M. C. et al. Photonic Floquet topological insulators. *Nature* **496**, 196–200 (2013).
- Perczel, J. et al. Topological quantum optics in two-dimensional atomic arrays. *Phys. Rev. Lett.* **119**, 023603 (2017).
- Kane, C. L. & Lubensky, T. C. Topological boundary modes in isostatic lattices. *Nat. Phys.* **10**, 39–45 (2014).
- Xiao, M. et al. Geometric phase and band inversion in periodic acoustic systems. *Nat. Phys.* **11**, 240–244 (2015).
- Paulose, J., Chen, B. G. & Vitelli, V. Topological modes bound to dislocations in mechanical metamaterials. *Nat. Phys.* **11**, 153–156 (2015).
- Nash, L. M. et al. Topological mechanics of gyroscopic metamaterials. *Proc. Natl Acad. Sci.* **112**, 14495–14500 (2015).
- Huber, S. D. Topological mechanics. *Nat. Phys.* **12**, 621–623 (2016).
- Murugan, A. & Vaikuntanathan, S. Topologically protected modes in non-equilibrium stochastic systems. *Nat. Commun.* **8**, 13881 (2017).
- Beenakker, C. W. J., van Houten, H. & van Wees, B. J. Skipping orbits, traversing trajectories, and quantum ballistic transport in microstructures. *Superlattices Microstruct.* **5**, 127–132 (1989).
- Davies, N. et al. Skipping and snake orbits of electrons: singularities and catastrophes. *Phys. Rev. B* **85**, 155433 (2012).
- Shi, L., Zhang, S. & Chang, K. Anomalous electron trajectory in topological insulators. *Phys. Rev. B* **87**, 161115 (2013).
- Montambaux, G. Semiclassical quantization of skipping orbits. *Eur. Phys. J. B* **79**, 215–224 (2011).
- Zhiron, O. V., Chepelianskii, A. D. & Shepelyansky, D. L. Towards a synchronization theory of microwave-induced zeroresistance states. *Phys. Rev. B* **88**, 035410 (2013).
- Mancini, M. et al. Observation of chiral edge states with neutral fermions in synthetic Hall ribbons. *Science* **349**, 1510–1513 (2015).
- Chappert, C. et al. Planar patterned magnetic media obtained by ion irradiation. *Science* **280**, 1919–1922 (1998).
- Kuświk, P. et al. Colloidal domain lithography for regularly arranged artificial magnetic out-of-plane monodomains in Au/Co/Au layers. *Nanotechnology* **22**, 095302 (2011).
- Loehr, J. et al. Lattice symmetries and the topologically protected transport of colloidal particles. *Soft Matter* **13**, 5044–5075 (2017).
- Loehr, J., Loenne, M., Ernst, A., de las Heras, D. & Fischer, Th. M. Topological protection of multiparticle dissipative transport. *Nat. Commun.* **7**, 11745 (2016).
- De las Heras, D., Loehr, J., Loenne, M. & Fischer, Th. M. Topologically protected colloidal transport above a square magnetic lattice. *New J. Phys.* **18**, 105009 (2016).
- Bernevig, B. A. & Zhang, S.-C. Quantum spin hall effect. *Phys. Rev. Lett.* **96**, 106802 (2006).
- Senyuk, B. et al. Topological colloids. *Nature* **493**, 200–205 (2013).
- Martinez, A., Hermsillo, L., Tasinkevych, M. & Smalyukh, I. I. Linked topological colloids in a nematic host. *Proc. Natl Acad. Sci.* **112**, 4546–4551 (2015).
- Tierno, P., Johansen, T. H. & Fischer, Th. M. Localized and delocalized motion of colloidal particles on a magnetic bubble lattice. *Phys. Rev. Lett.* **99**, 038303 (2007).
- Tierno, P. & Fischer, Th. M. Excluded volume causes integer and fractional plateaus in colloidal ratchet currents. *Phys. Rev. Lett.* **112**, 048302 (2014).
- Glotzer, S. C. & Solomon, M. J. Anisotropy of building blocks and their assembly into complex structures. *Nat. Mat.* **6**, 557–562 (2007).
- Poon, W. Colloids as big atoms. *Science* **304**, 830–831 (2004).

Acknowledgements

A.T. was supported by PhD fellowship of the University of Kassel. This work was supported by the University of Bayreuth open access fund.

Author contributions

J.L., D.d.l.H., and T.M.F. designed and performed the experiment, and wrote the manuscript with input from all the other authors. A.J., M.U., and F.S. produced the magnetic film. A.T., R.H., I.K., A.E., and D.H. performed the fabrication of the micro-magnetic domain patterns within the magnetic thin film.

Additional information

Supplementary information accompanies this paper at <https://doi.org/10.1038/s42005-017-0004-1>.

Competing interests: The authors declare no competing financial interests.

Reprints and permission information is available online at <http://npg.nature.com/reprintsandpermissions/>

Publisher's note: Springer Nature remains neutral with regard to jurisdictional claims in published maps and institutional affiliations.



Open Access This article is licensed under a Creative Commons Attribution 4.0 International License, which permits use, sharing, adaptation, distribution and reproduction in any medium or format, as long as you give appropriate credit to the original author(s) and the source, provide a link to the Creative Commons license, and indicate if changes were made. The images or other third party material in this article are included in the article's Creative Commons license, unless indicated otherwise in a credit line to the material. If material is not included in the article's Creative Commons license and your intended use is not permitted by statutory regulation or exceeds the permitted use, you will need to obtain permission directly from the copyright holder. To view a copy of this license, visit <http://creativecommons.org/licenses/by/4.0/>.

© The Author(s) 2018

Publication 5

Magnetic guidance of the magnetotactic bacterium *Magnetospirillum gryphiswaldense*

Soft Matter, **12**, 3631 (2016)

Johannes Loehr^a, Daniel Pfeiffer^b, Dirk Schüler^b and Thomas M.
Fischer^a

^a Experimental Physics, Faculty of Physics, Mathematics and Computer Science, University of
Bayreuth, 95447 Bayreuth, Germany.

^b Department of Microbiology, Faculty of Biology, Chemistry and Earth Science, University of
Bayreuth, 95447 Bayreuth, Germany.

My Contribution

I performed and analyzed the experiments. Thomas Fischer and myself developed the theoretical model, conducted the scientific discussion and wrote the manuscript.


 Cite this: *Soft Matter*, 2016,
12, 3631

 Received 15th February 2016,
Accepted 3rd March 2016

DOI: 10.1039/c6sm00384b

www.rsc.org/softmatter

Magnetic guidance of the magnetotactic bacterium *Magnetospirillum gryphiswaldense*†

Johannes Loehr, Daniel Pfeiffer, Dirk Schüler and Thomas M. Fischer

Magnetospirillum gryphiswaldense is a magnetotactic bacterium with a permanent magnetic moment capable of swimming using two bipolarly located flagella. In their natural environment these bacteria swim along the field lines of the homogeneous geomagnetic field in a typical run and reversal pattern and thereby create non-differentiable trajectories with sharp edges. In the current work we nevertheless achieve stable guidance along curved lines of mechanical instability by using a heterogeneous magnetic field of a garnet film. The successful guidance of the bacteria depends on the right balance between motility and the magnetic moment of the magnetosome chain.

1 Introduction

Bacteria are comparably simple organisms living in a low Reynolds number environment.¹ Active swimming in one forward or backward direction using periodic conformational changes of flagella requires non-reciprocal conformational pathways of the flagella. The additional capability of an active change in orientation of a bacterium requires a second non-reciprocal closed pathway in the flagella motion. Well studied bacteria like *Escherichia coli*^{2–4} take advantage of active locomotion (run) and active yet random reorientations (tumble). Chemotactic sensing enables bacteria to regulate the length of run-periods⁵ and thus to navigate in chemical gradients. Non-reciprocal counterclockwise rotation of a helical bundle of flagella lets the cell run straight forward, while a clockwise rotation randomly disintegrates the bundle and causes *Escherichia coli* to tumble *i.e.* to randomly reorient. The marine bacterium *Vibrio alginolyticus* that possesses a single left-handed polar flagellum seems to have another solution to the steering problem. It swims back and forth *via* clockwise or counterclockwise rotation of the single flagellum and uses flicks,⁶ *i.e.* conformational changes of the flagellum where the tip of the flagellum traces a hyperbolic spiral to change orientation.

The same flagellum with respect to the cell body is used to swim and to reorient. Consequently swimming and reorientation conformational changes are executed during different periods of time one after another. This results in a non-differentiable typical type of trajectory consisting of relatively straight segments that are interrupted by fast changes in orientation that when ignoring the different distribution of step sizes share some similarities to Levy walks.⁷ These trajectories are well adapted for chemotaxis.

However, their inability to swim along differentiable curves makes it hard to imagine a way of steering the bacteria along arbitrary smooth paths. In this work we will demonstrate that passive guidance of bacteria along lines of instability is possible.

Lines of instability are locations of vanishing force on immotile bacteria, but repelling force in the line surroundings. Therefore any deviation from the line of instability will induce forces pushing the bacteria away from this location (Fig. 1b). To counteract these forces one needs the interplay of a passive reorientation of the organism towards the line and of the active swimming of the bacterium against the forces that push it away from the line (Fig. 1c). Passive guidance is then possible if their swimming speed lets them dwell into regions of different magnetic field orientations faster than they passively reorient to the new field directions. We will show that *Magnetospirillum gryphiswaldense* is the apparent tightrope artist among the bacteria.

This magnetotactic bacterium has two bipolarly located flagella to swim back and forth^{8,9} and a permanent longitudinal magnetic moment¹⁴ $m \approx 1.5 \times 10^{-15} \text{ A m}^2$ that arises from magnetosomes (membrane vesicles filled with magnetite and attached to a cytoskeleton). In nature *Magnetospirillum gryphiswaldense* is preferentially oriented along the geomagnetic field lines. The magnetosome chain and the ability to sense oxygen are supposed to facilitate navigation to its growth-favoring zones close to the oxic-anoxic transition zone in aquatic environments.^{9–13} Swimming reversals occur when both flagella reverse their angular frequency of rotation.⁸ Trajectories are straight lines with sharp approximately π edges.

The design of magnetic patterns on garnet films causes heterogeneous magnetic fields differing substantially from the homogeneous field of the natural habitat. It enabled us to guide *Magnetospirillum gryphiswaldense* along lines of instability, if the bacteria's force of propulsion surmounts a certain threshold.

Experimentalphysik V, University of Bayreuth, 95440 Bayreuth, Germany.

E-mail: Johannes.Loehr@uni-bayreuth.de

† Electronic supplementary information (ESI) available. See DOI: 10.1039/c6sm00384b

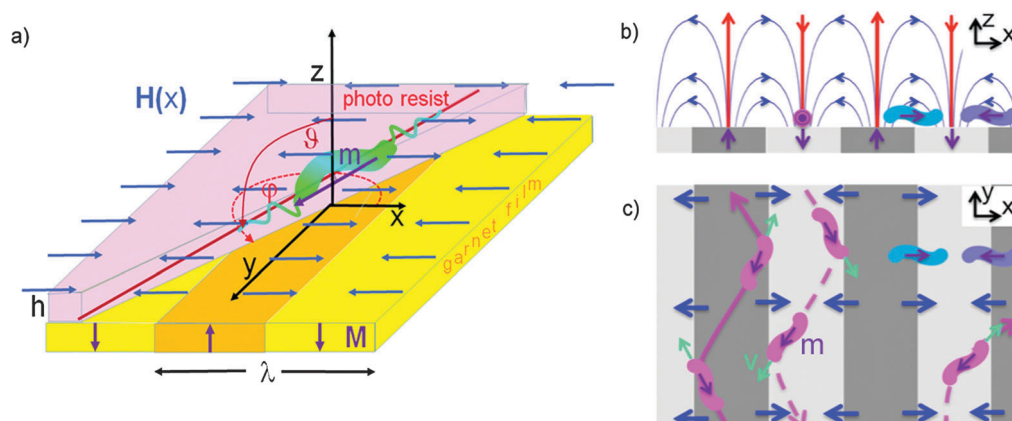


Fig. 1 Scheme of (a) *Magnetospirillum gryphiswaldense* with magnetic moment m (purple) on top of the stripe pattern of the garnet film of period λ with definitions of the orientational coordinates (θ, φ) at the position $(x = 0, y = 0, z = h)$ of the axial-symmetric bacterium. The height h of the photo-resist spin coated on top of the garnet film defines the elevation of the bacterium above the garnet surface. The blue arrows depict the basic features of the magnetic field texture. If the parameters of the habitat are designed appropriately one can guide the bacteria although evolution did not provide those microorganisms with sophisticated motion control. The ratio of the propulsion force of the bacteria to the magnetic force of the pattern on the magnetic moment defines a relative fitness f (eqn (6)). (b) Side view of the setup including the magnetic field lines (blue) of the garnet film. In the middle of the stripes the magnetic field (red lines) has no component parallel to the film. Therefore the force on immotile bacteria ($f < 1$) vanishes on these lines of instability (pink bacteria). For small deviations from these lines immotile bacteria will be forced to align along the field lines and ultimately be trapped over the domainwalls (blue and purple bacteria). (c) The magnetic torque, that tries to align the magnetic moment of the bacteria to the external field, reorients the bacteria in such a way that together with their active motion a passive guidance along the stripes can be achieved. Note that only one polarization (velocity v (green) parallel to the magnetic moment m (purple)) can be guided on top of the bright stripes (middle trajectory). The other polarization (v parallel to $-m$) can only be guided on top of the dark stripes (left trajectory). If the type of stripe does not match the type of bacterium the reorientation does not guide the bacterium (right trajectory).

The guided steering of *Magnetospirillum gryphiswaldense* works whether the line is straight or curved.

2 Experimental

It is reasonable to assume that the magnetosome chain is the only component of *Magnetospirillum gryphiswaldense* that responds to the magnetic field. A heterogeneous magnetic field will cause a magnetic Kelvin force $\mathbf{F} = \mu_0 \nabla(\mathbf{m} \cdot \mathbf{H})$ and a magnetic torque $\tau = \mu_0 \mathbf{m} \times \mathbf{H}$ on the bacteria without generating an active

feedback to the swimming behavior of the bacteria during the time of observation. Here μ_0 is the vacuum permeability.

We used a wild type strain of *Magnetospirillum gryphiswaldense* dispersed in flask standard growth medium (FSM)¹⁵ placed on top of two ferrite garnet films (FGFs) with a magnetic stripe pattern of period $\lambda = 4.8(6.3) \mu\text{m}$ with different effective magnetizations that are (or are not) coated with a photoresist of thickness $h = 1.2 \mu\text{m}$ ($h = 0$) (Fig. 1) to vary the magnetic forces. Video polarization microscopy is used for simultaneous visualization of the stripe pattern and the bacteria. Fig. 2 shows three polarization microscopy images of bacteria on the uncoated

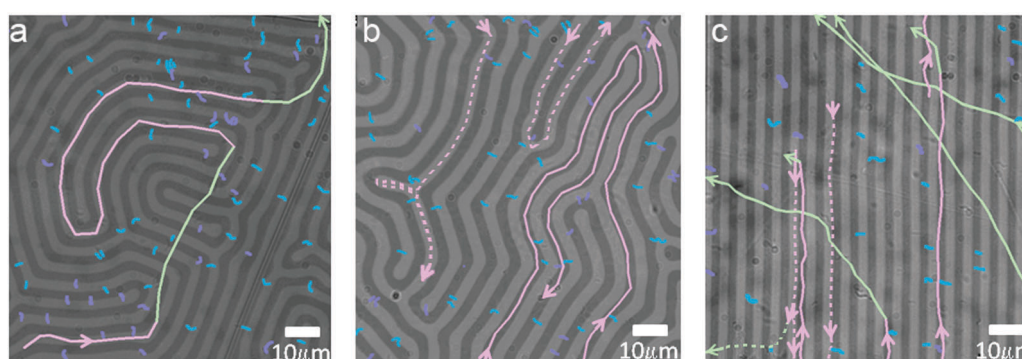


Fig. 2 Polarization microscopy images of trapped *Magnetospirillum gryphiswaldense* (colored blue and purple) on various garnet films with different effective magnetization and guided (pink) and ignorant (green) trajectories of the non-trapped bacteria. Initially downward starting trajectories are marked as dotted lines while upward trajectories are marked as solid lines. (a) Shows a high magnetization, (b) a low magnetization and (c) a coated high magnetization garnet film. This causes the relative fitness to increase from (a) ($f_a < 1$) over (b) ($f_b \approx 2$) to (c) ($f_c \approx 2.5$). Guided bacteria undulate around the central line in the middle of the stripe (see pink trajectories in (c)). Video clips of the bacteria on the three garnet films are supplied with the ESI.†

(a and b) and coated (c) garnet film together with the trajectories on top of the film. A homogeneous external magnetic field pulse ($\mathbf{H}_{\text{ext}} = H_{\text{ext}}\mathbf{e}_y$, $H_{\text{ext}} = 4000 \text{ A m}^{-1}$, and time duration $\Delta t = 1 \text{ s}$) in the y -direction (along the major direction $\varphi = \pi/2$ of the stripes of the garnet film pattern) preorients the magnetic moments of all bacteria in the same positive y -direction. The trajectories of the bacteria after the pulse are then recorded as a function of time. We distinguish between three types of bacteria: trapped (blue and purple) bacteria, guided (pink) bacteria, and ignorant (green) bacteria.

Most of the bacteria on the uncoated high magnetization film in Fig. 2a are bacteria that are trapped at the domain walls $x/\lambda = (n + 1/2)\pi$, $\varphi = n\pi$ with n even (purple) and n odd (blue), where they are oriented along the field lines perpendicular to the stripes and no longer move. Some (the pink trajectories) bacteria, however, are guided along the stripes. They swim on top of the stripe domains with an orientation along the stripes and apparently avoid the domain walls. Although they are oriented perpendicular to the magnetic field lines, a stable guidance is achieved. All guided bacteria swimming in the direction of their magnetic moment (dotted lines) swim on top of a downward magnetized (bright) stripe $x/\lambda = 2n\pi$, and all bacteria swimming antiparallel to their magnetic moment (solid lines) swim on upward magnetized stripes $x/\lambda = (2n + 1)\pi$ (dark stripes) (Fig. 2b). The guided bacteria remain on the same type of stripe when a stripe makes a U-turn, such that long after the pre-orienting pulse one observes guided bacteria swimming on either type of stripe in either direction. On a spin-coated garnet film (Fig. 2c) non-trapped bacteria become more frequent as compared to the uncoated film, however their ability to follow curved or even straight stripes decreases such that some guided bacteria ignore the stripes and are converted into ignorant bacteria (green trajectories) that follow their momentary swimming direction rather than the stripes. The behavior of the bacteria with orientation perpendicular to the stripes changes with the thickness of the coating. On coated garnet patterns they no longer get trapped (if they are motile) but follow trajectories crossing the stripe pattern and are thus ignorant bacteria.

3 Theoretical model

We can theoretically understand the classification of trapped, guided, and ignorant bacteria in terms of their relative fitness, defined as the ratio of propulsion to magnetic forces: we assume that magnetic forces normal to the garnet film and in plane magnetic torques are both balanced by hydrodynamic interactions with the solid garnet film such that neither the height z nor the tilt angle to the normal θ of the bacteria change with time. The leading term of the magnetic field above the stripe pattern of wavelength $\lambda = 2\pi/q$ and effective magnetization M^{16} can be written as

$$\mathbf{H} = \nabla\psi \quad (1)$$

where

$$\psi = \frac{M}{q} e^{-qz} \cos(qx) \quad (2)$$

We approximate the hydrodynamic mobility of the bacteria by that of a rigid rod of length l and diameter d placed in a liquid of shear viscosity η . We assume an isotropic translational mobility¹⁷

$$\mu_t = \frac{\ln(l/d) + 0.19315}{4\pi\eta l} \quad (3)$$

and a rotational mobility¹⁸

$$\mu_r = \frac{3(\ln(2l/d) - 0.8)}{\pi\eta l^3} \quad (4)$$

of the bacteria and a constant propulsion force F into the direction of the magnetic moment.

$$\mathbf{m} = m(\cos\varphi \sin\theta, \sin\varphi \sin\theta, \cos\theta) \quad (5)$$

Hence we assume that the bacteria are in the run-mode and perform conformational changes of the forward flagellum that are uncorrelated to the forces on the magnetosome chain. The bacteria are hence completely unaware of the stripe pattern such that the magnetic forces and torques are acting on their bodies without producing active counter actions of the flagella. We use dimensionless units defined by the dimensionless length $qx = \hat{x}$ and the dimensionless time $q\mu_t F t = \hat{t}$. Two dimensionless parameters govern the dynamics: the relative fitness

$$f = \frac{F e^{qh}}{q\mu_0 m M \sin\theta} \quad (6)$$

is defined as the ratio of the propulsion force of the bacterium to the maximum magnetic force exerted on it at an elevation h . The mobility parameter $\beta = \mu_r/q^2 \mu_t$ measures whether it is easier to turn ($\beta > 1$) or to translate ($\beta < 1$). Both parameters can be changed by changing either the properties of the bacteria or the properties of the stripe pattern. Using these abbreviations we end up with the differential equations

$$\begin{pmatrix} \dot{\hat{x}} \\ \dot{\hat{y}} \end{pmatrix} = \begin{pmatrix} (1 - f^{-1} \cos x) \cos\varphi \\ \sin\varphi \end{pmatrix} \quad (7)$$

$$\dot{\varphi} = \frac{\beta}{f} \sin\varphi \sin x,$$

where we have dropped the hat above the non-dimensional quantities. $\text{sign } p = \text{sign } f = \text{sign}(\mathbf{m} \cdot \mathbf{v})$ defines the polarization of the bacterium and measures whether its velocity \mathbf{v} is parallel or antiparallel to the magnetic moment.¹⁹ The differential equation is invariant under the transformation $f \rightarrow -f$ and $x \rightarrow x + \pi$ that maps bacteria of one polarization on one type of stripe on bacteria of opposite polarization on the opposite stripe. For the discussion we may therefore without the loss of generality assume that $f > 0$. The trajectories in x, φ space have the solutions

$$\frac{\sin\varphi}{\sin\varphi_0} = \left(\frac{f - \cos x}{f - \cos x_0} \right)^\beta \quad (8)$$

If $\dot{\hat{x}} = 0 = \dot{\varphi}$ then we have a fixed point in the subspace of the variables x and φ . There are motile fixed points if $\dot{\hat{y}} \neq 0$ *i.e.* bacteria that move and immotile fixed points if $\dot{\hat{y}} = 0$ and the bacteria do not move. The differential equation has motile fixed

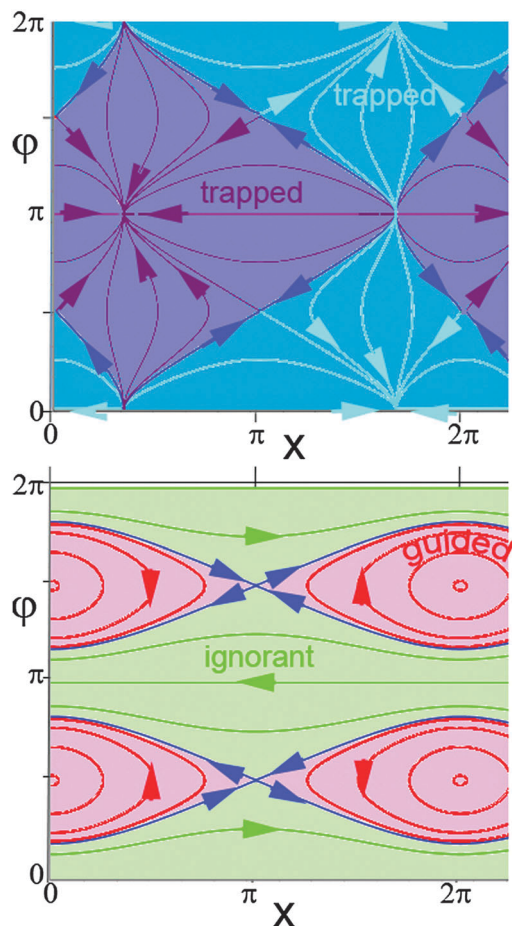


Fig. 3 Trajectories of bacteria of subcritical relative fitness $0 < f = 0.5 < 1$ (top) and of optimal relative fitness $f = 2 > 1$ (bottom) (mobility parameter $\beta = 0.6$).

points at $x_m = n\pi$, $\varphi_m = \pi/2, 3\pi/2$ and immotile fixed points at $x_i = \pm(-1)^n \arccos f$, $\varphi_i = n\pi$. For relative fitness $0 < f < 1$ the fixed points x_m, φ_m are unstable and the bacteria at $t \rightarrow \infty$ end up in the immotile fixed points $x_i = -(-1)^n \arccos f$, $\varphi_i = n\pi$ (cyan and purple arrows in Fig. 3 top). There is no motion in the immotile fixed points. For relative fitness $f > 1$ the motile fixed points $x_m = n\pi$, $\varphi_m = \pm\pi/2$ with even n correspond to a stable motion along or against the y -direction along the stripe (red circles around the fixed points in Fig. 3 bottom). The odd stripes (n odd) are unstable (fixed points in the crossing of the blue separatrix in Fig. 3 bottom). Bacteria can be guided only above one type of stripe not on the other. On the stripe center they then have the unperturbed speed $v_{||}$ and the angular frequency $\omega_{||} = v_{||}/\lambda = 1$ sets our clock of reference. The angular frequency of undulations ω_u of the guided bacteria and the angular frequency of traversing the pattern ω_{\perp} of the ignorant bacteria within the linearized solutions of (7) and for a relative fitness above the threshold $f > 1$:

$$\begin{aligned}\omega_u &= f^{-1} \sqrt{\beta(f-1)} \\ \omega_{\perp} &= \sqrt{1-f^{-2}}\end{aligned}\quad (9)$$

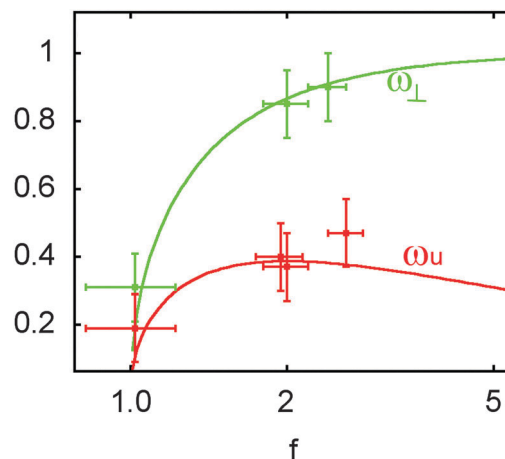


Fig. 4 Guidance reaction angular frequency ω_u and stripe traversing angular frequency ω_{\perp} as a function of the relative fitness for a mobility parameter of $\beta = 0.6$. The data are measurements of ω_u, ω_{\perp} , and f by using eqn (6) and the effective magnetization of the film as described in ref. 16.

The maximum frequency

$$\omega_{u,\max} = \frac{1}{2} \sqrt{\beta}. \quad (10)$$

of the undulations is reached when the relative fitness equals $f = 2$. It is the ideal relative fitness allowing the bacteria to cope the best with curved stripes. Guided bacteria coexist with ignorant bacteria. Apart from guided trajectories circulating around a fixed point there are extended trajectories in the region $\varphi = n\pi$. They correspond to ignorant bacteria crossing the stripe pattern. Non-magnetic bacteria ($m = 0$, $\hat{=} f \rightarrow \infty$) that have infinite relative fitness are not guided since the (pink) area enclosed by the separatrix shrinks to zero and the vanishing fraction of guided bacteria has zero reaction angular frequency such that they are unable to cope with curved stripes. At $f \rightarrow \infty$ all bacteria are ignorant bacteria. Guiding thus requires a finite magnetic moment. Increasing the magnetic moment reduces the relative fitness (6) since the bacteria have to cope with magnetic forces. The magnetic moment must be strong enough to reorient the bacteria in a reasonable time, but not too strong to keep the relative fitness above the threshold relative fitness.

We can vary the relative fitness of the bacteria by coating the garnet film with a photo-resist that levitates the bacteria to a value $z = h$ above the garnet surface. Without a photo-resist the bacteria relative fitness is below the threshold $f < 1$ and the bacteria get trapped in the magnetic pattern and cease to move (Fig. 2a). As the relative fitness (6) increases more and more bacteria are guided along the stripes (Fig. 2b). Even higher f causes more and more bacteria to become ignorant (Fig. 2c). Fig. 4 shows that measurements of the undulation and ignorant frequencies on different garnet films and different heights agree well with the theoretical predictions of eqn (9).

4 Conclusions

In conclusion, among the fit, fitter, and fittest (*cf.* eqn (6)) magnetotactic bacteria the fitter bacteria are guided best. The magnetic

pattern consists of two types of stripes creating opposite magnetic field textures that both are instable for immotile bacteria. Beyond the critical threshold fitness bacteria can be divided into guided and ignorant bacteria, coexisting with each other. Guided bacteria are guided on one of the stripes when in the forward swimming mode and on the other when in the backward swimming mode. The average orientation of guided bacteria is with their magnetic moment pointing into a non-equilibrium direction perpendicular to the average magnetic field. The guidance is an emergent phenomenon arising without the need of active reaction of the bacteria to the artificial environment.

Acknowledgements

We thank Katharina Silbermann for handling cultures of *Magnetospirillum gryphiswaldense*.

References

- 1 E. M. Purcell, Life at Low Reynolds-Number, *Am. J. Phys.*, 1977, **45**, 3–11.
- 2 H. C. Berg and R. A. Anderson, Bacteria swim by rotating their flagella filaments, *Nature*, 1973, **245**, 380.
- 3 M. Silverman and M. Simon, Flagellar rotation and the mechanism of bacterial motility, *Nature*, 1974, **249**, 73.
- 4 R. M. Macnab, Bacterial rotating in bundles: A study in helical geometry, *Proc. Natl. Acad. Sci. U. S. A.*, 1977, **74**, 221.
- 5 N. Vladimirov and V. Sourjik, Chemotaxis: how bacteria use memory, *Biol. Chem.*, 2009, **390**(11), 1097–1104.
- 6 L. Xie, T. Altindal, S. Chattopadhyay and X. L. Wu, Bacterial flagellum as a propeller and as a rudder for efficient chemotaxis, *Proc. Natl. Acad. Sci. U. S. A.*, 2011, **108**, 2246.
- 7 J. Klafter and G. Zumofen, Lévy Statistics in a Hamiltonian System, *Phys. Rev. E: Stat. Phys., Plasmas, Fluids, Relat. Interdiscip. Top.*, 1994, **49**, 4873.
- 8 D. Murat, M. Hérisse, L. Espinosa, A. Bossa, F. Alberto and L.-F. Wu, Opposite and Coordinated Rotation of Amphitrichous Flagella Governs Oriented Swimming and Reversals in a Magnetotactic Spirillum, *J. Bacteriol.*, 2015, **197**, 3275–3282.
- 9 F. Popp, J. P. Armitage and D. Schüler, Polarity of bacterial magnetotaxis is controlled by aerotaxis through a common sensory pathway, *Nat. Commun.*, 2014, **5**, 5398.
- 10 M. Bennet, A. McCarthy, D. Fix, M. R. Edwards, F. Repp, P. Vach, J. W. C. Dunlop, M. Sitti, G. S. Buller, S. Klumpp and D. Faivre, Influence of Magnetic Fields on Magneto-Aerotaxis, *PLoS One*, 2014, **9**, e101150.
- 11 C. T. Lefevre, M. Bennet, L. Landau, P. Vach, D. Pignol, D. A. Bazylinski, R. B. Frankel, S. Klumpp and D. Faivre, Diversity of Magneto-Aerotactic Behaviors and Oxygen Sensing Mechanisms in Cultured Magnetotactic Bacteria, *Biophys. J.*, 2014, **107**, 527–538.
- 12 R. B. Frankel, D. A. Bazylinski, M. S. Johnson and B. L. Taylor, Magneto-Aerotaxis in Marine Coccioid Bacteria, *Biophys. J.*, 1997, **73**, 994–1000.
- 13 M. J. Smith, P. E. Sheehan, L. L. Perry, K. O'Connor, L. N. Csonka, B. M. Applegate and L. J. Whitman, Quantifying the Magnetic Advantage in Magnetotaxis, *Biophys. J.*, 2006, **91**, 1098–1107.
- 14 P. Dhar, Y. Cao, T. Kline, P. Pal, C. Swayne, Th. M. Fischer, B. Miller, T. E. Mallouk, A. Sen and T. H. Johansen, Autonomously moving local nano probes in heterogeneous magnetic fields, *J. Phys. Chem. C*, 2007, **111**, 3607–3613.
- 15 U. Heyen and D. Schüler, Growth and magnetosome formation by microaerophilic *Magnetospirillum* strains in an oxygen-controlled fermentor, *Appl. Microbiol. Biotechnol.*, 2003, **61**, 536–544.
- 16 We use an effective magnetization that is roughly a twentieth of the saturation magnetization of the film. The effective magnetization arises since we retain only the first term of the Fourier series of the stripe film.
- 17 J. Happel and H. Brenner, *Low Reynolds number hydrodynamics*, Martinus Nijhoff Publishers, 1983.
- 18 J. M. Burgers, *Second report on Viscosity and plasticity*, North-Holland Publ. Co., Amsterdam, 1938.
- 19 We omit the possibility of a misalignment between the propulsion force and the magnetic moment.

Publication 6

Defect Dynamics in Artificial Colloidal Ice: Real-Time Observation, Manipulation, and Logic Gate

Physical Review Letters, **117**, 168001 (2016)

On the cover of *Physical Review Letters*, Volume 117, Issue 16

Johannes Loehr^{a,b}, Antonio Ortiz-Ambriz^{b,c} and Pietro Tierno^{b,c}

^a Experimental Physics, Faculty of Physics, Mathematics and Computer Science, University of Bayreuth, 95447 Bayreuth, Germany.

^b Departament de Física de la Matèria Condensada, Universitat de Barcelona, 08028 Barcelona, Spain.

^c Institut de Nanociència i Nanotecnologia, IN²UB, Universitat de Barcelona, 08028 Barcelona, Spain.

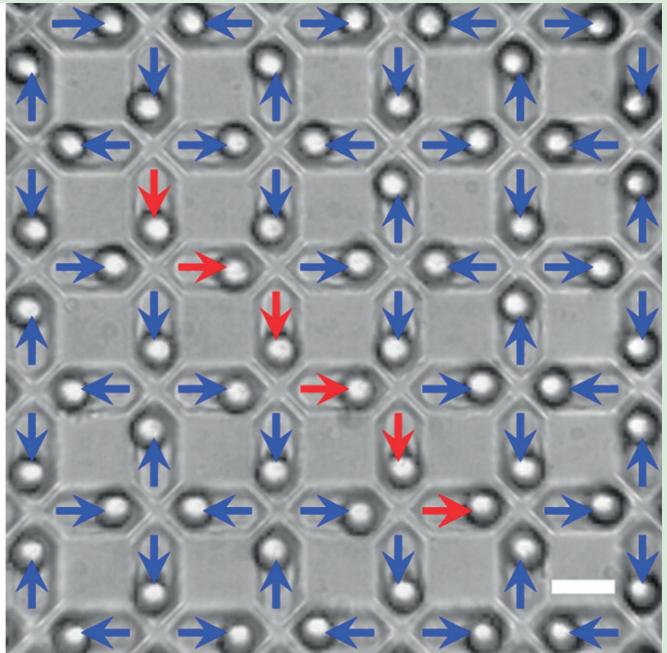
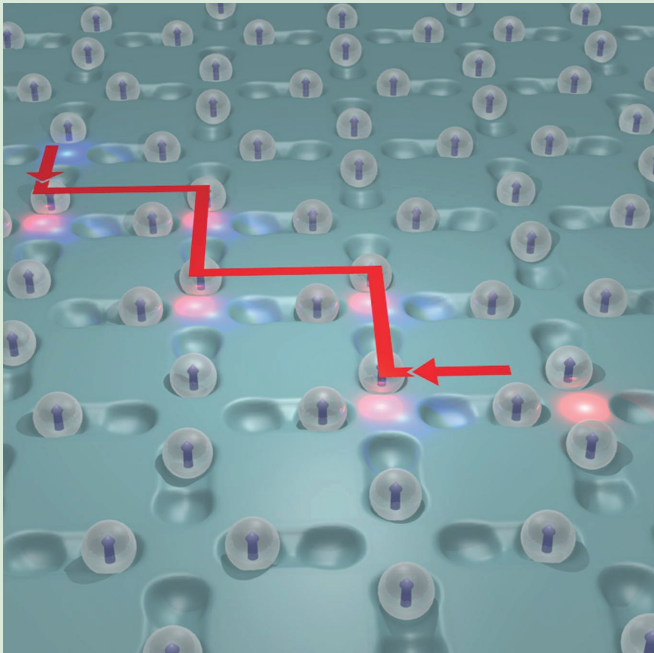
My Contribution

I designed the soft-lithographic structures and designed, performed and analyzed all experiments. In addition I performed the numerical simulations and had the idea to realize a logic gate and implemented it. I equally contributed to the interpretation of the experimental results and to the preparation of the manuscript.

PHYSICAL REVIEW LETTERS

Member Subscription Copy
Library or Other Institutional Use Prohibited Until 2017

Articles published week ending 14 OCTOBER 2016



Published by
American Physical Society

APS
physics

Volume 117, Number 16

Defect Dynamics in Artificial Colloidal Ice: Real-Time Observation, Manipulation, and Logic Gate

Johannes Loehr,^{1,2} Antonio Ortiz-Ambriz,^{1,3} and Pietro Tierno^{1,3,*}

¹*Departament de Física de la Matèria Condensada, Universitat de Barcelona, Barcelona 08028, Spain*

²*Physikalisches Institut, Universität Bayreuth, 95440 Bayreuth, Germany*

³*Institut de Nanociència i Nanotecnologia, IN²UB, Universitat de Barcelona, Barcelona 08028, Spain*

(Received 2 June 2016; revised manuscript received 16 August 2016; published 12 October 2016)

We study the defect dynamics in a colloidal spin ice system realized by filling a square lattice of topographic double well islands with repulsively interacting magnetic colloids. We focus on the contraction of defects in the ground state, and contraction or expansion in a metastable biased state. Combining real-time experiments with simulations, we prove that these defects behave like emergent topological monopoles obeying a Coulomb law with an additional line tension. We further show how to realize a completely resettable “NOR” gate, which provides guidelines for fabrication of nanoscale logic devices based on the motion of topological magnetic monopoles.

DOI: 10.1103/PhysRevLett.117.168001

Geometric frustration is a complex phenomenon which encompasses a broad range of systems, from magnetic materials [1], to ferroelectrics [2], trapped ions [3], confined microgel particles [4], and folding proteins [5]. It emerges when the spatial arrangement of the system elements cannot simultaneously minimize all interaction energies, and leads to exotic phases of matter with a low-temperature degenerate ground state, such as spin ice [6–8]. Artificial spin ice systems (ASI) are lattices of interacting nanoscale ferromagnetic islands, recently introduced as a versatile model to investigate geometrically frustrated states [9,10], including the role of disorder [11,12], thermalization [13–15], and the excitation dynamics [16–20]. In opposition to bulk spin ice such as pyrochlore compounds, ASI allow us to directly visualize the spin textures and to tailor the spatial arrangement of the system elements.

An intriguing aspect in ASI, which is attracting much theoretical interest, is the dynamics of defects [21–28]. The interactions between pairs of defects is one of the distinctive features between three dimensional (3D) and two dimensional (2D) spin ice. In a 3D pyrochlore compound, the spins are located on a lattice of corner-sharing tetrahedra, and can point either towards the tetrahedra center (spin *in*), or away from it (spin *out*). Thus the ground state (GS) follows the “ice rules,” with two spins coming *in* and two going *out* of each vertex in order to decrease the vertex energy. At finite temperature, defects that behave like “magnetic monopoles” [29,30] can emerge when a spin flips, producing a local increase of the magnetic energy. A way to overcome the system complexity is to use the “dumbbell” model [31], which only considers the magnetic charge distribution at the vertices of the lattice. Within this formalism, it was shown that in 3D spin ice, a pair of defects connected by strings of flipped spins only interact

through a magnetic Coulomb law at low temperature. In contrast, numerical simulations show that for a 2D square ASI, i.e., a projection of the 3D ice system on a plane, such a string requires an additional energetic term in the form of a line tension [21]. The reason is that, while in a 3D system all spin configurations that satisfy the ice rules have equal energy, in the 2D square ASI the distance at a vertex between opposing spins is greater than the distance between adjacent spins. This results in a lift of the degeneracy of the ground state, which is now represented by a twofold degenerate antiferromagnetic order.

String tension and the Coulombic interactions in ASI have been calculated by Monte Carlo simulations [22,23,27]; however, direct experimental measurements remain elusive. The difficulty of preparing the system in the GS and the extremely fast spin dynamics in nanoscale ASI makes real-time observation challenging, suggesting the use of alternative systems. Here we overcome these limitations by realizing an artificial colloidal spin ice system, a microscale soft matter analog of a frustrated nanoscale ASI. In this system we investigate the real-time dynamics of monopolelike defects via experiments and numerical simulations, and directly measure the line tension and Coulombic contributions. Further, we demonstrate defect manipulation via external field, and realize a logic operation based on magnetic current.

Our experimental system is inspired by previous theoretical works on electrostatically interacting colloids in bistable optical traps [32,33]. The schematic in Fig. 1(a) and the experimental realization in Fig. 1(b) illustrate the main idea. By soft lithography, we realize a square lattice of bistable topographic traps with lattice constant $a = 29 \mu\text{m}$. Each trap is composed of two wells of depth $\sim 3 \mu\text{m}$, connected by a small hill at the middle with average elevation $\langle h \rangle = 0.86 \mu\text{m}$, Figs. 1(d)–1(f) [34]. These traps

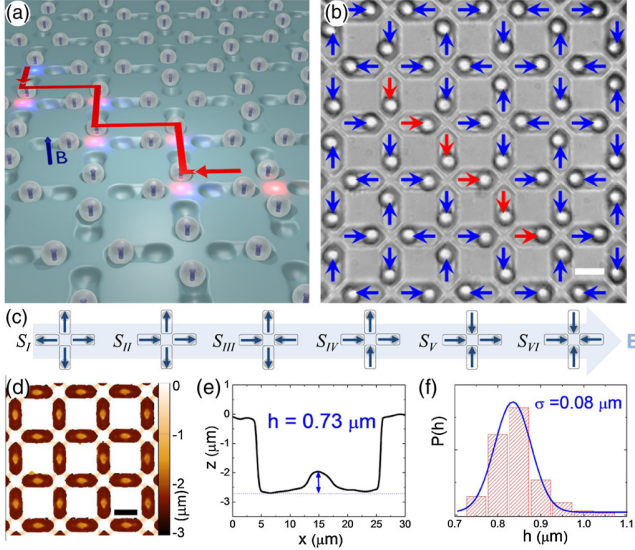


FIG. 1. (a) Schematic showing the colloidal spin ice composed by interacting colloids in a square lattice of double wells. The red line shows a defect line separating two $q = \pm 2$ defects in the GS. (b) Microscope image of an experimental defect line in a square lattice of lithographic double wells filled with paramagnetic colloids. Blue arrows denote spin directions, red arrows highlight the defect line. Scale bar is $15 \mu\text{m}$. (c) Vertex configurations for the colloidal square ice. Vertex energy increases from left to right. (d) Optical profilometer image of the lithographic square lattice. (e) Cross section of a typical double well characterized by a central hill of height $h = 0.73 \mu\text{m}$. (f) Distribution of hill height h fitted with a Gaussian function (continuous line).

are designed to confine a colloidal particle in one of the two sides, such that the particle can cross the hill when subjected to an external force, but it cannot escape from the bistable confinement. We induce repulsive interactions by using paramagnetic colloids with diameter $d = 10.3 \mu\text{m}$ and magnetic volume susceptibility $\chi = 0.08$ (Microparticles GmbH). Under an external magnetic field perpendicular to the particle plane, $\mathbf{B} = B_z \hat{z}$, the colloids repel by a tunable pair potential, $U_{ij}^m = \omega(a^3/r_{ij}^3)$, where $\omega = \mu_0 m^2 / (4\pi a^3)$ is the coupling constant with $\mathbf{m} = \pi d^3 \chi \mathbf{B} / (6\mu_0)$ the induced moment, $r_{ij} = |\mathbf{r}_i - \mathbf{r}_j|$, and r_i is the position of particle i . The gravitational potential for a particle to jump a hill is $U_g^{\text{hill}} = 910 k_B T$, and $U_g^{\text{wall}} = 3740 k_B T$ to leave the bistable trap. Here k_B is the Boltzmann constant, $T = 293 \text{ K}$, and we apply the external field such that $U_g^{\text{hill}} < U^m < U_g^{\text{out}}$ [37].

Once filled with one particle per double well, one can assign a vector (analogous to a spin) to each particle, such that it points from the free well to the well occupied by the particle. As shown in Fig. 1(c), it is possible to construct a set of ice rules for the colloidal artificial ice similar to the nanoscale ASI [32,38]. Vertices with three (S_V) or four (S_{VI}) colloids in are energetically unfavorable, and they are

topologically connected with low energy vertices having three (S_{II}) or four (S_I) colloids out. Thus, the GS is composed of S_{III} vertices [35], while the metastable biased state has high energy S_{IV} vertices. Both configurations satisfy the ice rules. According to the dumbbell model [31], we can associate to each spin a “magnetic charge,” which is positive (negative) for spin in (out). The total charge at each vertex i is given by the sum over all neighboring spins $q = \sum_i q_i$, and both the GS and the biased state correspond to $q = 0$, while all other vertices have a net charge.

We start by analyzing the contraction of a pair of $q = \pm 2$ (S_{II} and S_V) charged defects connected by a line of six flipped spins along the diagonal in the GS, Figs. 1(b) and 2(a) [39]. After preparing the system with the optical tweezers, we switch the field on and measure the relaxation toward equilibrium. As shown in Fig. 2(a) and VideoS1 in Ref. [34], both defects approach via a stepwise flipping of the colloids position and the system recovers the GS. Theoretical work [22] based on the dumbbell model [31] predicts the interaction potential between the two defects in the 2D ASI as $V(l) = -Q/l + \kappa l + c$. Here, Q is the topological Coulombic charge, κ the line tension, and c a constant associated with the creation of the defect pairs [25]. We confirm the validity of this assumption in our system, by explicitly calculating the energy cost $V(l) = E_{\text{exc}}(l) - E_{\text{GS}}$ of a defect line of length l in the GS, which can be obtained by subtracting the GS energy from the energy of the excited configuration. The magnetic energy is given by the sum of all dipole interactions as $E = \sum_i \sum_{j \neq i} U_{ij}^m$. In the inset of Fig. 2(b), we show the normalized potential $V(l)/\omega$. We subtract its linear part in order to emphasize the presence of a magnetic Coulombic term. Since $V(l)$ scales with the coupling constant, it follows that $Q, \kappa \sim \omega \sim H^2$. By fitting this potential, we obtain the ratio $Q/\kappa = 0.0290 \pm 0.0014 a^2$ between the Coulombic and line tension contribution, which is 1 order of magnitude lower than the corresponding one found for ASI [21].

Figure 2(b) shows experiments and simulations of the average line length $\langle l \rangle$ obtained by measuring the particle residence time within the traps [34]. We describe the dynamics of the defect line with an overdamped equation of motion with a friction coefficient γ :

$$\gamma \frac{dl}{dt} = -\frac{\partial V}{\partial l} = -\frac{Q}{l^2} - \kappa. \quad (1)$$

We assume negligible the thermal fluctuations given the large size of the employed particles, and we justify our choice of overdamped dynamics, as opposed to the underdamped dynamics in nanoscale ASI [27], by checking that the defect motion effectively shows a velocity profile linear with the applied force [34]. By solving Eq. (1), we fit its solution to the experimental data in Fig. 2(b) [34]. We use the ratio Q/κ obtained from the calculation of $V(r)$ [inset

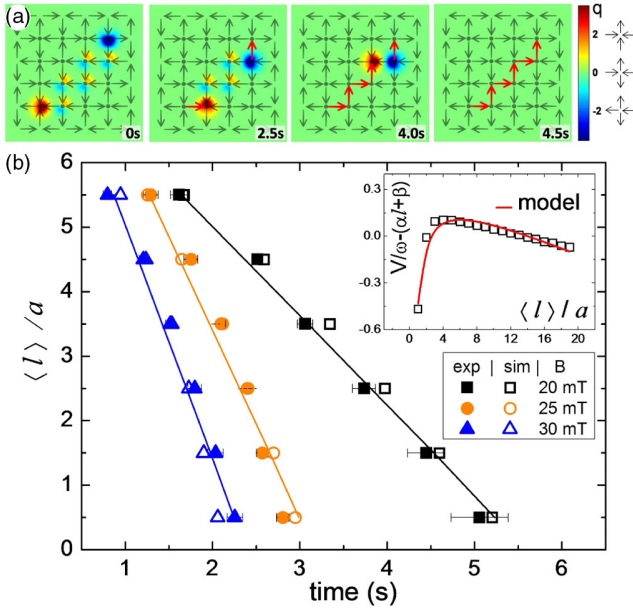


FIG. 2. (a) Color map showing the net vertex charges in the experiments for a defect line connecting two $q = \pm 2$ defects under a field $B_z = 25.7$ mT (VideoS1 in Ref. [34]). The line consists of high energy S_{IV} vertices with a zero charge but a net dipole, which give rise to the additional line-tension term. (b) Average line length $\langle l \rangle$ versus time for three different magnetic fields. Closed (empty) symbols denote experiments (numerical simulation), continuous lines are fit from Eq. (1) in the text. Inset: normalized interaction potential $V(l)/\omega$ between two topological defects minus its linear contribution ($\alpha l + \beta$). Red line is a fit using the potential described in the text.

Fig. 2(b)], and reduce to Q/γ the sole unknown parameter. Figure 2(b) shows the results of this procedure, confirming that the observed phenomena are well captured by Eq. (1). In all our analysis we use γ as the scaling factor for the topological Coulomb charge Q . However, Q may be estimated in first approximation by considering that the defects are composed by colloidal particles approaching at a constant speed in a liquid medium [40]. For an applied field of $B_z = 30$ mT, we obtain for the colloidal spin ice $Q_M \sim \sqrt{4\pi|Q|/\mu_0} = 5.7 \pm 1.5 \times 10^{-8}$ m/s. To further validate our analysis, we complement the experimental measurements with Brownian dynamics simulation, following the scheme described in Ref. [34]. In the simulation, we use the same experimental parameters and disorder level, and find again very good agreement with the measured data, Fig. 2(b).

We can clearly visualize the effect of the magnetic Coulombic contribution by studying defect motion in the biased system, which can be prepared by displacing all particles towards one of the system corners with the optical tweezers. In this state, it is possible to generate defect lines characterized by positive or negative line tension, or single defects with zero Coulombic contribution that propagate

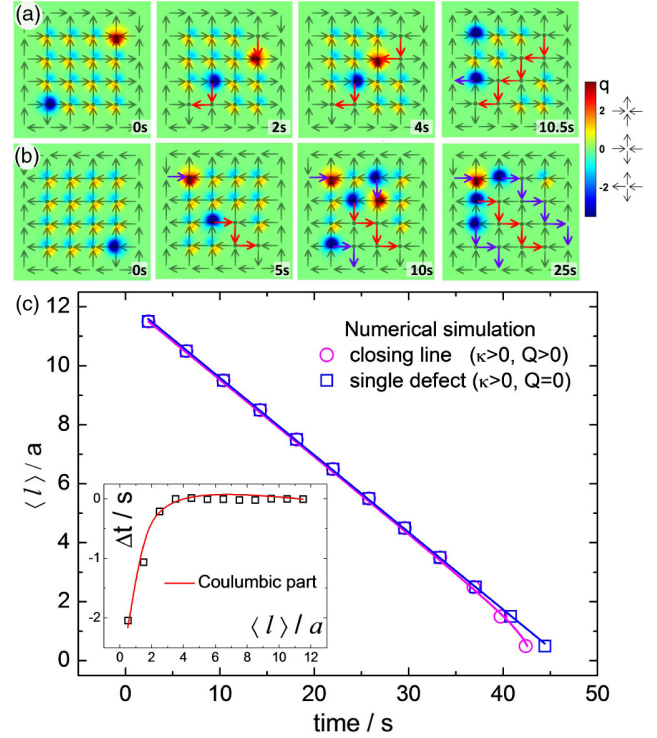


FIG. 3. (a),(b) Experimental vertex charges for a closing line (a) and for a single $q = -2$ propagating defect (b) in the biased state. Black (blue) arrows are spins flipped by the motion of the original (spontaneously emerged) defects. Corresponding movies (VideoS2, VideoS3) are in Ref. [34]. (c) Numerical simulation of case (a) (with one end fixed) and (b) showing the evolution of the line length $\langle l \rangle$ for an applied field $B_z = 18.8$ mT. Continuous lines are fits from Eq. (1). Bottom inset: difference between the two curves in the main panel (empty squares) versus line length plotted with Eq. (1) with $\kappa = 0$ (continuous line).

along a diagonal [41]. Of these three cases, Figs. 3(a) and 3(b) show the first and the last one; the rest is in Ref. [34]. The first case is shown in Fig. 3(a), where two $q = \pm 2$ defects approach when an external field $B_z = 25.7$ mT is applied, leaving a series of S_{III} vertices behind. This situation is similar to the defect motion in the GS, with attractive line tension and Coulombic interaction. We also calculate the interaction potential $V(l)$ (data not shown), obtaining an almost identical plot as the inset in Fig. 2(c). In contrast, in Fig. 3(b) a single $q = -2$ defect propagates along the lattice only due to line tension, since the absence of other charges sets the Coulombic term in Eq. (1) to 0. In the bias state we find that the defect dynamics are much slower than in the GS, and usually in the experiments the particles stop propagating due to disorder (Fig. 1(f)). We thus cannot directly measure the small Coulombic contribution in this state; however, we can resolve it by using simulations with the same experimental conditions as in Figs. 3(a) and 3(b) and a much larger, disorder free system. The results of these simulations are shown in Fig. 3(c), where we compare the motion of single ($Q_M = 0$)

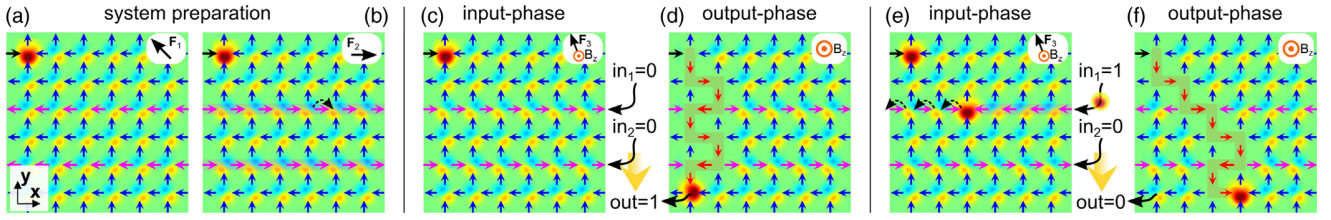


FIG. 4. Realization of a NOR gate via numerical simulation. (a),(b) Images showing the system preparation: (a) a force F_1 applied along the diagonal biases the system, except for one fixed spin; (b) a smaller force F_2 shifts two rows of particles (magenta) with high magnetic susceptibilities. (c),(d) Images showing a 1 output obtained from (0,0) inputs. In (c) an external field B_z is applied perpendicular to the plane to start defect propagation, while a small force F_3 along the diagonal prevents motion of other defects from the upper left corner. The final result shown in (d) is the 1 output. (e),(f) Images showing a 0 output obtained from (1,0) input. In (e) an input current causes the whole line of magenta spin to flip (1 input). The 0 output results from the changed trajectory of the propagating defect (f). All the corresponding videos can be found in Ref. [34].

and double defects ($Q_M > 0$). Both have the same line-tension contribution and therefore move at an identical speed for large distances. However, the closing line speeds up when the two defects are approaching at the end of the process due to sole Coulombic interaction. This time difference is shown in the inset of Fig. 3(c), and can be well fitted by Eq. (1) with $\kappa = 0$ (continuous line), resulting in a similar value for the topological Coulomb charge as in the GS.

A major driving interest in studying defect dynamics in ASI lays on the possibility of realizing dissipation-free “magnetronic” circuitry [10,42]. We demonstrate that the colloidal spin ice system can be used to perform logic operations based on the motion of topological monopole defects. Figure 4 shows the realization, by numerical simulation, of a NOR gate, which is a functionally complete port capable of generating all logical functions [43]. The gate is completely resettable, since it requires only external fields or gradients to work, and not individual manipulation via laser tweezers. It is realized in a biased system, which could be formed and reset by an external magnetic force $\mathbf{F} \sim (\mathbf{B} \cdot \nabla \mathbf{B})$ applied along one diagonal direction, $\mathbf{F}_1 = F_1(\hat{y} - \hat{x})$. In the preparation step [Fig. 4(a)] the system is biased by a force $F_1 = 2.8$ pN, which displaces all particles except for a pinned one which represents a fixed spin, [top left corner in Fig. 4(a)]. We use a second type of paramagnetic colloids with a higher magnetic susceptibility, χ_2 and ratio $\chi_2/\chi_1 = 1.15$, a prerequisite which forced us to restrict the realization only to the numerical scheme. These particles are placed along two parallel rows spaced by two lattice constants (magenta arrows in Fig. 4). In the second preparation step [Fig. 4(b)] these particles are selectively manipulated by a small in-plane force $\mathbf{F}_2 = F_2\hat{x}$, $F_2 = 1.6$ pN, while all other particles (χ_1) remain at rest. The two rows represent the inputs of the logic gate: a 0 (1) is associated with a shifted (unshifted) row. After preparation of the system, a $B_z = 15$ mT field perpendicular to the plane induces the defect propagation, Figs. 4(c)–4(f). The output of the gate is measured at the bottom left corner of the sample: it is 1 if

there is a magnetic current, 0 otherwise. Figures 4(c)–4(d) describe the situation of the input (0,0) with output 1, while Figs. 4(e)–4(f) have input (1,0) and output 0. In the third step [Figs. 4(c) and 4(e)] a small locking force $\mathbf{F}_3 = F_3(\hat{y} - \hat{x})$, $F_3 = 0.7$ pN is applied to hold the defect in place while the input is prepared. Now let us consider the case of the (1,0) input: an applied magnetic current causes the upper first magenta line to flip back into the $x < 0$ direction. In Fig. 4(f), F_3 is set to 0 and the defect starts moving. When it reaches the flipped input row, the defect changes its path, ending in a different place; thus the output is 0. Since only (0,0) input gives a 1 output, our logic port behaves like a NOR gate. A similar system could be engineered in nanoscale ASI using islands of different size or magnetic materials, which would give spins that behave differently under an external field. In this context, a recent work demonstrated the possibility to reorient the magnetization of the nanoislands in ASI with an MFM tip [44].

In summary, we studied the defect dynamics in an artificial colloidal spin ice in the GS and in the biased state and directly measure their energetic contributions. Our findings also confirm former theoretical assumptions and clearly demonstrate that these defects behave like bound magnetic monopoles. We finally demonstrate a resettable functionally complete NOR gate. The possibility to control topological monopole defects in spin ice states may foster the realization of novel memory and logic devices based on magnetic current [42,45,46].

We thank Andras Libal and Demian Levis for stimulating discussions. This work was supported by the ERC StG No. 335040. P. T. acknowledges support from Mineco (Project No. FIS2013-41144-P) and AGAUR (Project No. 2014SGR878).

*ptierno@ub.edu

- [1] S. T. Bramwell and M. J. P. Gingras, *Science* **294**, 1495 (2001).
- [2] N. Choudhury, L. Walizer, S. Lisenkov, and L. Bellaiche, *Nature (London)* **470**, 513 (2011).

- [3] K. Kim, M.-S. Chang, S. Korenblit, R. Islam, E. E. Edwards, J. K. Freericks, G.-D. Lin, L.-M. Duan, and C. Monroe, *Nature (London)* **465**, 590 (2010).
- [4] Y. Han, Y. Shokef, A. M. Alsayed, P. Yunker, T. C. Lubensky, and A. G. Yodh, *Nature (London)* **456**, 898 (2008).
- [5] D. Bryngelson and P. G. Wolynes, *Proc. Natl. Acad. Sci. U.S.A.* **84**, 7524 (1987).
- [6] M. J. Harris, S. T. Bramwell, D. F. McMorrow, T. Zeiske, and K. W. Godfrey, *Phys. Rev. Lett.* **79**, 2554 (1997).
- [7] A. P. Ramirez, A. Hayashi, R. J. R. J. Cava, R. B. Siddharthan, and S. Shastry, *Nature (London)* **399**, 333 (1999).
- [8] R. Moessner and A. P. Ramirez, *Phys. Today* **59**, 24 (2006).
- [9] R. F. Wang, C. Nisoli, R. S. Freitas, J. Li, W. McConville, B. J. Cooley, M. S. Lund, N. Samarth, C. Leighton, V. H. Crespi, and P. Schiffer, *Nature (London)* **439**, 303 (2006).
- [10] C. Nisoli, R. Moessner, and P. Schiffer, *Rev. Mod. Phys.* **85**, 1473 (2013).
- [11] S. A. Daunheimer, O. Petrova, O. Tchernyshyov, and J. Cumings, *Phys. Rev. Lett.* **107**, 167201 (2011).
- [12] Z. Budrikis, J. P. Morgan, J. Akerman, A. Stein, P. Politi, S. Langridge, C. H. Marrows, and R. L. Stamps, *Phys. Rev. Lett.* **109**, 037203 (2012).
- [13] U. B. Arnalds, A. Farhan, R. V. Chopdekar, V. B. Kapaklis, A. Balan, E. T. Papaioannou, M. Ahlberg, N. Frithjof, L. J. Heyderman, and B. Hjörvarsson, *Appl. Phys. Lett.* **101**, 112404 (2012).
- [14] S. Zhang, I. Gilbert, C. Nisoli, G.-W. Chern, M. J. Erickson, L. O. Brien, C. Leighton, P. E. Lammert, V. H. Crespi, and P. Schiffer, *Nature (London)* **500**, 553 (2013).
- [15] A. Farhan, P. M. Derlet, A. Kleibert, A. Balan, R. V. Chopdekar, M. Wyss, J. Perron, A. Scholl, F. Nolting, and L. J. Heyderman, *Phys. Rev. Lett.* **111**, 057204 (2013).
- [16] S. Ladak, D. E. Read, G. K. Perkins, L. F. Cohen, and W. R. Branford, *Nat. Phys.* **6**, 359 (2010).
- [17] J. P. Morgan, A. Stein, S. Langridge, and C. H. Marrows, *Nat. Phys.* **7**, 75 (2011).
- [18] E. Mengotti, L. J. Heyderman, A. F. Rodríguez, F. Nolting, R. V. Hügli, and H.-B. Braun, *Nat. Phys.* **7**, 68 (2011).
- [19] C. Phatak, A. K. Petford-Long, O. Heinonen, M. Tanase, and M. De Graef, *Phys. Rev. B* **83**, 174431 (2011).
- [20] V. Kapaklis, U. B. Arnalds, A. Farhan, R. V. Chopdekar, A. Balan, A. Scholl, L. J. Heyderman, and B. Hjörvarsson, *Nat. Nanotechnol.* **9**, 514 (2014).
- [21] L. A. Mól, R. L. Silva, R. C. Silva, A. R. Pereira, W. A. Moura-Melo, and B. V. Costa, *J. Appl. Phys.* **106**, 063913 (2009).
- [22] L. A. S. Mól, W. A. Moura-Melo, and A. R. Pereira, *Phys. Rev. B* **82**, 054434 (2010).
- [23] R. C. Silva, F. S. Nascimento, L. A. Mól, W. A. Moura-Melo, and A. R. Pereira, *New J. Phys.* **14**, 015008 (2012).
- [24] F. S. Nascimento, L. A. Mól, W. A. Moura-Melo, and A. R. Pereira, *New J. Phys.* **14**, 115019 (2012).
- [25] R. C. Silva, R. J. C. Lopes, L. A. S. Mól, W. A. Moura-Melo, G. M. Wysin, and A. R. Pereira, *Phys. Rev. B* **87**, 014414 (2013).
- [26] D. Levis and L. F. Cugliandolo, *Phys. Rev. B* **87**, 214302 (2013).
- [27] E. Y. Vedmedenko, *Phys. Rev. Lett.* **116**, 077202 (2016).
- [28] V. S. Bhat, F. Heimbach, I. Stasinopoulos, and D. Grundler, *Phys. Rev. B* **93**, 140401 (2016).
- [29] S. T. Bramwell, S. R. Giblin, S. Calder, R. Aldus, D. Prabhakaran, and T. Fennell, *Nature (London)* **461**, 956 (2009).
- [30] L. D. C. Jaubert and P. C. W. Holdsworth, *J. Phys. Condens. Matter* **23**, 164222 (2011).
- [31] C. Castelnovo, R. Moessner, and S. Sondhi, *Nature (London)* **451**, 42 (2008).
- [32] A. Libál, C. Reichhardt, and C. J. Olson Reichhardt, *Phys. Rev. Lett.* **97**, 228302 (2006).
- [33] A. Libál, C. Reichhardt, and C. J. Olson Reichhardt, *Phys. Rev. E* **86**, 021406 (2012).
- [34] See Supplemental Material at <http://link.aps.org/supplemental/10.1103/PhysRevLett.117.168001> for more details on the experimental system, the numerical simulation, and seven video clips illustrating the defect dynamics, which includes Refs. [35,36].
- [35] A. Ortiz-Ambriz and P. Tierno, *Nat. Commun.* **7**, 10575 (2016).
- [36] K. Jacobs, *Stochastic Processes for Physicists: Understanding Noisy Systems* (Cambridge University Press, Cambridge, England, 2010), ISBN .
- [37] To calculate the gravitational potentials we use the density mismatch $\Delta\rho = 0.9 \text{ gm}^{-3}$ between the particle and the suspending medium. Optical tweezers are used to load one particle per double well, to order the system or create defects.
- [38] C. Nisoli, *New J. Phys.* **16**, 113049 (2014).
- [39] The small system size was chosen in order to both make more evident the effect of Coulombic-like interactions, and to minimize the breaking of the defect line caused by small disorder related with the distribution of hills, Fig. 1(f).
- [40] The friction between such particles is given by $\gamma = 6\pi\eta d/2$, being $\eta = 10^{-3} \text{ Pa}\cdot\text{s}$ the viscosity of the medium (water).
- [41] It is possible to create a single topological monopole which propagates in the bias state purely due to line tension because of the finite system size. Once a charged defect is created, an oppositely charged one is needed in order to fulfill charge conservation. The flipped spins simply place one of the two defects outside the border region, such that it does not interact with the system.
- [42] S. R. Giblin, S. T. Bramwell, P. C. W. Holdsworth, D. Prabhakaran, and I. Terry, *Nat. Phys.* **7**, 252 (2011).
- [43] T. C. Bartee, *Computer Architecture and Logic Design* (McGraw-Hill, New York, 1991).
- [44] Y.-L. Wang, Z.-L. Xiao, A. Snezhko, J. Xu, L. E. Ocola, R. Divan, J. E. Pearson, G. W. Crabtree, and W.-K. Kwok, *Science* **352**, 962 (2016).
- [45] S. J. Blundell, *Phys. Rev. Lett.* **108**, 147601 (2012).
- [46] I. Gilbert, G.-W. Chern, B. Fore, Y. Lao, S. Zhang, C. Nisoli, and P. Schiffer, *Phys. Rev. B* **92**, 104417 (2015).

Publication 6

Supporting Information

Supporting Information for the article: Defect Dynamics in Artificial Colloidal Ice: Real-Time Observation, Manipulation and Logic Gate

Johannes Loehr^{1,2}, Antonio Ortiz-Ambriz^{1,3} and Pietro Tierno^{1,3*}

¹*Departament de Física de la Matèria Condensada, Universitat de Barcelona, Barcelona, Spain*

²*Physikalisches Institut, Universität Bayreuth, 95440 Bayreuth, Germany*

³*Institut de Nanociència i Nanotecnologia, IN²UB, Universitat de Barcelona, Barcelona, Spain*

(Dated: August 10, 2016)

REALIZATION OF THE SOFT LITHOGRAPHIC STRUCTURES.

We fabricate a mask containing a square lattice of double wells on a 5-inch glass wafer covered with a 500nm layer of Cr. To write the motifs on the mask, we use Direct Write Laser Lithography (DWL 66, Heidelberg Instruments Mikrotechnik GmbH) with a 405nm laser diode working at a speed of $5.7\text{mm}^2\text{min}^{-1}$. The structures are designed using a commercial software (CleWin 4, Phoenix Software). In contrast to Ref. [1], the mask design has been improved in order: (i) to obtain a reduced and more controlled degree of disorder of the central hill (Fig.1(f) of the main text), and (ii) to avoid the anisotropy of the double wells which could affect the measurements of the defect lines along the diagonals of the square lattice. The first issue is resolved by changing the design of the small hills. In previous work the hill was obtained by reducing the width of the elongated trap at the middle (see Supporting Information in Ref. [1]). In the new mask the hills are obtained by designing small rectangular spots at the center of the elliptical confinements, as shown in Fig.1(a). The outer ellipse has a length of $21\mu\text{m}$ and a width of $9\mu\text{m}$, while the spot covers an area of $4\mu\text{m} \times 2\mu\text{m}$. The size of the spot is below the vertical resolution of the lithographic process. Thus it blurs the exposing light resulting in a small hill with a lower height at the center of the islands. The anisotropy of the double wells result from the fact that the x and y direction have both an inherently different resolution in the mask writing process. This second issue was resolved by rotating the whole mask design by 45 degrees.

After being impressed above the Cr mask, the microfeatures are etched on a $2.8\mu\text{m}$ layer of photoresist AZ-1512HS, (Microchem, Newton, MA). The photoresist is deposited on top of a $100\mu\text{m}$ thick glass coverslip by spin coating (Spinner Ws-650Sz, Laurell) at 500 rpm for 5 second and afterwards at 1000 rpm for 30 seconds, both steps with an acceleration of 500 rpm/s. Different thickness of the photoresist could be obtained by varying the rotating speed, however we find that $\sim 3\mu\text{m}$ works well to create topographical traps capable of capturing the particles within the double wells for most of the applied fields. After the deposition process, the photoresist is irradiated with UV light passing through the Cr mask, for

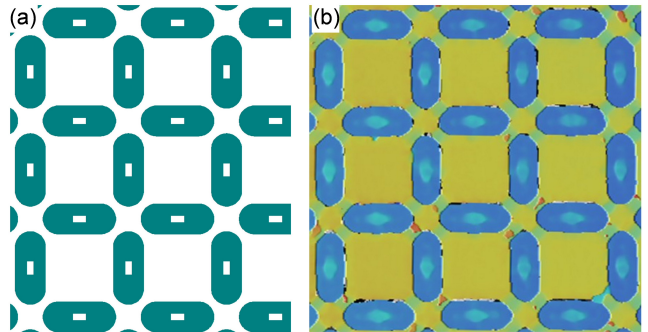


FIG. 1. (a) Schematic showing the design of the lattice of double wells with small rectangular holes in the middle. (b) Optical profilometer image of the square lattice of double wells after the lithographic process. Scale bars are $15\mu\text{m}$ for both images.

3.5s at power of $25\text{mW}/\text{cm}^2$ (UV-NIL, SUSS Microtech). The light passing through the motifs of the mask uncross-links only the exposed part of the photoresist. The exposed parts are then eliminated by submerging the film in a AZ726MF developer solution (Microchem, Newton MA) for 7 seconds.

MAGNETO-OPTICAL SET-UP

It is composed by an inverted homemade optical microscope equipped with a white light illumination LED (MCWHL5 from Thorlabs), a charge-coupled device (Basler A311f) and custom-made coil perpendicular to the sample cell such that the main axis points along the z -direction. The coil was connected to a programmable power supply (KEPCO BOP-20 10M) which is remotely controlled along with the image acquisition and recording with a custom made LabVIEW program. The photoresist is sensitive to UV light, so the white light of the LED is filtered with a long pass filter with a cut off at 500nm (FEL0500 Thorlabs). Optical tweezers are realized by tightly focusing a $\lambda = 975\text{nm}$, $P = 330\text{mW}$, Butterfly Laser Diode (Thorlabs) with a $100\times$ Achromatic microscope objective (Nikon, $NA = 1.2$) which is also used for observation purpose.

AVERAGING PROCEDURE IN THE DETERMINATION OF $\langle l \rangle$

During the experiments, we measure the shrinking of defect lines due to the presence of attractive line tension and topological "Coulombic" interactions. The defect line is composed by a total of 6 spins connecting the two charged defects. Although longer lines could be studied, we find that the presence of disorder in the distribution of hills breaks longer lines during shrinkage, making difficult to analyze their dynamics. Moreover, the optical tweezers setup forces us to have a limited field of view, and within this limitation, a defect line of 6 spins is still 2 spins away from the boundary, which helps minimize finite size effects.

Typical trajectories obtained from a single experiment of a closing line of two $q = \pm 2$ charged defects placed in the ground state are shown by the dashed curves in Fig.2. Since the line motion is caused by spin flips, which occur when the particles jump above the small hill connecting the two traps, the line length l of a single experiment always changes in integer multiples of the lattice constant a . In order to have enough statistical data for further processing, each experiment was repeated at least 24 times for each field. We also averaged over different sets of traps characterized by different degree of disorder, by repeating the experiments along the 2 diagonals of the square system and for all the 4 possible arrangements of the charged defects.

Fig.2 shows two possible averages of the experimental data along the vertical (blue line), and the horizontal (red line) direction. The first way of averaging introduces an artifact at the end of the line length. With the first lines having closed, the number of averaged data decreases, increasing the corresponding relaxation time. Performing the average along the horizontal direction instead reduces the number of points in the experiments, but gives more uniform statistics of the data, eliminating the artifact of the slowing down of the curve at the end point.

BROWNIAN DYNAMICS SIMULATION

We complement the experimental data with Brownian dynamics simulation in order to improve statistics and explore the system in the absence of disorder. The numerical scheme consists of solving the Langevin equation by Euler's method as described in Ref. [2]. We consider N particles arranged into an ensemble of double well traps. For each particle i at position $\mathbf{r}_i \equiv (x_i, y_i)$ we solve the set of overdamped equations:

$$\begin{aligned} \gamma \dot{x}_i &= \mathbf{F}_{tot} \cdot \hat{e}_x + \xi_x(t) \\ \gamma \dot{y}_i &= \mathbf{F}_{tot} \cdot \hat{e}_y + \xi_y(t) \end{aligned} \quad (1)$$

where γ is the friction coefficient, $\mathbf{F}_{tot} = \mathbf{F}_g + \mathbf{F}_N + \mathbf{F}_M$ is the sum of external forces acting on the particle, com-

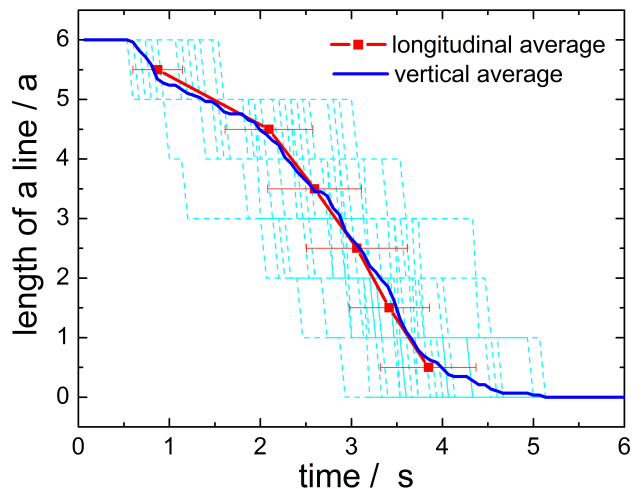


FIG. 2. Length of a defect line l versus time t in the ground state under an applied field $B_z = 25.7\text{mT}$. The dashed cyan lines are individual experiments, the blue line is the vertically averaged line-length, while the red line is obtained from an horizontally average. Error bars represent the distribution (standard deviation) of the single experiments.

posed by the gravitational force, \mathbf{F}_g , the normal force exerted by the double wall confinement, \mathbf{F}_N and the magnetic dipolar force \mathbf{F}_M . We express $\mathbf{F}_g = gV\Delta\rho\hat{e}_z$, with V the particle volume and $\Delta\rho$ the density mismatch. The shape of the double well potential, was approximated by parabolic functions,

$$U(\delta\mathbf{r}) = |\mathbf{F}_g| k \times \begin{cases} \delta\mathbf{r} \cdot \hat{e}_\perp + \left(|\delta\mathbf{r} \cdot \hat{e}_\parallel| - \frac{d}{2} \right)^2 & \text{if } |\delta\mathbf{r} \cdot \hat{e}_\parallel| > \frac{d}{2} \\ \delta\mathbf{r} \cdot \hat{e}_\perp + \frac{h}{k} \left[1 - \left(\frac{2}{d} \delta\mathbf{r} \cdot \hat{e}_\parallel \right)^2 \right] & \text{if } |\delta\mathbf{r} \cdot \hat{e}_\parallel| \leq \frac{d}{2} \end{cases} \quad (2)$$

where $\delta\mathbf{r}$ is the displacement vector from the center of the trap, $d = 10\ \mu\text{m}$ is the distance between the two stable minima, $k = H/r^2$ is the spring constant, that is determined by the radius r of the particles and the substrate height $H = 3\ \mu\text{m}$ and h the hill height. The two unit vectors \hat{e}_\parallel and \hat{e}_\perp define the orientation of the trap: the first is the vector that joins the two stable positions, while the second connect the transverse axis. Assuming a small inclination angle of the walls, the normal force can be then calculated as $\mathbf{F}_N = \nabla_t U$. The magnetic interaction between the particles with an induced magnetic moment $\mathbf{m}_i = |\mathbf{B}|\chi V/\mu_0\hat{z}$, is given by,

$$\mathbf{F}_M = \sum_{j=1}^N \frac{3\mu_0}{2\pi|\mathbf{r}_{ij}|^4} \hat{\mathbf{r}}_{ij} \cdot \quad (3)$$

Here $\mathbf{B} = B_z\hat{e}_z$ is the amplitude of the magnetic field, χ the magnetic volume susceptibility, $\mu_0 = 4\pi \times 10^{-7}\text{H/m}$

and \mathbf{r}_{ij} is the vector that goes from particle i to particle j . Thermal noise $\xi(t)$ is modeled as a Gaussian white noise with zero mean, and a correlation function $\langle \xi(t)\xi(t') \rangle = 2\gamma k_B T \delta(t-t')$, with k_B the Boltzmann constant and $T \sim 293\text{K}$ the experimental temperature. The equations of motion are numerically solved using a time step of $\Delta t = 0.01\text{s}$. Using the experimental parameters, we achieved very good agreement between simulation and experimental data.

OVERDAMPED DYNAMICS OF DEFECT LINE

In our colloidal spin ice system we describe the interaction between defects using an overdamped equation of motion, namely Eq.(1) in the main text. This equation has the form of a nonlinear first order Chini equation, which admits as solution an implicit function which can be written as,

$$t - t_0 = \frac{1}{\beta} \left[l_0 - r + \sqrt{\alpha} \left(\arctan \left(\frac{r}{\sqrt{\alpha}} \right) - \arctan \left(\frac{l_0}{\sqrt{\alpha}} \right) \right) \right]. \quad (4)$$

We next shows the result of an additional series of numerical simulations of the shrinkage of a line connecting a pair of $q = \pm 2$ defects in the ground state of the artificial colloidal ice with different magnetic fields and under experimental conditions, as shown in Figure 3(a). We use Eq. (4) to fit these numerical data and also the experimental data in the main text (Fig.3 and 4). In all cases, we use as parameters $\alpha = Q/\kappa$, $\beta = \kappa/\gamma$ and $l_0 = l(t = t_0)$ which is the initial position of the line length. The first one was fixed to $\alpha = (0.0290 \pm 0.0014)a^2$, since it was independently determined by fitting the potential $V(r)$ calculated in the inset Fig.2(b) of the main text.

In Fig.3(b) we plot the obtained values of Q/γ (m^3s^{-1}) versus the square of the magnetic field B_z , in order to emphasize the linear dependence of the topological Coulomb charge with the applied magnetic force $F_m = -\frac{\partial V_z}{\partial r}$. This results from the proportionality $F_m \sim m^2 \sim B_z^2$ of the dipolar magnetic force.

Finally, we use the simulation data to confirm the validity of our assumption of overdamped dynamics in Eq.(1) of the manuscript. Already the fact that particle motion occurs at very low Reynolds (Re) number suggests the negligible role of inertial forces. We estimate this number as $\text{Re} = \frac{\alpha v_p}{\eta} \sim 10^{-6}$ for pair of particles with radius a (assumed the same as the colloidal radius) approaching at a maximum speed of $v_p = 120\mu\text{m}\text{s}^{-1}$ in water. From the simulation data we measured the average speed of the contracting line $\langle v_l \rangle$, and observe a linear dependence with the square of the magnetic field B_z^2 , as shown in Fig.3(c), continuous line. Thus we confirm our assumption of overdamped dynamics of the defects in artificial colloidal ice moving at an average speed

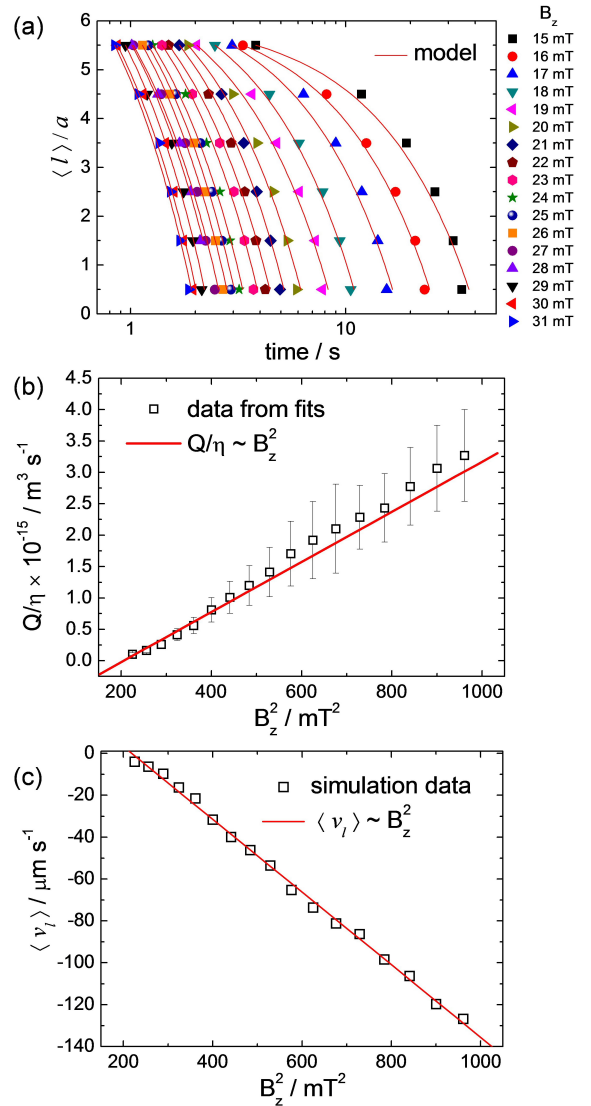


FIG. 3. (a) Numerical simulation of the average line length $\langle l \rangle$ versus time in a semilogarithmic plot of a defect line contracting due to different applied fields B_z in the ground state. Scattered points refer to numerical simulations while continuous line are a fit of Eq. (4) in this Supporting Information. (b) Normalized topological Coulomb charge Q/γ versus square of the applied field B_z^2 calculated from the fits in Fig.3(a). (c) Average speed of contracting line $\langle v_l \rangle$ versus B_z^2 . Continuous red lines in Figs.3(b,c) are linear fits.

$\langle v_l \rangle \sim F_m \sim B^2$ proportional to the applied force.

DEFECT REPULSION AND LOGIC OPERATIONS

We show in Fig.4 the left situation for a pair of $q = \pm 2$ charged defect placed in the biased state and repelling upon application of an $B_z = 25.7\text{mT}$ magnetic field. In

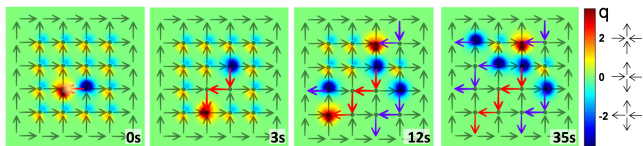


FIG. 4. Color map showing the net vertex charges in the experiments for a pair of $q = \pm 2$ defects repelling in the biased system upon application of an external field with amplitude $B_z = 25.7\text{mT}$.

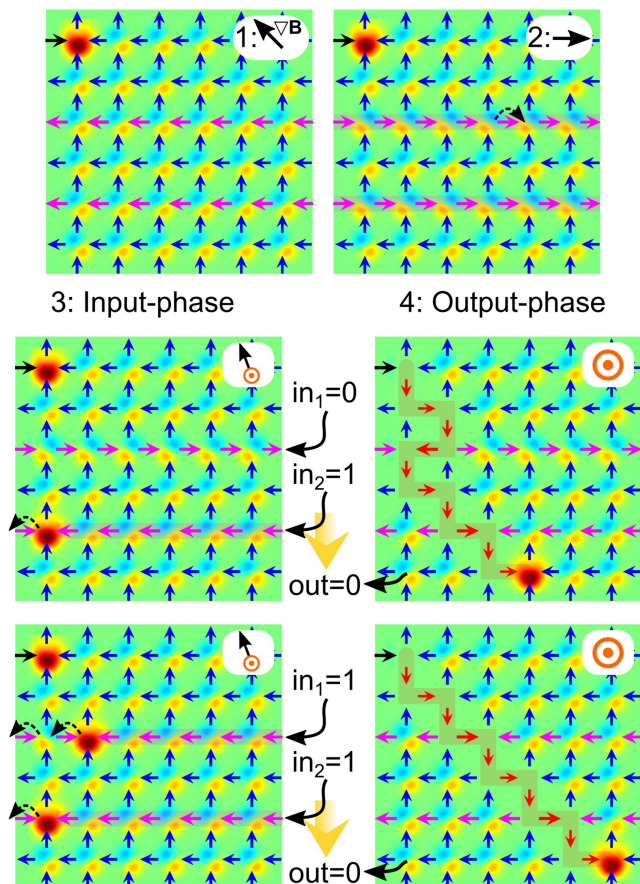


FIG. 5. Top row: Images showing the system preparation. In (1) a force F_1 applied along the diagonal bias the system, (2) a smaller force F_2 shifts two rows of particles (pink) with high magnetic susceptibilities. Middle row: images showing a 0 output obtained from inputs (0, 1). Bottom row: images showing a 0 output obtained from inputs (1, 1). The corresponding videos can be found in the Supporting Information.

the biased state, the pair of defects are introduced by flipping a single particle (spin), as shown in Fig.4, $t = 0\text{s}$. Upon application of the external field, the two defect shows repulsion due to line tension and attraction because of Coulumbic interaction, which result in a slowest motion of the defect line. The spins flipped due to the

motion of the initially placed defects are marked in red. In the biased state, further spin flips which spontaneously occur are marked in blue. Moreover, due to the strong Coulumbic attraction, we found that sometimes (depending on the noise distribution) the defect line was unable to open, but rather the particle flip back in the biased state configuration. This problem was avoided by fixing one particle with the laser tweezers.

Figure 5 shows the remaining two cases left to demonstrate the NOR gate described in the last image of the main text.

SUPPORTING VIDEOS

With the article there are 7 videoclips as supplements of the Figures and Main text.

- **MovieS1(.AVI):** Dynamics of a defect line connecting a pair of approaching $q = \pm 2$ charged defects in the ground state. The external magnetic field has amplitude $B_z = 25\text{mT}$. The corresponding process is illustrated in Fig. 2(a) of the article.
- **MovieS2(.AVI):** Dynamics of a defect line connecting a pair of approaching $q = \pm 2$ charged defects in the biased system. The external magnetic field has amplitude $B_z = 25\text{mT}$. The corresponding process is illustrated in Fig. 3(a) of the article.
- **MovieS3(.AVI):** Dynamics of a single $q = -2$ charged defect propagating along the diagonal in the biased system due to line tension alone. The applied field has amplitude $B_z = 25\text{mT}$. The corresponding process is illustrated in Fig. 3(b) of the article.
- **MovieS4(.AVI):** Video illustrating the logic operation of the NOR gate for inputs (0, 0) and its corresponding 1 output. The defect motion is triggered by an external field of amplitude $B_z = 15\text{mT}$. Forces used are: $F_1 = 2.8\text{pN}$, $F_2 = 1.6\text{pN}$ and $F_3 = 0.7\text{pN}$ as described in the main text. The corresponding process is described in Fig. 4(a-d) of the article. The video is displayed 10 times faster.
- **MovieS5(.AVI):** Video illustrating the logic operation of the NOR gate for inputs (1, 0) and its corresponding 0 output. The values of the parameters $B_z, F_{1,2,3}$ are the same as in MovieS4. The corresponding process is described in Fig. 4(a-f) of the article. The video is displayed 10 times faster.
- **MovieS6(.AVI):** Logic operation of the NOR gate for inputs (0, 1) and its corresponding 0 output. The values of the parameters $B_z, F_{1,2,3}$ are the same as in MovieS4. The corresponding process is illustrated in this Supporting Information. The video is displayed 10 times faster.

- **MovieS7(.AVI):** Logic operation of the *NOR* gate for a inputs (1,1) and its corresponding 0 output. The values of the parameters $B_z, F_{1,2,3}$ are the same as in MovieS4. The corresponding process is illustrated in this Supporting Information. The video is displayed 10 times faster.

- [1] A. Ortiz-Ambriz and P. Tierno, *Nat. Commun.*, **7**, 021406 (2016).
- [2] K. Jacobs, *Stochastic Processes for Physicists: Understanding Noisy Systems* (Cambridge University Press, 2010) ISBN 9780521765428.

* ptierno@ub.edu

Eidesstattliche Versicherung

Hiermit versichere ich an Eides statt, dass ich die vorliegende Arbeit selbstständig verfasst und keine anderen als die von mir angegebenen Quellen und Hilfsmittel verwendet habe.

Zusätzlich erkläre ich hiermit, dass ich keinerlei frühere Promotionsversuche unternommen habe.

Weiterhin erkläre ich, dass ich die Hilfe von gewerblichen Promotionsberatern bzw. -vermittlern oder ähnlichen Dienstleistern weder bisher in Anspruch genommen habe, noch künftig in Anspruch nehmen werde.

Johannes Löhr
Hummeltal, 28.11.2017